Ε Θ Ν Ι Κ Ο   Μ Ε Τ Σ Ο Β Ι Ο   Π Ο Λ Υ Τ Ε Χ Ν Ε Ι Ο
ΣΧΟΛΗ ΠΟΛΙΤΙΚΩΝ ΜΗΧΑΝΙΚΩΝ - ΤΟΜΕΑΣ ΓΕΩΤΕΧΝΙΚΗΣ
Ηρώων Πολυτεχνείου 9, Πολυτεχνειούπολη Ζωγράφου 157 80
Τηλ: 210 772 3780, Fax: 210 772 3428, e-mail: gbouck@central.ntua.gr
www.georgebouckovalas.com

ΠΡΑΞΗ:

«ΘΑΛΗΣ- ΕΜΠ: ΠΡΩΤΟΤΥΠΟΣ ΣΧΕΔΙΑΣΜΟΣ ΒΑΘΡΩΝ ΓΕΦΥΡΩΝ ΣΕ ΡΕΥΣΤΟΠΟΙΗΣΙΜΟ ΕΔΑΦΟΣ ΜΕ ΧΡΗΣΗ ΦΥΣΙΚΗΣ ΣΕΙΣΜΙΚΗΣ ΜΟΝΩΣΗΣ»

MIS 380043

Επιστημονικός Υπεύθυνος: Καθ. Γ. ΜΠΟΥΚΟΒΑΛΑΣ

ΔΡΑΣΗ 3

Αναλυτική μεθοδολογία σχεδιασμού επιφανειακών θεμελιώσεων σε ρευστοποιημένο έδαφος

ΠΑΡΑΔΟΤΕΑ:

Τεχνική Έκθεση Πεπραγμένων (Π3)

Ιανουάριος 2014

Ευρωπαϊκή Ένωση
Ευρωπαϊκό Κοινωνικό Ταμείο
ΕΠΙΧΕΙΡΗΣΙΑΚΟ ΠΡΟΓΡΑΜΜΑ
ΕΚΠΑΙΔΕΥΣΗ ΚΑΙ ΔΙΑ ΒΙΟΥ ΜΑΘΗΣΗ
επένδυση στην κοινωνία της γνώσης
ΥΠΟΥΡΓΕΙΟ ΠΑΙΔΕΙΑΣ & ΘΡΗΣΚΕΥΜΑΤΩΝ, ΠΟΛΙΤΙΣΜΟΥ & ΑΘΛΗΤΙΣΜΟΥ
ΕΙΔΙΚΗ ΥΠΗΡΕΣΙΑ ΔΙΑΧΕΙΡΙΣΗΣ
ΕΣΠΑ 2007-2013
πρόγραμμα για την ανάπτυξη
ΕΥΡΩΠΑΪΚΟ ΚΟΙΝΩΝΙΚΟ ΤΑΜΕΙΟ
Με τη συγχρηματοδότηση της Ελλάδας και της Ευρωπαϊκής Ένωσης

Εκτενής Περίληψη

(Οι βιβλιογραφικές αναφορές παραπέμπουν στην πλήρη Τεχνική Έκθεση η οποία ακολουθεί)

ΕΙΣΑΓΩΓΗ

Η παρούσα Τεχνική Έκθεση αποτελεί το **3ο Παραδοτέο (Π3)** του Ερευνητικού Προγράμματος με τίτλο:

ΘΑΛΗΣ-ΕΜΠ (MIS 380043)
Πρωτότυπος Σχεδιασμός Βάθρων Γεφυρών σε Ρευστοποιήσιμο Έδαφος με Φυσική Σεισμική Μόνωση

με Συντονιστή (Ερευνητικό Υπεύθυνο) τον Γεώργιο Μπουκοβάλα Καθηγητή ΕΜΠ.

Συγκεκριμένα, παρουσιάζονται τα αποτελέσματα της **Δράσης Δ3**, με τίτλο:

«Αναλυτική μεθοδολογία σχεδιασμού επιφανειακών θεμελιώσεων σε ρευστοποιημένο έδαφος».

Το αντικείμενο της Δράσης Δ3 περιγράφεται στην εγκεκριμένη ερευνητική πρόταση ως ακολούθως:

«Οι δραστηριότητες που θα απαιτηθούν για την διατύπωση της εν λόγω αναλυτικής μεθοδολογίας σχεδιασμού είναι οι ακόλουθες:

(α) *Θα διατυπωθούν αναλυτικές λύσεις για τον υπολογισμό της απομειωμένης στατικής Φ.Ι. επιφανειακών θεμελιώσεων, μετά το πέρας της σεισμικής δόνησης και ενόσω το έδαφος τελεί ακόμη υπό καθεστώς ρευστοποίησης.*

(β) *Θα διατυπωθούν αναλυτικές λύσεις για τον υπολογισμό των καθιζήσεων κατά την περίοδο της δόνησης, οι οποίες θα λαμβάνουν υπόψη τη δυναμική αλληλεπίδραση εδάφους-ανωδομής, καθώς και τη συζευγμένη ανάπτυξη πίεσης πόρων και αντίστοιχη μείωση της διατμητικής αντοχής του εδάφους.*

(γ) *Προ της εξαγωγής τελικών συμπερασμάτων, η αξιοπιστία των αναλυτικών λύσεων θα αξιολογηθεί σε σύγκριση με δημοσιευμένα αποτελέσματα από καλά τεκμηριωμένα πειράματα υπό κλίμακα (σε φυγοκεντριστή ή σε σεισμική τράπεζα μεγάλων διαστάσεων), καθώς και καταγεγραμμένα πραγματικά περιστατικά αστοχίας (ή/και ευστοχίας) επιφανειακών θεμελιώσεων σε ρευστοποιημένο έδαφος».*

Τα ανωτέρω στάδια της έρευνας ολοκληρώθηκαν επιτυχώς και οδήγησαν στην διατύπωση μιας ολοκληρωμένης μεθοδολογίας για τον υπολογισμό των καθιζήσεων (ολικών, διαφορικών και στροφών), καθώς και της απομειωμένης φέρουσας ικανότητας των βάθρων θεμελίωσης της γέφυρας, όπως περιγράφεται ακολούθως.

ΠΡΟΤΕΙΝΟΜΕΝΗ ΜΕΘΟΔΟΛΟΓΙΑ

(Α) Παράμετροι Επιτελεστικότητας Βάθρων Γεφυρών

Η εφαρμογή κριτηρίων επιτελεστικότητας για τον σχεδιασμό οποιασδήποτε κατασκευής επιβάλλει την εκτίμηση της συμπεριφοράς σε όλες τις πιθανές μορφές παραμόρφωσης. Για την περίπτωση γεφυρών αυτές απεικονίζονται σχηματικά στο **Σχήμα 1** και περιλαμβάνουν τα ακόλουθα (Barker et al. 1991):

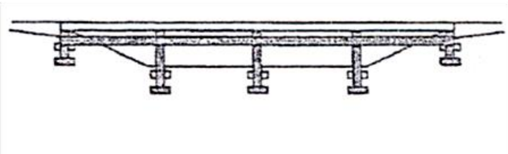

a. Ομοιόμορφη καθίζηση

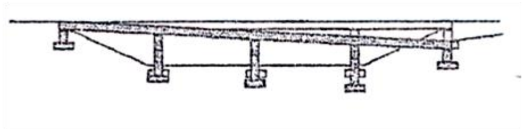

b. Ομοιόμορφη στροφή (θ)

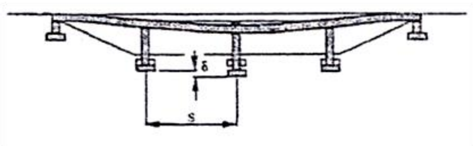

c. Διαφορική καθίζηση
(Συμμετρικής μορφής)

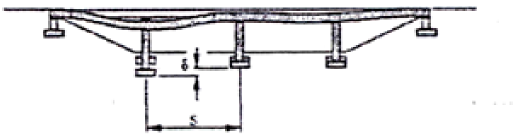

d. Διαφορική καθίζηση
(Μη-συμμετρικής μορφής)

Σχήμα 1: Μορφές καθίζησης και στροφικής καταπόνησης γεφυρών (Barker et al., 1991).

- **Ομοιόμορφη καθίζηση (ρ).-** Στην περίπτωση αυτή κάθε βάθρο παρουσιάζει την ίδια υποχώρηση (**Σχήμα 1α**). Παρόλο που η ομοιόμορφη καθίζηση δεν καταπονεί την γέφυρα, η ανάπτυξη της σε υπερβολικό βαθμό μπορεί να προκαλέσει λειτουργικά προβλήματα, όπως ανεπαρκές ύψος διαβάσεων, ασυνέχειες μεταξύ δοκών προσέγγισης και καταστρώματος καθώς και ανεπαρκή στράγγιση στα άκρα της γέφυρας.
- **Ομοιόμορφη στροφή (θ) γύρω από τον διαμήκη άξονα.-** Σχετίζεται με την ανάπτυξη καθιζήσεων που μεταβάλλονται γραμμικά κατά μήκος του άξονα της γέφυρας (**Σχήμα 1β**). Η ανάπτυξη στροφής είναι πιο συνήθης σε δύσκαμπτες γέφυρες με ένα άνοιγμα. Δεν συνοδεύονται από καταπόνηση της ανωδομής, παρά μόνον στην περίπτωση μη μονολιθικών συνδέσεων ανάμεσα στα επιμέρους τμήματα της γέφυρας. Ωστόσο, από πλευράς λειτουργικότητας, είναι πιθανόν να παρατηρηθούν τα ίδια προβλήματα με την περίπτωση των ομοιόμορφων καθιζήσεων.
- **Διαφορική καθίζηση (δ).-** Η ανάπτυξη διαφορικής καθίζησης οδηγεί σε καταπόνηση της ανωδομής στην περίπτωση που το κατάστρωμα είναι συνεχές και εδράζεται σε περισσότερα των τριών θεμελίων. Μπορεί να είναι συμμετρικής ή μη-συμμετρικής μορφής όπως φαίνεται στο **Σχήμα 1γ και 1δ**. Σχετίζεται με την δημιουργία λειτουργικών προβλημάτων όπως ανεπαρκές ύψος διαβάσεων, δυσχέρεια στράγγισης και παραμόρφωση του οδοστρώματος στις ενώσεις με τις δοκούς προσέγγισης.

Με βάση τα ανωτέρω, ο σχεδιασμός επιφανειακών θεμελίων σε γέφυρες με βάση κριτήρια επιτελεστικότητας θα πρέπει να συμπεριλαμβάνει την εκτίμηση των ακόλουθων μεγεθών:

- Δυναμικές καθιζήσεις, ρ_{dyn}
- Διαφορικές καθιζήσεις, δ
- Στροφή, θ

(Β) Δυναμικές Καθιζήσεις, ρ_{dyn} – ΑΡΓΙΛΙΚΗ κρούστα εδάφους

Στην περίπτωση όπου η μη-ρευστοποιήσιμη κρούστα αποτελείται από μια αδιαπέραστη αργιλική στρώση, ο σχεδιασμός μπορεί να πραγματοποιηθεί με τη μεθοδολογία των Karamitros et al. (2013).

Απομειωμένη φέρουσα ικανότητα, $q_{ult,deg}$

Η απομειωμένη φέρουσα ικανότητα, $q_{ult,deg}$, υπολογίζεται με βάση το σύνθετο μηχανισμό αστοχίας τωνMeyerhof and Hanna (1978), ως εξής:

$$q_{ult,deg} = \min\begin{Bmatrix}(\pi+2)c_u F_{cs} \\ q_{ult,deg}^{c-s}\end{Bmatrix} \tag{1}$$

$$q_{ult,deg}^{c-s} = 2c_u \frac{H}{B} s - \gamma' H + \frac{1}{2}\gamma' B N_\gamma F_{\gamma s} + \gamma' H N_q F_{qs} \tag{2}$$

όπου B το πλάτος του θεμελίου, H το πάχος της αργιλικής κρούστας, c_u η αστράγγιστη διατμητική αντοχή της κρούστας και γ′ το υπο-άνωση ειδικό βάρος, το οποίο θεωρείται ενιαίο για την άμμο και για την άργιλο. Οι συντελεστές φέρουσας ικανότητας υπολογίζονται κατά Vesic (1973):

$$N_q = \tan^2\left(45 + \frac{\phi}{2}\right) e^{\pi \tan\phi_{deg}}$$

$$N_\gamma = 2\left(N_q + 1\right)\tan\phi_{deg}$$

Οι συντελεστές σχήματος υπολογίζονται κατά De Beer (1970):

$$F_{cs} = 1 + \frac{1}{\pi+2}\frac{B}{L}$$

$$F_{\gamma s} = 1 - 0.4\frac{B}{L}$$

$$F_{qs} = 1 + \frac{B}{L}\tan\phi$$

και η παράμετρος s στην Εξίσωση (2) υπολογίζεται κατά Meyerhof & Hanna (1978):

$$s = 1 + \frac{B}{L}$$

Στις παραπάνω εξισώσεις, η επίδραση της ρευστοποίησης λαμβάνεται υπόψη μέσω της απομείωσης της γωνίας τριβής της άμμου:

$$\phi_{deg} = a\tan\left[(1-U)\tan\phi_o\right] \tag{3}$$

όπου:

ϕ_o	η αρχική γωνία τριβής της μη-ρευστοποιημένης άμμου
U	ο δείκτης υπερπιέσεων πόρων που αναπτύσσεται στην άμμο

Ο ενιαίος δείκτης υπερπιέσεων πόρων U υπολογίζεται ως εξής:

$$U = \frac{U_{foot} + \left(1 + B/L\right) \cdot U_{ff}}{2 + B/L} \tag{4}$$

όπου:

$U_{ff} \approx 1.0$: Δείκτης υπερπιέσεων πόρων στο ελεύθερο πεδίο

U_{foot}: Δείκτης υπερπιέσεων πόρων κάτω από το θεμέλιο

Ο δείκτης υπερπιέσεων πόρων κάτω από το θεμέλιο υπολογίζεται ως εξής:

$$U_{foot} = \frac{1 - 6.0\,\rho_{dyn}/B}{1 + \Delta\sigma_{v,c}/\sigma'_{vo,c}} \tag{5}$$

όπου:

ρ_{dyn}: Δυναμικές καθιζήσεις

$\Delta\sigma_{v,c}$: Πρόσθετη κατακόρυφη τάση που επιβάλλεται από το φορτίο του θεμελίου στο χαρακτηριστικό βάθος z_c

$\sigma'_{vo,c}$: Αρχική (πριν τη δόνηση) κατακόρυφη ενεργός τάση που ασκείται στο χαρακτηριστικό βάθος z_c

Τέλος, το χαρακτηριστικό βάθος z_c υπολογίζεται ως εξής:

$$z_c = H + \left[1.0 - 0.5\left(\frac{B}{L}\right)^3\right]B \tag{6}$$

Δυναμικές καθιζήσεις, ρ_{dyn}

Οι δυναμικές καθιζήσεις, ρ_{dyn} υπολογίζονται από την παρακάτω εξίσωση:

$$\rho_{dyn} = c \cdot a_{max} T^2 N \left(\frac{Z_{liq}}{B}\right)^{1.5} \left(\frac{1}{FS_{deg}}\right)^3 \tag{7}$$

όπου:

a_{max}: Μέγιστη εδαφική επιτάχυνση

T: Περίοδος της διέγερσης

N: Αριθμός κύκλων φόρτισης

Z_{liq}: Πάχος ρευστοποιήσιμης άμμου

B: Πλάτος θεμελίου

FS_{deg}: Απομειωμένος συντελεστής ασφαλείας (μετά τη ρευστοποίηση)

Ο συντελεστής c στην Εξίσωση (7) είναι ίσος με 0.008 και 0.035 για τετραγωνικό και λωριδωτό θεμέλιο, ενώ για ενδιάμεσες τιμές της αναλογίας πλευρών L/B, μπορεί να υπολογιστεί ως εξής:

$$c = c'\left(1 + 1.65\frac{L}{B}\right) \le 11.65c' \tag{8}$$

όπου c′=0.003

Τέλος, για την περίπτωση μη-αρμονικής σεισμικής διέγερσης η εξίσωση (7) επιβάλλεται αντικαθιστώντας τον όρο $a_{max}T^2N$ με $\pi^2 \cdot \int |v(t)| dt$ όπου v(t) η χρονο-ιστορία της επιβαλλόμενης ταχύτητας.

(Γ) Δυναμικές Καθιζήσεις, ρ_{dyn} – Κρούστα ΒΕΛΤΙΩΜΡΝΟΥ ΕΔΑΦΟΥΣ

Η μεθοδολογία για την περίπτωση θεμελίου που εδράζεται σε βελτιωμένο έδαφος συνοψίζεται στα παρακάτω βήματα:

Βήμα 1: Καθορισμός του συντελεστή αντικατάτασης α_s.- Ο συντελεστής αντικατάστασης α_s υπολογίζεται από το **Σχήμα 2**, συναρτήσει:

- Της αρχικής σχετικής πυκνότητας του εδάφους $D_{r,o}$,
- Του πάχους της βελτίωσης H_{imp},
- (γ) Της μέγιστης τιμής του λόγου υπερπιέσεων πόρων $r_{u,max}$ που επιτρέπεται να αναπτυχθεί εντός της βελτιωμένης ζώνης, (στην πράξη $r_{u,max}$= $r_{u,design}$=0.30 - 0.50).

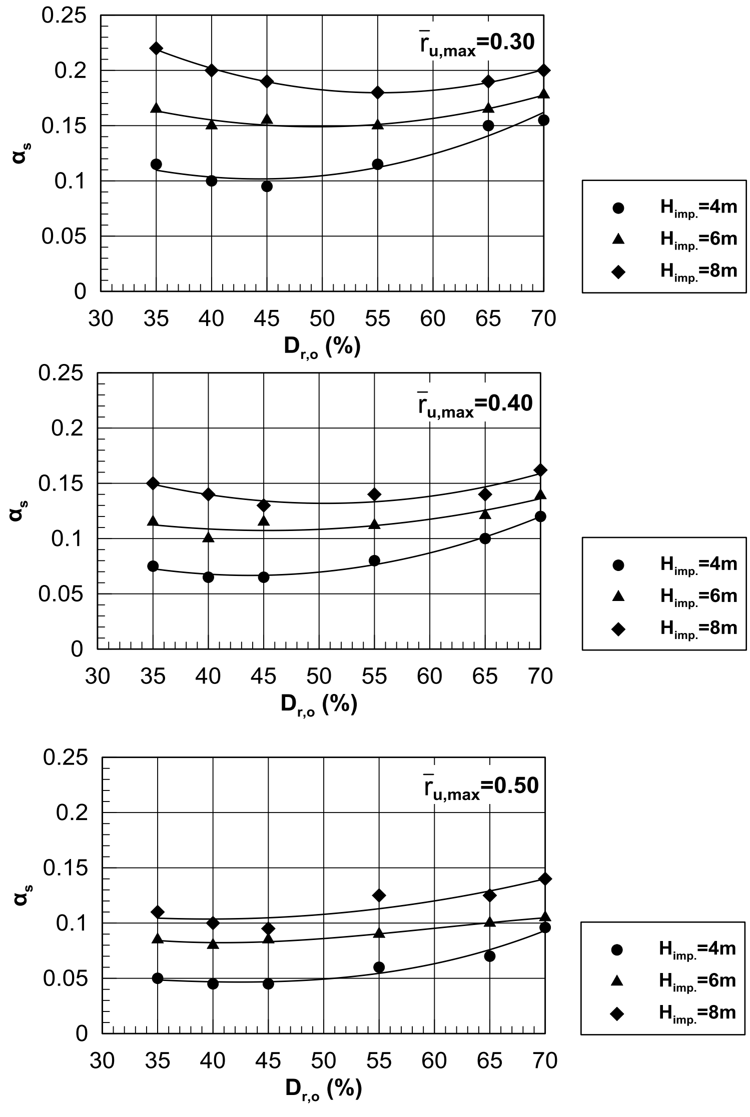

Σχήμα 2: Απαιτούμενος λόγος αντικατάστασης α_s συναρτήσει της αρχικής σχετικής πυκνότητας $Dr_{,o}$(%) και τρία επιτρεπόμενα επίπεδα λόγου $r_{u,max}$.

Βήμα 2: Προσδιορισμός των ισοδύναμων ιδιοτήτων του βελτιωμένου εδάφους.- Η διαπερατότητα k_{eq} και η σχετική πυκνότητα $D_{r,imp}$ της βελτιωμένης ζώνης υπολογίζονται από το **Σχήμα 3** συναρτήσει του συντελεστή αντικατάστασης α_s και της αρχικής σχετικής πυκνότητας του ρευστοποιημένου εδάφους $D_{r,o}$.

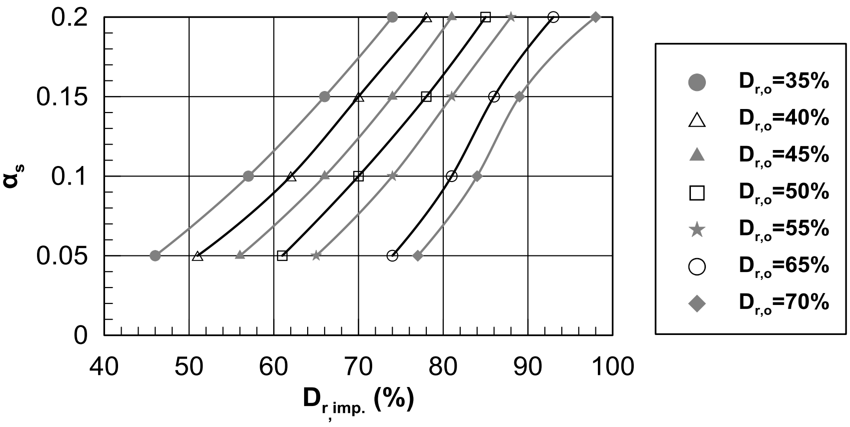

(a)

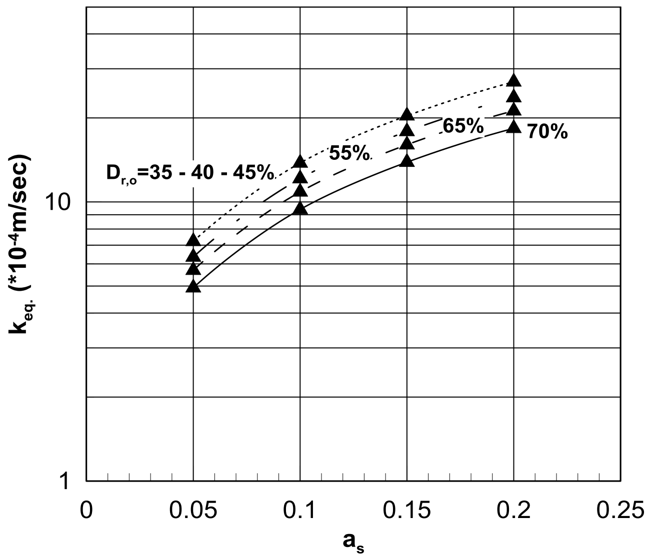

(b)

Σχήμα 3: Εκτίμηση ιδιοτήτων βελτιωμένου εδάφους (α) σχετική πυκνότητα $D_{r,imp}$ και (β) διαπερατότητα $k_{eq.}$, συναρτήσει του λόγου αντικατάστασης $α_s$.

<u>Βήμα 3</u>: Σχεδιασμός σε συνθήκες «άπειρης» βελτίωσης.

<u>Δυναμικές καθιζήσεις $ρ_{dyn}^{inf}$</u>

Οι δυναμικές καθιζήσεις για άπειρη βελτίωση υπολογίζονται ως εξής:

$$ρ_{dyn}^{inf} = 0.019 \cdot α_{max} \left(T_{exc} + 0.633 \cdot T_{soil}\right)^2 \cdot \left(N_o + 2\right) \cdot \left(\frac{1}{FS_{deg}^{inf}}\right)^{0.45} \cdot \left[1 + 0.25 \cdot \left(\frac{1}{FS_{deg}^{inf}}\right)^{4.5}\right] \quad (9)$$

όπου:

a_{max}: Μέγιστη εδαφική επιτάχυνση

T_{exc}: Δεσπόζουσα περίοδος της διέγερσης

T_{soil}: Ελαστική ιδιοπερίοδος της εδαφικής στήλης

N_o: Αριθμός σημαντικών κύκλων φόρτισης

FS_{deg}^{inf}: Απομειωμένος συντελεστής ασφαλείας

Απομειωμένη φέρουσα ικανότητα, $q_{ult,deg}^{inf}$

Η απομειωμένη φέρουσα ικανότητα $q_{ult,deg}^{inf}$ υπολογίζεται σύμφωνα με την παρακάτω αναλυτική σχέση, που προέκυψε από τροποποίηση της εξίσωσης των Meyerhof & Hanna (1978):

$$q_{ult,deg}^{inf} = \min \left\{ \begin{array}{c} \frac{1}{2}\gamma' \cdot B \cdot N_{\gamma 1} \\ \gamma' H_1^2 K_s \frac{\tan\varphi_{1,deg}}{B} + \gamma'[(1+\alpha)^2 - 1] H_1^2 K_s \cdot \frac{\tan\varphi_{2,deg}}{B} - \gamma'(1+\alpha)H_1 + \\ + \frac{1}{2}\gamma' B N_{\gamma 2} + \gamma'(1+\alpha)H_1 N_{q2} \end{array} \right\} \quad (10)$$

όπου B το πλάτος του θεμελίου, H_1 το πάχος της βελτιωμένης κρούστας και γ΄ το ενεργό ειδικό βάρος του εδάφους. Οι συντελεστές N_q και N_γ υπολογίζονται κατά Vesic (1973):

$$\begin{aligned} N_q &= \tan^2(45+\varphi_{deg}/2)e^{\pi\tan\varphi_{deg}} \\ N_\gamma &= 2(N_q+1)\tan\varphi_{deg} \end{aligned} \quad (11)$$

Μεταξύ της βελτιωμένης κρούστας και της ρευστοποιήσιμης άμμου σχηματίζεται μια μεταβατική ζώνη μερικώς ρευστοποιημένου φυσικού εδάφους ($0< r_u < 1.0$), ως αποτέλεσμα της ταχείας αποτόνωσης των υπερπιέσεων πόρων προς την, αρκετά πιο διαπερατή, βελτιωμένη κρούστα. Οι συντελεστές α και K_s σχετίζονται με το πάχος και την διατμητική αντοχή της μεταβατικής ζώνης:

$$\alpha = 3.76 \cdot \left[\frac{k_{eq} \cdot T \cdot N}{H_{imp}} \right]^{0.256} \quad (12)$$

$$K_s = 1.0 \cdot \left(\frac{q}{p_\alpha}\right)^{-0.30} \left(\frac{H_{imp}}{B} \right)^{-0.50} \quad (13)$$

Η επίδραση της ρευστοποίησης και της ανάπτυξης υπερπιέσεων πόρων λαμβάνεται υπόψη μειώνοντας κατάλληλα τη γωνία τριβής της άμμου:

$$\varphi_{i,deg} = \tan^{-1}\left[(1-U_i)\tan\varphi_{i,ini}\right] \quad (14)$$

όπου ο δείκτης «ini» αναφέρεται στη γωνία τριβής του εδάφους στην αρχή της δόνησης, το i=1 στη βελτιωμένη ζώνη, το i=2 στην μεταβατική ζώνη και το i=3 στη ρευστοποιήσιμη άμμο. Οι αντίστοιχοι λόγοι υπερπιέσεων πόρων U_i υπολογίζονται ως εξής:

- **Δείκτης υπερπιέσεων πόρων στη βελτιωμένη ζώνη *U_1*.-** Ο μέσος δείκτης υπερπιέσεων πόρων U_1 αναφέρεται σε συνθήκες ελεύθερου πεδίου και στο τέλος της δόνησης και εκφράζεται ως συνάρτηση του επιτρεπόμενου δείκτη υπερπιέσεων πόρων U_{design}:

$$U_1 = 0.54 U_{design} \quad (15)$$

- **Δείκτης υπερπιέσεων πόρων στη μεταβατική ζώνη *U₂*.-** Η παράμετρος U_2 αναφέρεται στο μέσο δείκτη υπερπιέσεων πόρων στην μεταβατική μη-ρευστοποιημένη ζώνη του φυσικού εδάφους και υπολογίζεται σαν ο μέσος όρος του U_1 και του δείκτη υπερπιέσεων πόρων στο ρευστοποιημένο έδαφος:

$$U_2 = \frac{(1+U_1)}{2} = \frac{(1+0.54U_{design})}{2} \tag{16}$$

- **Δείκτης υπερπιέσεων πόρων στο ρευστοποιημένο έδαφος *U₃*.-** Ο δείκτης υπερπιέσεων πόρων U_3 αναφέρεται στο ρευστοποιημένο έδαφος, σε μια αντιπροσωπευτική περιοχή κάτω από το θεμέλιο και την βελτιωμένη κρούστα:

$$U_3 = 086 \cdot \left(\frac{q_{ult,deg}^{inf}}{p_a}\right)^{-0.18} \leq 1.00 \tag{17}$$

Λόγω της εξάρτησης του U_3 από το $q_{ult,deg}$, οι Εξισώσεις (10) και (17) λύνονται επαναληπτικά μέχρι να υπάρξει σύγκλιση και, στη συνέχεια, υπολογίζεται ο απομειωμένος συντελεστής ασφάλειας $F.S._{deg}^{inf*}$. Για την περαιτέρω αύξηση της ακρίβειας της προτεινόμενης μεθοδολογίας, επιβάλλεται ο παρακάτω διορθωτικός συντελεστής:

$$FS_{deg}^{inf} = \frac{FS_{deg}^{inf*}}{0.05 + 0.60\left(FS_{deg}^{inf*}\right)^{0.85}} > 0.60FS_{deg}^{inf*} \tag{18}$$

<u>Βήμα 4</u>: Σχεδιασμός σε συνθήκες «πεπερασμένης» βελτίωσης.

<u>Δυναμικές καθιζήσεις ρ_{dyn}</u>

Ο λόγος $\rho_{dyn}^{inf}/\rho_{dyn}$ υπολογίζεται αναλυτικά ως εξής:

$$\frac{\rho_{dyn}^{inf}}{\rho_{dyn}} = 1 - \exp\left[-1.05\left(\frac{H_{imp}}{B}\right)^{-1}\left(\frac{L_{imp}}{B}\right)^{0.30}\right] \tag{19}$$

όπου H_{imp} και L_{imp} το πάχος και το πλάτος της βελτιωμένης ζώνης αντίστοιχα.

<u>Απομειωμένη φέρουσα ικανότητα και $q_{ult,deg}$ και αντίστοιχος FS_{deg}</u>

Ο λόγος $F.S._{deg}/F.S._{deg}^{inf}$ υπολογίζεται από την παρακάτω μη-γραμμική εξίσωση:

$$\left(\frac{FS_{deg}}{FS_{deg}^{inf}}\right)^{-0.45} = \left\{1 - \exp\left[-1.05\left(\frac{H_{imp}}{B}\right)^{-1}\left(\frac{L_{imp}}{B}\right)^{0.30}\right]\right\}\frac{\left(FS_{deg}^{inf}\right)^{4.5} + 0.25\left(\frac{FS_{deg}}{FS_{deg}^{inf}}\right)^{4.5}}{\left(FS_{deg}^{inf}\right)^{4.5} + 0.25} \tag{20}$$

Δεδομένης της πολυπλοκότητας της Εξίσωσης (20), προτείνεται μια σειρά από απλοποιημένες αναλυτικές εξισώσεις, που επιτρέπει την απευθείας εκτίμηση του απομειωμένου συντελεστή ασφαλείας FS_{deg} για «πεπερασμένο» πλάτος βελτίωσης συναρτήσει του απαιτούμενου λόγου L_{imp}/H_{imp} και του εύρους τιμών του FS_{deg}^{inf}:

$$FS_{deg}^{inf} = 1.50 - 2.50: \quad \frac{F.S._{deg}}{F.S._{deg}^{inf}} = 1 - \exp\left[-0.82\left(\frac{H_{imp}}{B}\right)^{-1.03}\left(\frac{L_{imp}}{B}\right)^{0.29}\right] \tag{21}$$

$$FS_{deg}^{inf} = 2.50 - 3.50: \frac{F.S._{deg}}{F.S._{deg}^{inf}} = 1 - \exp\left[-0.64\left(\frac{H_{imp}}{B}\right)^{-1.30}\left(\frac{L_{imp}}{B}\right)^{0.34}\right] \tag{22}$$

$$FS_{deg}^{inf} = 3.50 - 4.50: \frac{F.S._{deg}}{F.S._{deg}^{inf}} = 1 - \exp\left[-0.56\left(\frac{H_{imp}}{B}\right)^{-1.30}\left(\frac{L_{imp}}{B}\right)^{0.38}\right] \tag{23}$$

<u>Βήμα 5</u>: Ανάλυση Κόστους - Οφέλους.- Ο σχεδιασμός της ζώνης βελτίωσης (ώστε να θεωρείται βέλτιστος) πρέπει να πραγματοποιείται τόσο σε όρους επιτελεστικότητας όσο και σε όρους κόστους. Για τον σκοπό αυτό, οι παραπάνω απλοποιημένες αναλυτικές σχέσεις μετασχηματίζονται κατάλληλα ώστε να συμπεριλάβουν τον αντίστοιχο όγκο βελτίωσης V_{imp}, ο οποίος για λωριδωτό φορτίο ορίζεται ως το γινόμενο του βάθους H_{imp} με το πλάτος L_{imp}:

$$\frac{\rho_{dyn}^{inf}}{\rho_{dyn}} = 1 - \exp\left[-1.05\left(\frac{H_{imp}}{B}\right)^{-1.30}\left(\frac{V_{imp}}{B^2}\right)^{0.30}\right] \tag{24}$$

$$FS_{deg}^{inf} = 1.50 - 2.50: \frac{FS_{deg}}{FS_{deg}^{inf}} = 1 - \exp\left[-0.82\left(\frac{H_{imp}}{B}\right)^{-1.32}\left(\frac{V_{imp}}{B^2}\right)^{0.29}\right] \tag{25}$$

$$FS_{deg}^{inf} = 2.50 - 3.50: \frac{FS_{deg}}{FS_{deg}^{inf}} = 1 - \exp\left[-0.64\left(\frac{H_{imp}}{B}\right)^{-1.54}\left(\frac{V_{imp}}{B^2}\right)^{0.34}\right] \tag{26}$$

$$FS_{deg}^{inf} = 3.50 - 4.50: \frac{FS_{deg}}{FS_{deg}^{inf}} = 1 - \exp\left[-0.56\left(\frac{H_{imp}}{B}\right)^{-1.68}\left(\frac{V_{imp}}{B^2}\right)^{0.38}\right] \tag{27}$$

Οι παραπάνω εξισώσεις παρουσιάζονται σε διαγράμματα σχεδιασμού, που επιτρέπουν την άμεση εκτίμηση των δυναμικών καθιζήσεων και του απομειωμένου συντελεστή ασφαλείας. Πιο συγκεκριμένα, στο **Σχήμα 4** παρουσιάζεται ο λόγος των δυναμικών καθιζήσεων $\boldsymbol{\rho_{dyn}/\rho_{dyn}^{inf}}$ δίνεται συναρτήσει του V_{imp}/B^2, για επτά διακριτές τιμές του H_{imp}/B. Αντίστοιχα στο **Σχήμα 5** υπολογίζεται ο απομειωμένος συντελεστής ασφαλείας $\boldsymbol{F.S._{deg}/F.S._{deg}^{inf}}$. Στα ανωτέρω Σχήματα επισημαίνεται το εύρος για το οποίο περαιτέρω αύξηση του όγκου V_{imp} δίνει μικρό όφελος (δυσανάλογη αύξηση του κόστους), το οποίο και συγκρίνεται με τις αντίστοιχες προβλέψεις των JDFA (1974) και Tsuchida et al. (1976). Σημειώνεται, ωστόσο, ότι οι τελευταίες δεν λαμβάνουν υπόψη την ευεργετική δράση των στραγγιστηρίων όσον αφορά την αποτόνωση των υπερπιέσεων πόρων.

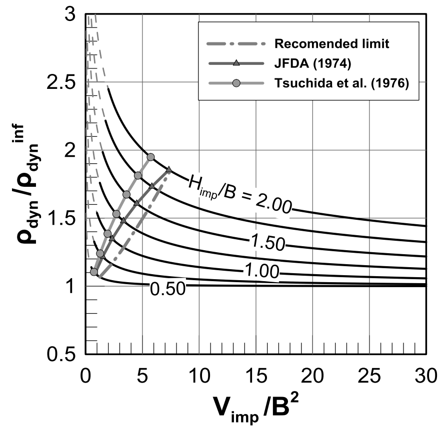

Σχήμα 4: Αδιαστατοποιημένες δυναμικές καθιζήσεις συναρτήσει του λόγου V_{imp}/B^2 για διάφορες τιμές του αδιαστατοποιημένου πάχους βελτίωσης H_{imp}/B.

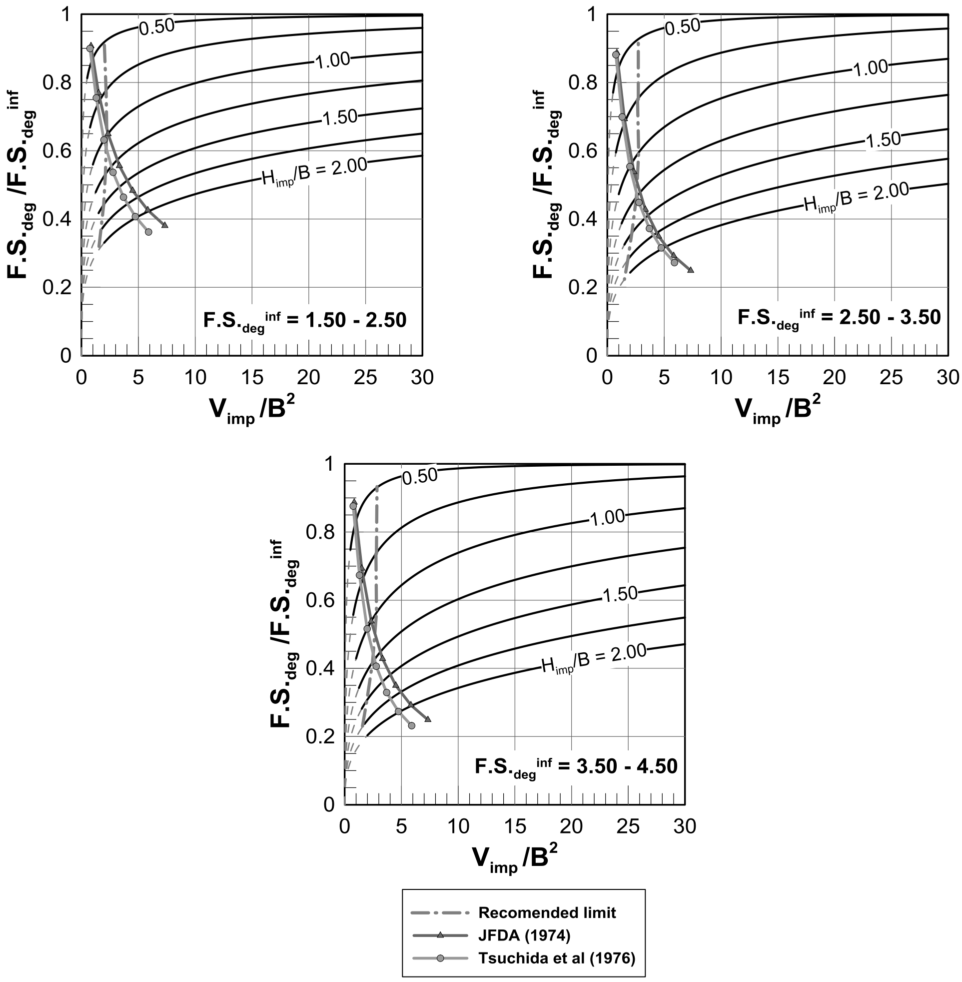

Σχήμα 5: Αδιαστατοποιημένος απομειωμένος συντελεστής ασφαλείας συναρτήσει του λόγου V_{imp}/B^2 για διάφορες τιμές του αδιαστατοποιημένου πάχους H_{imp}/B και τρεις τιμές του FS_{deg}^{inf}.

<u>Βήμα 6</u>: Επίδραση μήκους θεμελίου, L.- Για την περίπτωση πεδίλων πλάτους B και μήκους L (B<L), ένα *ασφαλές άνω όριο* των δυναμικών καθιζήσεων και του απομειωμένου συντελεστή ασφαλείας εκτιμάται ως εξής:

$$\rho_{dyn} = \left(1 - \frac{0.6}{L/B}\right) \cdot \rho_{dyn,strip}$$

$$FS_{deg} = \left(1 - \frac{0.4}{L/B}\right) \cdot FS_{deg,strip}$$

(28)

οπου, $\rho_{dyn,strip}$ και $FS_{deg,strip}$, οι δυναμικές καθιζήσεις και ο απομειωμένος συντελεστής ασφαλείας ισοδύναμου λωριδωτού θεμελίου πλάτους B_{strip}, το οποίο υπολογίζεται συναρτήσει των B και L ως εξής:

$$B_{strip} / B = 0.33 + 0.234 \cdot \ln(B/L) \quad (29)$$

(Δ) Διαφορικές καθιζήσεις, δ & Στροφή, θ

Για τον υπολογισμό της διαφορικής καθίζησης και της στροφής συνεκτιμήθηκαν οι ακόλουθες ομάδες εμπειρικών συσχετίσεων:

α. Εμπειρικές σχέσεις εκτίμησης **διαφορικής καθίζησης (δ) και γωνιακής παραμόρφωσης (β) μεμονωμένων πεδίλων λόγω στατικής καθίζησης** (Skempton & MacDonald, 1956; Sowers, 1962; Bjerrum, 1963; Justo, 1987).

β. Εμπειρικές σχέσεις εκτίμησης **διαφορικής καθίζησης (δ) και γωνιακής παραμόρφωσης (β) κοιτωστρώσεων λόγω στατικής καθίζησης** (Skempton & MacDonald, 1956).

γ. Εμπειρικές σχέσεις εκτίμησης **στροφής (θ) λόγω δυναμικής καθίζησης** (Yasuda et al., 2014).

Όπως προκύπτει από τα παραπάνω, η υπάρχουσα βιβλιογραφία για την εκτίμηση της διαφορικής καθίζησης και στροφής λόγω δυναμικής φόρτισης είναι πολύ περιορισμένη. Για τον σκοπό αυτό οι «στατικές» σχέσεις των ομάδων (α) και (β) συναξιολογήθηκαν με αυτήν της κατηγορίας (γ) θεωρώντας ότι η στροφή του θεμελίου θα είναι ίση με την γωνιακή παραμόρφωση (β=θ). Για την περίπτωση κοιτοστρώσεων αυτή είναι μια εύλογη παραδοχή, ωστόσο για την περίπτωση μεμονωμένων πεδίλων μπορεί να ληφθεί μόνο ως μια αδρή προσέγγιση. Εν κατακλείδι, συγκριτική αξιολόγηση των παραπάνω συσχετίσεων οδήγησε στις παρακάτω απλοποιητικές σχέσεις υπολογισμού της διαφορικής καθίζησης, δ, και της στροφής, θ, συναρτήσει της ολικής καθίζησης, ρ:

$$\delta = (0.60 \div 0.75) \cdot \rho \leq \rho \quad (30)$$

$$\theta(deg) = \alpha_D \cdot (0.030 \div 0.042) \cdot \rho(cm) \quad (31)$$

Όπου α_D συντελεστής ώστε να ληφθεί υπόψη ο τύπος της φόρτισης:

$$\alpha_D = \begin{cases} 1.00 \ (\text{στατική φόρτιση}) \\ 1.35 \ (\text{δυναμική φόρτιση}) \end{cases} \quad (32)$$

NATIONAL TECHNICAL UNIVERSITY OF ATHENS
SCHOOL OF CIVIL ENGINEERING – GEOTECHNICAL DEPARTMENT
9 Iroon Polytechniou str., 15780, Zografou Campus, Zografou, Greece
Tel: +30 210 772 3780, Fax: +30 210 772 3428, e-mail: gbouck@central.ntua.gr
www.georgebouckovalas.com

PROJECT:

«THALIS-NTUA: INNOVATIVE DESIGN OF BRIDGE PIERS ON LIQUEFIABLE SOILS WITH THE USE OF NATURAL SEISMIC ISOLATION»

MIS: 380043

Coordinator: PROF. G. BOUCKOVALAS

WORK PACKAGE 3

Analytical methodology for the design of shallow foundations on liquefiable soil

DELIVERABLES

Technical Report (D3)

January 2014

European Union
European Social Fund
OPERATIONAL PROGRAMME
EDUCATION AND LIFELONG LEARNING
investing in knowledge society
MINISTRY OF EDUCATION & RELIGIOUS AFFAIRS, CULTURE & SPORTS
MANAGING AUTHORITY
Co-financed by Greece and the European Union
NSRF 2007-2013
programme for development
EUROPEAN SOCIAL FUND

Table of Contents

1

Introduction

This Technical Report constitutes Final Deliverable 3 of the Research Project with title:

THALIS-NTUA (MIS 380043)

Innovative Design of Bridge Piers on Liquefiable Soils with the use of Natural Seismic Isolation

performed under the general coordination of Professor **George Bouckovalas** (Scientific Responsible).

Namely, it presents the actions taken and the associated results of **Work Package WP3**, entitled:

"Analytical methodology for the design of shallow foundations on liquefiable soil".

The Scope of **Work Package WP3**, has been described in the approved Research Proposal as follows:

"The work tasks required to establish an integrated methodology for the design of shallow foundations on liquefiable soil are the following:

(a) *Develop analytical solutions for the computation of the degraded static bearing capacity of shallow foundations, at the end of shaking, while the soil is still in a liquefied state. This problem will be originally treated with the help of existing static analytical solutions for 2-layered soil profiles, where the top layer (non liquefiable "crust") will retain its initial shear strength, while the underlying (liquefiable) layer will undergo significant shear strength degradation. Next, the effect of the various (soil, excitation and foundation) problem parameters will be evaluated numerically, with the upgraded methodology developed in W.P. 2. The analytical static solutions will guide this later numerical part of the study.*

(b) *The computation of footing settlements is considerably more challenging than the previous task, since it concerns the stage of shaking and consequently has to take into account the dynamic soil-foundation interaction, as well as the coupled excess pore pressure build and shear strength degradation in the liquefiable soil. Hence, this problem will be approached both analytically and numerically. Initially, an analytical solution will be pursued using the Newmark's simplified "sliding block" model. Next, the problem will be investigated* *numerically, with the upgraded methodology developed in W.P. 2, so that the various (soil, excitation and foundation) parameters which affect the problem are identified and their effect is quantitatively evaluated. The analytical solution obtained with Newmark's sliding block method will guide the numerical part of the study.*

(c) *Before concluding on this W.P., the accuracy of any proposed relations will be evaluated and calibrated against published results from well documented:*

- *model tests performed in centrifuge or large shaking table facilities in Japan, U.S.A. (e.g. U.C. Davis and R.P.I.) and the United Kingdom (e.g. University of Cambridge),*
- *actual case studies from seismic foundation failures in liquefiable soils, from the recent strong earthquakes in Japan, Chile, New Zealand, Turkey or Philippines."*

Work Tasks (a), (b) and (c) above have been successfully executed, as described in the following Chapters.

2

Literature review

2.1 General

Liquefiable soils are currently categorized by all seismic codes as extreme ground conditions where, following a positive identification of this hazard, the construction of surface foundations is essentially allowed only after proper soil treatment. For instance, according to Eurocode 8, Part 5:

"If the soils are found to be susceptible to liquefaction and the ensuing effects are deemed capable of affecting the load bearing capacity or the stability of the foundations, adequate foundation safety shall be obtained by appropriate ground improvement methods and/or by pile foundations transferring loads to layers not susceptible to liquefaction…Ground improvement against liquefaction should either compact the soil to increase its penetration resistance beyond the dangerous range, or use drainage to reduce the excess pore-water pressure generated by ground shaking."

Thus, much research has been invested in the previous years, focusing on the evaluation of the degraded bearing capacity and the associated seismic settlements of shallow foundations resting on liquefiable soil. The accurate estimation of the above could potentially ensure a viable performance-based design, at least for the case where a sufficiently thick and shear resistant non-liquefiable soil crust exists between the foundation and the liquefiable soil. In the present chapter current simplified (analytical or empirical) methodologies for the estimation of the bearing capacity degradation and the seismic settlement accumulation of footings on liquefiable subsoil are thoroughly described. Special emphasis is placed on the integrated methodology recently proposed by Karamitros, Bouckovalas, Chaloulos, et al. (2013) and Karamitros, Bouckovalas, and Chaloulos (2013) which served as a starting point for the investigation performed during the present research program.

2.2 Simplified methodologies for the estimation of seismic settlements and bearing capacity degradation

2.2.1 Free-field conditions

Liquefaction-induced settlements under free-field conditions may be evaluated using the empirical charts of Tokimatsu and Seed (1987) and Ishihara and Yoshimine (1992). Both these methods have been based on laboratory test data, which indicate that the volumetric strain resulting from the dissipation of pore water pressures following initial liquefaction varies with the relative density of the sand and the maximum shear strain induced during earthquake shaking. In the first case (Tokimatsu & Seed, 1987), the relative density was correlated to the corrected SPT value $(N_1)_{60}$ of the sand, while shear strain was estimated using the $(N_1)_{60}$ value and the cyclic stress ratio CSR (Seed and Idriss 1971; Youd et al. 2001). This led to design charts for the direct estimation of liquefaction-induced volumetric strain (**Figure 2.1a**). In the approach of Ishihara & Yoshimine (1992), liquefaction-induced volumetric strain may be estimated using the family of curves shown in **Figure 2.1b**, as functions of either the factor of safety against liquefaction FS_L (Seed & Idriss, 1971, Youd et al. 2001), or the maximum cyclic shear strain γ_{max}, as well as the relative density D_r, the SPT resistance N_1 or the CPT resistance q_{c1}. Integration of the volumetric strain over the thickness of the liquefied layer consequently produces the liquefaction-induced settlement.

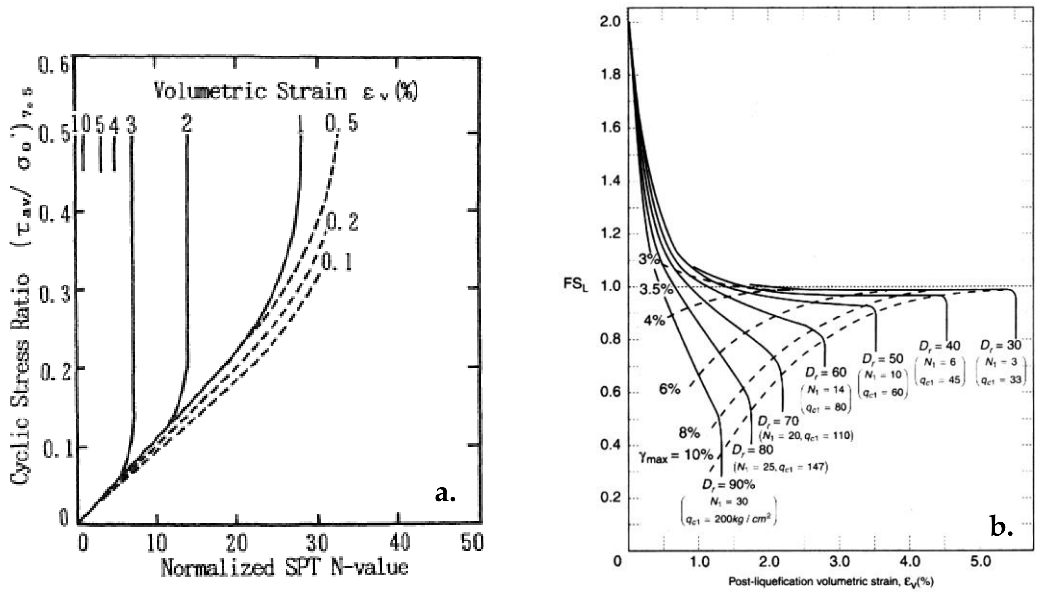

Figure 2.1: Chart for the estimation of post-liquefaction volumetric strain of clean sand, after (a) Tokimatsu & Seed (1987) and (b) Ishihara & Yoshimine (1992).

Σχήμα 2.1: Διάγραμμα εκτίμησης ογκομετρικής παραμόρφωσης λόγω ρευστοποίησης καθαρής άμμου (a) Tokimatsu & Seed (1987) and (b) Ishihara & Yoshimine (1992).

Both these methodologies have been verified against case studies from recent earthquakes, and have been proved to provide a level of accuracy suitable for many engineering purposes. However, these methodologies cannot be used to predict liquefaction-induces settlements of footings, as the controlling mechanisms of this phenomenon differ from the free-field conditions. More specifically, free-field settlements are induced by volume densification, and consequently they take place during the dissipation of earthquake–induced excess pore pressures, mostly after the end of shaking. On the contrary, footing settlements are associated with the presence of static shear stresses in the foundation soil, and take place mostly during (not after) shaking.

2.2.2 Ishihara (1995)

Having examined the conditions under which the effects of liquefaction (e.g. sand boils) are manifested or not on the ground surface Ishihara (1985) and Ishihara (1995) attempted to propose a guideline to identify conditions causing or not causing damage to foundations, embedded at depth D, in level ground comprising of a surface, non-liquefiable soil layer with thickness H_1, underlain by a liquefiable sand layer with thickness H_2. More specifically, he assumed that if the footing is embedded to a stiff non-liquefiable soil layer, which lies below the liquefied sand deposit, it will not be affected by liquefaction and it will be therefore free of damage. Moreover, if the footing is placed within the sand deposit undergoing liquefaction, then damage will occur. Finally, when the foundation is installed within the non-liquefiable surface layer, it will be necessary to be placed far from the underlying liquefiable deposit. Then, if H_1 is sufficiently large compared to H_2, the footing will be free from damage.

Based on these considerations, he proposed the boundary curves of **Figure 2.2**, which may be applied to identify conditions of damage or no-damage. These curves were verified against the following case studies:

- A steel framed tower for cables of electric power transmission, which remained intact after the liquefaction of alluvial and reclaimed deposits along the east coast of the Tokyo Bay, during the 1987 Chiba-toho-oki earthquake. The tower foundation was at 4.5m depth, resting on bedrock, which was overlaid by 3m of saturated sand and 1.5 of dry sand.
- Pipelines for the transmission of liquefied natural gas along the coastal line southeast of Chiba City, which remained intact during the same earthquake, as they were laid down on bedrock, at a depth of 2.5m, while liquefaction occurred at depths from 0.6 to 1.8m.
- A large number of damaged and undamaged pile foundations from the 1964 Niigata earthquake (Oshaki, 1966), with an average embedment depth of 8m, located in places with different thickness of liquefiable sand layer H_2 and non-liquefiable surface layer H_1.
- Two factory buildings in the industrial area of Tiangin, which were damaged during the 1976 Tangshan earthquake in Chine. The first was embedded at a depth of 2m, in a 4m thick, non-liquefiable surface mantle, underlain by 5m of liquefiable sand, while the second was founded at a depth of 4m, in a 5.5m thick surface layer, underlain by a 5m thick liquefiable sand layer.
- The column footings of 3 buildings which were damaged during the 1959 Jaltipan earthquake in Mexico. They were placed at 0.8m below the surface of a 1.3m thick silty sand layer, underlain by 1 to 5m of liquefiable sand.

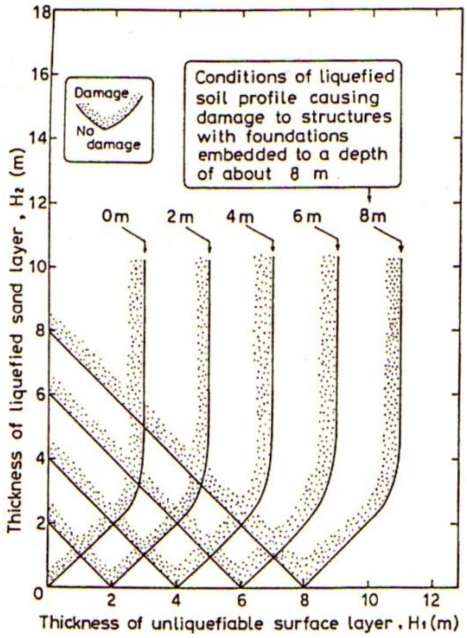

Figure 2.2: Boundary curves identifying conditions of liquefaction-induced damage or non-damage to foundations (Ishihara, 1995).

Σχήμα 2.2: Καμπύλες διαχωρισμού κατάστασης βλάβης και μη-βλάβης λόγω ρευστοποίησης σε θεμελιώσεις (Ishihara, 1995).

2.2.3 Men & Cui (1997)

Men and Cui (1997) presented a simplified methodology for the evaluation of liquefaction potential under buildings. Their method is based on the assumption of a rigid building, with no rocking component of building motion, founded on the surface of an elastic soil, shaken by a vertically upwards propagating SH wave. The method accounts for either a given input displacement, or a given stress. Since the seismic response analysis of buildings is usually based on the base shearing force defined by seismic design codes, focus is given to the "stress" method, which is after all more reliable in the case of large deformation conditions:

According to the method, the free field shear stress τ_f at a depth z below the soil surface is computed using Equation (2.1):

$$\tau_f = 0.65\gamma z \frac{a_{max}}{g} \tag{2.1}$$

where:

γ saturated soil unit weight

a_{max} peak ground acceleration

The additional shear stress τ_{ad} induced by the presence of the building is computed from Equation (2.2), using the Cone Models by Meek and Wolf (1993):

$$\tau_{ad} = \left(\frac{z_0^\tau}{z_0^\tau + z}\right)^i \frac{W}{A}\frac{a_{max}}{g} \tag{2.2}$$

where:

$z_0^\tau = 0.655 r_0$	for poisson's ratio $\nu = 1/3$, with r_0 being the footing's dimension (width or diameter)
i	takes the value of 1 for strip footings and 2 for circular footings
W	building's weight
A	area of foundation

The total dynamic stress τ_t is computed using Equation (2.3):

$$\tau_t = \tau_f + \tau_{ad} \quad (2.3)$$

In a similar way, normal stresses σ_t are computed from free field stresses σ_f and additional footing stresses σ_{ad} as follows:

$$\sigma_t = \sigma_f + \sigma_{ad} \quad (2.4)$$

$$\sigma_f = \gamma' z \quad (2.5)$$

$$\sigma_{ad} = \left(\frac{z_0^\sigma}{z_0^\sigma + z} \right)^i \frac{W}{A} \left(1 \pm \frac{a_{max}}{2g} \right) \quad (2.6)$$

where:

γ'	buoyant soil unit weight
$z_0^\sigma = 2.094 r_0$	for poisson's ratio $\nu = 1/3$

According to the above, three zones may be defined (**Figure 2.3**), namely Zone I, where $\tau_t = \tau_f + \tau_{ad}$ and $\sigma_t = \sigma_f + \sigma_{ad}$, Zone II, where $\tau_t = \tau_f + \tau_{ad}$ and $\sigma_t = \sigma_f$ and Zone III, where $\tau_t = \tau_f$ and $\sigma_t = \sigma_f$. Finally, the τ_t / σ_t ratio may be used in combination with the well-known simplified methods (Seed & Idriss, 1971, Youd et al, 2001), in order to evaluate liquefaction potential.

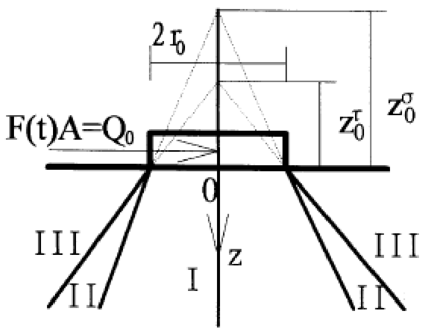

Figure 2.3: Simplified model Men & Cui (1997) for the evaluation of liquefaction potential (Men & Cui 1997).

Σχήμα 2.3: Απλοποιημένο μοντέλο για την εκτίμηση του κινδύνου ρευστοποίησης (Men & Cui 1997).

2.2.4 Naesgaard et al (1998)

Naesgaard et al. (1998) used a simplified, yet inspiring numerical methodology in order to evaluate the behavior of light structures founded on clay crust over liquefied sand. Both static and dynamic analyses were carried out. In the static analyses, a bearing stress was applied to a strip foundation, at the surface of the clay crust, and after equilibrium had been achieved, the loose sand underlying the crust was artificially liquefied, by setting the stress state equal to that of a heavy liquid, i.e. $\sigma_h = \sigma_v$ and $\tau_{vh} = 0$. Post-liquefaction response was modeled using an elasto-plastic constitutive model, with a softer modulus (Byrne 1991), friction angle $\phi = 0$ and cohesion equal to the residual strength of the liquefied soil, i.e. $c = \tau_{res}$. In the dynamic analyses, an irregular two-story building frame was subjected to a velocity time-history, corresponding to a magnitude 7 earthquake event. After a pre-selected time period of strong shaking, the sand layer was artificially brought to liquefaction, while post-liquefaction response was modeled using a modified version of the Mohr-Coulomb model, with a stiffer unloading modulus, compared to the loading modulus (Byrne and Beaty 1998).

The authors investigated the effects of the footing width B, the applied footing load Q (per unit length), the crust thickness H and undrained shear strength c_u, as well as the thickness of the liquefied layer Z_{liq}, its residual shear strength τ_{res} and its residual modulus τ_{res}/γ_{lim}. This study suggested that the settlement estimated by the static analyses was representative of the cumulative settlement from the dynamic analyses. It must be stressed though, that only one time-history was considered and, consequently, the effects of acceleration, period and number of cycles of shaking were not evaluated.

Furthermore, statistical processing of the results of the numerical analyses indicated that a relatively good correlation can be obtained between footing settlements and post-liquefaction factor of safety FS. The latter is computed as shown by Equation (2.7), based on the Meyerhof and Hanna (1978) combined failure mechanism for static loading. More specifically, punching shear failure through the clay crust, and wedge-type failure within the liquefied sand layer are assumed to occur, while the liquefied sand is considered to have zero friction angle $\phi = 0$ and cohesion equal to the residual shear strength $c = \tau_{res}$. Improved correlations for the computation of footing settlements were achieved by taking into account the thickness and the stiffness of the liquefied soil, through a "post-liquefaction factor" X_S, computed by Equation (2.8). Both correlations are presented in **Figure 2.4**. It is observed that safety factors $FS \geq 3$ or post-liquefaction factors $X_S \geq 1$ are required to maintain slight to no building damage (i.e. settlement less than 15-20cm).

$$FS = \frac{2c_u H + (\pi + 2)\tau_{res} B}{Q} \tag{2.7}$$

$$X_S = \frac{FS}{Z_{liq}^{1/2}\gamma_{lim}^{1/2}Q^{1/4}} \qquad (2.8)$$

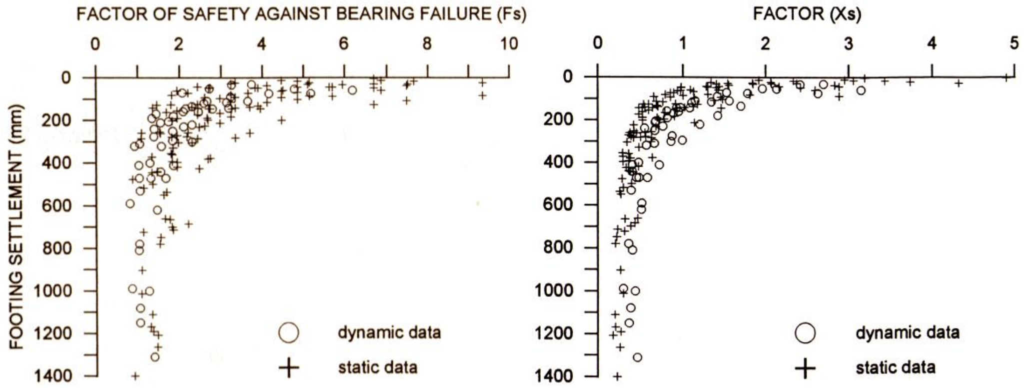

Figure 2.4: Correlation of footing settlement with safety factor FS and post-liquefaction factor X_S (Naesgaard et al 1998).

Σχήμα 2.4: Συσχέτιση καθίζησης και φέρουσας ικανότητας θεμελίου με τον συντελεστή X_s μετά την ρευστοποίηση (Naesgaard et al 1998).

Finally, the authors stress out that settlements resulting from liquefaction-induced consolidation (volumetric strain) and liquefied sand ejecta (sand-boils) should be added to the ones assessed through **Figure 2.4**.

2.2.5 Cascone and Bouckovalas (1998)

Shear strength degradation due to earthquake-induced pore pressure build-up, and the consequent reduction of effective stresses may result in bearing capacity failure of shallow foundations. A theoretical approach to the special case of a footing resting upon a thin clay cap, underlain by a deep layer of liquefiable sand, was made by Cascone and Bouckovalas (1998). Their simplified solution is based on the following assumptions:

- A uniform excess pore pressure ratio $U = \Delta u/\sigma'_{v,o}$ is assumed to develop over the entire liquefiable layer. Excess pore pressures may be either estimated with the aid of special experimental data, or computed using empirical relations proposed by the authors, derived from the statistical analysis of 113 cyclic triaxial and simple shear tests (Bouckovalas et al. 1984, 1986).
- Shear strength degradation of the liquefied sand is introduced using a degraded friction angle ϕ, computed by Equation (2.9):

  $$\tan\phi = (1 - U)\tan\phi_o \qquad (2.9)$$

  where ϕ_o is the actual friction angle of the sand.
- The degraded bearing capacity calculation is based on the limit analysis method proposed by Meyerhof & Hanna (1978), concerning the ultimate bearing capacity of a shallow, rough foundation, supported by a strong soil layer underlain by weaker soil. According to this method, if the interface depth H is relatively small compared to the width of the foundation B, a punching shear failure will develop

in the top (stronger) soil layer, followed by a wedge-type failure in the underlying (weaker) soil layer. This composite failure mechanism is shown in **Figure 2.5**. When the thickness of the top clay layer is relatively large, a conventional wedge-type failure is expected to occur within the top layer. Consequently, the degraded bearing capacity for the simple case of strip foundations with embedment depth $D=0$ and effective unit weights $\gamma_1' = \gamma_2' = \gamma'$, is given as:

$$q_{ult,deg} = \min \begin{cases} cN_c \\ 2c\frac{H}{B} - \gamma' H + \frac{1}{2}\gamma' B N_\gamma + \gamma' H N_q \end{cases} \quad (2.10)$$

where c is the undrained shear strength of the clay, $N_c = \pi + 2$, while N_γ and N_q are computed according to Meyerhof & Hanna (1978) in terms of the degraded friction angle ϕ:

$$N_\gamma = \left(N_q - 1\right)\tan\left(1.4\phi\right) \quad (2.11)$$

$$N_q = \tan^2\left(45 + \frac{\phi}{2}\right)\exp\left(\pi \tan\phi\right) \quad (2.12)$$

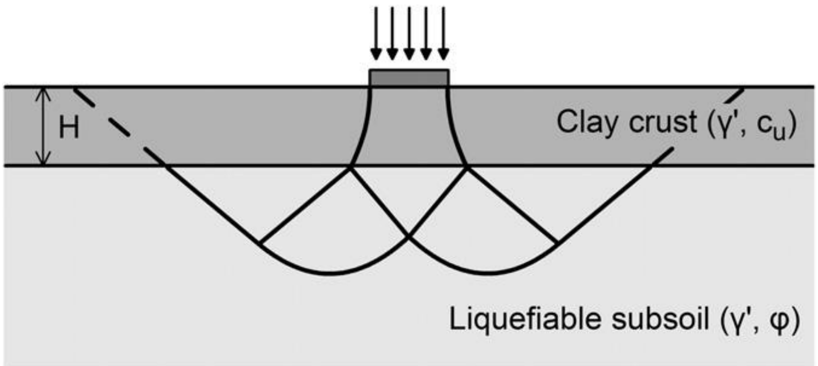

Figure 2.5: Composite failure mechanism proposed by Meyerhof & Hanna (1978).
Σχήμα 2.5: Σύνθετος μηχανισμός αστοχίας κατά Meyerhof & Hanna (1978).

- In the case of square footings, Equation (2.10) becomes:

$$q_{ult,deg} = \min \begin{cases} cN_c \\ 4c\frac{H}{B} - \gamma' H + \frac{1}{2}\gamma' B N_\gamma \lambda_\gamma + \gamma' H N_q \lambda_q \end{cases} \quad (2.13)$$

where $\lambda_\gamma = \lambda_q = \tan^2\left(45 + \phi/2\right)$ are the involved shape factors.

Based on the above approach, the authors end up with two basic design parameters:

- The first is the critical thickness of the clay crust H_{cr}, beyond which failure occurs totally within the crust, and consequently any partial or complete liquefaction of the sand does not have any significant effect on the bearing capacity. Design charts are proposed for the estimation of $(H/B)_{cr}$, in terms of the degraded friction angle ϕ of the sand and the normalized undrained shear strength $C^* = c/\gamma' B$ of the clay (**Figure 2.6**).

- The second design parameter is the bearing capacity degradation factor ζ defined as the ratio of the degraded bearing capacity $q_{ult,deg}$, normalized against the ultimate bearing capacity of the clay layer $q_c = cN_c$. Design charts are provided for ζ, in terms of the actual friction angle ϕ_o of the sand, the excess pore pressure ratio U, the normalized undrained shear strength $C*$ of the clay and the normalized thickness of the crust H/B (**Figure 2.7**).

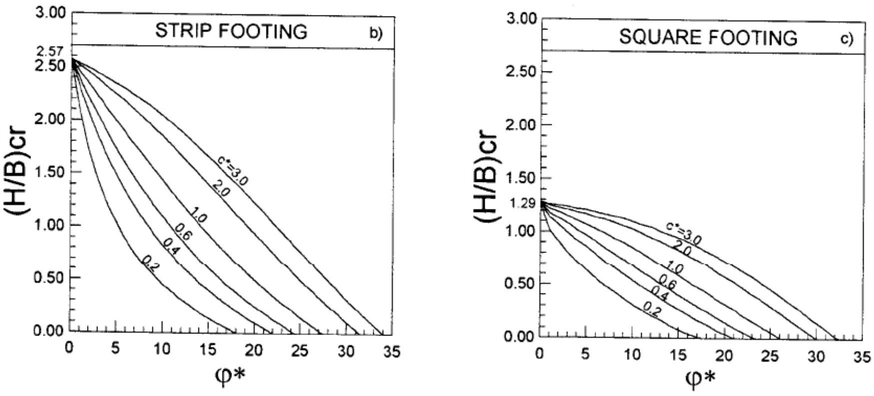

Figure 2.6: Normalized critical thickness of the clay crust.
Σχήμα 2.6: Κανονικοποιημένο κρίσιμο πάχος αργιλικής κρούστας

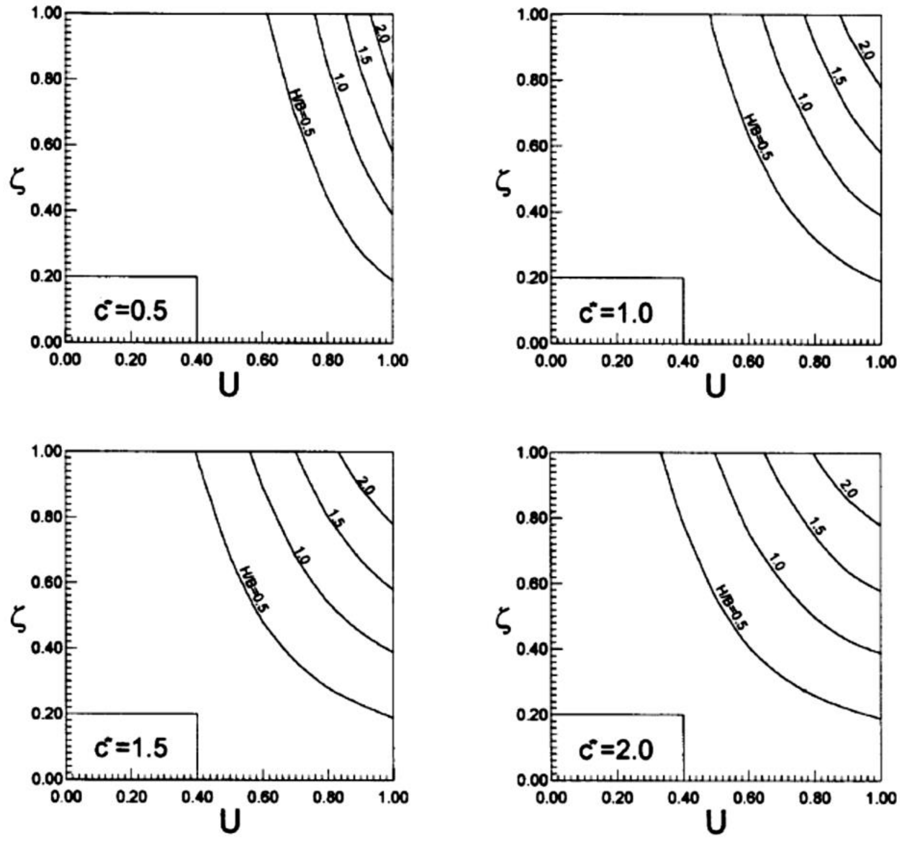

Figure 2.7: Bearing capacity degradation factors, for strip footings ($\phi_o = 35°$).
Σχήμα 2.7: Συντελεστής απομειωμένης φέρουσας ικανότητας για λωριδωτά θεμέλια ($\phi_o = 35°$).

2.2.6 Bouckovalas et al. (2005)

Bouckovalas et al. (2005) attempted to improve the simplified solution of Cascone & Bouckovalas (1998), introducing the following refinements:

- They considered an inclined (instead of a vertical) slip surface in the clay crust, and computed the inclination angle using limit equilibrium analysis. However, this modification was proved to have minor effects on the value of the degradation factor ζ (**Figure 2.8**).
- They introduced the residual shear strength of the liquefied sand, in terms of a residual friction angle ϕ_{res}, as shown in Equation (2.14):

$$\tan\phi = (1-U)\tan\phi_o + U\tan\phi_{res} \tag{2.14}$$

This refinement also had a minor effect on the degradation factor ζ (**Figure 2.9**).

- Finally, they attempted to quantify the shear strength degradation of the liquefiable sand, using a reduced unit weight $\gamma^* = (1-U)\gamma' + U\gamma_{res}$, instead of a degraded friction angle. These two different methods led to considerably different values for the bearing capacity degradation factor ζ (**Figure 2.9**), while the numerical analyses performed by the authors were rather simplified and they did not allow them to reach a final conclusion on the correct simulation of the shearing resistance of partially liquefied sand.

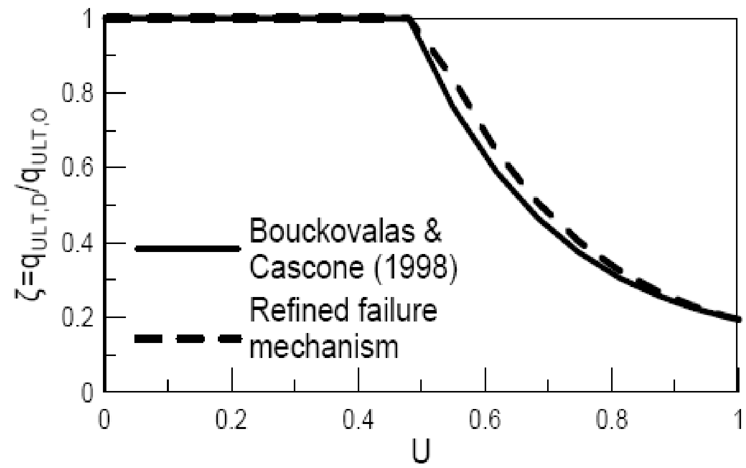

Figure 2.8: Effect of punching failure mechanism on the bearing capacity degradation factor ($C^* = 1.0$, $\phi_o = 30°$, $H/B = 0.5$).

Σχήμα 2.8: Επίδραση μορφής μηχανισμού αστοχίας διείσδυσης στον συντελεστή απομειωμένης φέρουσας ικανότητας ($C^* = 1.0$, $\phi_o = 30°$, $H/B = 0.5$).

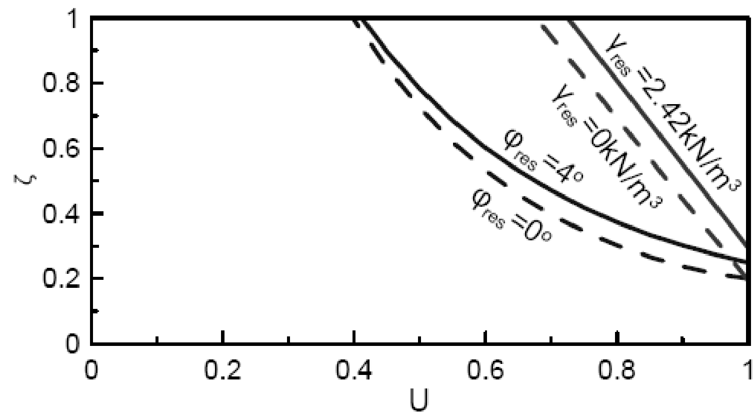

Figure 2.9: Effect of residual strength, and shear strength degradation model on the bearing capacity degradation factor ($C^* = 1.0$, $\phi_o = 30°$, $H/B = 0.5$).

Σχήμα 2.9: Επίδραση παραμένουσας αντοχής, και θεωρητικού μοντέλου απομείωσης διατμητικής αντοχής στον συντελεστή απομειωμένης φέρουσας ικανότητας ($C^* = 1.0$, $\phi_o = 30°$, $H/B = 0.5$).

2.2.7 Yasuda et al (1999)

Yasuda et al. (2001) proposed a simplified methodology for the estimation of liquefaction-induced ground and structure displacements, named ALID (Analysis for Liquefaction-Induced Deformation). The methodology is based on the Finite Element Method, which is applied twice:

- In the first step, ground deformation due to static loading is numerically analyzed using the soil shear modulus $G_{o,i}$ of the soil before any shaking.
- The numerical analysis is repeated using the degraded shear modulus of the liquefied soil G_1, for static loading under the condition of no volume change (undrained conditions).
- Finally, liquefaction-induced deformation is computed as the difference of the computed deformations in the above steps.

The key issue of this procedure is to estimate the shear modulus of the liquefied soil G_1. Simple charts for the reduction of shear modulus, in terms of relative density, fines content and the safety factor against liquefaction F_L were derived from torsional shear tests (Yasuda et al. 1998) and shown in **Figure 2.10**. The tests indicated that in the liquefied specimen shear strain increased with very low shear stress, up to very large strains, where, after a resistance transformation point (turning point) the shear stress increased more rapidly. This behavior was modeled by the bilinear model of **Figure 2.10**, defined in terms of G_1, G_2 and γ_1.

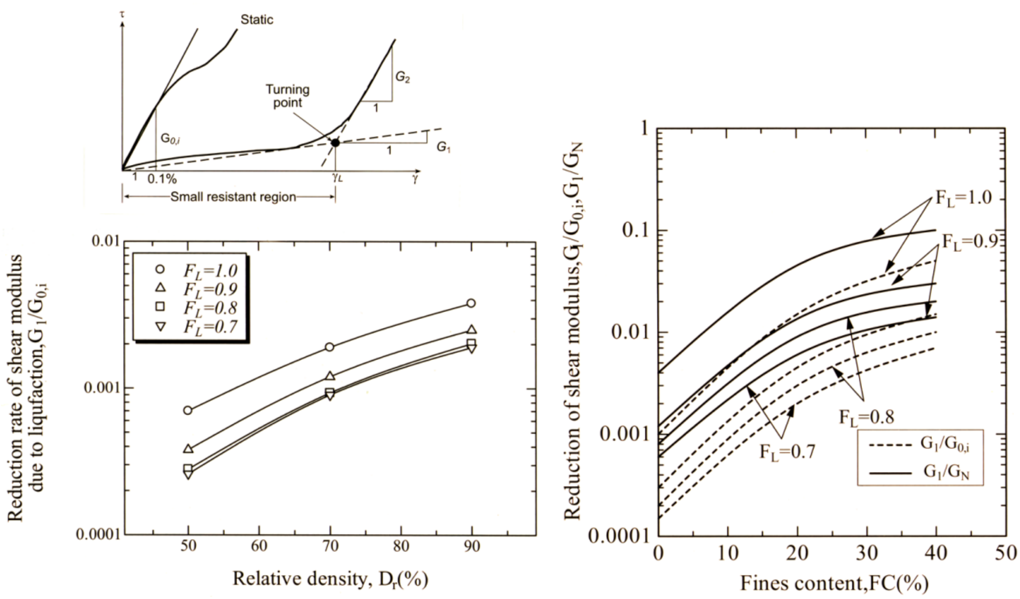

Figure 2.10: Reduction of shear modulus due to liquefaction (Yasuda et al 1999).
Σχήμα 2.10: Απομείωση μέτρου διάτμησης λόγω ρευστοποίησης (Yasuda et al 1999).

This methodology has been evaluated against a number of case studies:

- The estimated maximum lateral spreading displacements behind a quay wall at Uozakihama in Kobe (Hyogoken-nambu – Kobe earthquake, 1995) and on a slope with gradient 1% in Noshiro City (Nihonkai-chubu earthquake, 1983) were 1.2m and 5.0m respectively, compared to the actual values of 2.0m and 5m (Yasuda et al. 1999).
- The estimated settlement of seven damaged and non-damaged river levees, during the 1993 Hokkaido-nansei-oki earthquake and the 1995 Hyogoken-nambu earthquake did not agree well with the actual values, as the scatter exceeded 200% (Yasuda et al. 2000).
- The numerical simulation of the centrifuge tests performed by Kawasaki et al. (1998), concerning the seismic behavior of a transmission tower footing. Note that this application resulted in an over-prediction of settlements, of the order of 260% (Yasuda et al. 2001). Despite the lack in quantitative accuracy, the experimentally deduced effect of most involved parameters was correctly predicted by the numerical analyses. However, the centrifuge tests indicated that settlements decrease with increasing footing width. This trend could not be predicted by the ALID methodology, due to the model's inability to model the non-liquefied zone under the foundation. Centrifuge tests were also performed for counter-measures, such as soil densification or the connection of individual footings with slabs. In this case, the effects of the counter-measures were correctly predicted by the numerical methodology.

It becomes evident that the methodology proposed by Yasuda et al (1998) can be readily used for the qualitative evaluation of liquefaction-induced deformation and the estimation of the effect of various counter-measures, though it cannot provide quantitatively accurate results that can be incorporated in performance-based design.

2.2.8 Acacio et al (2001)

Acacio et al. (2001) developed a numerical methodology for the prediction of liquefaction-induced footing settlements, based on the methodology of Towhata et al. (1999) for the computation of lateral displacement. The main assumptions are summarized in the following:

- Based on the results of shaking-table tests, the horizontal displacement of the liquefied ground was modeled using two displacement modes, as shown in **Figure 2.11**.
- The vertical displacement is computed from the horizontal displacement, by assuming constant volume deformation.
- The maximum vertical displacement is consequently calculated mathematically, by finding the overall deformation shape which minimizes the overall potential energy.
- Punching failure through the surface non-liquefiable layer was taken into account by adding the frictional shear stress, multiplied by the slip plane area, to the energy dissipation terms.
- It was demonstrated that the solution became indeterminate, in the sense that more than one solution satisfied the minimum-energy requirement. This disadvantage was overcome by applying a solution scheme in the time domain. This modification required to account for kinetic energy terms, and energy dissipation, and for this purpose the liquefied subsoil was modeled as a viscous liquid. Note that the determination of an appropriate value for the viscous coefficient of the liquefied sand is still under research.
- The resulting set of equations is rather complicated. Thus, it was expressed in discrete form, in order to be solved using numerical methods, under relevant boundary and initial conditions.

The proposed methodology was evaluated against the measured subsidence of buildings in the city of Dagupan, Philippines, during the 1990 Luzon earthquake. It was shown that the method was conservative, and might overestimate settlements by up to 300%. This was attributed to the extent of liquefaction, which was relatively small, for the soil to be modeled as a viscous fluid.

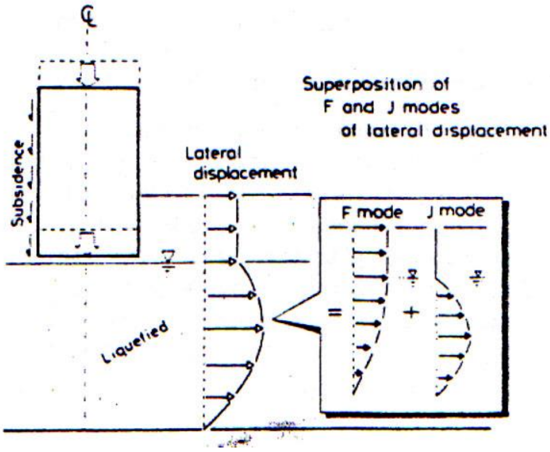

Figure 2.11: Horizontal displacement modes beneath shallow foundations (Acacio et al 2001).
Σχήμα 2.11: Ιδιομορφές οριζόντιας μετακίνησης κάτω από επιφανειακές θεμελιώσεις (Acacio et al 2001).

2.2.9 Juang et al (2005)

Juang et al. (2005) proposed an empirical procedure for estimating the severity of liquefaction-induced damage at or near foundations or existing buildings, based on 30 case histories from the 1999 Kocaeli earthquake, in Turkey. These case histories were classified into 3 damage categories, as shown in **Table 2.1**. The Damage Severity Index (DSI) was consequently correlated to the Liquefaction Potential Index (I_L) proposed by Iwasaki et al. (1978, 1982), as well as to the Probability of Ground Failure (P_G) proposed by Juang et al. (2002).

Table 2.1: Liquefaction-induced foundation damage severity index (Juang et al 2005).
Πίνακας 2.1: Δεικτης εκτίμησης βλάβης θεμελίωσης λόγω ρευστοποίησης

Damage Severity Index	Description	Interpretation
DSI=1	No observed ground damage	No settlement, no tilt and no lateral movement or sand boils
DSI=2	Minor to moderate ground damage	Settlement <25cm, tilt <3°, or lateral movement <10cm
DSI=3	Major ground damage	Settlement ≥25cm, tilt ≥3°, or lateral movement ≥10cm, or collapse of buildings

It is reminded that the Liquefaction Potential Index I_L (Iwasaki et al. 1978, 1982) is defined as:

$$I_L = \int_0^{20} F_1 W(z) dz \tag{2.15}$$

$$F_1 = \begin{cases} 1 - F_S & F_S \leq 1.0 \\ 0 & F_S > 1.0 \end{cases} \tag{2.16}$$

$$W(z) = 10 - 0.5z \tag{2.17}$$

where:

F_S is the factor of safety against liquefaction, defined as the ratio of CRR (cyclic resistance ratio) over CSR (cyclic stress ratio), which may be computed according to Youd et al (2001)

z is the depth from the ground surface

Integration is carried out from the ground surface to a depth of 20m, as the effects of liquefaction at greater depths on ground failure potential are considered negligible. Iwasaki et al (1978, 1982) proposed the following criteria for assessing liquefaction-induced ground failure potential:

- $I_L = 0$: No failure
- $0 < I_L \leq 5$: Low failure potential
- $5 < I_L \leq 15$: High failure potential
- $15 < I_L$: Extremely high failure potential

Juang et al (2002) noted that Iwasaki's method was calibrated using an old version (JSHE, 1990) of an SPT-based simplified method for the evaluation of liquefaction potential and needed to be re-calibrated. Therefore, they proposed the mapping function of Equation (2.18) for the determination of the probability of liquefaction-induced ground failure P_G, based on 154 case histories (**Figure 2.12**).

$$P_G = \frac{1}{1 + e^{4.83 - 0.74 I_L}} \tag{2.18}$$

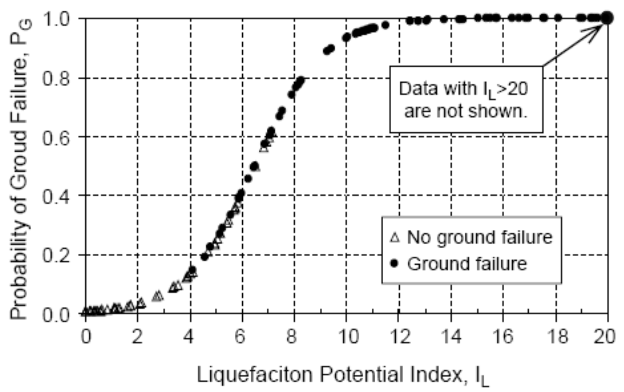

Figure 2.12: Probability of Ground Failure P_G as a function of the Liquefaction Potential Index I_L (Juang et al 2002).

Σχήμα 2.12: Πιθανότητα αστοχίας P_G συναρτήσει του δείκτη δυναμικού ρευστοποίησης I_L (Juang et al 2002).

Finally, using plots of the Damage Severity Index DSI versus the Liquefaction Potential Index I_L and the Probability of Ground Failure P_G (**Figure 2.13**), they proposed the following criteria:

- DSI=1 for $I_L \le 5$ or $P_G \le 0.35$
- DSI=2 for $5 < I_L \le 12$ or $0.35 < P_G \le 0.90$
- DSI=3 for $12 < I_L$ or $0.90 < P_G$

It should be noted that this methodology is only applicable to level ground conditions (slope less than 1°), earthquake magnitude $M_w = 7.4 - 7.6$ and depth of liquefaction less than 20m.

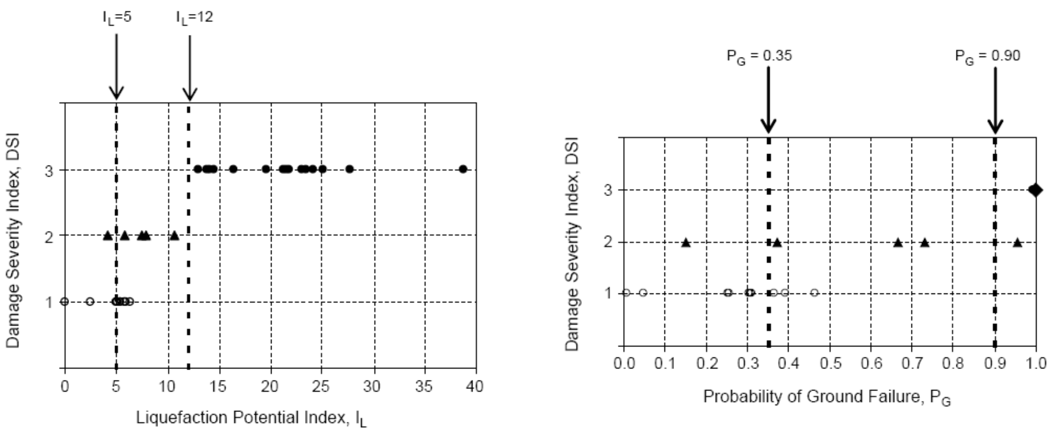

Figure 2.13: Damage Severity Index versus Liquefaction Potential Index I_L and Probability of Ground Failure P_G (Juang et al 2002).

Σχήμα 2.13: Συσχέτιση Δείκτη βλαβών με τον δείκτη δυναμικού ρευστοποίησης I_L και την πιθανότητα εδαφικής αστοχίας P_G (Juang et al 2002).

2.3 Integrated methodology for footings on clay crust

Karamitros et al. (2013) investigated thoroughly the response of strip and rectangle footings resting upon a uniform liquefiable layer overlaid by a non-liquefied clay crust. Based on a large set of fully coupled dynamic numerical analyses, with a critical-state constitutive model, a simplified methodology was developed for the evaluation of the post-liquefaction degraded bearing capacity ($q_{ult,deg}$) and the accumulated dynamic settlements (ρ_{dyn}).

2.3.1 Degraded Bearing Capacity, $q_{ult,deg}$

The degraded bearing capacity, $q_{ult,deg}$, can be estimated based on the composite failure mechanism of Meyerhof and Hanna (1978) shown in **Figure 2.5**, i.e.:

$$q_{ult,deg} = \min \begin{Bmatrix} (\pi+2) c_u F_{cs} \\ q_{ult,deg}^{c-s} \end{Bmatrix} \tag{2.19}$$

$$q_{ult,deg}^{c-s} = 2c_u \frac{H}{B} s - \gamma' H + \frac{1}{2} \gamma' B N_\gamma F_{\gamma s} + \gamma' H N_q F_{qs} \tag{2.20}$$

where B is the width of the foundation, H is the thickness of the clay crust, c_u is the crust's undrained shear strength and γ' is the buoyant weight, which is considered to be the same for both the sand and the clay layers. The bearing capacity factors are computed according to Vesic (1973):

$$N_q = \tan^2\left(45+\frac{\phi}{2}\right)e^{\pi\tan\phi_{deg}}$$

$$N_\gamma = 2\left(N_q+1\right)\tan\phi_{deg}$$

The shape factors are computed according to De Beer (1970):

$$F_{cs} = 1+\frac{1}{\pi+2}\frac{B}{L}$$

$$F_{\gamma s} = 1-0.4\frac{B}{L}$$

$$F_{qs} = 1+\frac{B}{L}\tan\phi$$

and the factor s in Equation (2.20) is computed according to Meyerhof & Hanna (1978):

$$s = 1+\frac{B}{L}$$

In the above equations, the effect of liquefaction is taken into account as a degradation of the sand's friction angle:

$$\phi_{deg} = a\tan\left[\left(1-U\right)\tan\phi_o\right] \tag{2.21}$$

where:

ϕ_o the initial friction angle of the non-liquefied sand

U the excess pore pressure ratio developing in the sand layer

The uniform excess pore pressure ratio U is computed as:

$$U = \frac{U_{foot}+\left(1+B/L\right)\cdot U_{ff}}{2+B/L} \tag{2.22}$$

where:

$U_{ff}\approx1.0$: Excess pore pressure ratios at the free field

U_{foot}: Excess pore pressure ratios underneath the footing

The excess pore pressure ratio underneath the footing can be estimated as follows:

$$U_{foot} = \frac{1-6.0\,\rho_{dyn}/B}{1+\Delta\sigma_{v,c}/\sigma'_{vo,c}} \tag{2.23}$$

where:

- ρ_{dyn}: Dynamic settlements
- $\Delta\sigma_{v,c}$: Additional vertical stress imposed by the foundation load at the characteristic depth z_c
- $\sigma'_{vo,c}$: Initial (pre-shaking) vertical effective stress applied at the characteristic depth z_c

Finally, the characteristic depth z_c is estimated as:

$$z_c = H + \left[1.0 - 0.5\left(\frac{B}{L}\right)^3\right]B \tag{2.24}$$

2.3.2 Dynamic settlements, ρ_{dyn}

Dynamic settlements, ρ_{dyn} can be evaluated from the following expression:

$$\rho_{dyn} = c \cdot a_{max} T^2 N \left(\frac{Z_{liq}}{B}\right)^{1.5} \left(\frac{1}{FS_{deg}}\right)^3 \tag{2.25}$$

where:

a_{max}: Peak input acceleration

T: Excitation period

N: Number of cycles

Z_{liq}: Thickness of the liquefiable sand layer

B: Footing width

FS_{deg}: Post-liquefaction degraded factor of safety

Coefficient c in Eq. (2.25) is equal to 0.008 and 0.035 for square and strip foundations, while for intermediate aspect ratios L/B, it may be approximately computed as:

$$c = c'\left(1 + 1.65\frac{L}{B}\right) \le 11.65c' \tag{2.26}$$

where c′=0.003

Finally, for the case of non-sinusoidal input motions equation (2.25) is applied by substituting the term $a_{max}T^2N$ with $\pi^2 \cdot \int |v(t)| dt$ where v(t) is the applied velocity time-history.

2.3.3 Design Charts

The equations presented in the previous paragraphs were consequently used to derive practice-oriented design charts. More specifically, seismic settlements ρ_{dyn} of both strip footings and square foundations, normalized against the footing's width B, can be computed in terms of the following non-dimensional problem parameters:

- the average bearing pressure $q/\gamma' B$,
- the thickness of the clay crust H/B,

- the undrained shear strength of the clay crust $c_u / \gamma' H$, and
- the intensity of seismic motion and the extent of liquefaction expressed as ρ_o / B, according to Equation (2.27):

$$\frac{\rho_o}{B} = \left(\frac{a_{max} T^2 N}{B} \right) \left(\frac{Z_{liq}}{B} \right)^{1.5} \tag{2.27}$$

Figure 2.14a, **b** and **c** show the corresponding design charts for strip foundations and ρ_o/B=1.0, 2.0 and 5.0, respectively. Similarly, the design charts for square footings are shown in **Figure 2.15a**, **b** and **c**.

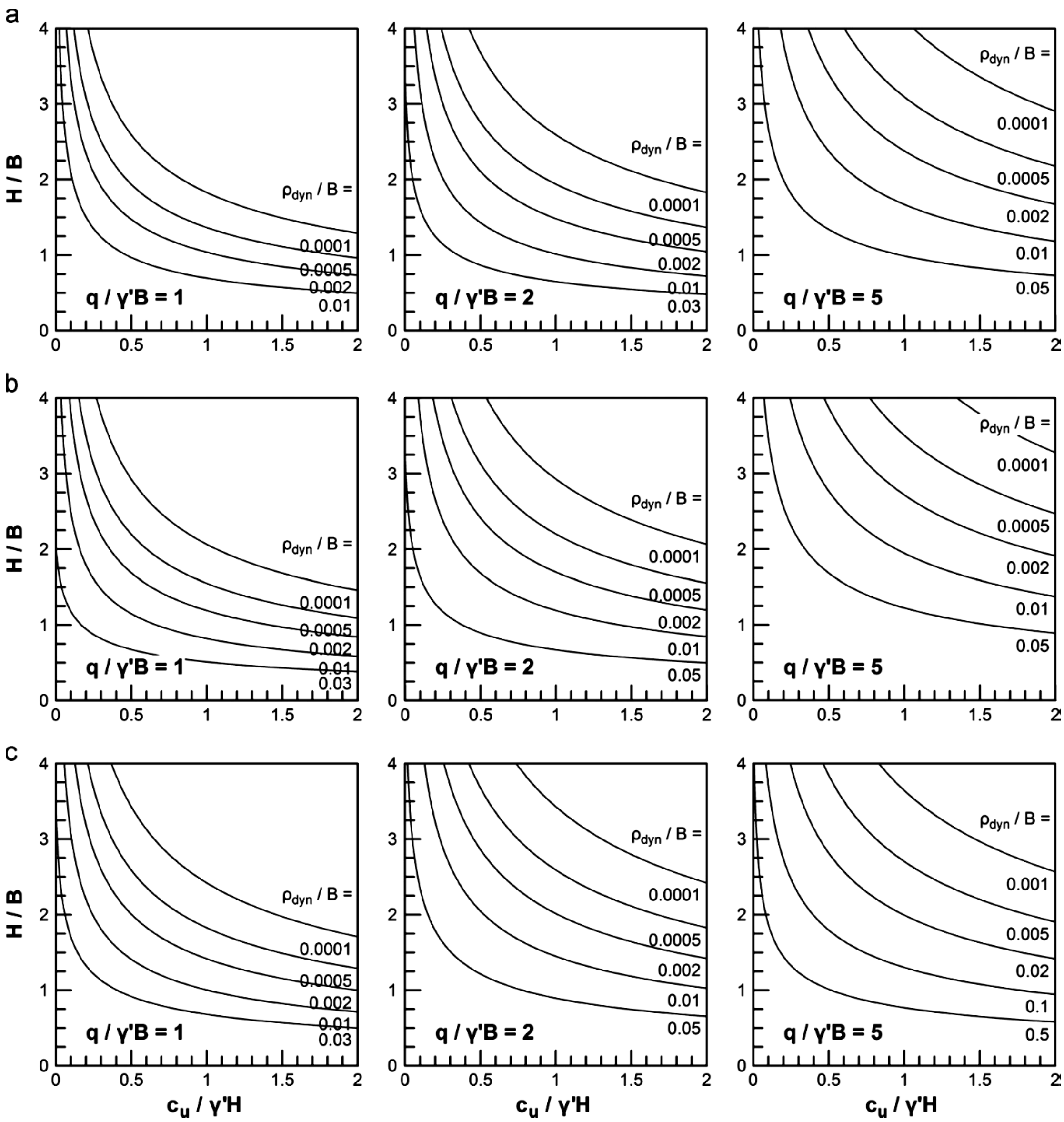

Figure 2.14: Design charts for the estimation of ρ_{dyn} for (a) ρ_o/B = 1.0, (b) ρ_o/B = 2.0 and (c) ρ_o/B = 5.0 – Strip footings

Σχήμα 2.14: Διαγράμματα σχεδιασμού για τον υπολογισμό των δυναμικών καθιζήσεων ρ_{dyn} για (a) ρ_o/B = 1.0, (b) ρ_o/B = 2.0 and (c) ρ_o/B = 5.0 – Λωριδωτά θεμέλια

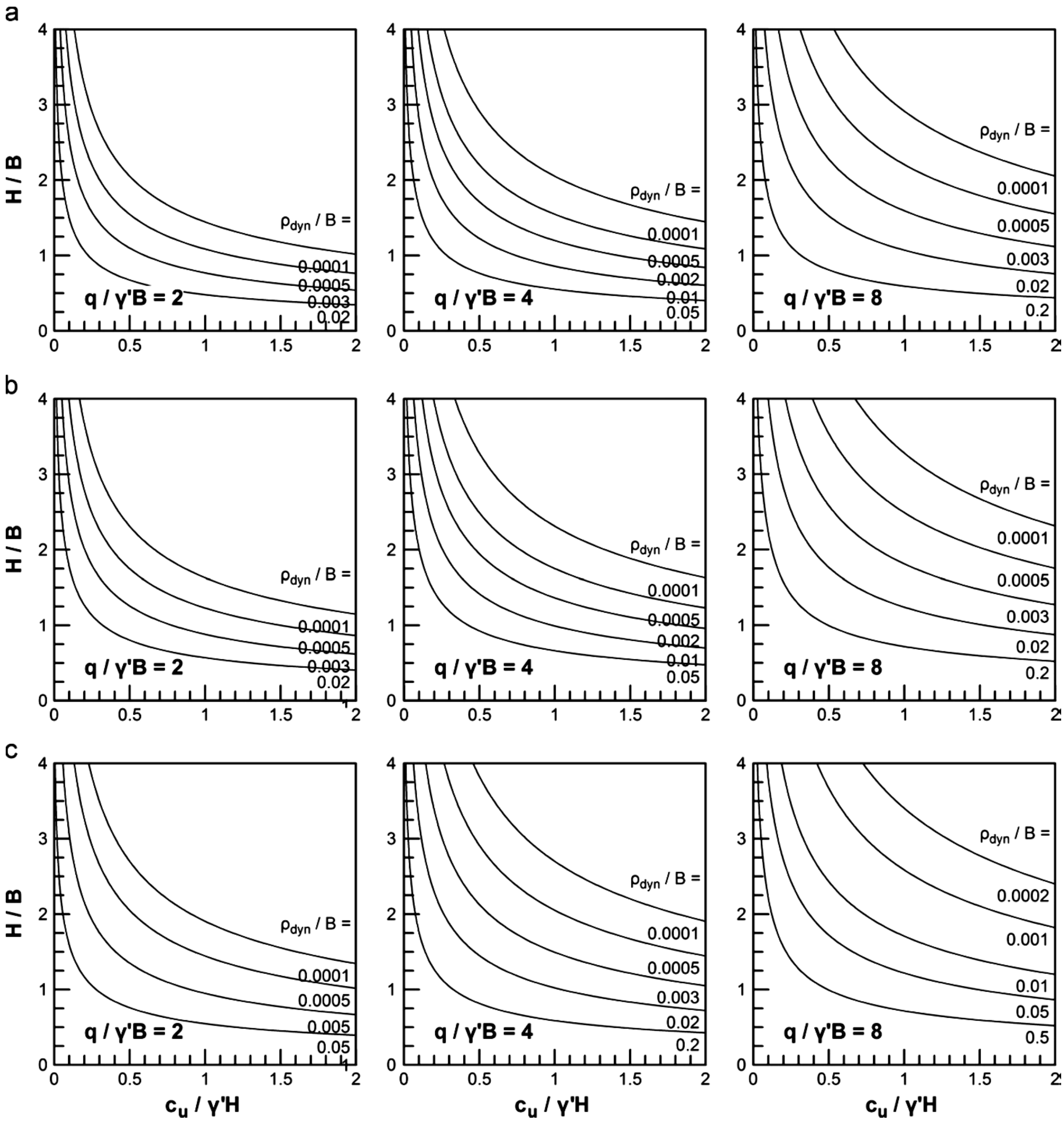

Figure 2.15: Design charts for the estimation of ρ_{dyn} for (a) ρ_o/B = 1.0, (b) ρ_o/B = 2.0 and (c) ρ_o/B = 5.0 – Square footings

Σχήμα 2.15: Διαγράμματα σχεδιασμού για τον υπολογισμό των δυναμικών καθιζήσεων ρ_{dyn} για (a) ρ_o/B = 1.0, (b) ρ_o/B = 2.0 and (c) ρ_o/B = 5.0 – Τετραγωνικά θεμέλια

3

Simulation of Footing Response

3.1 Introduction

The present chapter thoroughly describes the numerical model built to simulate the problem at hand, namely the response of footings resting upon a uniform layer of Nevada Sand. The upper part of the layer has been improved, using vibro-compaction or vibro-replacement, thus providing an artificial non-liquefiable crust. Creation of gravel drains and associated soil densification yields a quite complex pattern regarding the density distribution, the shear strength and the excess pore pressure dissipation mechanism in the crust of the improved ground. Namely:

- The relative density of gravel piles is different than that of the surrounding soil, while the relative density of the densified soil decreases radially from the axis of the gravel drain and outwards.
- The shear strength of the gravel pile is also different than that of the surrounding sand, even if the aforementioned radial variation in relative density is not considered.
- Finally, the improved ground drains both in the radial and the vertical directions while the underlying liquefied sand drains practically vertically towards the gravel drains installed on top of it.

Currently available numerical codes (e.g. FLAC and FLAC3D), combined with the use of advanced constitutive models, allow for the simulation of the above complicated patterns. Nevertheless, the time required for such analyses would be restrictive for performing an extensive parametric study, while a number of the input parameters (e.g. permeability coefficient, mechanical parameters of gravel drains under monotonic and cyclic loading) are not well-established, thus reducing the accuracy of the analyses despite any elaborate numerical computations.

In view of the above objective difficulties, the detailed numerical simulation of the liquefied ground response in the presence of a surface crust of improved ground, becomes cumbersome and outside the scope and the extent of this study. Consequently, the "*Equivalent Uniform Improved Ground*" concept (noted hereafter as *E.U.I.G.*) is adopted, which is widely accepted in practice for the design of geostructures and foundations on weak soil improved with gravel piles. According to *E.U.I.G.*, the improved ground layer is considered uniform with appropriately computed uniform soil parameters, which take into account the properties of the natural ground, the properties of the gravel piless, as well as the extent of ground improvement. Possible means of estimating the related properties of the improved surface crust are described in the first part of the present chapter.

Subsequently, the numerical methodology developed to simulate the problem is thoroughly described, and verified against the well-established centrifuge experiments performed by Liu and Dobry (1997). Special emphasis is placed on the appropriate value for the permeability coefficient of unstable soil skeletons due to liquefaction and excess pore-pressure build-up.

3.2 Equivalent Uniform Improved Ground (E.U.I.G.)

3.2.1 Relative density of improved ground

The effects of soil improvement on the relative density of the soil can be evaluated using the design charts shown in **Figure 3.1** [Japanese Geotechnical Society (JGS), 1998]. The charts correlate the corrected (for overburden pressure and fines content) SPT blowcount of the natural soil (N_o) with the corresponding SPT number after improvement ($N_{imp.}$) as a function of the replacement ratio α_s[1] of the gravel drain geometry (ground improvement scheme).

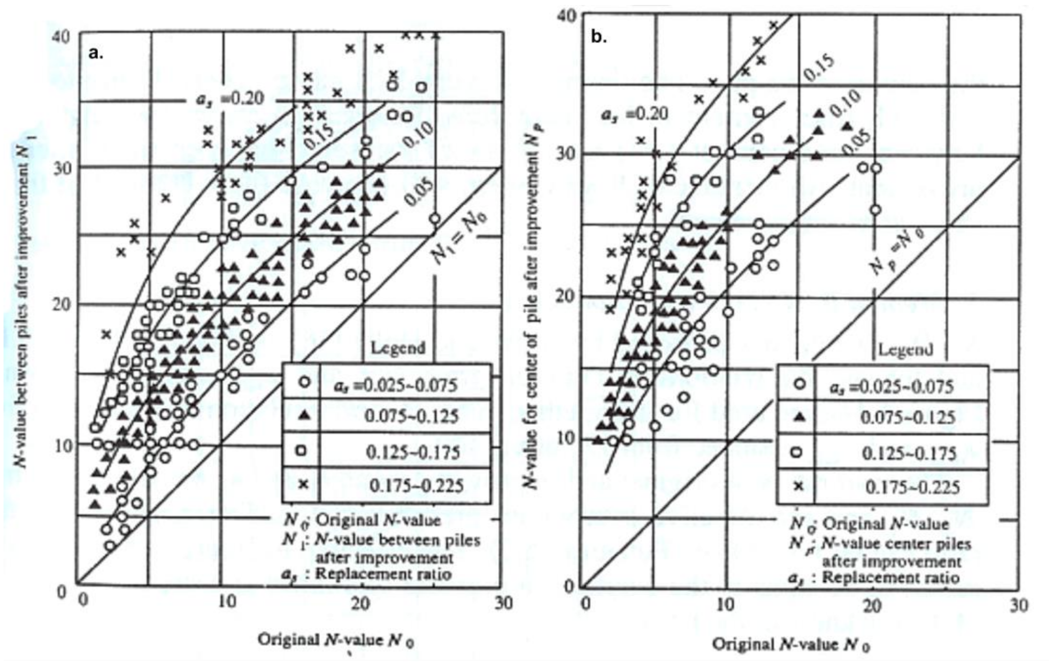

Figure 3.1: Estimation of equivalent SPT blowcount due to soil improvement (JGS 1998)
Σχήμα 3.1: Εκτίμηση ισοδύναμου αριθμού κρούσεων λόγω βελτίωσης του εδάφους (JGS 1998)

[1] Replacement ratio, a_s, is defined as the ratio of the plan view area of the gravel drain, over the area of the influence zone around the drain.

Namely, given the initial relative density of the natural soil, D_{ro}, an equivalent corrected SPT number [$(N_1)_{60}$] can be estimated based on the empirical relationship proposed by Tokimatsu & Seed (1987):

$$(N_1)_{60} = N_o = 44 \cdot D_{ro}^2 \quad (3.1)$$

Table 3.1: N_{SPT} values in the improved ground (according to JGS, 1998) and related relative density values (based on Tokimatsu & Seed, 1987) for six initial relative density scenarios

Πίνακας 3.1: Τιμές N_{SPT} στο βελτιωμένο έδαφος (κατά JGS, 1998) και αντίστοιχες τιμές σχετικής πυκνότητας (με βάση τους Tokimatsu & Seed, 1987) για έξι αρχικά σενάρια σχετικής πυκνότητας

Dr_o (%)	35				Dr_o (%)	40			
$(N_1)_{60,ini}$	5.5				$(N_1)_{60,ini}$	7			
a_s	N_{ground}	N_{pile}	$(N_1)_{60,imp.}$	$Dr_{imp.}$ (%)	a_s	N_{ground}	N_{pile}	$(N_1)_{60,imp.}$	$Dr_{imp.}$ (%)
0.05	9	15	9	46	0.05	11	17	12	51
0.1	14	19	14	57	0.1	16	22	17	62
0.15	18	24	19	66	0.15	21	27	22	70
0.2	23	28	24	74	0.2	26	31	27	78

Dr_o (%)	45				Dr_o (%)	55			
$(N_1)_{60,ini}$	9				$(N_1)_{60,ini}$	13			
a_s	N_{ground}	N_{pile}	$(N_1)_{60,imp.}$	$Dr_{imp.}$ (%)	a_s	N_{ground}	N_{pile}	$(N_1)_{60,imp.}$	$Dr_{imp.}$ (%)
0.05	14	20	14	56	0.05	19	24	19	65
0.1	19	24	19	66	0.1	23	29	24	74
0.15	23	29	24	74	0.15	28	33	29	81
0.2	29	33	29	82	0.2	33	38	34	88

Dr_o (%)	65				Dr_o (%)	70			
$(N_1)_{60,ini}$	18.5				$(N_1)_{60,ini}$	21.5			
a_s	N_{ground}	N_{pile}	$(N_1)_{60,imp.}$	$Dr_{imp.}$ (%)	a_s	N_{ground}	N_{pile}	$(N_1)_{60,imp.}$	$Dr_{imp.}$ (%)
0.05	24	30	24	74	0.05	26	33	26	77
0.1	28	33	29	81	0.1	31	35	31	84
0.15	33	36	33	86	0.15	35	39	36	89
0.2	37	38	37	93	0.2	38	40	38	98

Next, according to JGS (1998), the corrected N_{SPT} value for the improved ground ($N_{imp.}$) is computed as follows:

$$N_{imp.} = \alpha_s N_{pile} + (1 - \alpha_s) N_{ground} \quad (3.2)$$

where:

N_{pile}: Corrected N_{SPT} blow count value corresponding to the location of the gravel pile(**Figure 3.1b**) and

N_{ground}: Corrected N_{SPT} blow count value obtained at the mid-distance between two gravel drains (**Figure 3.1a**).

The above procedure was applied for natural soil deposits with initial relative density D_{ro} = 35, 40, 45, 55, 65 & 70% and replacement ratios α_s = 5, 10 15 & 20%. The results are summarized in **Table 3.1** for the range of initial relative densities mentioned above.

3.2.2 Permeability Coefficient for the Improved Ground

The permeability coefficient of the improved ground layer is a critical input for the numerical analysis, however, its evaluation applying the *E.U.I.G.* concept is not straightforward. As a first approximation, flow through the improved crust may be considered vertical so that, a weighted average of the permeabilities for the natural soil and the gravel drains might be used:

$$k_{eq.} = \alpha_s \cdot k_{drain} + (1 - \alpha_s) \cdot k_{sand} \tag{3.3}$$

Taking into account that k_{drain}/k_{sand} must be greater than about 200 and also that a_s ranges from 0.05 to 0.20 it comes out that $k_{eq.}$> (11 – 41)k_{sand}.

It is also well known that the permeability coefficient under seismic loading is initially less than the equivalent static value but may increase in proportion to the excess pore pressure ratio r_u. Parametric analyses performed by Chaloulos et al. (2013) for the simulation of centrifuge tests of a pile into liquefied and laterally spreading ground revealed that the static value of permeability is a reasonable average for liquefied and non liquefied states and can be used for the numerical computations without significant loss in accuracy. For the case of Nevada sand considered herein, constant head permeability test performed by Arulmoli et al. 1992), yielded the permeability values shown in **Table 3.2**.

Table 3.2: Permeability coefficient values and relative density for the liquefiable sand layer (Arulmoli et al., 1992)

Πίνακας 3.2: Τιμές συντελεστή διαπερατότητας και σχετικής πυκνότητας για το στρώμα ρευστοποιήσιμης άμμου (Arulmoli et al., 1992)

D_r (%)	k_{sand} (*10^{-5}m/s)
40	6.6
60	5.6
90	2.3

The variation of the coefficient of permeability with relative density is plotted in **Figure 3.2**, from which it can be concluded that the permeability coefficient remains essentially constant and equal to 6.6*10^{-5} m/s for relative densities up to 40-50%. Therefore, for initial values of relative density (35, 40 & 45%) the permeability coefficient was set equal to 6.6*10^{-5} m/s, whereas for the three remaining values (55, 65 & 70%), it was set equal to 5.8, 5.2 and 4.5(*10^{-5}) m/s respectively. Finally, as for the improved crust, the values of the permeability coefficient were estimated according to equation (3.3), and are summarized in **Table 3.3**.

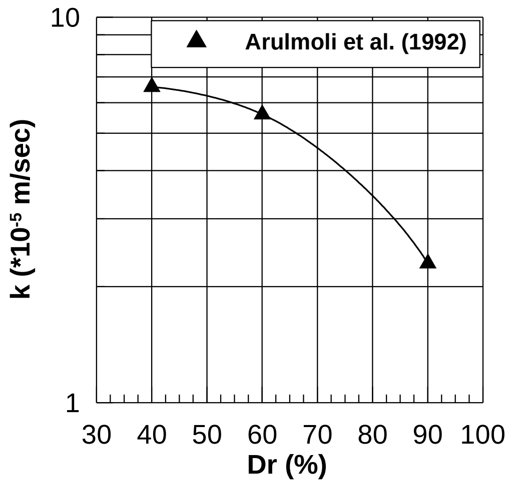

Figure 3.2: Change in the permeability coefficient with regard to relative density for Nevada sand (Arulmoli et al. 1992a)

Σχήμα 3.2: Μεταβολή του συντελεστή διαπερατότητας με την Σχετική Πυκνότητα του εδάφους για άμμο Nevada (Arulmoli et al. 1992a)

Table 3.3: Equivalent permeability coefficient for the natural and the improved soil

Πίνακας 3.3: Ισοδύναμοι συντελεστές διαπερατότητας για το φυσικό και το βελτιωμένο έδαφος

Dr_o (%)	35, 40, 45	
k_{sand} (m/s)	6.60E-05	
a_s	k_{drain} (m/s)	$k_{eq.}$ (m/s)
0.05	1.32E-02	7.23E-04
0.1		1.38E-03
0.15		2.04E-03
0.2		2.69E-03

Dr_o (%)	55		Dr_o (%)	65		Dr_o (%)	70	
k_{sand} (m/s)	5.80E-05		k_{sand} (m/s)	5.20E-05		k_{sand} (m/s)	4.50E-05	
a_s	k_{drain} (m/s)	$k_{eq.}$ (m/s)	a_s	k_{drain} (m/s)	$k_{eq.}$ (m/s)	a_s	k_{drain} (m/s)	$k_{eq.}$ (m/s)
0.05	1.16E-02	6.35E-04	0.05	1.04E-02	5.69E-04	0.05	9.00E-03	4.93E-04
0.1		1.21E-03	0.1		1.09E-03	0.1		9.41E-04
0.15		1.79E-03	0.15		1.60E-03	0.15		1.39E-03
0.2		2.37E-03	0.2		2.12E-03	0.2		1.84E-03

3.3 Outline of (reference) numerical analysis.

Mesh discretization.- Initially the case of strip footing was considered through 2-dimensional numerical analyses. The general outline of the configuration is illustrated in **Figure 3.3**. The total thickness of the liquefiable layer was set equal to H_{tot}=20m while three potential improvement depths were considered, i.e. H_{crust}=4, 6 & 8m. In the vicinity of the footing 1.0×1.0m zones were generated while the zone-width was gradually increased to 1.5×1.0m and 2.0×1.0m, at the boundaries of the model.

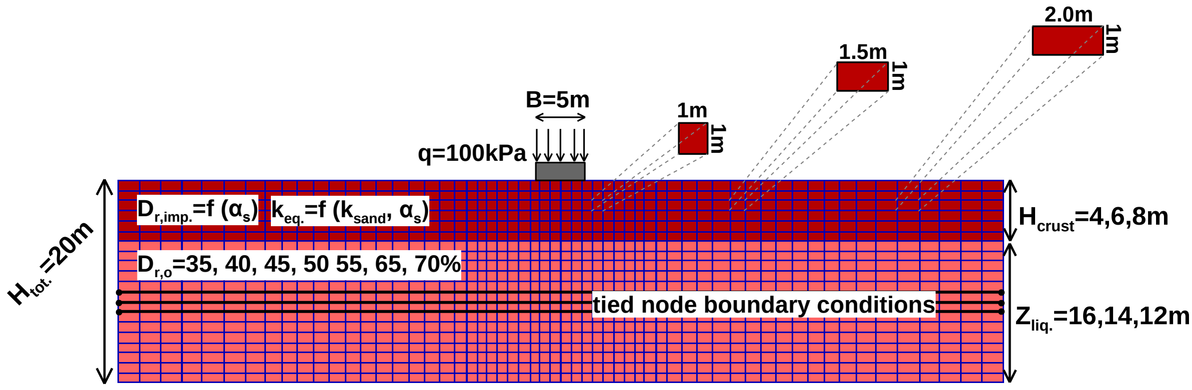

Figure 3.3: Mesh used in the 2-D numerical analyses
Σχήμα 3.3: Κάνναβος 2-Διάστατων αριθμητικών αναλύσεων

Excitation.- The model was subjected to a harmonic sinusoidal excitation, consisting of 12 cycles with period T=0.35sec and peak acceleration α_{max}=0.15g (**Figure 3.4**).

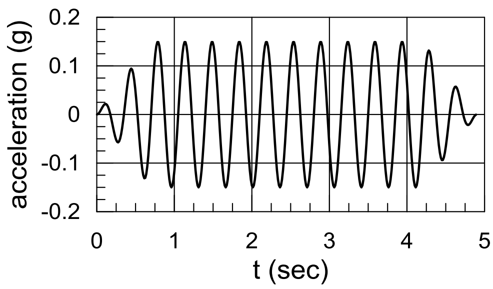

Figure 3.4: Input acceleration time history in the baseline numerical analysis
Σχήμα 3.4: Επιβαλλόμενη επιτάχυνση στην βάση του καννάβου για την ανάλυση αναφοράς

Constitutive Model.- The liquefiable sand response is simulated using the advanced constitutive model NTUA–Sand developed and implemented to FLAC codes in the Foundation Engineering Laboratory of the National Technical University of Athens as part of Work Package 2 (Deliverables D1 & D2). Early versions of this methodology, prior to the advancements implemented as part of the present research project (Bouckovalas et al. 2012a), have been verified against well-documented centrifuge experiments (Arulmoli et al. 1992b), and have also been used for the parametric analysis of a number of common geotechnical earthquake engineering problems (Chaloulos et al. 2014; Karamitros et al. 2012; Valsamis et al. 2010).

The updated NTUA-Sand constitutive model is a bounding surface, critical state, plasticity model with a vanished elastic region. From the onset of its development, this model was aimed at the realistic simulation of the rate-independent response of non-cohesive soils (sand, silts, etc.) under small, medium, as well as large (cyclic) shear strains and also liquefaction. This is achieved using a single set of values for the model constants, irrespective of initial stress and density conditions, as well as loading direction. The model is equally efficient in simulating the monotonic and the cyclic soil response.

Building upon earlier efforts of Manzari & Dafalias (1997) and Papadimitriou & Bouckovalas (2002), the NTUA-Sand model features the following key constitutive ingredients:

(a) The inter-dependence of the critical state, the bounding and the dilatancy (open cone) surfaces, that depict the deviatoric stress-ratios at critical state, peak strength and phase transformation, on the basis of the state parameter $\psi = e - e_{cs}$ (e being the void ratio and e_{cs} being the critical state void ratio at the same mean effective stress p) initially defined by Been & Jefferies (1985).

(b) A Ramberg-Osgood type, non-linear hysteretic formulation for the "elastic" strain rate that governs the response at small to medium (cyclic) shear strains.

(c) A relocatable stress projection center r^{ref} related to the "last" shear reversal point, which is used for mapping the current stress point on model surfaces and as a reference point for introducing non-linearity in the "elastic" strain rate.

(d) An empirical index for the directional effect of sand fabric evolution during shearing, which scales the plastic modulus, and governs the rate of excess pore pressure build-up and permanent strain accumulation under large cyclic shear strains potentially leading to liquefaction and cyclic mobility.

Table 3.4: NTUA-Sand model constants: physical meaning and values for Nevada sand
Πίνακας 3.4: Παράμετροι προσομοιώματος NTUA-SAND: φυσική σημασία και τιμές για άμμο Nevada

#	Physical meaning	Value
M_c^c	Deviatoric stress ratio at critical state in triaxial compression (TC)	1.25
c	Ratio of deviatoric stress ratios at critical state in triaxial extension (TE) over TC	0.72
Γ_{cs}	Void ratio at critical state for p=1kPa	0.910
λ	Slope of critical state line in the [e-lnp] space	0.022
B	Elastic shear modulus constant	600*
v	Elastic Poisson's ratio	0.33
k_c^b	Effect of ψ on peak deviatoric stress ratio in TC	1.45
k_c^d	Effect of ψ on dilatancy deviatoric stress ratio in TC	0.30
γ_1	Reference cyclic shear strain for non-linearity of "elastic" shear modulus	0.025%
α_1	Non-linearity of "elastic" shear modulus	0.6*
A_o	Dilatancy constant	0.8
h_o	Plastic modulus constant	15,000
N_o	Fabric evolution constant	40,000

** for monotonic loading of Nevada sand: B = 180, a_1 = 1.0*

The model requires the calibration of eleven (11) dimensionless and positive constants for monotonic loading, and an additional two (2) for cyclic loading. Ten

(10) out of the above thirteen (13) model constants may be directly estimated on the basis of monotonic and cyclic element tests, while the remaining three (3) constants require trial-and-error simulations of element tests. Details regarding the model formulation and the calibration procedure of the model constants can be found in Andrianopoulos et al. (2010) and in Deliverable (technical report) D1 of Work Package 2: "Software development for the numerical analysis of the coupled liquefiable soil-foundation-bridge pier response" (Bouckovalas et al. 2012). The model constants are summarized in **Table 3.4** along with their values for Nevada sand, i.e. the uniform fine sand used in the VELACS project (Arulmoli et al. 1992a) and also used for the calibration of the NTUA-Sand model.

Boundary conditions.- Different Boundary Conditions were used for static and for dynamic loading conditions. For the former, which involves the establishment of the geostatic stress field and the application of initial static loading to the foundation, vertical and horizontal rollers were considered at the lateral and bottom boundaries respectively. During dynamic loading, the well-known "tied-node" method, widely used in numerical simulations (Elgamal et al. 2005; Ghosh and Madabhushi 2003; Popescu et al. 2006), was incorporated. The method essentially reproduces kinematic conditions imposed by laminar boxes used in centrifuge and shaking table experiments by enforcing equal horizontal displacements to grid points of the same elevation. The main drawback of the particular type of boundary conditions is that horizontally propagating seismic waves are reflected back into the main area of interest and may affect the numerical outcome. Nevertheless, in highly non-linear problems, such as the liquefaction phenomena studied herein, the associated hysteretic damping practically absorbs reflected waves.

Footing.- The 5m wide strip footing is simulated by applying a uniform contact pressure on top of the improved crust. The footing was considered to have zero mass, to avoid the generation of inertia effects. Furthermore, the grid points at which the vertical loading was imposed were rigidly connected through a structural cable element ensuring the development of uniform vertical displacements, simulating a rigid foundation.

Loading Sequence.- All analyses are conducted in three separate phases, which are schematically presented in **Figure 3.5.**

Phase 1: Initial geostatic stresses are generated and the foundation load under static conditions is gradually applied at increments of 5kPa until the desired contact pressure Q is reached (branch a-b).

Phase 2: A fully-coupled effective stress dynamic analysis is executed, subjecting the soil-foundation system to a harmonic excitation, with parallel pore water flow throughout the grid. During this phase, excess pore pressures develop and dynamic settlements accumulate under constant load Q (branch b-c). Note that seismic settlements may become large and even exceed the static ones.

Phase 3: After the end of shaking, the static load Q is increased until bearing capacity failure, while the underlying un-improved layer remains liquefied (branch c-d).

Branch c-d in the figure, practically renders a degraded bearing capacity of the footing, compared to the initial static value (branch b-b'), as the subsoil remains liquefied and its shearing resistance has practically vanished. The post-shaking stage is performed under drained conditions, nevertheless, to account for the effects of liquefaction, excess pore pressures generated during shaking are maintained constant. This is achieved by prohibiting water flow and setting the water bulk modulus to a very small value (1kPa instead of 2×10^6kPa) so that pore pressures are not affected by the applied static loading.

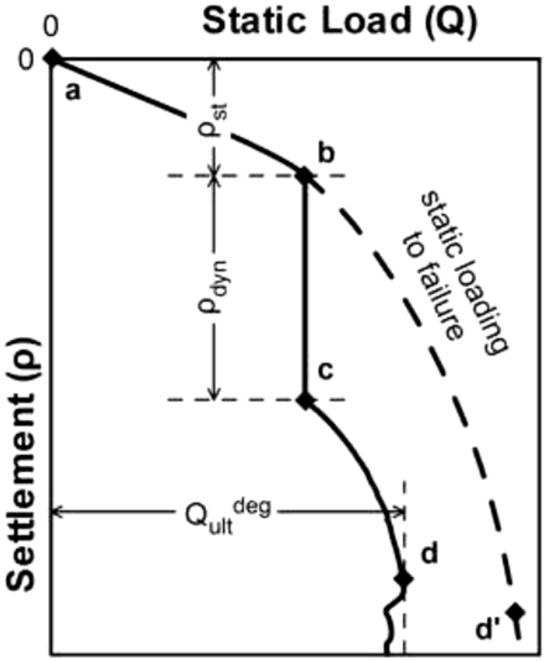

Figure 3.5: Typical load-displacement curve for the three-step analysis
Σχήμα 3.5: Τυπική καμπύλη φορτίου-μετατόπισης για την ανάλυση σε τρία στάδια

Damping.- As far as damping is concerned, the hysteretic response of the soil and the associated damping is captured through the use of NTUA Sand. Furthermore, a small value of 2% Rayleigh damping was assigned in the model to simulate viscous damping at small strain levels.

Lateral Dimensions.- Appropriate selection of lateral boundaries is critical for the accurate estimation of the overall response of the system. According to DIN 4017 the static failure mechanism of a surface footing resting on top of a relatively stiff cohesionless soil may extend up to 8.51 times the footing width B, for a friction angle of $\varphi=40^o$, as shown in **Figure 3.6**. Thus, for the 5m wide strip footing examined herein, an 85m wide configuration would be at minimum required.

For the problem examined herein, soil improvement can significantly increase the relative density of the top crust up to 85-90% [depending on the replacement ratio α_s and the initial relative density $D_{r,o}$(%)]. The use of the recalibrated NTUA-SAND constitutive model in the simulation of the particularly dense sand, implies the prediction of friction angle values greater than 40 degrees, especially under simple shear conditions. This particular observation, in combination with **Figure 3.6**, implies that even wider grid configurations may be necessary for the free and unobstructed development of the post-shaking failure mechanism and the determination of the degraded bearing capacity of the footing.

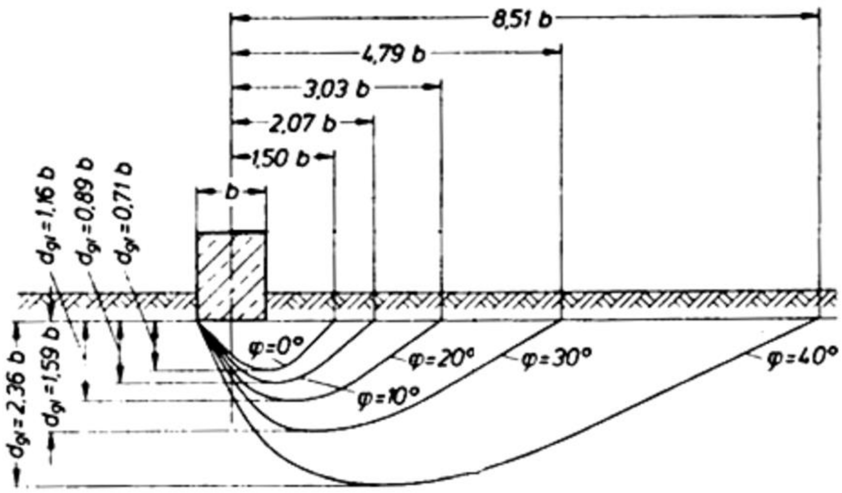

Figure 3.6: Bearing failure wedge sizes for strip footings, with different friction angles φ, (DIN4017)

Σχήμα 3.6: Έκταση μηχανισμού αστοχίας λωριδωτού θεμελίου συναρτήσει της γωνίας τριβής φ (DIN4017)

The lateral sufficiency of the considered grid is parametrically investigated for a 20m thick sand layer of initial relative density equal to $D_{r,o}$=65%, three depths of improvement, namely $H_{imp.}$=4, 6, & 8m and an average relative density in the improved crust equal to 85%. Initially, four grid arrangements are tested for each scenario, considering L_x/B ratios equal to 12, 16.8, 21.2 and 24.8, rendering total horizontal dimensions equal to L_x=60, 84, 106 and 124 meters, respectively. Later on, additional analyses are executed for the case of $H_{imp.}$=6 & 8m, for L_x=140 meters, to fully visualize the observed trend between the width of the grid - L_x(m) -and the load required to reach failure, $q_{ult.}$ (kPa).

Three of the overall five different grid configurations are shown in **Figure 3.7**. The narrowest grid considered in the particular investigation (L_x=60m) consists of 42×20=840 zones, with dimensions varying from 1.0×1.0m around the axis of symmetry to 1.5×1.0m and 2.0×1.0m, as approaching the boundaries of the model. The 84×20m grid arrangement resulted after increasing the number of zones in the x-direction to 58, thus generating 58×20=1160 zones, preserving at the same time the same discretization pattern. The following grid arrangement (L_x=106m) is discretized in 72×20=1440 zones, the L_x=124m mesh in 84×20=1680 zones and the widest mesh (L_x=140m) in 96×20=1920 zones, always preserving the discretization outline of the initial configuration.

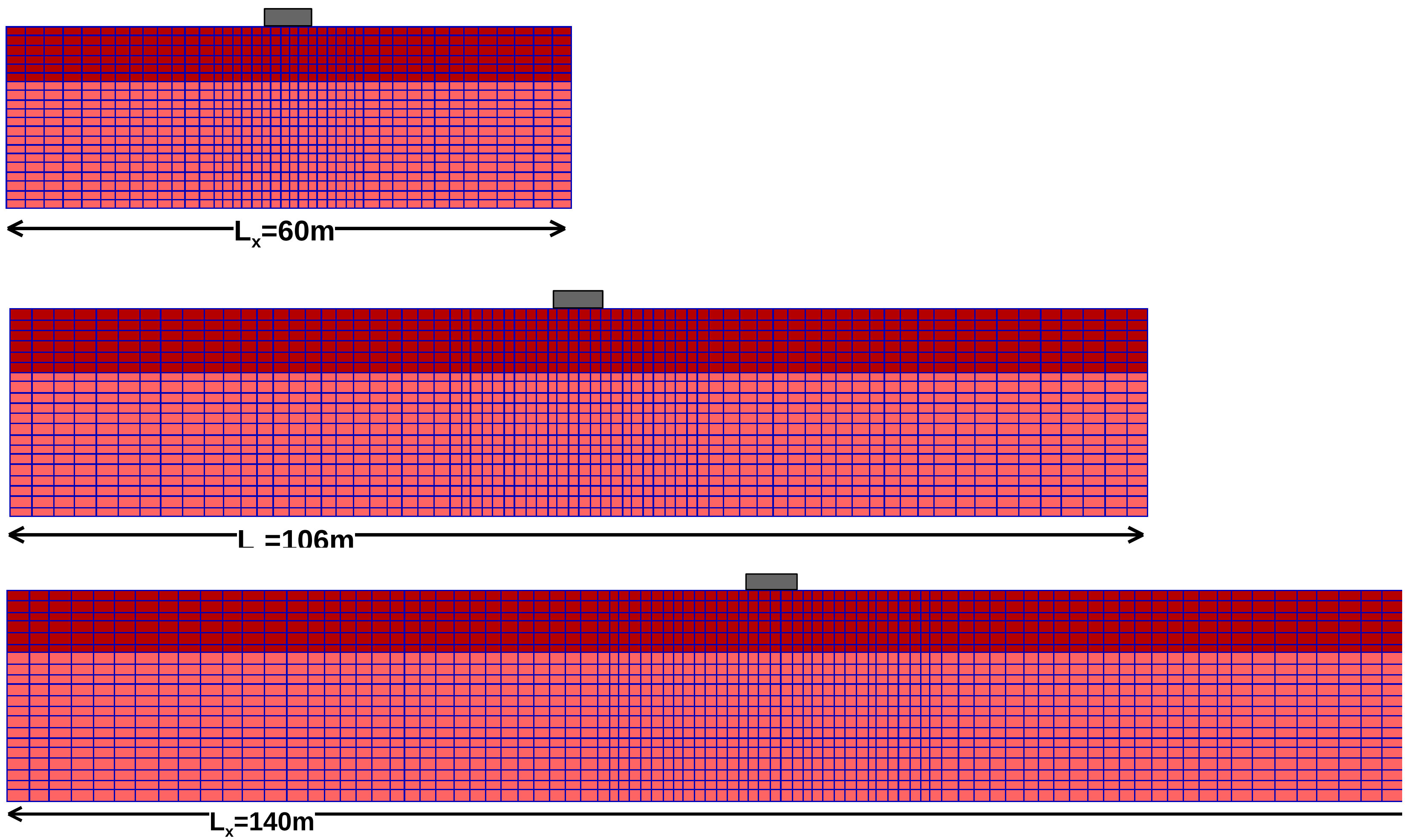

Figure 3.7: Parametric investigation of grid width for the execution of the 2-D analyses. Typical grid configurations for L_x=60, 106 & 140m.

Σχήμα 3.7: Παραμετρική διερεύνηση επαρκούς πλάτους καννάβου για την εκτέλεση 2-Διάστατων αριθμητικών αναλύσεων. Τυπικές διατάξεις για Lx=60, 106 & 140m

Figure 3.8 summarizes the effect of the grid width on dynamic settlements. The three different curves correspond to the three different improvement depths, $H_{imp.}$(m). The observed effect is particularly minor and practically independent of the width of the considered configuration for L_x/B values greater than about 15.

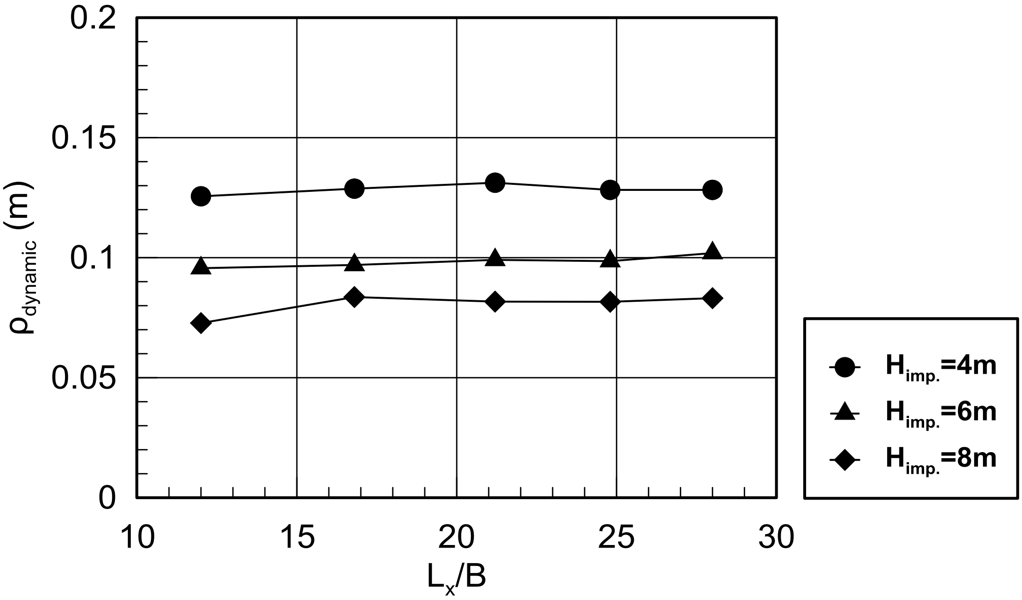

Figure 3.8: Dynamic settlements as a function of width L_x(m) normalized by the footing width B(m)

Σχήμα 3.8: Δυναμικές καθιζήσεις συναρτήσει του πλάτους L_x(m) κανονικοποιημένο προς το πλάτος του θεμελίου

Figure 3.9 exhibits the effect of the mesh width on the post-shaking degraded bearing capacity of the foundation, again with regard to the normalized width L_x/B. It is observed that unlike the previous figure, the load to failure ($q_{ult.}$) significantly decreases with increasing grid-width L_x(m), disclosing that major boundary effects take place in the narrower grid arrangements, regardless of the improvement depth. The particular observation essentially implies that unless the grid is wide enough, the failure mechanism during the post-shaking phase cannot fully develop because the grid-boundaries provide substantial lateral resistance, hence leading to false and considerably non-conservative estimates of the post-shaking load required to failure. Additionally to the above, it appears that the grid demands are higher for deeper improvement schemes, considering that for $H_{imp.}$=8m the derived curve levels off after L_x/B=25. Based on the previous remarks, all analyses with $H_{imp.}$=4 & 6m will be performed hereafter with L_x=106m while for $H_{imp.}$=8m the width will be increased to L_x=124m to eliminate potential boundary induced effects.

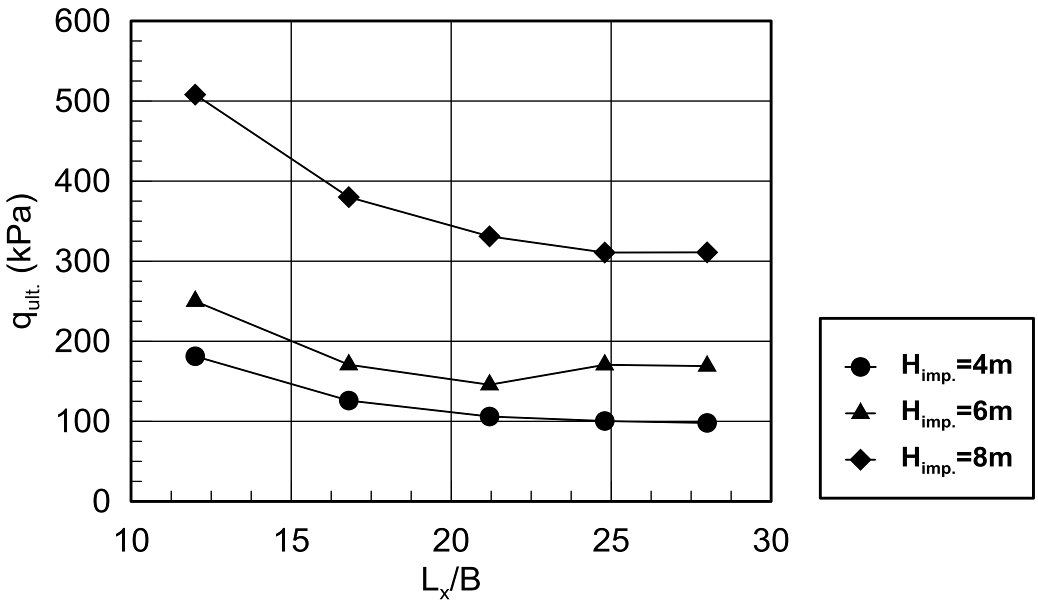

Figure 3.9: Ultimate bearing capacity $q_{ult.}$ (kPa) as a function of width L_x(m) normalized by the footing width B(m)

Σχήμα 3.9: Φέρουσα ικανότητα $q_{ult.}$ (kPa) συναρτήσει του πλάτους L_x(m) κανονικοποιημένο προς το πλάτος του θεμελίου

A last, yet substantial, observation is that, provided the optimum grid width is used, the thickness of the improved crust has a distinct effect on both the dynamic-induced settlements and the post-shaking bearing capacity. Indeed, dynamic-induced settlements greatly diminish from 0.13m to 0.10 and 0.08m after increasing the improvement depth from 4 to 6m and then to 8 meters respectively. The opposite trend is observed for the post-shaking bearing capacity, which increases with increasing depth of improvement. Namely, after doubling the thickness of the improved crust from 4 to 8meters, the post-shaking bearing capacity increases by a factor of 3, i.e. from 100kPa to 300kPa. All the above, disclose the controlling role of the thickness of the performed improvement, on the seismic performance of a shallow foundation, which is going to be thoroughly examined in subsequent chapters.

3.4 Typical numerical results.

The reference analysis, depicted in **Figure 3.10**, refers to a 20m thick liquefiable sand layer, with initial relative density $D_{r,o}$=45% and initial coefficient of permeability k_{sand}=6.6*10^{-5}m/s, improved at the top 4 meters at a replacement ratio equal to α_s=0.07. The improved crust attains a relative density equal to $D_{r,imp.}$=60% and coefficient of permeability $k_{eq.}$=9.85*10^{-4} m/s. The shallow foundation on top of the above soil profile applies a contact pressure equal to q=75kPa. All other associated assumptions involved in the numerical analysis have already been described previously.

The various properties were intentionally selected as above, aiming at providing the maximum compatibility to the reference case analyzed by Karamitros et al. (2012). In such way, possible similarities and discrepancies in the response mechanisms for the case of an impermeable, non-liquefiable crust (Karamitros 2010) and a permeable, partially liquefied crust (present study) can be more easily identified. The comparisons will be performed in terms of the mechanisms of excess pore pressure generation, the accumulations of seismic-induced settlements as well as the degradation of the footing's bearing capacity.

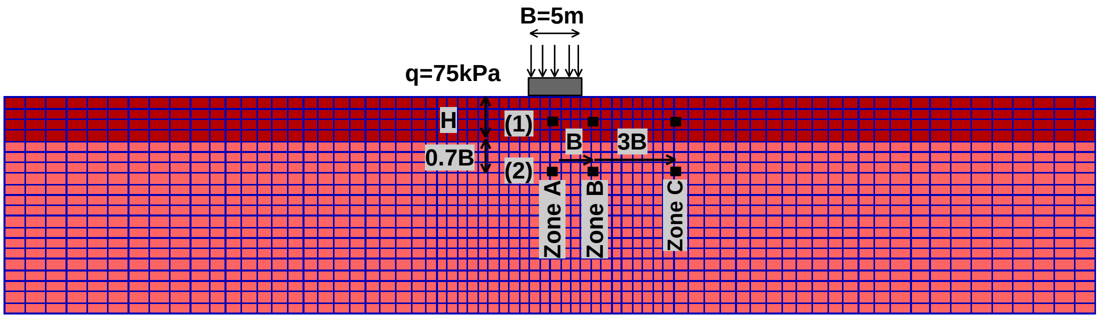

Figure 3.10: Location of characteristic zones
Σχήμα 3.10: Θέση χαρακτηριστικών ζωνών

3.4.1 Excess pore water pressure generation

The mechanisms of excess pore pressure generation and evolution during shaking as well as the post-shaking behavior of the partially or entirely liquefied soil are examined in the present paragraph. For that purpose, **Figure 3.11** and **Figure 3.12**, summarize the excess pore pressure and excess pore pressure ratio time-histories respectively, at six different positions in the grid (**Figure 3.10**), namely underneath the footing (A), at the corner (B) and in the free field (C), and at two distinct depths, namely inside the improved crust (A1, B1, C1) and the liquefiable ground (A2, B2, C2).

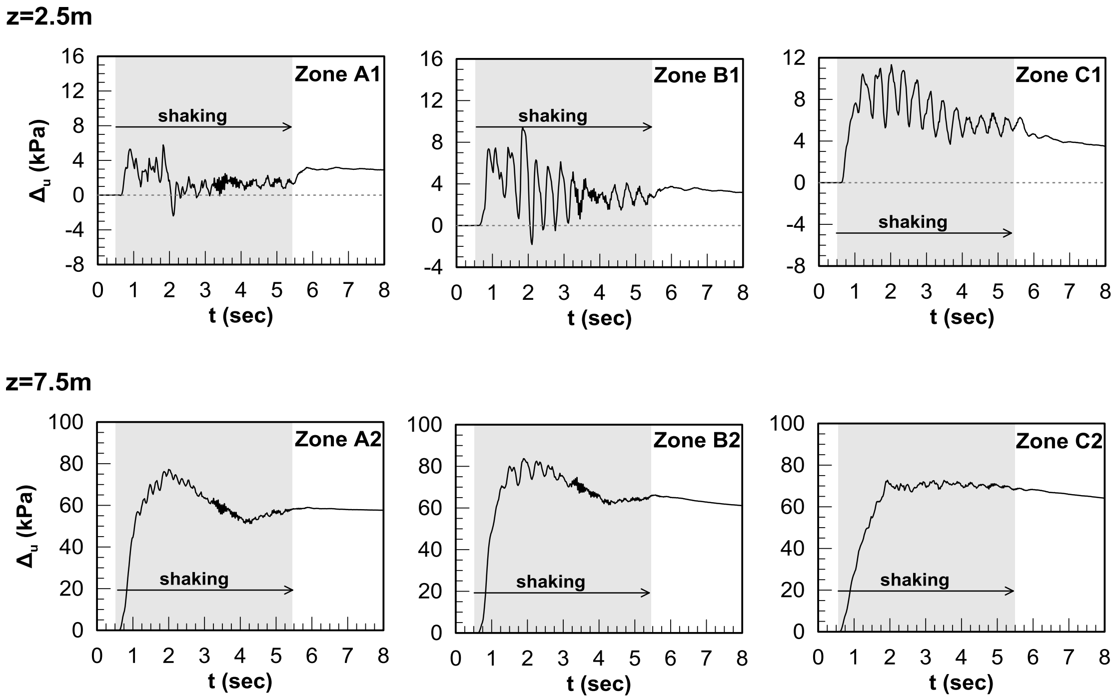

Figure 3.11: Excess pore pressure time-histories
Σχήμα 3.11: Χρονοϊστορίες υπερπιέσεων πόρων

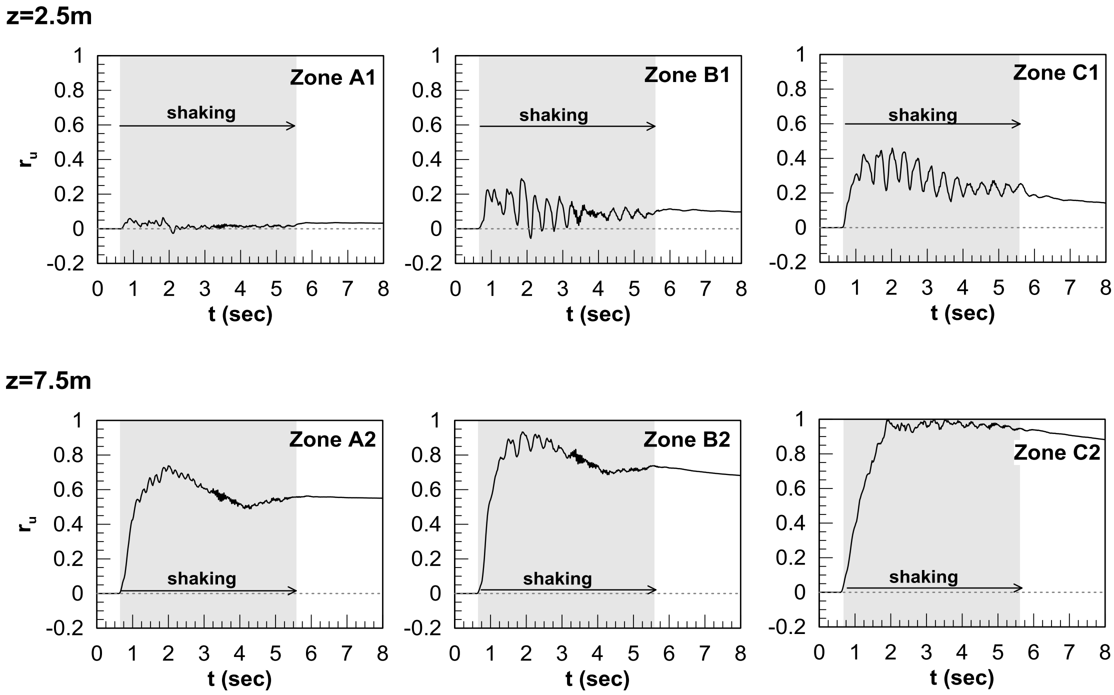

Figure 3.12: Excess pore pressure ratio time-histories
Σχήμα 3.12: Χρονοϊστορίες δείκτη υπερπιέσεων πόρων

One of the main observations that stand out is the fact that the soil underneath the footing experiences lower excess pore pressures compared to the soil in the free-field, regardless of elevation. The explanation behind the above pattern, draws upon the foundation-induced static deviatoric stresses, preventing excess pore pressures under the foundation to reach or exceed the free-field values. The particular observation was originally noticed by Yoshimi and Tokimatsu (1977) in their field observations after the Niigata earthquake in 1964. Shaking table tests performed by themselves as well as additional shaking table and centrifuge experiments performed by other researchers [e.g. Adalier et al. (2003); Coelho et al. (2004); Kawasaki et al. (1998); Liu and Dobry (1997)] provided additional support to the particular remark.

The previous pattern is repeated in the excess pore pressure ratio time histories, which are lower underneath the footing and increase with distance from the footing (zones A2, B2, C2). The explanation to the particular effect lays in the definition of the excess pore pressure ratio itself, also noted by Karamitros et al. (2012). Taking into account the additional vertical stress applied by the footing, it is mathematically established that the excess pore pressure ratio under the footing will be defined as:

$$r_{u,foot} = \frac{\Delta u_{foot}}{\sigma'_{vo,foot}} = \frac{\Delta u_{foot}}{\sigma'_{vo,ff} + \Delta\sigma'_{v,foot}} \tag{3.4}$$

Nevertheless, as mentioned above, due to the foundation-induced static deviatoric stresses the excess pore pressures developing in the free field are greater than the ones underneath the footing. Particularly, under liquefaction, excess pore pressures will equal the effective vertical stresses, i.e. $\Delta u_{,ff} = \sigma'_{vo,\,ff} = \sigma'_{vo,\,foot}$. Therefore the above expression becomes:

$$r_{u,foot} \le \frac{\Delta u_{ff}}{\sigma'_{vo,ff} + \Delta\sigma'_{v,foot}} = \frac{\sigma'_{v,o,foot}}{\sigma'_{vo,ff} + \Delta\sigma'_{v,foot}} = \frac{1}{1 + \Delta\sigma'_{v,foot} / \sigma'_{vo,ff}} \tag{3.5}$$

The above mathematical expression also explains the gradual increase of excess pore pressure ratio values with depth (zones A1-A2 & B1-B2). Namely, the additional vertical stress applied by the footing gradually decreases with depth, therefore, the resulting excess pore pressure ratio will increase.

Lower excess pore pressure ratios developing underneath the footing have also been mentioned by Liu & Dobry (1997), after performing centrifuge tests to examine the mechanism of liquefaction-induced settlement of a shallow foundation, as well as the effect of sand densification in a specified area under a shallow footing. They attributed the lower excess pore pressure ratios to the dilative response of the soil, induced by the applied static shear stresses. Moreover, Adalier et al. (2003) observed that excess pore pressures increased with depth and distance from the footing and that the footing values did not exceed the excess pore pressures in the free field. They attributed this behavior to the inability of the liquefied free-field soil to provide sufficient lateral resistance beyond its initial vertical effective stress.

Regarding locations C1 and C2, it is inferred that the obtained excess pore pressure ratio within the crust (zone C1) barely exceeds $r_{u,max}$=0.4, as a result of the performed improvement. On the other hand, within the unimproved sand layer, liquefaction occurs already from the early stages of loading, as indicated by the excess pore pressure ratio which becomes equal to $r_u = \Delta_u / \sigma'_{vo} = 1$.

Another interesting characteristic concerns the excess pore pressure generation pattern in the vicinity of the footing and inside the improved crust, namely locations A1 & B1. The excess pore pressure time-history in location A1, essentially verifies the observation by Coelho et al. (2004) about positive peaks of Δu, gradually evolving to intense negative peaks as a result of soil dilation. The negative peaks though are not preserved for long, due to the groundwater flow emerging to the specific location from the surrounding area. Moreover, at the edge of the footing, the previously reported positive spikes appear more intense up to about 2secs and consequently reduce to negative values. At the later stages of loading the particular effect is smoothed, probably due to the groundwater flow taking place in the permeable crust. The decrease in the excess pore pressure time histories in the deeper location of the configuration is explained on the same basis of soil dilation. The main difference is that the footing-induced static stresses are lower at greater depths and therefore greater excess pore pressures are allowed to develop.

The post-shaking increase of excess pore pressures under the footing, evident in the presented time-histories, is explained on the basis of groundwater flow occurring upwards as well as from the free field towards the footing. This is also verified by the groundwater flow vectors at the end of shaking illustrated in **Error! Reference ource not found.**. Note that the post-shaking increase of excess pore pressures within the crust is substantially greater, compared to locations within the liquefiable sand, as a consequence of the greater permeability of the drain improved upper layer. Liu & Dobry (1997) noted the post-shaking increase in the excess pore pressures under the footing as well, which was also attributed to a substantial groundwater flow from the surrounding areas towards the footing. The particular observation is also mentioned by Adalier et al. (2003), and Kawasaki et al. (1998).

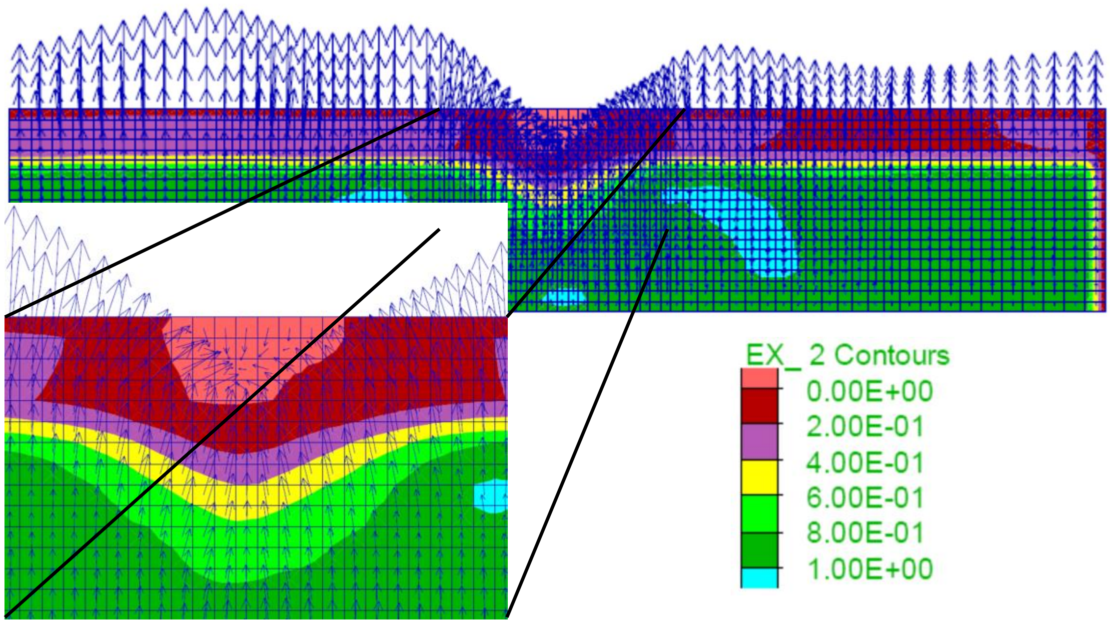

Figure 3.13: Excess pore pressure ratio contours and flow vectors under the footing area at the end of shaking

Σχήμα 3.13: Ισοκαμπύλες λόγου υπερπιέσεων πόρων και διανύσματα ροής κάτω από την περιοχή του θεμελίου στο τέλος της διέγερσης

3.4.2 Settlement accumulation

The seismic settlement time-history of the footing is illustrated in **Figure 3.14**. It is observed that settlements accumulate linearly with time and mainly develop during shaking, with only a minor part being added post-shaking, probably due to excess pore pressure dissipation. The specific pattern has also been observed by Liu & Dobry (1997), Adalier et al. (2003) as well as Dashti et al. (2010) in centrifuge experiments examining the seismically induced settlements of shallow foundations on different configurations of improved densified ground.

Moreover, the deformed mesh at the end of shaking and the associated displacement vectors are exhibited in **Figure 3.15**. Evidently, at the footing location displacement vectors are totally vertical, as a result of the consideration of a rigid beam element, as explained previously. More importantly, the footing's settlement accumulation, leads to significant lateral flow of the liquefied underlying sand towards the partially liquefied surface. The particular deformation pattern has also been observed in centrifuge tests performed by Adalier et al. (2003) and Dashti et al. (2010).

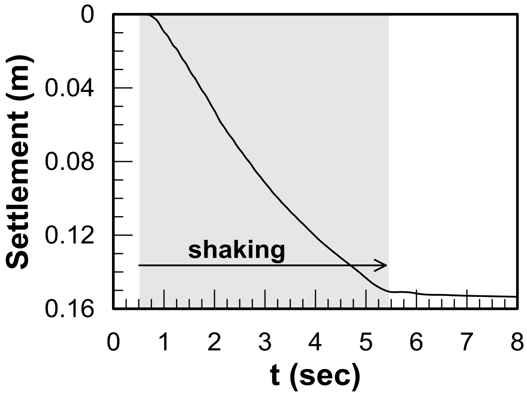

Figure 3.14: Footing settlement accumulation time-history
Σχήμα 3.14: Χρονοϊστορία συσσώρευσης καθιζήσεων στο θεμέλιο

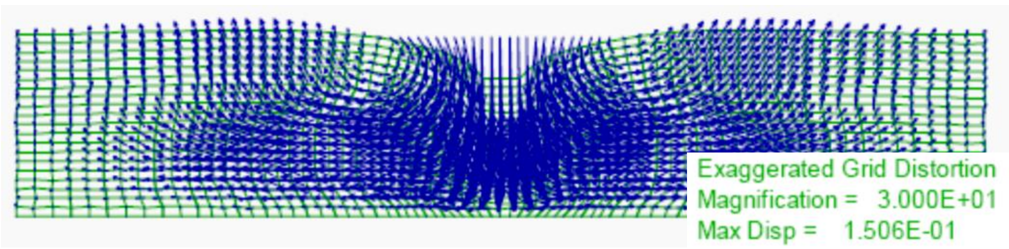

Figure 3.15: Deformed mesh and displacement vectors at the end of shaking
Σχήμα 3.15: Παραμορφωμένος κάνναβος και διανύσματα μετακινήσεων στο τέλος της δόνησης

To further analyze the mechanisms behind settlement accumulation, **Figure 3.16**, summarizes the horizontal and vertical components of the footing's motion including acceleration, velocity and displacement time-histories. The particular time-histories refer to the baseline case described in the previous section. It is observed that the onset of liquefaction leads to a significant de-amplification of the horizontal motion without any significant horizontal displacement. On the other hand, the much smaller in magnitude, vertical component of motion does not reduce its amplitude and presents a ratio of 2:1 regarding the predominant frequency of the vertical over the horizontal acceleration, as it has also been observed by Coehlo et al. (2004). More importantly, from the above figure it is implied that the "plateau-shaped" velocity time-history is responsible for the linear accumulation of settlement with time, plotted beneath.

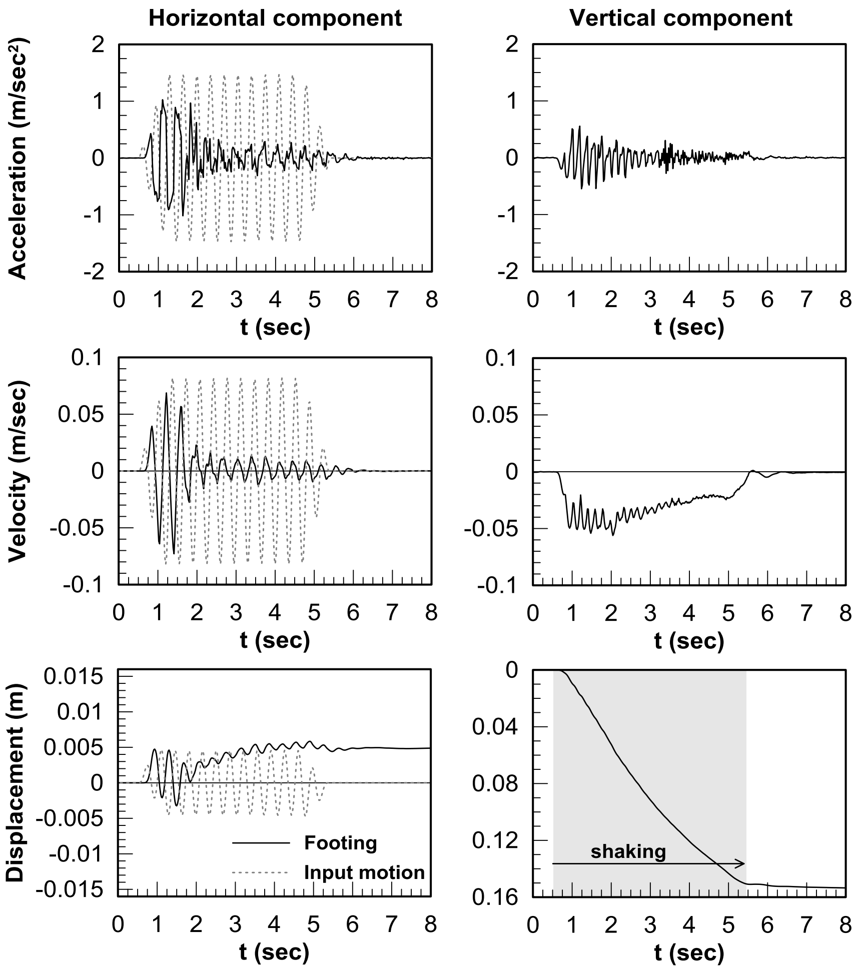

Figure 3.16: Horizontal and vertical acceleration, velocity and displacement time-histories at the footing

Σχήμα 3.16: Χρονοϊστορίες οριζόντιων και κατακόρυφων επιταχύνσεων, ταχυτήτων και μετακινήσεων στο θεμέλιο

The particular pattern was initially identified by Richards et al. (1993), who employed the Richards and Elms (1979) sliding-block approach for retaining walls to calculate seismic displacements of foundations on uniform dry sand. Namely, they considered a simplified Coulomb active-passive wedge failure mechanism, which is activated every time the critical acceleration level is exceeded. As a result, the active wedge underneath the footing moves downward and sideways, while the passive wedge is displaced laterally. Hence, displacements accumulate incrementally during shaking and may be easily computed as a function of the excitation characteristics and the seismic counterpart of the active critical angle of rupture (ρ_{AE}).

The above work by Richards et al. (1993) may be extended to describe the liquefaction – induced settlement accumulation of shallow foundations in saturated liquefiable sands. **Figure 3.17** illustrates the velocity vectors and shear strain rate contours justifying the above mechanism. More specifically, the combination of the footing's bearing pressure along with the developing horizontal inertia forces in the subsoil trigger the activation of the same one-sided wedge-type failure mechanisms. The particular wedge system develops twice within one loading cycle, one on each side of the footing and opposite to the ever-current direction of the input motion. As a result, during one total loading cycle, one vertical and two opposite and equal - therefore cancelling - horizontal footing displacements occur. The above observations are also verified by Karamitros et al. (2013), who examined the relevant issue of a shallow foundation on liquefiable soil with a clay crust.

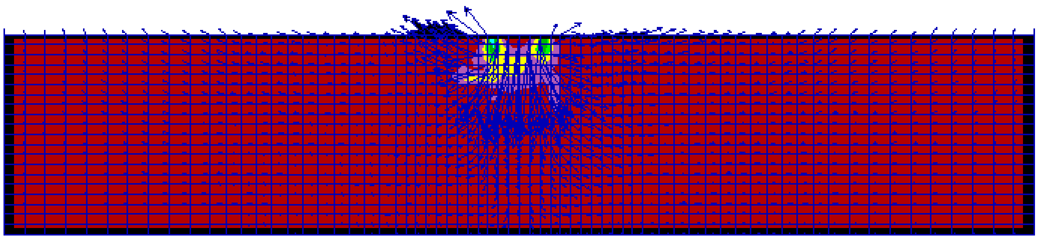

(a) Static load failure mechanism

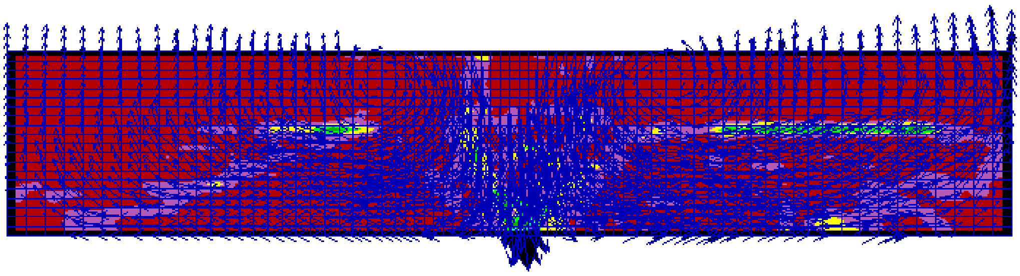

(b) Post-shaking failure mechanism

Figure 3.17: Shear strain rate contour and velocity vectors related to (a) static and (b) post-shaking bearing capacity failure

Σχήμα 3.17: Ρυθμός ανάπτυξης διατμητικών παραμορφώσεων και διανύσματα ταχύτητας λόγω (α) στατικής και (β) μετασεισμικής αστοχίας σε φέρουσα ικανότητα

3.4.3 Post-shaking bearing capacity degradation

The onset of subsoil liquefaction apart from the accumulation of dynamic settlements causes total loss of shear strength in the unimproved soil and partial loss of shear strength inside the improved crust, due to the inevitable but controlled development of excess pore pressures. The particular effect leads to the degradation of the shallow foundation's bearing capacity, for a specific period of time, defined as the time required for the total excess pore pressure dissipation. As a result, the allowable post-shaking factor of safety may become much lower than the conventional values for static loads.

Figure 3.17a & **b**, exhibit shear strain rate contours and velocity vectors at failure developing for static non-liquefied conditions and the liquefied state respectively, providing a useful insight to the developing mechanisms. It is evident that under static conditions, failure occurs within a very confined area within the crust. On the contrary, in the case of liquefaction occurrence, the footing appears to punch through the partially liquefied crust, into the liquefied subsoil whose shearing resistance has practically minimized as a consequence of the excess pore pressure generation. The specific failure pattern is also referred to as "punching shear failure" (Vesic, 1963) and is encountered in cases of fairly loose soils.

The developing failure pattern is very similar to the mechanism incorporated by Meyerhoff & Hanna (1978) for shallow foundations on layered soil profiles, illustrated in **Figure 3.18a** & **b**. In the proposed methodology, it is specified that punching shear failure (**Figure 3.18a**) occurs in relatively thin top layers, thus depending on the H/B ratio, in which H is the thickness of the upper layer, and B the width of the footing. In cases where H is relatively large, the failure surface develops entirely within the top stronger layer, as illustrated in **Figure 3.18b**.

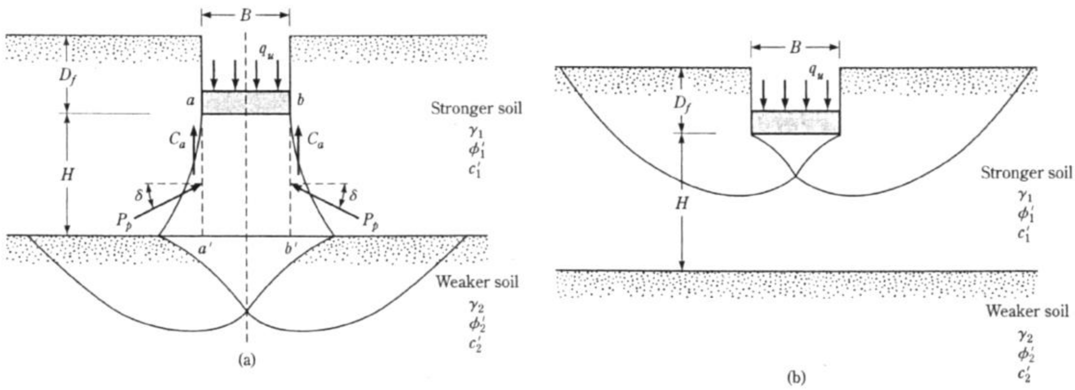

Figure 3.18: Bearing capacity of a continuous foundation on layered soil (Meyerhof & Hanna, 1978)

Σχήμα 3.18: Φέρουσα ικανότητα θεμελίωσης σε δίστρωτο έδαφος (Meyerhof & Hanna, 1978)

Figure 3.19 exhibits the load-displacement curves for static loading and the post-shaking part of the reference analysis (Phase 3 as described previously). The static bearing capacity failure was numerically simulated by incrementally increasing the footing's contact pressure (Phase 1 of **Figure 3.5**) up to the failure load of 1550kPa. The theoretically derived ultimate bearing capacity of a 2-layer sand formation was estimated between q_t=1410 and 1660kPa, therefore, essentially verifying the numerical prediction. As a result, the factor of safety under static conditions is estimated to be equal to $F.S._{stat.}$=1550/100=15.5. The post-shaking bearing capacity was computed to be slightly above 105kPa, reducing the safety factor to

$F.S._{deg.}$=105/100 ≈ 1.05, indicating a marginal avoidance of total structural failure, due to the onset of liquefaction in the subsoil.

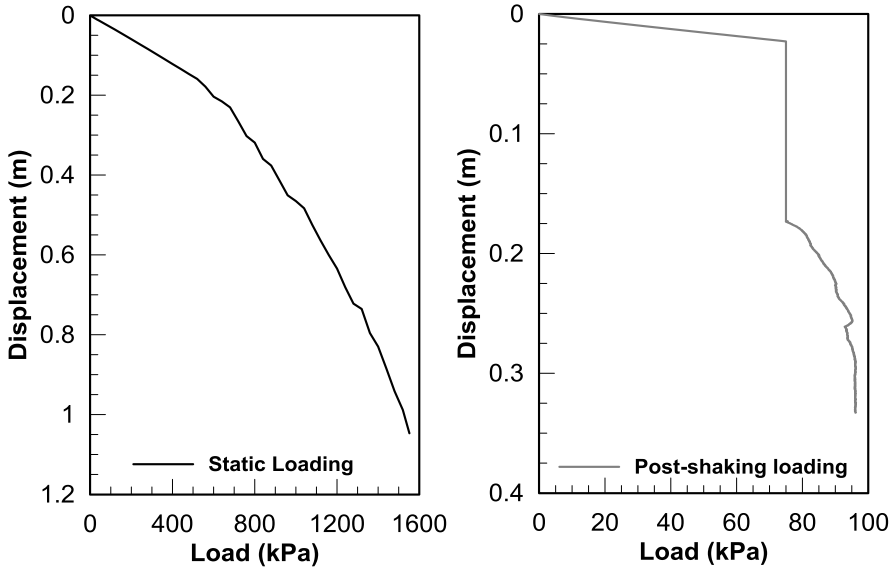

Figure 3.19: Load-displacement curves for initial static loading and post-shaking loading
Σχήμα 3.19: Καμπύλες φορτίου-μετατόπισης για την αρχική στατική φόρτιση και την μετασεισμική φόρτιση

3.5 Verification of numerical methodology [Liu & Dobry (1997)].

The subsequent verification will focus on the effectiveness of the methodology to accurately predict the seismically induced excess pore pressure generation and the associated dynamic settlements. The selected data are obtained from a series of centrifuge tests performed by Liu & Dobry (1997). In brief, Liu & Dobry (1997) investigated the mechanism of liquefaction-induced settlement of a shallow foundation, as well as the effectiveness of sand densification by vibrocompaction in a cylindrical area under a shallow footing. Overall, eight centrifuge experiments were performed at the centrifuge facility of the Rensselaer Polytechnic Institute (RPI), Troy, NY, considering a circular footing placed on top of a medium dense saturated sand layer overlying an impervious rigid base. The first series of tests focused on the effect of the depth of compacted soil under the foundation on the footing's acceleration and settlement. The second group consisted of three tests in which the effect of soil permeability on excess pore pressure built up and footing settlement is investigated, with no densification performed. For the purposes of the specific verification, the first group of five tests was considered.

3.5.1 Test description and numerical simulation

Model Configuration and Instrumentation Layout.- The rigid foundation is a circular footing of prototype diameter 4.56m applying an average contact pressure of q=100kPa (in prototype scale, for a centrifugal acceleration field of 80g). The soil used in all tests is a fine, uniform Nevada #120 sand with initial relative density D_r =

52±3% and a total thickness equal to 12.5m in prototype scale (**Figure 3.20a**). The vibro-compacted zone extends to an area of about 1.6 times the width of the footing, as illustrated in **Figure 3.20b**, while the compaction depth varies from Z_c = 0 to 2.76B, essentially covering to the full thickness of the soil stratum. The relative density of the compacted zone was estimated around 90%. The different testing parameters are summarized in **Table 3.5** for all five models. The average relative density of the compacted cylindrical soil in test C1 was computed equal to Dr,c=106%, which according to Liu & Dobry (1997), is probably due to errors in estimating the compacted soil volume.

Table 3.5: Soil properties of series C tests (Liu & Dobry, 1997)
Πίνακας 3.5: Εδαφικές ιδιότητες της σειράς δοκιμών C (Liu & Dobry, 1997)

Test	$D_{r,ini}$ (%)	Z_c (m)	Zc/B	$D_{r,c}$ (%)
C0	54	0	0	-
C1	51	3.22	0.71	>100
C2	55	6.72	1.47	88
C3	49	9.45	2.07	91
C4	51	12.58	2.76	89

The permeability of Nevada #120 sand tested in the laboratory at 1g is reported to be equal to the dynamic value, i.e. k=0.0021cm/s. The pore fluid used in the particular test series is water, therefore, according to the applying scaling laws, the permeability of the prototype soil will be n times larger than that obtained in the laboratory test at 1g. Hence, at 80g n equals 80 and the permeability coefficient is equal to k=80*0.0021=0.168cm/s, corresponding to a coarse sand.

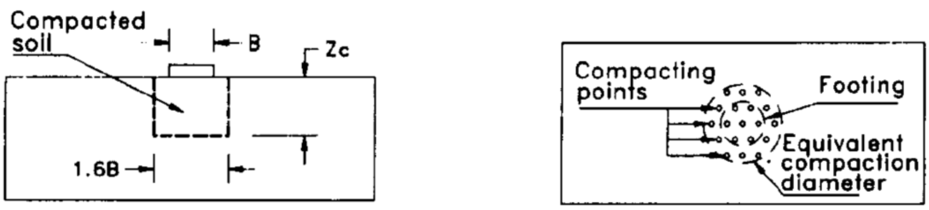

(a) (b)

Figure 3.20: Centrifuge test soil compaction- (a) profile (b) plan view
Σχήμα 3.20: Εδαφική συμπύκνωση στο πείραμα φυγοκεντριστή (α) τομή (β) κάτοψη

Figure 3.21 shows the model configuration and the instrumentation of the tests. Three horizontal accelerometers were installed, the first at the model base, α_i, the second on the soil surface away from the footing, α_s, and the third on the footing itself, α_f. Settlements were monitored at the center of the footing (S_f) and the free field (S_s), with vertical linear voltage differential transformers (LVDT). Also, seven pore pressure transducers were placed in the soil at different depths under the center of the footing (locations PC1, PC2 and PC3), close to the edge of the footing (location PE) and away from the footing (locations PF1, PF2 and PF3). The specific configuration was constructed in a rigid rectangular bucket with dimensions 454×204×241mm³. All test configurations were subjected to the same 10-cycle uniform sinusoidal excitation with frequency equal to f=1.5Hz and an average acceleration amplitude of 0.2g.

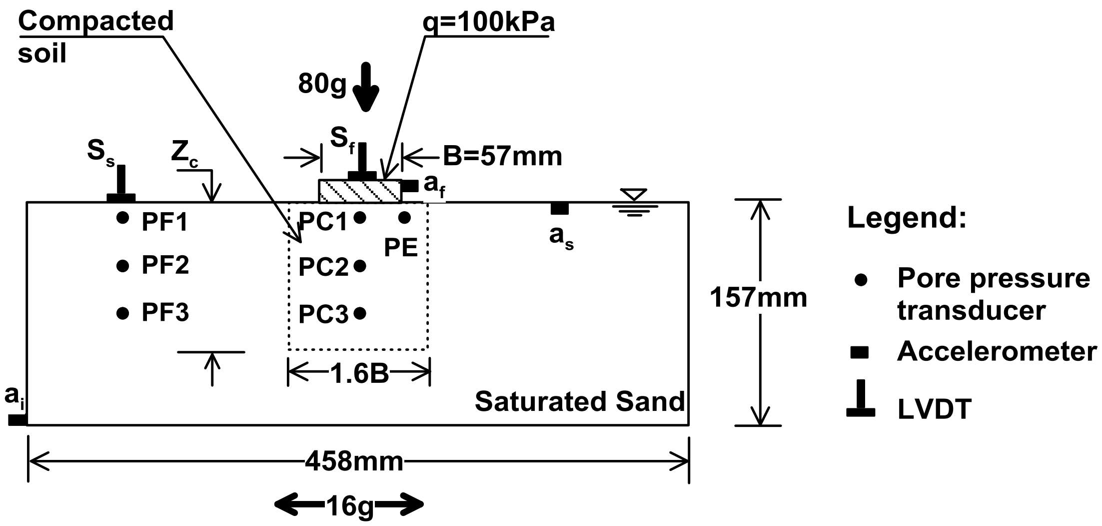

Figure 3.21: Model configuration and instrumentation of test series
Σχήμα 3.21: Πειραματική διάταξη και θέσεις μετρητών

Model Preparation and Test Procedure.- The model sand deposit was constructed to a relative density of $D_{r,o}$=52% using the dry pluviation process with the help of a sand rainer. Pore pressure transducers and accelerometers were placed in the model during the deposition process. After the construction of the uniform sand layer, the densified zone around the assumed footing locaion was constructed with a vibrating tube, 6.4mm in diameter (0.50m in prototype), which was inserted in 19 locations over a circular area of about 1.6 the diameter of the footing. The depth of compaction differs between the tests and it was assumed to reach about 1.5 tube diameters below the tip of the tube. During the densification process some settlement in the area occurred but the soil was leveled by adding additional sand at the ground surface to preserve its initial elevation.

Following compaction, the container was sealed and de-aired by applying a negative vacuum pressure of 101kPa for one hour. De-aired water was then inserted very slowly to the bottom of the model in order to achieve fully saturated conditions. When the water reached 10mm above the free soil surface, vacuum was removed and the model was loaded on the centrifuge platform to be spun at 80g. After consolidation, at the geostatic stresses, the centrifuge was stopped and the model footing was placed on the soil surface. The soil-foundation system was spun back at 80g until the stabilization of all output of the instruments and the dynamic excitation was applied.

Numerical Simulation.- Due to the three-dimensional nature of the above test series, the numerical analyses were performed with the finite difference code FLAC-3Dv4.0.

According to Liu & Dobry (1997) the rigid rectangular bucket has plan dimensions $454\times204mm^2$, this corresponding to prototype dimensions of $36.64\times16.32m^2$ and the sand layer measures a thickness of 12.5m. Also, the dynamic loading is applied along the x-direction, thus the system's response is symmetrical along the y-direction. To take advantage of this symmetry, only half the footing was modeled, by generating a $36.80\times8\times12.5m^3$ grid as presented in **Figure 3.22**. The specific grid was discretized at $0.8\times0.8\times0.5m^3$ brick zones, thus creating a total of 11500 zones.

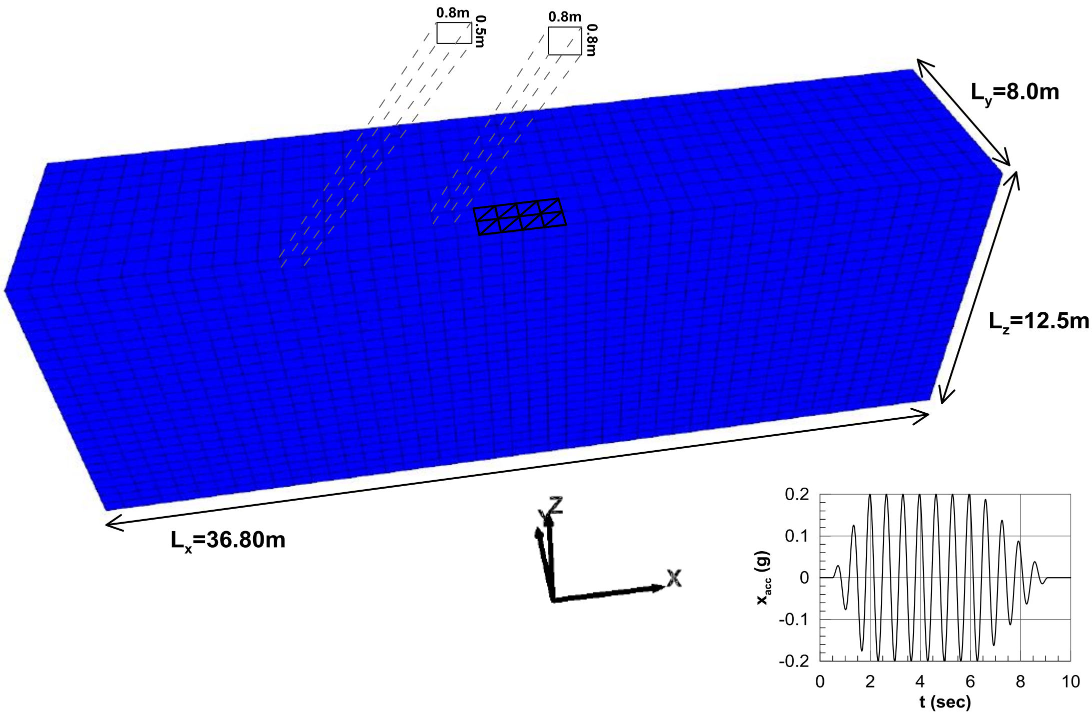

Figure 3.22: Model simulation in FLAC3D – grid configuration and excitation applied at the base

Σχήμα 3.22: Αριθμητικό προσομοίωμα FLAC3D – διάταξη καννάβου και επιβαλλόμενη δόνηση στη βάση

Footing simulation.- It is reminded that in FLAC3D, the bearing pressure of a foundation is simulated through vertical velocity applied at specific gridpoints. This velocity varies linearly from the value at the last gridpoint upon which it is applied, to zero at the adjacent gridpoint. Therefore, in such problems, half the width of the adjacent zones should be added to the actual footing width. Based on the above and the brick-zone discretized grid, it turned out that the application of velocity on a group of gridpoints corresponding to a circular footing would lead to a very approximate simulation which would introduce significant deviations. Therefore to maintain the configuration outline as accurate as possible, it was decided to consider a square footing with an equivalent width B, so that the same contact pressure of q=100kPa-or a load $Q=100\times\pi\times R^2\approx1600kN$ is applied. Based on this simplifying approach, the width of the equivalent square footing was computed as $B=(1600/100)^{0.5}=4.0m$. The square foundation was simulated through shell elements, because rigid elements are not supported by FLAC3D. To appropriately reproduce the symmetrical conditions, the rotational degree of freedom around the x-axis of the shell nodes laying on the symmetry plane, was fixed. The shell elements were assigned the elastic properties of concrete, namely Young's modulus E=30MPa and Poisson's ratio v=0.20.

Nevada #120 sand.- was simulated using the advanced constitutive model NTUA-SAND, which has already been described in previous sections. For static loading, and the application of initial stresses, horizontal displacements were restrained in the lateral boundaries, whereas along the vertical direction only the bottom boundaries were restrained, allowing the system to freely settle. Moreover, the bottom boundaries were allowed to move horizontally, to avoid the generation of parasitic shear stresses.

Permeability Coefficient.- As mentioned earlier, the permeability coefficient does not remain constant during seismic loading, but fluctuates proportionally to the ever-current excess pore pressure ratio, r_u. Also, according to Chaloulos (2012), the static value of permeability can be considered to be a reasonable average between liquefied and non-liquefied states. In the present problem, two different sets of analyses were performed, the first considering the dynamic value of permeability, which is also reported by the Authors, and the second, setting the permeability of the sand equal to k=80*0.0066 = 0.528cm/s, corresponding to the static value of permeability for Nevada sand, as proposed by Arulmoli et al. (1992). The third option of a varying permeability coefficient was excluded, due to the excessively large computed permeability values. Such (prototype scale) values were dramatically decreasing the required numerical time-step set by FLAC3D and increased the computational time, rendering the particular analyses practically unfeasible.

Boundary conditions.- The centrifuge model is reported to have been constructed in a rigid container. Additionally, even though it is quite usual in such containers to apply a soft, flexible dux-seal material at the interior, the Authors do not specify whether such a material was used. The purpose of such a material aims at disengaging the container oscillation from the soil response as well as minimizing wave reflections from the rigid boundaries towards the soil.

Numerically, the simulation of a rigid box was performed by allowing all motion across the x-direction and applying the uniform sinusoidal excitation plotted in **Figure 3.22**, at the base as well as the lateral boundaries of the configuration. Reference test C_0, was initially performed without considering a dux-seal material and the outcome indicated extended motion amplification in the ground surface. Slightly lower levels of excess pore pressures, presenting intense fluctuations throughout shaking were recorded and almost twice footing settlements developed, compared to the centrifuge recordings.

Andrianopoulos (2006), in the numerical simulation of VELACS centrifuge test No12, examining the response of a rigid footing on top of a thin non-plastic silt underlain by liquefiable sand, examined the effect of boundary conditions -rigid against flexible container and rigid with elastic boundaries- on the particular test results.

Note that the consideration of an elastic material, at the boundaries of the configuration, essentially corresponds to the use of dux-seal material in the centrifuge test. He concluded that there is a distinct but somehow restricted effect of the considered boundary conditions on the numerical results, particularly noticeable in the soil ground surface acceleration timehistories and accumulating seismic settlements. He also suggested that the flexible, laminar box type of boundary conditions, provided the most efficient approach to the numerical simulation of liquefaction related problems.

Following, a numerical analysis was performed, considering a lateral zone of elastic flexible material with significantly low Young's modulus. The obtained results indicated a definite improvement regarding the acceleration time histories and accumulated settlements being in satisfactory comparison with the centrifuge recordings. Nevertheless, the elastic properties and thickness of the potentially used dux-seal material are not known, therefore the particular solution could not be firmly established. To resolve the boundary conditions issue, also based on the previous detailed investigation by Andrianopoulos (2006), tied node boundary conditions were finally selected in all five simulations. The particular type essentially allows the unconfined soil oscillation during the applied excitation and as stated above has systematically proven to effectively and accurately simulate the actual soil behavior.

3.5.2 Interpretation of numerical results

Reference test C_0.- Typical results in prototype units from the reference test are summarized in **Figure 3.23**. In brief, the results presented below refer to the analysis with the static value of permeability. Both sets of numerical results are evaluated in the subsequent section, against the overall influence of the densification depth, where the effect of permeability became more tangible. The available centrifuge data are plotted with black color and include **(i)** acceleration time histories at the free-field (a_s), and the footing (a_f), **(ii)** excess pore pressure time histories at selected locations, as well as **(iii)** settlement accumulation at two locations, namely underneath the footing and away from the footing, thus corresponding to free field conditions. The numerically obtained results at the same locations are plotted with gray color.

Acceleration time histories.- Satisfactory agreement is obtained between the centrifuge recordings and the numerical results, with minor deviations relative to the magnitude of the measured acceleration, as exhibited in **Figure 3.23**. Note in both cases, how the magnitude of the horizontal acceleration in the ground surface (a_s) is drastically reduced already from the 2nd loading cycle, implying the occurrence of extensive liquefaction in the lower parts of the sand layer, which restrains the propagation of the seismic motion to the upper parts of the configuration. The same phenomenon is also observed underneath the footing (a_f), where the motion cut-off is slightly delayed and occurs at the end of the 4th cycle, as a consequence of the higher initial vertical effective stresses induced by the footing.

Excess pore pressure built-up.- The numerically derived results, presented in **Figure 3.23**, are in good accordance with the centrifuge recordings, with the exception perhaps of location PC_1, in which the numerical predictions underestimate the developed excess pore pressure. Nevertheless, it should be stressed out that during spinning of the container, and as the soil surrounding the transducer liquefied, it is possible that the pore pressure transducer located at position PC_1 slipped and sunk deeper into the ground, thus measuring pore pressures at a deeper location than the one originally assigned. The particular observation becomes even more crucial when comparing the pore pressures recorded at locations PC_1 and PC_2, which are very similar to each other. Apart from the above inconsistency, it is concluded that excess pore pressures are realistically simulated by the numerical model developed herein.

Settlement accumulation.- Seismic induced settlements under the footing and in the free field are plotted in **Figure 3.23**. Settlements are slightly underestimated up to the first 5sec of loading but the rate of settlement accumulation is accelerated and renders a total settlement of 0.67m by the end of shaking, (at about 9sec), as opposed to the 0.56m measured at the centrifuge test. Overall, it is concluded that the settlement evolution with time is satisfactorily described by the applied numerical methodology.

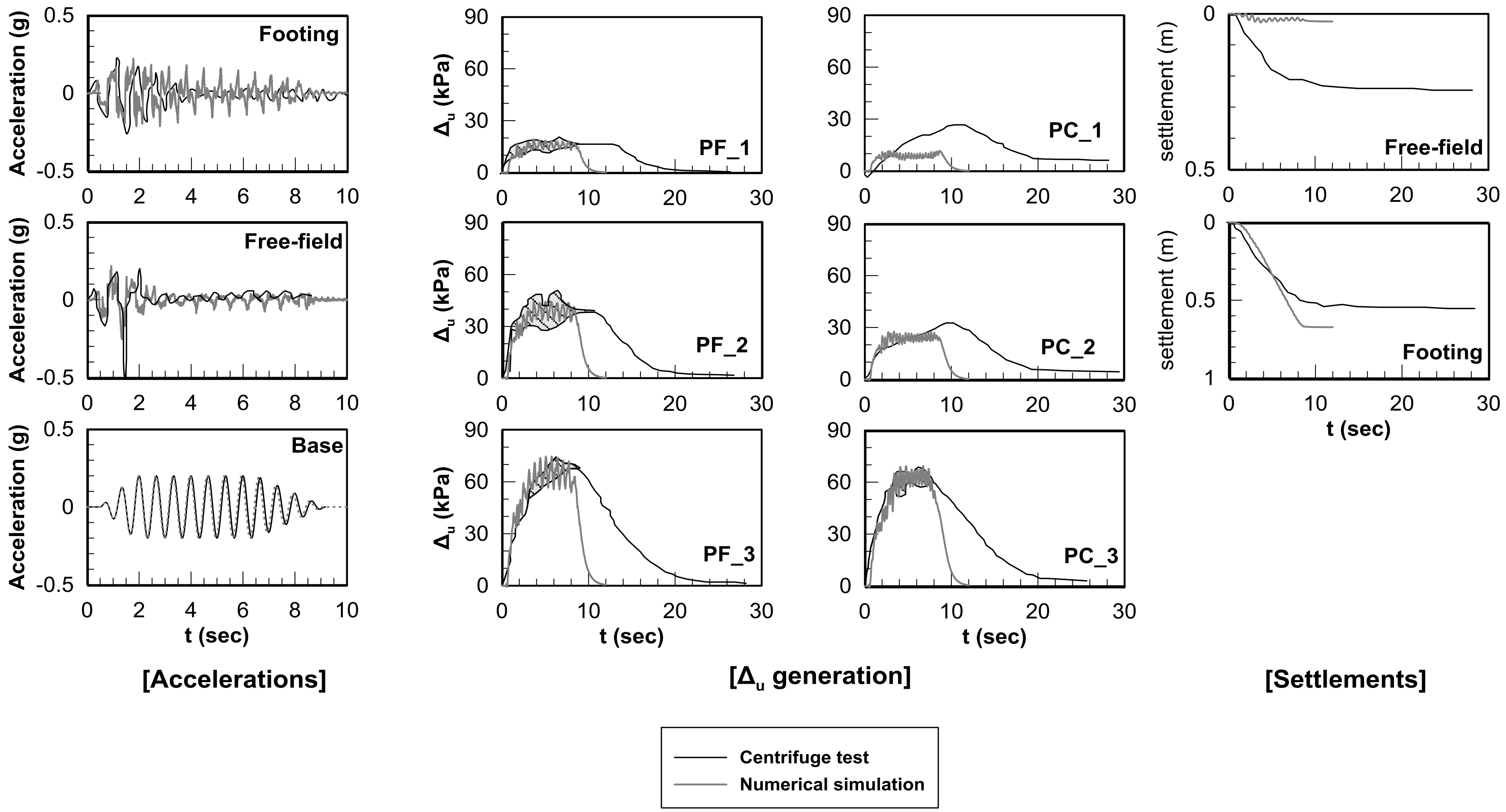

Figure 3.23: Typical results for test C_0
Σχήμα 3.23: Τυπικά αποτελέσματα του πειράματος C_0

The ground surface settlement in the free field is numerically computed equal to 0.03m, and in contrast to the centrifugal value of 0.25m is substantially underestimated, as it is also illustrated in the corresponding figure. The particular inconsistency may be explained with reference to the arrangement which is usually employed to monitor the seismic induced settlements in the free-field. **Figure 3.24** illustrates a typical arrangement used in the majority of centrifuge tests. The depicted configuration was used in a series of centrifuge tests performed at the centrifuge facility of the University of Cambridge, UK, by the research team of Prof. Bouckovalas in the context of the TNA project entitled "Experimental Verification of Shallow Foundation Performance under Earthquake-Induced Liquefaction". The arrangement consists of a vertical Linear Voltage Differential Transformer (LVDT) which is connected to a specially-made small footing used to acquire the required data during flight. In the present case, under the centrifugal acceleration of 80g, the prototype weight of the small footing is scaled by a factor of 80 and therefore may become significant. The particular remark, in combination with the triggering of liquefaction already from the 2nd loading cycle, in the underlying sand, may have induced the settlement of 0.25m. Thus, the measured settlement reported in the experiment could be the product of the above mechanism, which of course cannot be numerically predicted.

Figure 3.24: LVDT arrangement, typically used in centrifuge tests (Bouckovalas et al., 2011)
Σχήμα 3.24: Τυπική διάταξη LVDT που χρησιμοποιείται σε πειράματα φυγοκεντριστή (Bouckovalas et al., 2011)

Tests C_0 – C_4.- The evaluation of the obtained numerical predictions against the experimental results, for all five tests, will be performed with regard to:

i. The dynamic settlement of the footing and its correlation to all considered densification depths Z_c.
ii. The excess pore pressure distribution with depth and its variation during the seismic excitation.
iii. The effect of the densification depth to the propagation of the seismic motion towards the soil surface

The accumulated dynamic settlement of the footing and their variation with the improvement depth Z_c is illustrated in **Figure 3.25.** The centrifuge data are plotted with the black squares while the numerical predictions with different shades of gray, corresponding to the effect of the dynamic and static value of permeability respectively. The use of the static value of the permeability appears to slightly over-estimate the dynamic footing settlements, as opposed to the set of analyses assuming the dynamic coefficient. At an average, both sets of analyses capture the centrifuge results rather well, up to Z_c/B = 1.5, by forming an upper and lower boundary. For Z_c/B greater than about 1.5, both approaches over-estimate the footing settlements. Apart from the above quantitative differentiations, in both cases, the numerical outcome confirms the experimentally observed reducing trend of the footing settlements with increasing depth of densification Z_c.

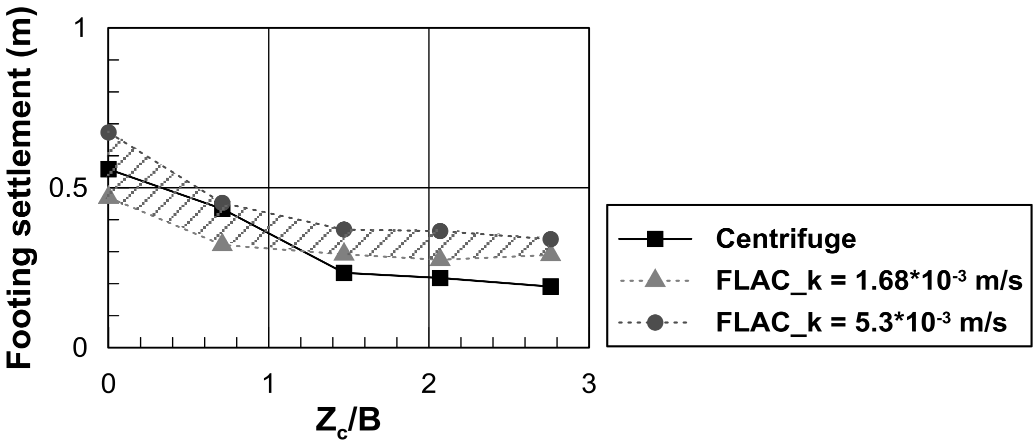

Figure 3.25: Footing settlement $S_{foot.}$ versus densification depth Z_c normalized with the footing width B

Σχήμα 3.25: Καθιζήσεις θεμελίου $S_{foot.}$ συναρτήσει του βάθους συμπύκνωσης Z_c κανονικοποιημένο με το πλάτος του θεμελίου B

The excess pore pressure distribution with depth and its change with time for both permeability coefficients is presented in **Figure 3.26 - Figure 3.30**. The results are obtained at t=3.5sec and the end of shaking, and two different locations, namely under the footing and away from it. The dashed black lines without symbols correspond to the initial vertical effective stresses as they were calculated in the free field and under the footing as $\sigma'_{vo}=\gamma_b+\Delta\sigma'_v$, where $\Delta\sigma'_v$ the effect of the foundation load estimated using the elastic theory.

As a general interpretation of the obtained response, it is stated that under free field conditions, the numerical analyses verify the propagation of the liquefaction front from the shallower towards the deeper locations extending to depths ranging from 6 to 8meters. Under the footing, liquefaction is also systematically prevented since the developing excess pore pressures are substantially lower than the effective vertical stresses.

Focusing on the use of the dynamic coefficient of permeability, higher excess pore pressures than the experimentally reported, are numerically predicted principally in the deeper locations of the configuration, as a result of the limited drainage capacity at the specific depths. Moreover, the influence of the permeability coefficient becomes even more obvious for increasing thickness of the performed densification (Z_c) as observed in the case of test C_4. The related excess pore pressures clearly indicate the triggering of liquefaction throughout the improved depth already from the early stages of loading.

The consideration of the static value of permeability in the numerical analyses, significantly improves the previous numerical predictions in both considered time instants. Especially at the deeper locations, excess pore pressures are reduced and the liquefaction front does not propagate as deep as previously, thus rendering a very reasonable agreement to the centrifuge data as well. Especially in the case of test C_4, there is still an obvious divergence nevertheless the distribution of excess pore pressures with depth indicates the successful mitigation of liquefaction in the improved area of the sand layer.

The effect of the depth of improvement Z_c normalized against the footing width B, on the propagation of the seismic motion to the ground surface, expressed as the footing/base acceleration is summarized in **Figure 3.31**. Again the results from both sets of analyses are plotted and compared against the reported centrifuge data, preserving the same line and symbol layout as above.

Notice that the use of the dynamic coefficient of permeability systematically leads to lower amplification ratios, compared to the centrifuge results. It is of particular interest that for the maximum considered ratio $Z_c/B=2.76$ the numerically computed amplification ratio separates from the previously established trend and drops. The particular behavior, is explained on the basis of the high developing excess pore pressures along the soil column underneath the footing, provided previously. Namely, as a result of the insufficient drainage capacity the high excess pore pressures drastically reduce the sand's shear strength and the related shear wave velocity, impeding the propagation of the seismic motion to the top.

The successful liquefaction mitigation illustrated in the previous figures, for the static value of permeability, provides the necessary justification to the improved amplification ratio predictions, plotted in **Figure 3.31**. Indeed the increase of the coefficient of permeability by about 5.28/1.68 = 3 times considerably improves the observed motion transmission to the top, as a result of the generation of lower excess pore pressures with depth.

In the last two tests (C_3 & C_4) still a noticeable deviation is observed, which may attributed to resonance effects, as subsequently explained. Focusing on test C_4, a soil column of thickness H=12.5m and relative density Dr=89% and average mean effective pressure p=40kPa, is estimated to roughly have a shear wave velocity equal to 200m/sec, thus calculating an elastic period T, equal to T=4*H/Vs = 0.25sec and $T_{soil}/T_{exc.}$=0.25/0.67=0.37. Based on a conservative estimate, as a result of the performed densification, the average excess pore pressure over depth, during shaking, under free field conditions, is not expected to rise above $r_{u,avg}$=0.80, which is going to reduce the soil's shear wave velocity to $Vs_{liq}=\sqrt[4]{1-r_u}*Vs_{,o}$= 130m/sec. In that case, the period of the soil column is going to climb up to T=0.40sec, therefore $T_{soil}/T_{exc.}$=0.40/0.67=0.60. The increase in the $T_{soil}/T_{exc.}$ ratio implies that the soil column moves closer to resonance and higher amplification ratio values are obtained.

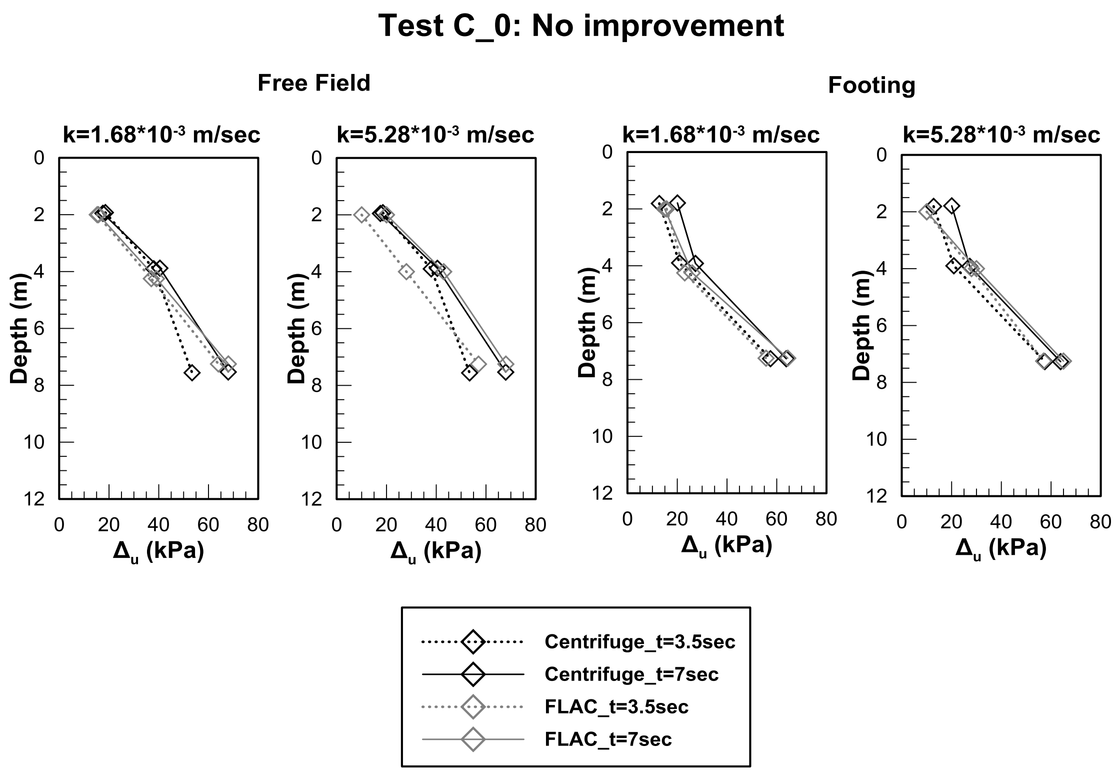

Figure 3.26: Excess pore pressures distribution with depth for test C_0
Σχήμα 3.26: Κατανομή υπερπιέσεων πόρων με το βάθος στο πείραμα C_0

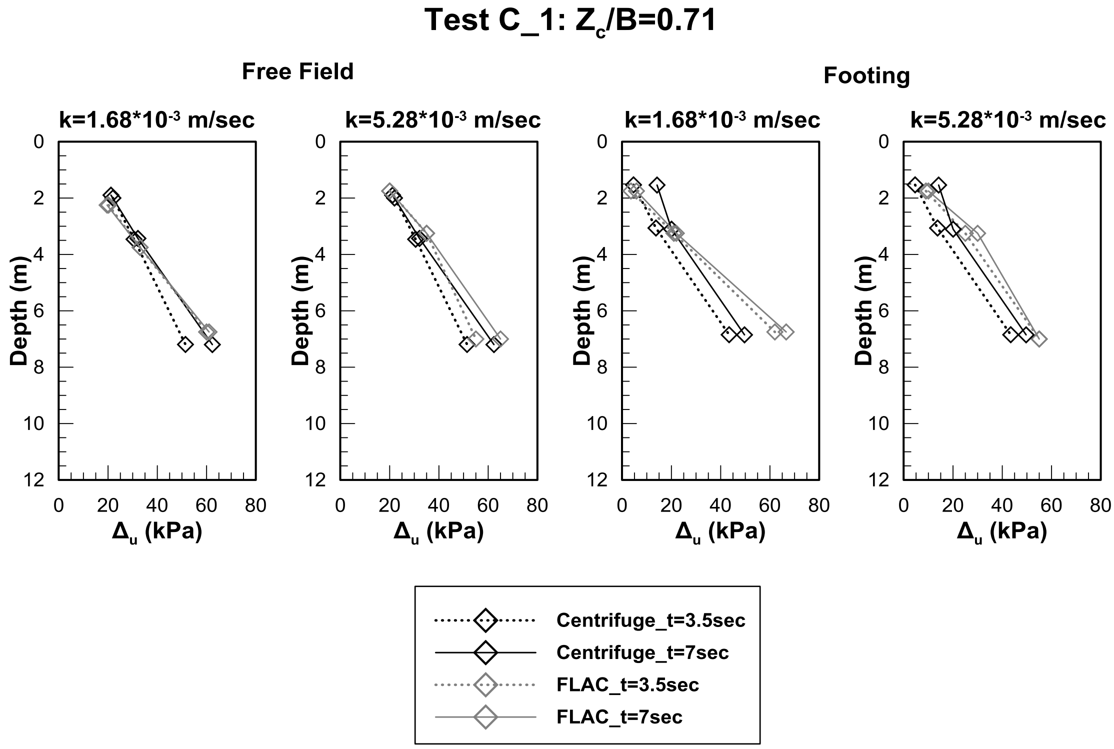

Figure 3.27: Excess pore pressures distribution with depth for tests C_1
Σχήμα 3.27: Κατανομή υπερπιέσεων πόρων με το βάθος στο πείραμα C_1

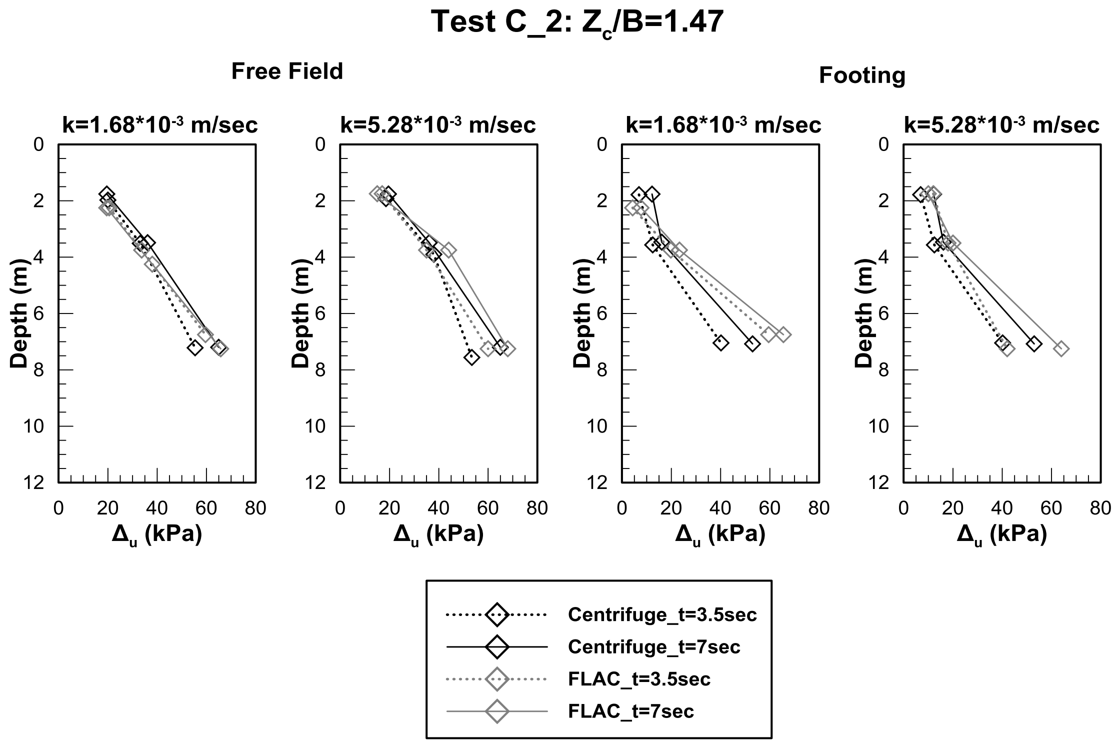

Figure 3.28: Excess pore pressures distribution with depth for test C_2
Σχήμα 3.28: Κατανομή υπερπιέσεων πόρων με το βάθος στο πείραμα C_2

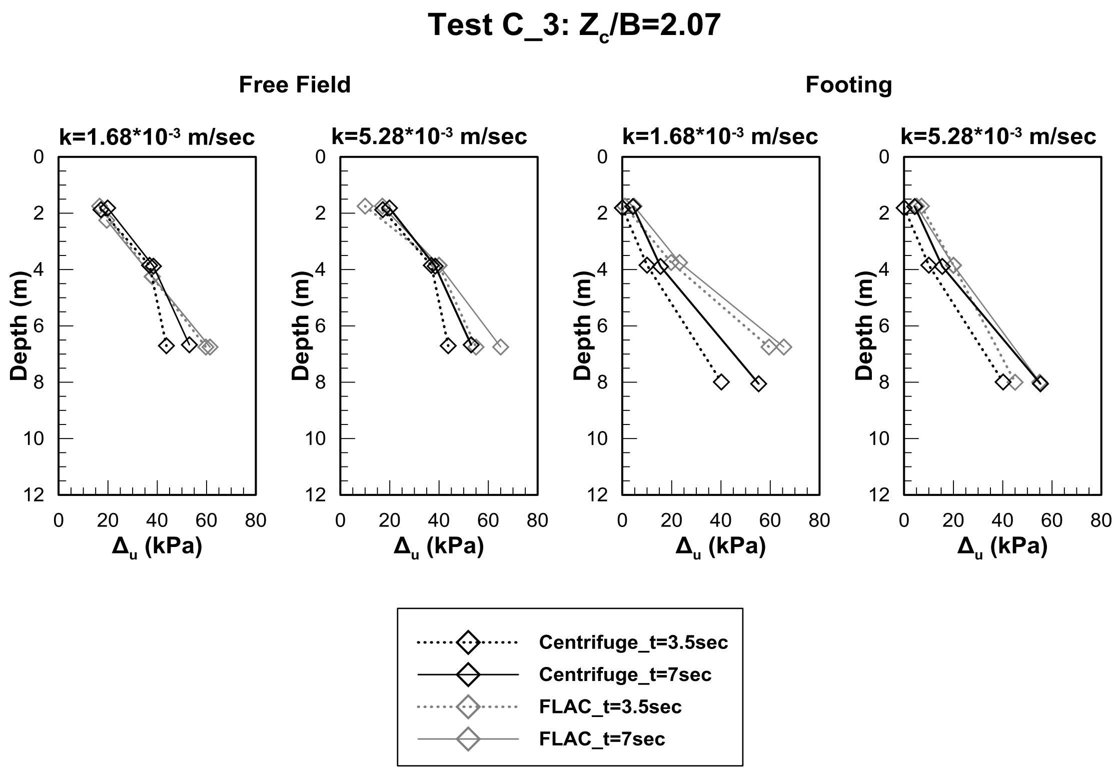

Figure 3.29: Excess pore pressures distribution with depth for test C_3
Σχήμα 3.29: Κατανομή υπερπιέσεων πόρων με το βάθος στο πείραμα C_3

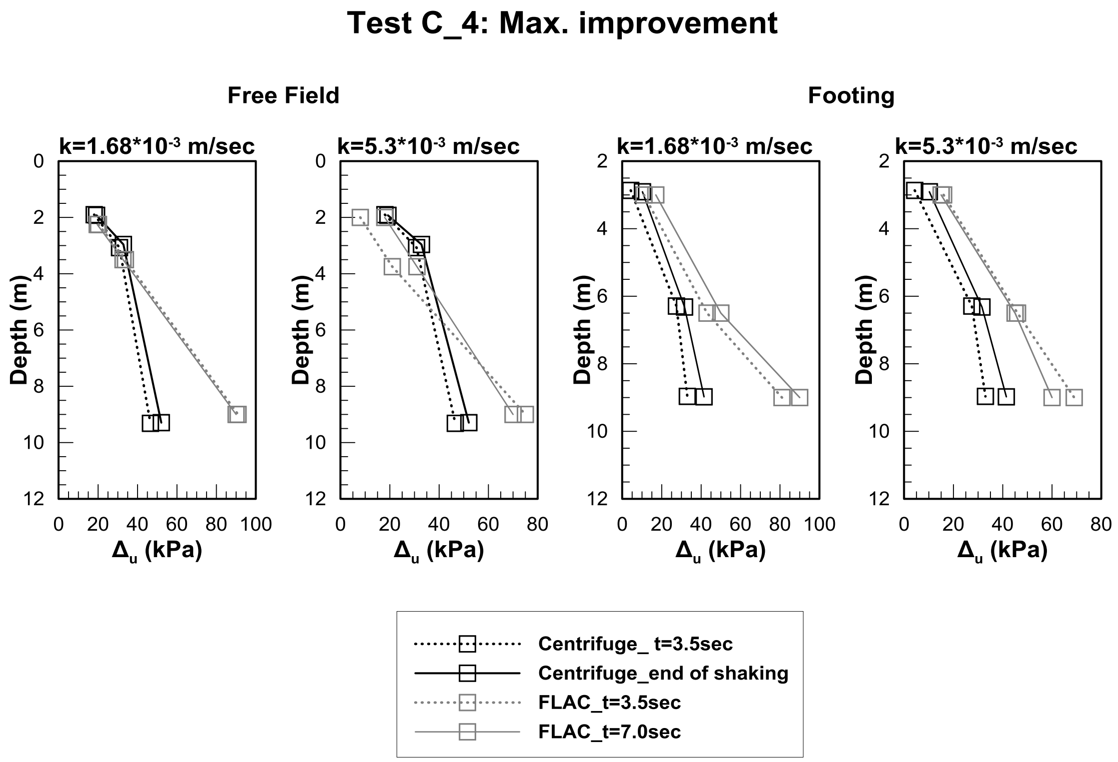

Figure 3.30: Excess pore pressures distribution with depth for test C_4
Σχήμα 3.30: Κατανομή υπερπιέσεων πόρων με το βάθος στο πείραμα C_4

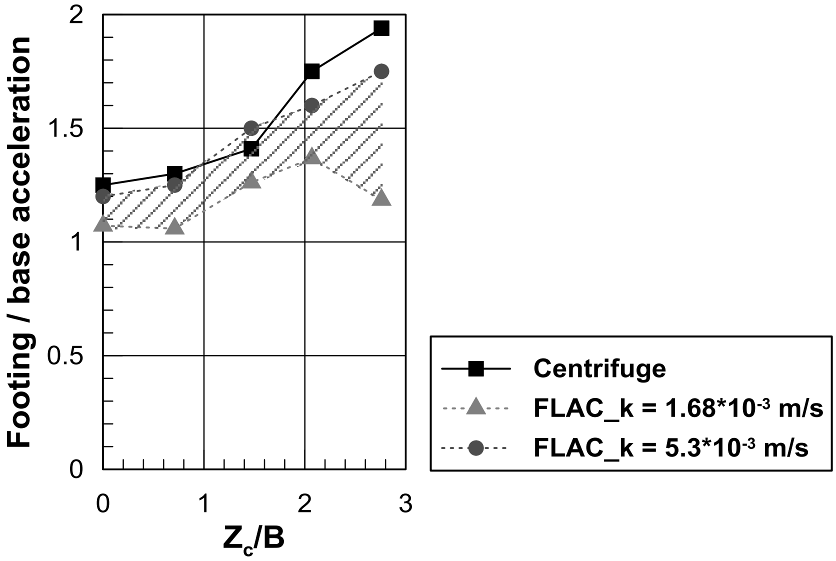

Figure 3.31: Footing/base acceleration versus Z_c/B for all five centrifuge test

Σχήμα 3.31: Επιτάχυνση θεμελίου/βάσης συναρτήσει του Z_c/B για τα πέντε πειράματα φυγοκεντριστή

4

Parametric Analysis of Footing Response

4.1 Introduction

The simplified concept of *"Equivalent Uniform Improved Ground"*, thoroughly described in the previous chapter, essentially led to a 2-layer configuration with the following basic characteristics:

a. A liquefiable sand layer of given uniform density and relatively large thickness, covered by a non-liquefiable surface layer, of the same origin as the liquefiable one but with larger relative density (due to the vibrocompaction) and larger overall permeability due to the presence of the gravel drains.
b. Following the current design practice, the average over-depth excess pore pressure ratios in the top layer should not exceed a safe value, well below 1 (e.g. $\bar{r}_{u,max}$ = 0.3 – 0.5)

In relation to the above objectives, it was first necessary to specify a methodology to predict beforehand the developing excess pore pressures in the improved crust. For that purpose, a number of 1-D numerical analyses was performed, simulating the free-field response of the improved ground. The ultimate intention is to identify the replacement ratio α_s which is required in order to restrain excess pore pressure development in the improved ground within the target range of $\bar{r}_{u,max}$ = 0.30 – 0.50. The particular analyses and associated results are described in sections 4.2 and 4.3 respectively.

Following, a number of 2D parametric analyses were performed in order to examine the seismic response of a shallow footing on the above specified soil profile. Additionally, a separate set of analyses is performed to examine the effect of the lateral extent of improvement on the seismic response of the shallow footing. The basic problem parameters are identified and a detailed description of the plan of the parametric investigation is provided in the corresponding sections.

4.2 Free field numerical analyses

To evaluate the appropriate replacement ratio α_s required to restrain the average excess pore pressure ratios within the desired range, of $\bar{r}_{u,max}$ = 0.30 – 0.50, a series of 1-D free-field numerical analyses was performed. The particular numerical investigation was performed for a wide range of initial relative densities (i.e. $D_{r,o}$=35, 40, 45, 55, 60, 65 & 70%) and related permeability coefficients.

The grid configuration initially consisted of a 28m wide and 20m thick uniform liquefiable sand layer, as illustrated in **Figure 4.1**. Overall, 24×20=480 zones were generated, with dimensions varying from 1.0×1.0m around the axis of symmetry to 1.5×1.0m, at the boundaries of the configuration. With the initial relative density being the controlling parameter, three different depths of improvement were considered in each case, i.e. 4, 6 and 8m, as well as four different replacement ratios – α_s = 0.05, 0.10, 0.15 and 0.20. In total, 72 numerical analyses were performed.

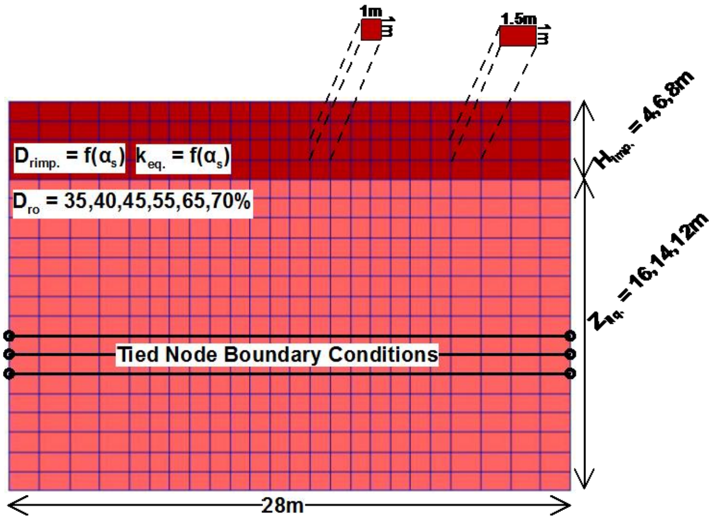

Figure 4.1: Grid configuration used in the 2-dimensional free-field numerical analyses
Σχήμα 4.1: Διάταξη καννάβου 2-Διάστατων αριθμητικών αναλύσεων ελεύθερου πεδίου

The associated assumptions of the 1-D numerical analyses regarding the applied excitation, type of damping, imposed boundary conditions, constitutive model, and water level are the same as in the reference case of a surface footing on top of the 2-layered profile and will not be repeated herein. Hence, the rest of this section is devoted to the investigation concerning the lateral dimensions of the grid configuration.

Lateral dimensions.- The tied-node boundary conditions during dynamic loading, combined with the high permeability coefficient used for the improved crust, were found to generate significant boundary effects, concerning the excess pore pressure ratio distribution within the improved crust and the associated flow during shaking. The particular effect became more intense in the case of increased improvement thickness. For instance, **Figure 4.2** illustrates the excess pore pressure ratio distribution and flow vectors at the end of the 4th cycle for the case of a soil layer with initial relative density of $D_{r,o}$=65%, improved at the maximum considered depth and with the highest replacement ratio, i.e. $H_{imp.}$=8m & α_s=0.20. Excess pore pressure ratio distribution appears highly non-uniform and flow vectors indicate pretty much irregular flow taking place across the improved crust.

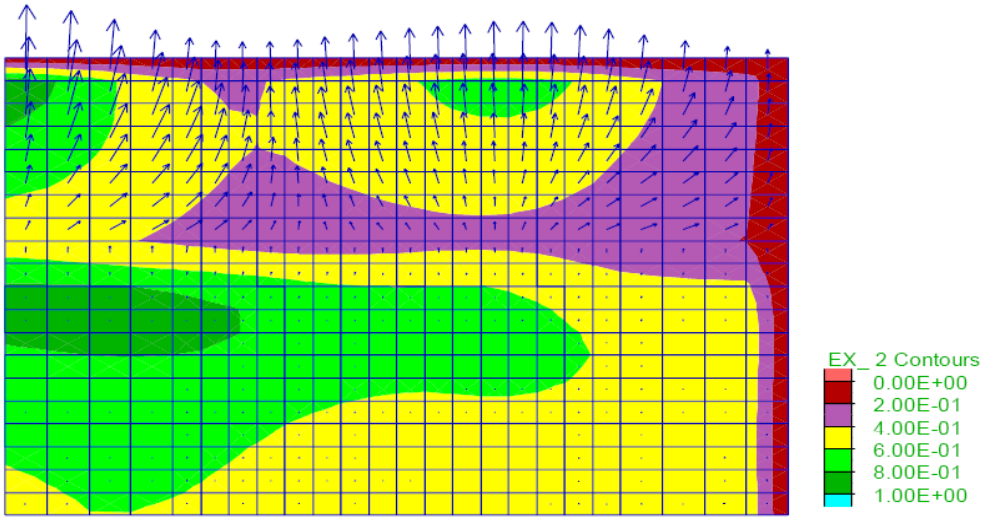

Figure 4.2: Non-uniform excess pore pressure ratio distribution and associated flow vectors at the end of the 4th loading cycle for $Dr_{,o}$=65%, H_{imp}=8m, α_s=0.20

Σχήμα 4.2: Ανομοιόμορφη κατανομή του δείκτη υπερπιέσεων πόρων και αντίστοιχα διανύσματα ροής στο τέλος του 4ου κύκλου φόρτισης για $Dr_{,o}$=65%, H_{imp}=8m, α_s=0.20

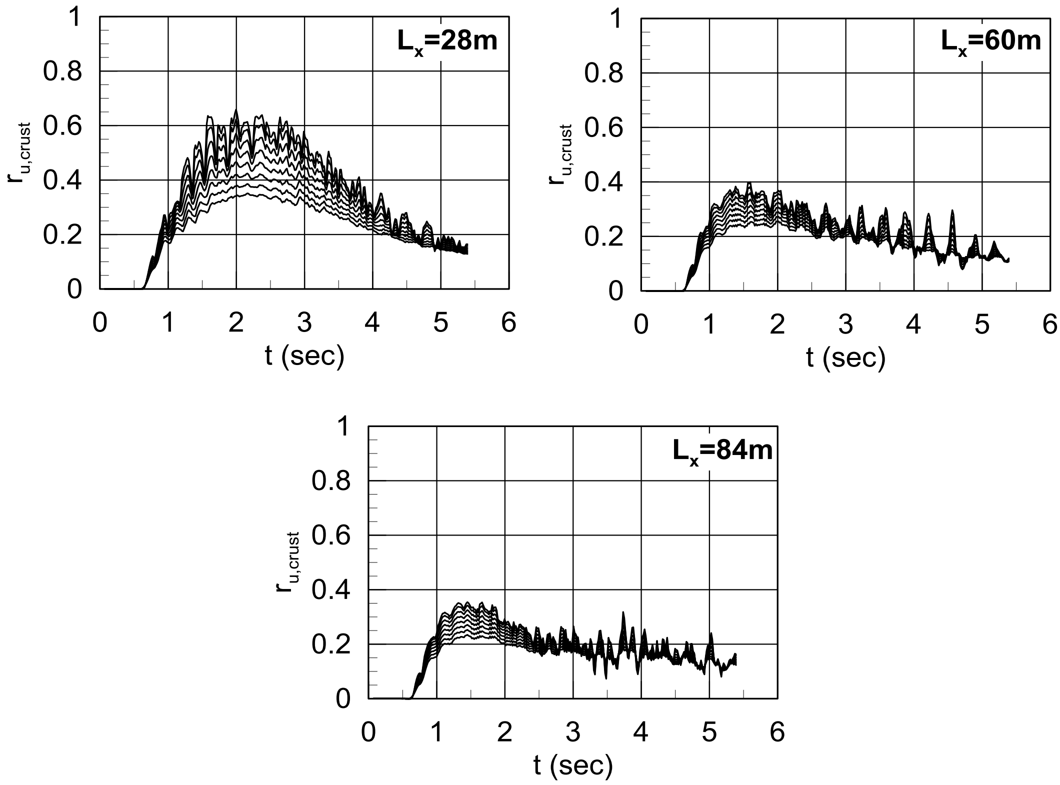

Figure 4.3: Parametric investigation of lateral grid dimensions- excess pore pressure ratio timehistories inside the crust

Σχήμα 4.3: Παραμετρική διερεύνηση των πλευρικών διαστάσεων του καννάβου – χρονοϊστορίες δείκτη υπερπιέσεων πόρων εντός της κρούστας

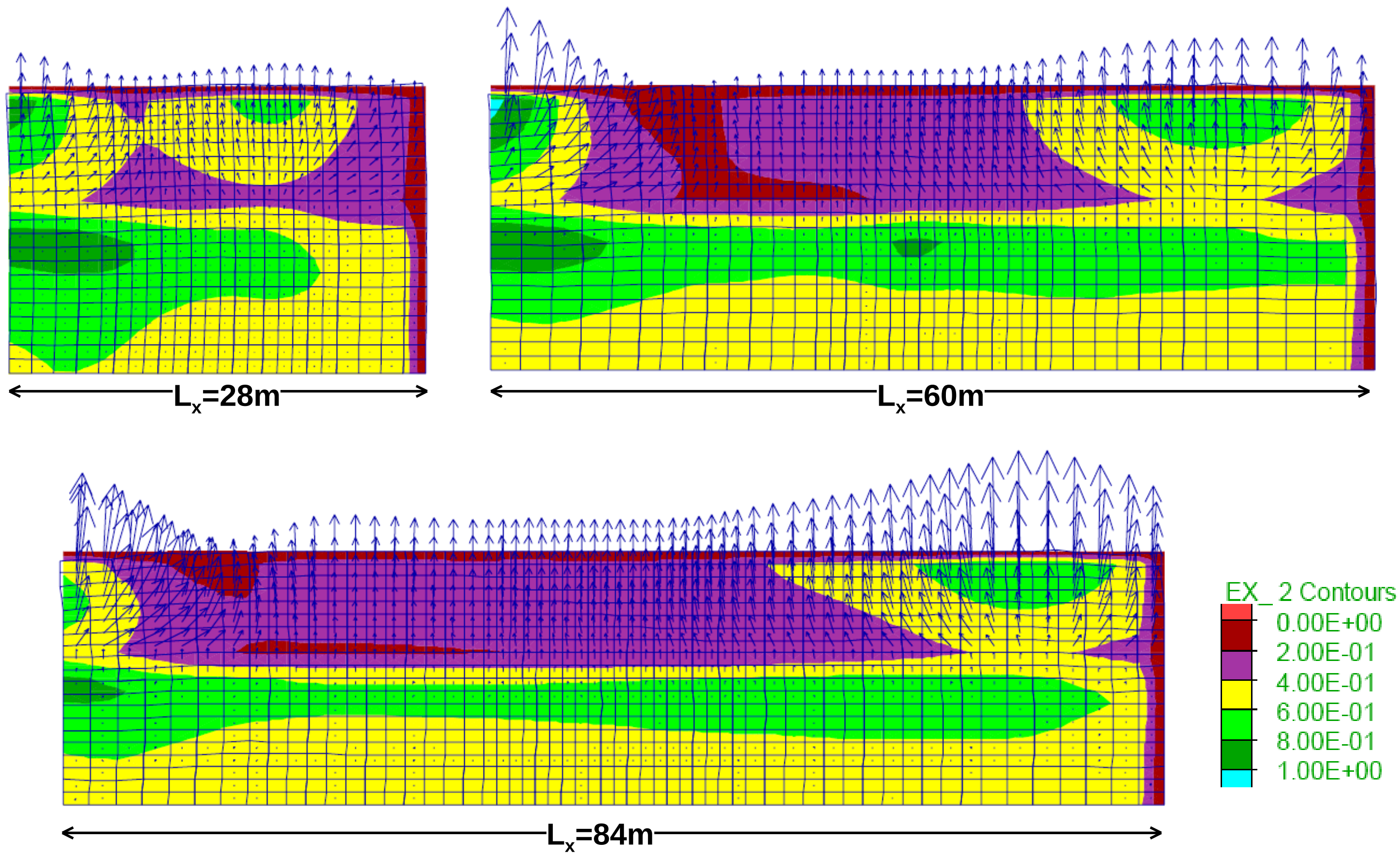

Figure 4.4: Parametric investigation of lateral grid dimensions- excess pore pressure ratio contours at the end of the 4th loading cycle
Σχήμα 4.4: Παραμετρική διερεύνηση των πλευρικών ορίων του καννάβου - χρονοϊστορίες δείκτη υπερπιέσεων στο τέλος του 4^{ου} κύκλου φόρτισης

To achieve a uniform field of excess pore pressure ratios and pure vertical flow towards the surface, a parametric investigation was performed by laterally extending the boundaries of the grid from 28m, to 60m and subsequently to 84 meters. The outcome of the above analyses is summarized in **Figure 4.3**, presenting r_u time histories derived inside the crust and the axis of symmetry, for the three different cases. Moreover, snapshots of excess pore pressure ratio contours and flow vectors at the end of the 4th loading cycle are presented in

Figure 4.4. It is observed that increasing the lateral dimension of the grid diminishes and confines the irregularity in the r_u distribution around the edges of the configuration, thus leaving the central area unaffected. Moreover, flow vectors are vertical flow around the axis of symmetry, with localized fluctuations at the boundaries. As a result, to ensure a uniform excess pore pressure field development and pure vertical flow, across the improved crust, the wider grid configuration of 84 m is selected to perform the following 1-D free-field numerical analyses.

4.3 Evaluation of 1-D Numerical Predictions

Due to the large number of parametric analyses, three typical cases are selected and presented below, reflecting the response of a loose (Dr_o=40%), medium dense (Dr_o=55%) and dense (Dr_o=70%), but still liquefiable, sand under seismic loading. In all three examples different replacement ratio (α_s) values are selected, achieving to restrain the average in-crust excess pore pressure ratio to acceptable levels, i.e $\bar{r}_{u,max}$ = 0.3 – 0.4. The above analyses will be assessed, in terms of:

a. the excess pore pressure ratio (r_u) distribution with depth at the axis of symmetry. The particular distributions are plotted for two different time moments **(i)** the time of the maximum r_u occurrence within the improved crust and **(ii)** the end of shaking.
b. the excess pore pressure ratio time histories at different depths of the grid configuration, namely 3m, 7m, 12m and 16m.
c. the excess pore pressure ratio time histories within the improved crust.

Predictions for Dr_o=40%.- Figure 4.5a,b & **c**, summarize the outcome for the case of initial relative density of 40% and improvement depth 4m. Notice that, excess pore pressure ratio values within the improved crust, illustrated in **Figure 4.5c**, are confined within the pre-defined desirable range of $\bar{r}_{u,max}$ = 0.3 – 0.4. To achieve this, the performed mitigation against liquefaction was materialized for a replacement ratio equal to α_s=0.10. The slightly increased r_u values which are recorded at the shallower zones of the grid configuration are attributed to the vertical drainage occurring from the deeper parts of the crust towards the surface, thus increasing the excess pore pressure (Δu) at the specific depths.

Additionally, from the distribution of excess pore pressure ratios with depth, (**Figure 4.5a**) it is obvious that the underlying sand develops much higher r_u values, which gradually increase from the interface of the two layers towards the bottom of the configuration. By the end of the imposed shaking, liquefaction is evident and extends practically to an area starting 2-3 m below the interface of the two layers, up to the bottom of the configuration. As a result, the thickness of the performed improvement ($H_{imp.}$) decisively controls the extent of the liquefied area underneath, by delaying or even preventing the occurrence of liquefaction. This indirect advantage is translated to extra shear strength, contributing to the shear strength provided by the overlying denser crust.

Figure 4.5b summarizes r_u time histories derived from selected depths of the configuration. It is of particular interest that the r_u time history derived at 7 m clearly indicates liquefaction already from the 3rd loading cycle. However, there is a very limited drainage effect present, which prevails over the rate of r_u built up at the later stages of loading and causes a slight lowering of the r_u values. The specific effect indicates the beneficial action of the top improved crust which restrains excess pore pressures beyond the improvement limits, as it is also illustrated in the following cases.

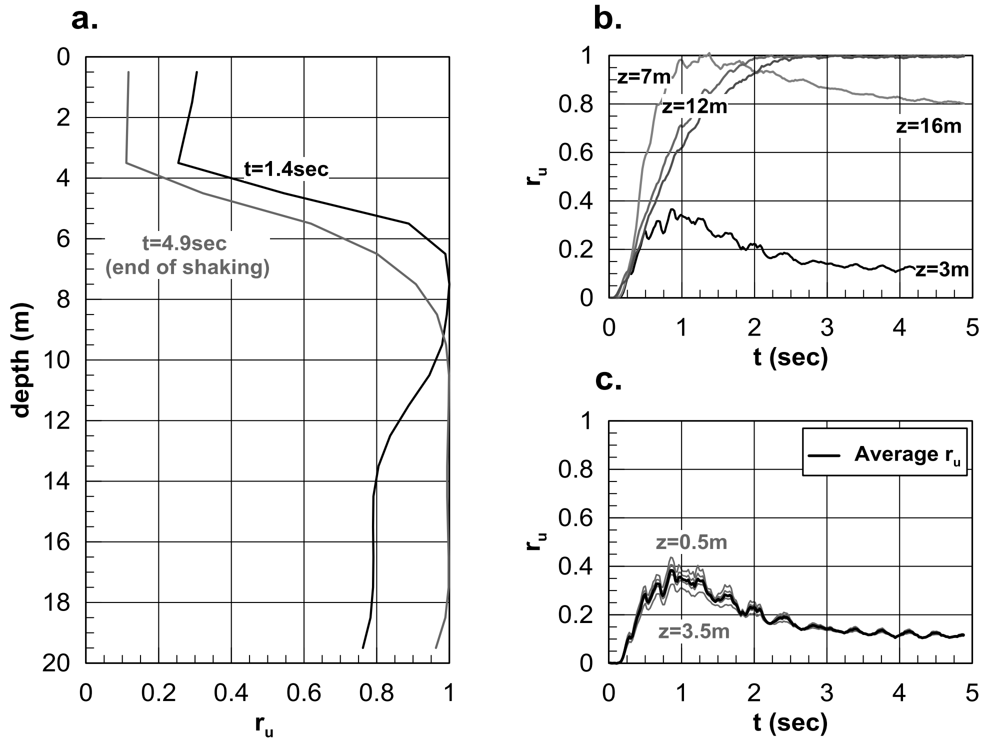

Figure 4.5: Typical results for Dr_o=40%, improvement depth H_{imp}=4m and $α_s$=0.10 (a) r_u distribution with depth at t=1.4 and t=4.9sec, r_u time histories (b) at selected depths of the configuration and (c) within the improved crust

Σχήμα 4.5: Τυπικά αποτελέσματα για Dr_o=40%, βάθος βελτίωσης H_{imp}=4m και $α_s$=0.10 a. κατανομή r_u με το βάθος στα t=1.4 και t=4.9sec, χρονοϊστορίες r_u (b) σε επιλεγμένα βάθη του καννάβου και (c) εντός της βελτιωμένης κρούστας

Predictions for Dr_o=55%.- Figure 4.6a,b & **c**, summarize the outcome for the case of initial relative density of 55% and improvement depth equal to 8m. Notice that, excess pore pressure ratio values within the improved crust, illustrated in **Figure 4.6c**, are confined within the pre-defined desirable range of $\bar{r}_{u,max}$ = 0.3 – 0.4. To achieve this, the performed mitigation against liquefaction was materialized for a replacement ratio equal to α_s=0.15. The slightly increased r_u values which are recorded at the shallower zones of the grid configuration are attributed to the vertical drainage occurring from the deeper parts of the crust towards the surface, thus increasing the excess pore pressure (Δu) at the specific depths. The r_u distribution with depth (**Figure 4.6a**) attains an average value of r_u=0.35, at the mid-depth of the improvement, which fluctuates from 0.27 at the deepest locations to 0.40 at the shallow parts of the improved layer, at the end of the 3rd cycle of the excitation. **Figure 4.6b** summarizes excess pore pressure time histories at selected depths of the configuration. In this example the improved crust extends up to 8m, therefore the corresponding time history derived at 7m indicates a successful liquefaction mitigation.

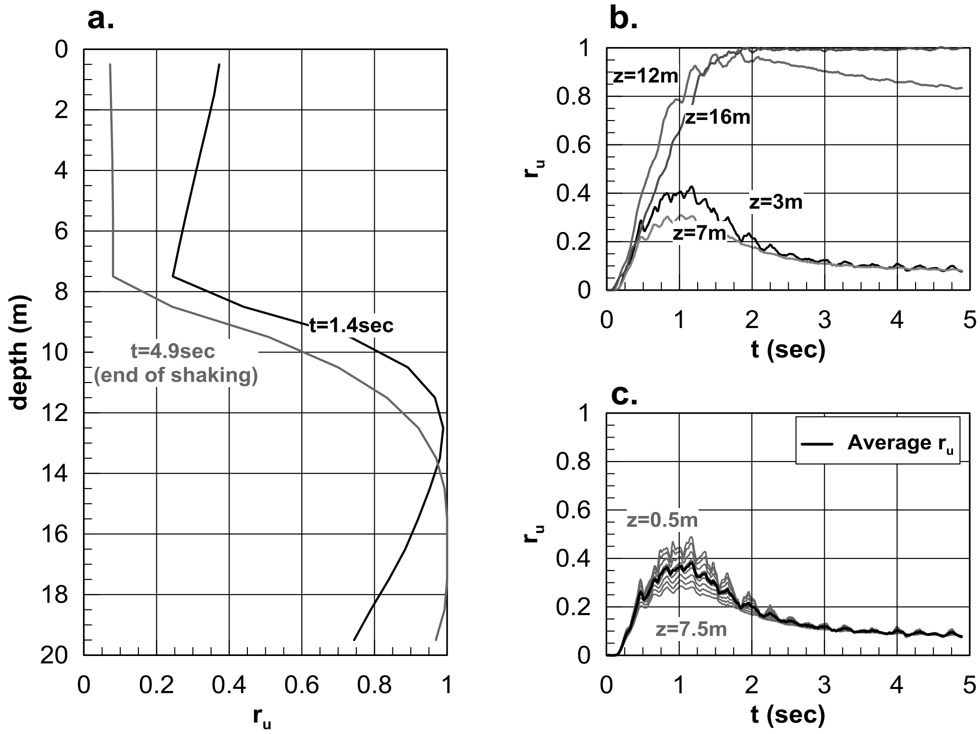

Figure 4.6: Typical results for Dr_o=55%, improvement depth H_{imp}=8m and α_s=0.15 (a) r_u distribution with depth at t=1.4 and t=4.9sec, r_u time histories (b) at selected depths of the configuration and (c) within the improved crust

Σχήμα 4.6: Τυπικά αποτελέσματα για Dr_o=55%, βάθος βελτίωσης H_{imp}=8m και α_s=0.15 a. κατανομή r_u με το βάθος στα t=1.4 και t=4.9sec, χρονοϊστορίες r_u (b) σε επιλεγμένα βάθη του καννάβου και (c) εντός της βελτιωμένης κρούστας

Predictions for Dr_o=65%.- The particular example refers to the remediation of a 65% initial relative density sand layer by improving the top 6 meters. **Figure 4.7a,b** & **c,** indicate that the desired response is obtained for a replacement ratio equal to α_s=0.20. Maximum excess pore pressures attain roughly $r_{u,max}$=0.25, especially in the shallower parts of the improved crust, while, at an average, maximum excess pore pressure values reach approximately $\bar{r}_{u,max}$ = 0.23. **Figure 4.7b**, proves the beneficiary effect of the improvement which affects the excess pore pressure built up beyond its actual thickness. Proof of this is the r_u time history derived at a depth of 7 m which remains well below liquefaction triggering.

Overview of results.- To fully visualize the replacement ratio value (α_s) required to achieve an acceptable level of excess pore pressure built-up, for all the examined combinations of initial relative density (D_{ro}-%) and depth of improvement ($H_{imp.}$) the following figures summarize the excess pore pressure ratio time histories within the improved crust for all the executed numerical analyses. For each case of initial relative density Dr_o (%), and all four examined replacement ratio (α_s) values, namely α_s=0.05, 0.10, 0.15 and 0.20, excess pore pressure ratio time histories, are derived at increments of 0.5m starting from the ground surface and proceeding to the bottom of the improved crust.

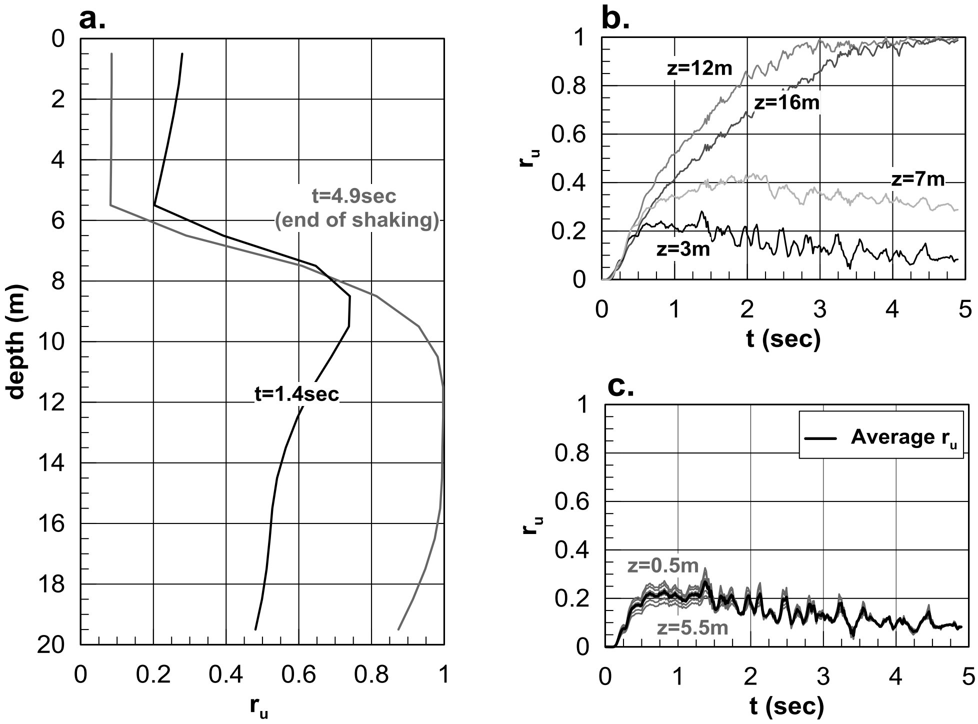

Figure 4.7: Typical results for Dr_o=65%, improvement depth $H_{imp.}$=6m and α_s=0.20 (a) r_u distribution with depth at t=1.4 and t=4.9sec, r_u time histories (b) at selected depths of the configuration and (c) within the improved crust

Σχήμα 4.7: Τυπικά αποτελέσματα για Dr_o=65%, βάθος βελτίωσης H_{imp}=6m και α_s=0.20 a. κατανομή r_u με το βάθος στα t=1.4 και t=4.9sec, χρονοϊστορίες r_u (b) σε επιλεγμένα βάθη του καννάβου και (c) εντός της βελτιωμένης κρούστας

Set of Proposed Design Charts.- The average maximum excess pore pressure ratio within the improved crust is plotted with regard to the corresponding replacement ratio α_s in an attempt to provide an easy-to-use design chart. The outcome is exhibited in **Figure 4.8**, for all six different initial relative density scenarios and three depths of improvement. The particular figure essentially illustrates the effectiveness of every examined combination of initial properties of the sand layer and considered improvement depth.

Following, **Figure 4.9** summarizes the replacement ratio α_s required for every initial relative density value D_{ro} (%) for three distinct average $\bar{r}_{u,max}$ values expected to develop within the improved crust, namely 0.30, 0.40 & 0.50. Additionally, depending on the replacement ratio α_s obtained from the above figure, the properties of the improved crust, i.e. relative density $D_{r,imp}$ (%) and equivalent coefficient of permeability $k_{eq.}$ (m/sec) may be easily obtained through **Figure 4.10a** & **b**. More specifically, **Figure 4.10a** correlates replacement ratio α_s to the relative density of the improved crust through seven different curves, each one for a separate initial relative density $D_{r,o}$ (%). **Figure 4.10b**, associates the replacement ratio α_s to the equivalent coefficient of permeability $k_{eq.}$ (m/sec) as a function of the permeability of the natural sand layer.

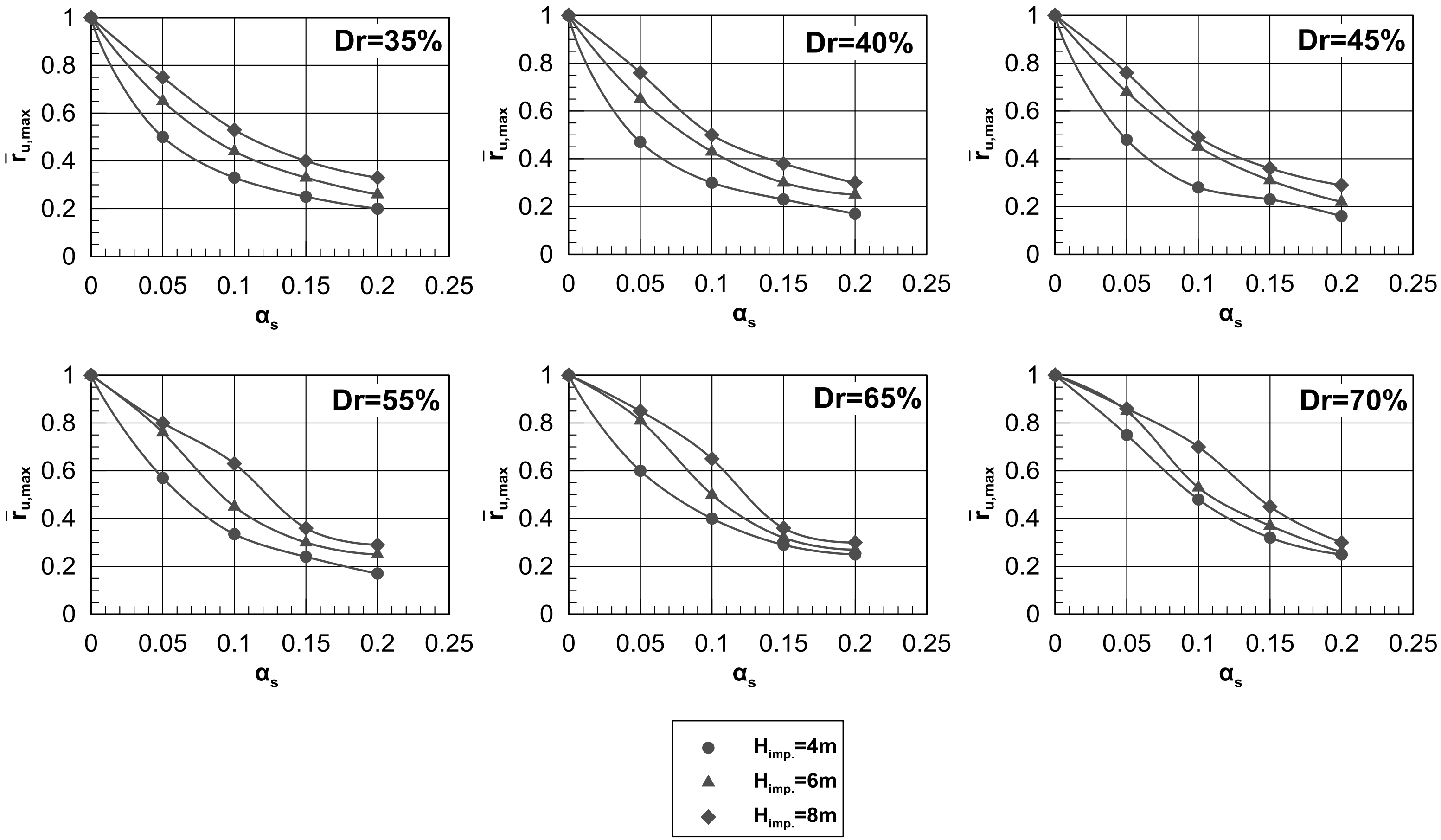

Figure 4.8: Average r_u within the improved crust as a function of replacement ratio α_s, for all examined scenarios of initial relative density and improvement thicknesses

Σχήμα 4.8: Μέση τιμή του r_u εντός της βελτιωμένης κρούστας συναρτήσει του συντελεστή αντικατάστασης α_s, για όλους τους εξεταζόμενους συνδυασμούς της αρχικής σχετικής πυκνότητας με το πάχος βελτίωσης

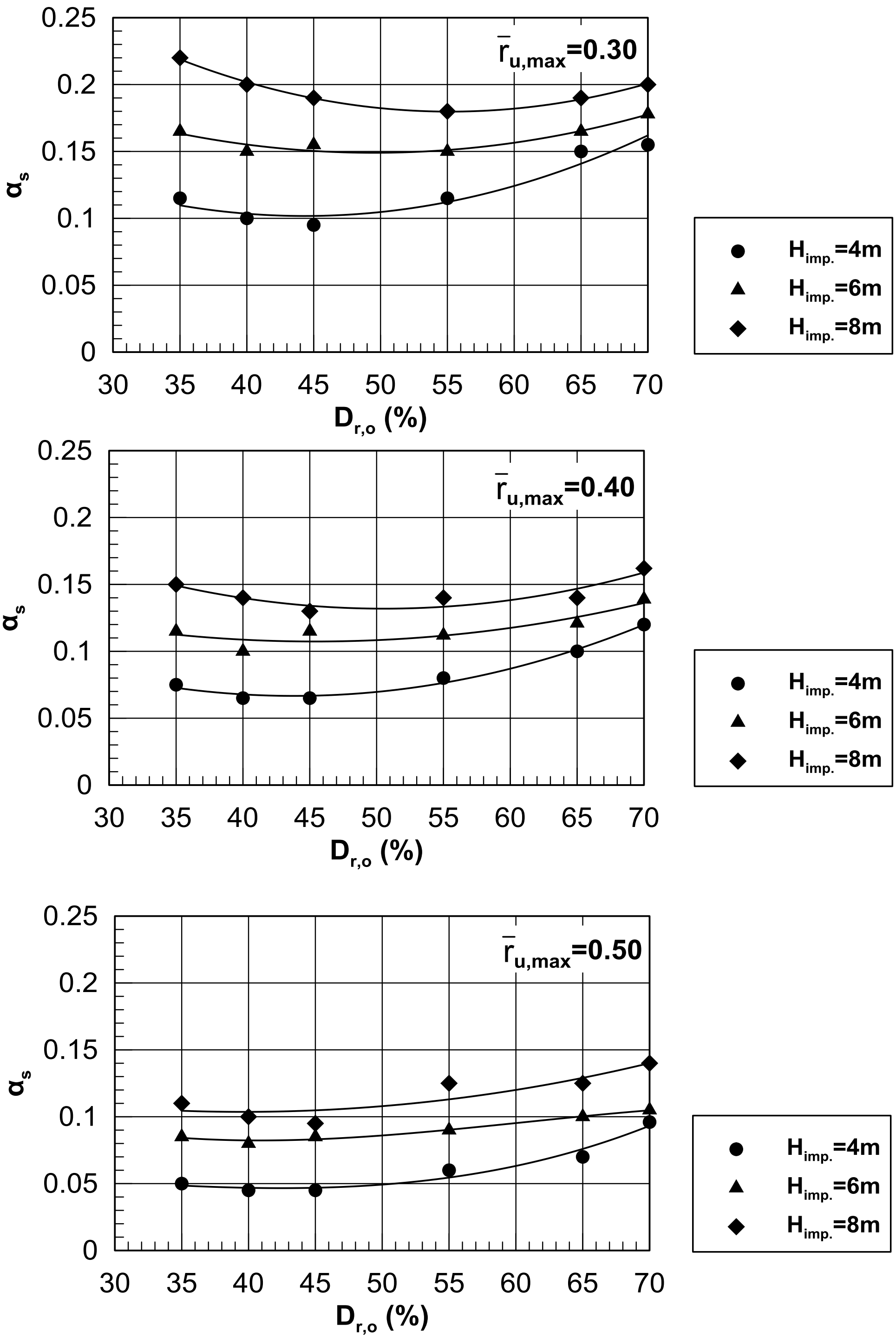

Figure 4.9: Required replacement ratio α_s with regard to initial relative density $Dr_{,o}$(%) and three allowable levels of $r_{u,max}$

Σχήμα 4.9: Απαιτούμενος συντελεστής αντικατάστασης α_s συναρτήσει της αρχικής σχετικής πυκνότητας $Dr_{,o}$(%) για τρεις επιτρεπόμενες τιμές του $r_{u,max}$

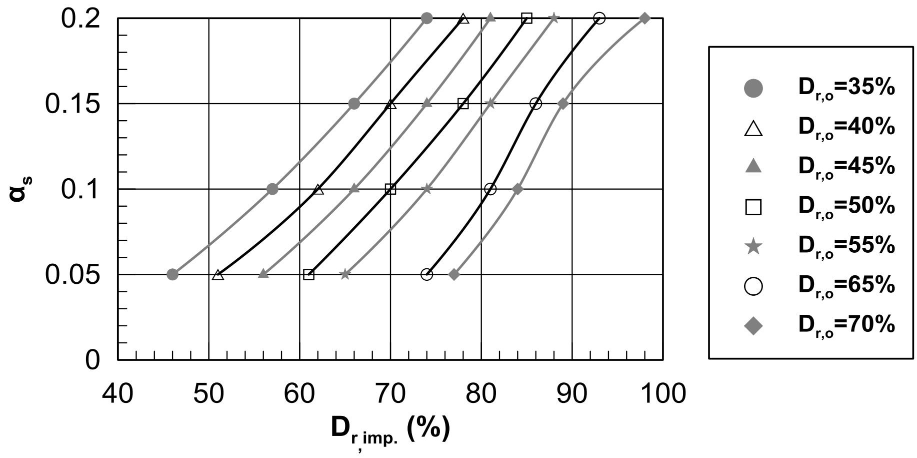

(a)

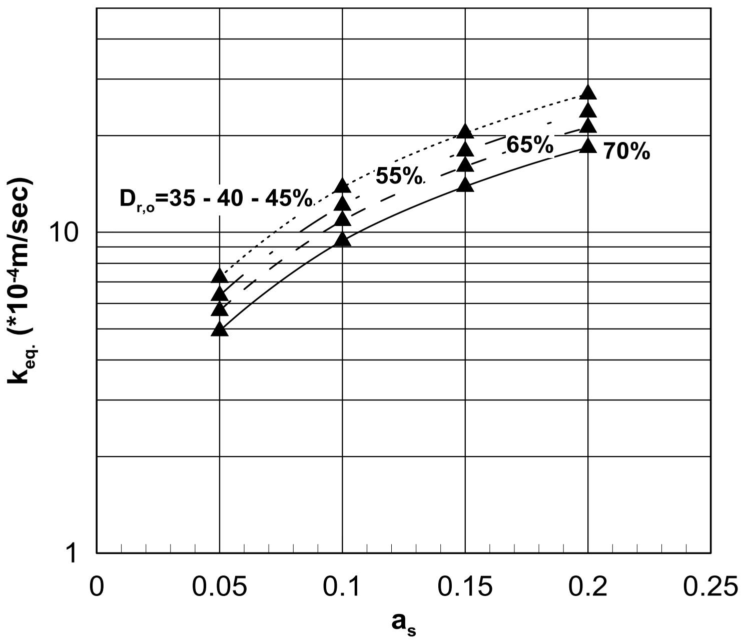

(b)

Figure 4.10: Assessment of the improved properties (a) relative density $Dr_{,imp}$(%) and (b) permeability $k_{eq.}$(m/sec), as a function of replacement ratio α_s

Σχήμα 4.10: Εκτίμηση των βελτιωμένων ιδιοτήτων (a) σχετική πυκνότητα $Dr_{,imp}$(%) και (b) διαπερατότητα $k_{eq.}$(m/sec), συναρτήσει του συντελεστή αντικατάστασης α_s

4.4 Parameter identification

Following the numerical simulation presented in Chapter 3, the liquefaction performance of a strip foundation is parametrically investigated focusing on two main objectives:

- the seismically induced footing settlements ρ_{dyn}, and
- the degraded post-shaking bearing capacity of the footing $q_{ult.}$

To simplify the problem at hand, it is assumed that the improved zone extends up to the limits of the considered grid. Hence, the liquefaction response of the footing is initially examined under conditions of "infinite" improvement. Nevertheless, in reality, the improved crust is going to be artificially manufactured around the shallow foundation, disclosing the last examined independent problem parameter, namely that of the extent of the performed improvement, L_{imp}. For that purpose, an additional set of analyses is executed, in which the lateral extent of improvement is gradually reduced, to evaluate the effect on the previously established liquefaction performance of the footing.In the following sections, the two groups of parametric analyses are explained in detail.

4.4.1 "Infinitely" extending improvement

The sliding-block mechanism described as part of the dynamic settlement accumulation mechanism in the previous chapter, allows the identification of two groups of basic problem parameters:

Loading and strength parameters.- They are associated to the activated failure mechanism and include: **(i)** the average foundation bearing pressure q, **(ii)** characteristics of the drain-improved crust, namely the normalized thickness H_{imp}/B, the friction angle $\varphi_{improved}$, as well as **(iii)** properties of the liquefiable sand layer, including the normalized thickness Z_{liq}/B and the relative density $D_{r,o}$.

Excitation characteristics.- These parameters control the amount of accumulated settlement, and include: the peak bedrock acceleration a_{max}, the peak bedrock velocity v_{max} and the number of significant loading cycles N. The peak bedrock velocity v_{max} may be alternatively incorporated in the parametric investigation through the predominant excitation period T.

Note that the shear strength of the crust is expressed through the improved relative density $D_{r,imp.}$, which is directly linked to the initial relative density of the underlying liquefiable sand, through the replacement ratio α_s. Additionally, the improved crust allows the dissipation of excess pore pressures and consequently the formation of a flow front propagating upwards from the deepest to the shallower locations. The permeability of the crust is practically related to the permeability of the original sand layer again through the selected replacement ratio α_s. Also, as suggested by the design charts provided in **Figure 4.9,** replacement ratio α_s, is directly controlled by the maximum excess pore pressure ratio $r_{u,max}$ expected to develop under free field conditions within the improved crust. Hence, it is concluded that the key-parameter controlling the properties assigned in the improved crust is the maximum anticipated excess pore pressure ratio $r_{u,max}$, which is set equal to 0.4 for the majority of the numerical analyses.

The plan of parametric analyses is summarized in **Table 4.1**. The range of each parameter included in the parametric investigation is summarized below. Note that the effect of each parameter was examined separately, with the other parameters being given the reference values provided in the parentheses.

- Average contact pressure applied by the foundation q=52, 60, 70, 75, 80, 90, 100, 110kPa (52, 100kPa)
- Relative density of the liquefiable sand layer $D_{r,o}$=35, 45, 55, 65% (45%)
- Thickness of the liquefiable layer $Z_{liq.}$=6, 8, 10, 12, 14, 16m (16m)
- Depth of the performed improvement $H_{imp.}$=4, 5, 6, 7 & 8m (4m)
- Width of the foundation B=3, 5, 7, 9m (5m)
- Peak input acceleration, applied at the base of the liquefiable layer α_{max}=0.10, 0.15, 0.20, 0.25, 0.30, 0.35g (0.15g)
- Number of cycles of the sinusoidal motion N=5, 10, 12, 15 (10)
- Excitation period T=0.15, 0.20, 0.25, 0.35, 0.50sec (0.35sec)
- Maximum excess pore pressure ratio inside the crust $r_{u,max}$=0.15, 0.20, 0.30, 0.40 (0.40).

To isolate the influence of the improved relative density from the concurrent change in the permeability, a separate set of analyses was performed. Namely, the improved crust was assigned the appropriate relative density resulting from the design charts but different values for the permeability the natural sand were applied. Also, the effect of the relative density of the liquefiable sand was separately examined, by preserving the properties ($D_{r,imp.}$ & $k_{eq.}$) of the crust and altering only $D_{r,o}$ (%). Moreover, the ultimate bearing capacity for crust thicknesses $H_{imp.}$=6 & 8m was investigated, by increasing the initial contact pressure q up to immediate post-shaking failure.

The first set of parametric analyses was performed for an average contact pressure equal to q=100kPa and the parameter combination of case No7 of **Table 4.1.** Nevertheless, it turned out that the specific arrangement was in a meta-stable area, with regard to parameter Z_{liq}/B, as illustrated in **Figure 4.11**. In other words, for $Z_{liq.}/B$=3.2 (Z_{liq} = 16m) the degraded factor of safety is well above unity, but for lower values the footing has experienced post-shaking failure. For that reason, a second set of analyses was performed, with a considerably reduced average contact pressure, equal to q=52kPa, ensuring that the particular arrangement is far from post-shaking failure.

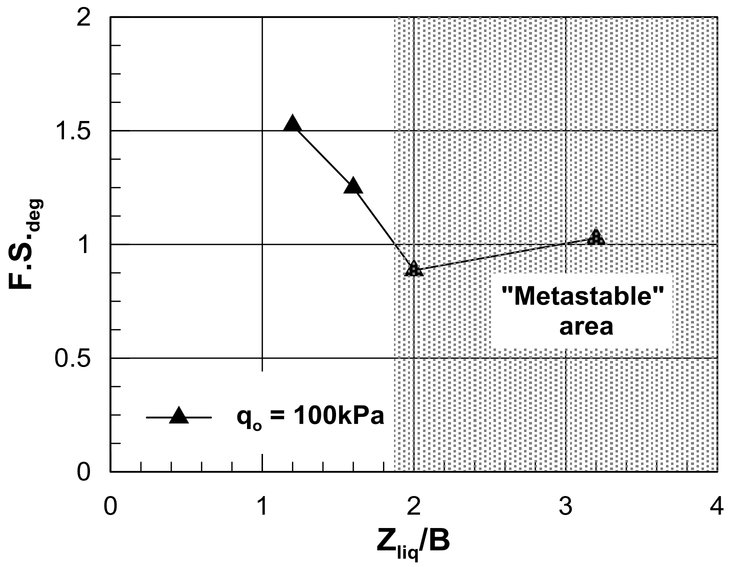

Figure 4.11: Variation of the degraded bearing capacity $F.S._{deg}$ versus Z_{liq}/B for constant footing presure q = 100kPa and footing width B = 5m

Σχήμα 4.11: Διακύμανση της απομειωμένης φέρουσας ικανότητας $F.S._{deg}$ συναρτήσει του Z_{liq}/B για σταθερό φορτίο θεμελίου q = 100kPa και πλάτος θεμελίου B = 5m

The discovery of a meta-stable area in the post-shaking response of the shallow footing is particularly interesting. It is possible that the thickness of the liquefiable layer, which determines the depth of liquefaction occurrence, plays a key role in the particular phenomenon. The meta-stable area was also observed, when incrementally increasing the footing pressure, q (kPa), independently of the thickness of the improved crust and the other parameters of the configuration. Namely, the increase of the applied pressure did not provide a continuously reducing degraded factor of safety, but rather its fluctuation around unity. The particular observation may be attributed to secondary dilation phenomena in the vicinity of the footing, which locally increase the shear strength of the improved crust. The observed meta-stable cases were excluded from the statistical processing regarding the degraded bearing capacity of the footing.

Table 4.1: Summary of parametric analyses plan
Πίνακας 4.1: Σύνοψη παραμετρικών αναλύσεων

No	Analysis Name	q (kPa)	$D_{r,o}$ (%)	$Z_{liq.}$ (m)	$r_{u,max}$	$H_{imp.}$ (m)	B (m)	a_{max}(g)	T	N	$k_{eq.}$ ($*10^{-4}$m/s)	$D_{r,imp}$ (%)	$L_{imp.}$ (m)
1	q=52kPa	**52**	45	16	0.4	4	5	0.15	0.35	10	f(α_s)	f(α_s)	inf.
2	q=60kPa	**60**	45	16	0.4	4	5	0.15	0.35	10	f(α_s)	f(α_s)	inf.
3	q=70kPa	**70**	45	16	0.4	4	5	0.15	0.35	10	f(α_s)	f(α_s)	inf.
4	q=75kPa	**75**	45	16	0.4	4	5	0.15	0.35	10	f(α_s)	f(α_s)	inf.
5	q=80kPa	**80**	45	16	0.4	4	5	0.15	0.35	10	f(α_s)	f(α_s)	inf.
6	q=90kPa	**90**	45	16	0.4	4	5	0.15	0.35	10	f(α_s)	f(α_s)	inf.
7	q=100kPa	**100**	45	16	0.4	4	5	0.15	0.35	10	f(α_s)	f(α_s)	inf.
8	Dr_o (%)-35	52	**35**	16	0.4	4	5	0.15	0.35	10	f(α_s)	f(α_s)	inf.
9	Dr_o (%)-55	52	**55**	16	0.4	4	5	0.15	0.35	10	f(α_s)	f(α_s)	inf.
10	Dr_o (%)-65	52	**65**	16	0.4	4	5	0.15	0.35	10	f(α_s)	f(α_s)	inf.
11	$Z_{liq.}$=14m	52	45	**14**	0.4	4	5	0.15	0.35	10	f(α_s)	f(α_s)	inf.
12	$Z_{liq.}$=12m	52	45	**12**	0.4	4	5	0.15	0.35	10	f(α_s)	f(α_s)	inf.
13	$Z_{liq.}$=10m	52	45	**10**	0.4	4	5	0.15	0.35	10	f(α_s)	f(α_s)	inf.
14	$Z_{liq.}$=8m	52	45	**8**	0.4	4	5	0.15	0.35	10	f(α_s)	f(α_s)	inf.
15	$Z_{liq.}$=6m	52	45	**6**	0.4	4	5	0.15	0.35	10	f(α_s)	f(α_s)	inf.
16	$r_{u,max}$=0.30 (α_s=0.09)	52	45	16	**0.3**	4	5	0.15	0.35	10	f(α_s)	f(α_s)	inf.
17	$r_{u,max}$=0.20 (α_s=0.175)	52	45	16	**0.2**	4	5	0.15	0.35	10	f(α_s)	f(α_s)	inf.
18	$r_{u,max}$=0.15 (α_s=0.20)	52	45	16	**0.15**	4	5	0.15	0.35	10	f(α_s)	f(α_s)	inf.
19	$H_{imp.}$-5	52	45	15	0.4	**5**	5	0.15	0.35	10	f(α_s)	f(α_s)	inf.
20	$H_{imp.}$-6	52	45	14	0.4	**6**	5	0.15	0.35	10	f(α_s)	f(α_s)	inf.
21	$H_{imp.}$-7	52	45	13	0.4	**7**	5	0.15	0.35	10	f(α_s)	f(α_s)	inf.
22	$H_{imp.}$-8	52	45	12	0.4	**8**	5	0.15	0.35	10	f(α_s)	f(α_s)	inf.
23	B=3m	52	45	16	0.4	4	**3**	0.15	0.35	10	f(α_s)	f(α_s)	inf.
24	B=7m	52	45	16	0.4	4	**7**	1.15	0.35	10	f(α_s)	f(α_s)	inf.
25	B=9m	52	45	16	0.4	4	**9**	2.15	0.35	10	f(α_s)	f(α_s)	inf.
26	B=3m	52	45	16	0.4	**5**	**3**	0.15	0.35	10	f(α_s)	f(α_s)	inf.
27	a_{max}=0.10g	52	45	16	0.4	4	5	**0.10**	0.35	10	f(α_s)	f(α_s)	inf.
28	a_{max}=0.20g	52	45	16	0.4	4	5	**0.2**	0.35	10	f(α_s)	f(α_s)	inf.
29	a_{max}=0.25g	52	45	16	0.4	4	5	**0.25**	0.35	10	f(α_s)	f(α_s)	inf.
30	a_{max}=0.30g	52	45	16	0.4	4	5	**0.30**	0.35	10	f(α_s)	f(α_s)	inf.
31	a_{max}=0.35g	52	45	16	0.4	4	5	**0.35**	0.35	10	f(α_s)	f(α_s)	inf.
32	T=0.15sec	52	45	16	0.4	4	5	0.15	**0.15**	10	f(α_s)	f(α_s)	inf.
33	T=0.25sec	52	45	16	0.4	4	5	0.15	**0.20**	10	f(α_s)	f(α_s)	inf.
34	T=0.50sec	52	45	16	0.4	4	5	0.15	**0.25**	10	f(α_s)	f(α_s)	inf.
35	T=0.50sec	52	45	16	0.4	4	5	0.15	**0.50**	10	f(α_s)	f(α_s)	inf.
36	N=5 cycl.	52	45	16	0.4	4	5	0.15	0.35	**5**	f(α_s)	f(α_s)	inf.
37	N=12 cycl.	52	45	16	0.4	4	5	0.15	0.35	**12**	f(α_s)	f(α_s)	inf.
38	N=15 cycl.	52	45	16	0.4	4	5	0.15	0.35	**15**	f(α_s)	f(α_s)	inf.

	Analysis Name	q (kPa)	$D_{r,o}$ (%)	$Z_{liq.}$ (m)	$r_{u,max}$	$H_{imp.}$ (m)	B (m)	a_{max}(g)	T	10	$k_{eq.}$ (m/sec)	$D_{r,imp}$ (%)	$L_{imp.}$ (m)
39	$D_{r,o\text{-}ind}$ = 35%	52	**35**	16	0.4	4	5	0.15	0.35	10	**10.87**	**82**	inf.
40	$D_{r,o\text{-}ind}$ = 45%	52	**45**	16	0.4	4	5	0.15	0.35	10	**10.87**	**82**	inf.
41	$D_{r,o\text{-}ind}$ = 55%	52	**55**	16	0.4	4	5	0.15	0.35	10	**10.87**	**82**	inf.
42	$D_{r,o\text{-}ind}$ = 65%	52	**65**	16	0.4	4	5	0.15	0.35	10	**10.87**	**82**	inf.
43	k_{sand}=6.6*10^{-6}m/s (α_s = 0.23)	52	45	16	0.4	4	5	0.15	0.35	10	**3.09**	86	inf.
44	k_{sand}=1*10^{-5}m/s (α_s = 0.2)	52	35	16	0.4	4	5	0.15	0.35	10	**4.08**	82	inf.
45	k_{sand}=1*10^{-4}m/s (α_s = 0.06)	52	55	16	0.4	4	5	0.15	0.35	10	**12.9**	58	inf.
46	Dr_o (%)-35	100	**35**	16	0.4	4	5	0.15	0.35	10	f(α_s)	f(α_s)	inf.
47	Dr_o (%)-55	100	**55**	16	0.4	4	5	0.15	0.35	10	f(α_s)	f(α_s)	inf.
48	Dr_o (%)-65	100	**65**	16	0.4	4	5	0.15	0.35	10	f(α_s)	f(α_s)	inf.
49	$Z_{liq.}$=10m	100	45	**10**	0.4	4	5	0.15	0.35	10	f(α_s)	f(α_s)	inf.
50	$Z_{liq.}$=8m	100	45	**8**	0.4	4	5	0.15	0.35	10	f(α_s)	f(α_s)	inf.
51	$Z_{liq.}$=6m	100	45	**6**	0.4	4	5	0.15	0.35	10	f(α_s)	f(α_s)	inf.
52	$r_{u,max}$=0.30	100	45	16	**0.3**	4	5	0.15	0.35	10	f(α_s)	f(α_s)	inf.
53	$r_{u,max}$=0.20	100	45	16	**0.2**	4	5	0.15	0.35	10	f(α_s)	f(α_s)	inf.
54	$r_{u,max}$=0.15	100	45	16	**0.15**	4	5	0.15	0.35	10	f(α_s)	f(α_s)	inf.
55	$H_{imp.}$-5	100	45	15	0.4	**5**	5	0.15	0.35	10	f(α_s)	f(α_s)	inf.
56	$H_{imp.}$-6	100	45	14	0.4	**6**	5	0.15	0.35	10	f(α_s)	f(α_s)	inf.
57	$H_{imp.}$-7	100	45	13	0.4	**7**	5	0.15	0.35	10	f(α_s)	f(α_s)	inf.
58	$H_{imp.}$-8	100	45	12	0.4	**8**	5	0.15	0.35	10	f(α_s)	f(α_s)	inf.
59	B=3m	100	45	16	0.4	4	**3**	0.15	0.35	10	f(α_s)	f(α_s)	inf.
60	B=3m_H_{imp}=5m	100	45	15	0.4	5	**3**	0.15	0.35	10	f(α_s)	f(α_s)	inf.
61	B=3m_H_{imp}=6m	100	45	14	0.4	6	**3**	0.15	0.35	10	f(α_s)	f(α_s)	inf.
62	a_{max}=0.10g	100	45	16	0.4	4	5	**0.10**	0.35	10	f(α_s)	f(α_s)	inf.
63	a_{max}=0.25g	100	45	16	0.4	4	5	**0.25**	0.35	10	f(α_s)	f(α_s)	inf.
64	a_{max}=0.35g	100	45	16	0.4	4	5	**0.35**	0.35	10	f(α_s)	f(α_s)	inf.
65	T=0.15sec	100	45	16	0.4	4	5	0.15	**0.15**	10	f(α_s)	f(α_s)	inf.
66	T=0.25sec	100	45	16	0.4	4	5	0.15	**0.25**	10	f(α_s)	f(α_s)	inf.
67	T=0.50sec	100	45	16	0.4	4	5	0.15	**0.50**	10	f(α_s)	f(α_s)	inf.
68	N=5 cycl.	100	45	16	0.4	4	5	0.15	0.35	**5**	f(α_s)	f(α_s)	inf.
69	N=12 cycl.	100	45	16	0.4	4	5	0.15	0.35	**12**	f(α_s)	f(α_s)	inf.
70	N=15 cycl.	100	45	16	0.4	4	5	0.15	0.35	**15**	f(α_s)	f(α_s)	inf.
71	$D_{r,o\text{-}ind}$ = 35%	100	**35**	16	0.4	4	5	0.15	0.35	10	**10.87**	**82**	inf.
72	$D_{r,o\text{-}ind}$ = 45%	100	**45**	16	0.4	4	5	0.15	0.35	10	**10.87**	**82**	inf.
73	$D_{r,o\text{-}ind}$ = 55%	100	**55**	16	0.4	4	5	0.15	0.35	10	**10.87**	**82**	inf.
74	$D_{r,o\text{-}ind}$ = 65%	100	**65**	16	0.4	4	5	0.15	0.35	10	**10.87**	**82**	inf.
75	$H_{imp.}$-6	**124**	45	14	0.4	**6**	5	0.15	0.35	11	f(α_s)	f(α_s)	inf.
76	$H_{imp.}$-6	**152**	45	14	0.4	**6**	5	0.15	0.35	12	f(α_s)	f(α_s)	inf.
77	$H_{imp.}$-6	**176**	45	14	0.4	**6**	5	0.15	0.35	13	f(α_s)	f(α_s)	inf.
78	$H_{imp.}$-6	**200**	45	14	0.4	**6**	5	0.15	0.35	14	f(α_s)	f(α_s)	inf.
79	$H_{imp.}$-8	**152**	45	14	0.4	**8**	5	0.15	0.35	15	f(α_s)	f(α_s)	inf.
80	$H_{imp.}$-8	**200**	45	14	0.4	**8**	5	0.15	0.35	16	f(α_s)	f(α_s)	inf.
81	$H_{imp.}$-8	**250**	45	14	0.4	**8**	5	0.15	0.35	17	f(α_s)	f(α_s)	inf.
82	$H_{imp.}$-8	**300**	45	14	0.4	**8**	5	0.15	0.35	18	f(α_s)	f(α_s)	inf.

4.4.2 Effect of Lateral Extent of Improvement (L_{imp})

The influence of lateral extent of improvement is investigated comparatively to the footing response for conditions of "infinite" improvement. Namely, out of the parametric analyses plan presented above, twelve (12) characteristic cases were selected, which exhibit different soil, excitation and geometric characteristics. In each set of analyses, the infinitely extending improved layer is the reference analysis. Subsequently, the width of the improved layer (L_{imp}) is progressively reduced down to nearly the width of the footing itself. The selected cases as well as the various improvement width values are provided in **Table 4.2.** The improvement width is expressed as a portion of the footing width B.

The range of each parameter examined in the parametric investigation is summarized below. Note that the effect of each parameter is examined separately, with the other parameters being given the reference values provided in the parentheses.

- <u>Average contact pressure applied by the foundation</u> q = 52kPa
- <u>Relative density of the liquefiable sand layer</u> $D_{r,o}$ = 45, 55% (45%)
- <u>Thickness of the liquefiable layer</u> Z_{liq} = 8, 12, 16m (16m)
- <u>Depth of the performed improvement</u> H_{imp} = 4, 6, 8m (4m)
- <u>Width of the foundation</u> B = 3, 5m (5m)
- <u>Peak input acceleration, applied at the base of the liquefiable layer</u> α_{max} = 0.15, 0.30g (0.15g)
- <u>Number of cycles of the sinusoidal motion</u> N = 5, 10 (10)
- <u>Excitation period</u> T = 0.35, 0.50sec (0.35sec)
- <u>Combined effect of the thickness of the improved zone (H_{imp} = 6,8m) and the input peak acceleration</u> α_{max} = 0.30g.

Observe that the L_{imp}/B ratio systematically receives values greater than unity. The particular observation is attributed to numerical reasons and particularly to the simulation approach of the shallow footing. As it is mentioned in Chapter 3, the numerical simulation of the bearing pressure q of the shallow footing is performed through applying vertical velocity at specific grid points. This velocity varies linearly from the value at the last grid point upon which it is applied, to zero at the adjacent grid point. Hence, half the width of the adjacent zones should be added to the actual footing width. On the other hand, soil properties are assigned to zones, implying that the width of the improved zone is always going to be at least equal to the number of zones upon which the bearing stresses are applied, further increased by two, one at each side of the footing.

Table 4.2: Overview of numerical analyses
Πίνακας 4.2: Επισκόπηση αριθμητικών αναλύσεων

Case No.	**Examined Parameter**	**L_{imp}/B**
1	q= 52Kpa (B=5m)	1.2, 2, 5.4, 7.8, 10.2, 12, 13.2, 14.8, 17.2, 19.6, 21
2	B=3m	1.3, 4, 7.3, 12.33, 17,21
3	D_{ro}= 55% (B=5m)	1.2, 2, 5.4, 7.8, 10.2, 12, 13.2, 14.8, 17.2, 19.6, 21
4	Z_{liq} = 8m (B=5m)	1.2, 2, 5.4, 10.2, 13.2, 14.8, 17.2, 19.6
5	Z_{liq} = 12m (B=5m)	1.2, 2, 5.4, 10.2, 13.2, 14.8, 17.2, 19.6, 21
6	a_{max}= 0.30g (B=5m)	1.2, 2, 5.4, 7.8, 10.2, 12, 13.2, 14.8, 17.2, 19.6, 21
7	N= 5 (B=5m)	1.2, 2, 5.4, 10.2, 13.2, 14.8, 17.2, 19.6, 21
8	T= 0.50sec (B=5m)	1.2, 2, 5.4, 7.8, 10.2, 12, 13.2, 14.8, 17.2, 19.6, 21
9	H_{imp}=6m (B=5m)	1.2, 2, 5.4, 10.2, 13.2, 14.8, 21
10	H_{imp}= 8m (B=5m)	1.2,2, 5, 5.4, 9.8, 13.4, 15.2, 20, 24.8
11	H_{imp}=6m (a_{max}=0.30g)	1.2, 2, 5.4, 10.2, 13.2, 14.8, 21
12	H_{imp}= 8m (a_{max}=0.30g)	1.2, 2, 5, 5.4, 9.8, 13.4, 15.2, 20, 24.8

5

Analytical Relations for Seismic Settlement & Degraded Bearing Capacity: Infinite Improvement Width

5.1 Introduction

The present chapter is devoted to the statistical processing of the numerical results obtained from the parametric analysis described earlier. The aim of the statistical evaluation is first to identify the parameters controlling the accumulation of dynamic settlements (ρ_{dyn}) and the post-shaking degraded factor of safety ($F.S._{deg.}$) and consequently to quantify their effect. As a result, analytical expressions are established for the prediction of seismic settlements of the shallow foundation, at the end of shaking, as well as the associated degraded bearing capacity $q_{ult.}$ and factor of safety $F.S._{deg}$.

5.2 Earthquake-induced foundation settlements

5.2.1 Newmark-based analytical expression

Systematic examination of the numerical results, combined with observations from relevant centrifuge and large-scale experiments published in the literature, suggests that dynamic settlement accumulation of shallow foundations is not the result of sand densification, but rather that of the activation of a Newmark-type sliding block failure mechanism. Namely, as it has been thoroughly explained in Chapter 3, settlement accumulation is associated with the activation of two one-sided wedge type failure mechanisms, occurring twice during one full loading cycle.

The correlation of dynamic settlement accumulation to a failure mechanism, may potentially lead to its association with the degraded factor of safety, also referred to as $F.S._{deg}$. Hence, to investigate this option, the effect of the different groups of examined problem parameters (i.e. loading, excitation, geometry and soil characteristics) are jointly evaluated for both, the footing settlements and the inverse degraded factor of safety, as shown in **Figure 5.1** through **Figure 5.4**. This parallel evaluation discloses that contact pressure q, as well as all geometry and soil characteristics have qualitatively the same effect on both $\rho_{dyn.}$ and $1/F.S._{deg.}$. Hence, dynamic settlements may be directly related to the inverse of the degraded factor of safety, thus reducing the total number of the independent variables for estimating ρ_{dyn}. It is also evident that this is hardly the case when examining the effect of the excitation characteristics on $\rho_{dyn.}$ and $1/F.S._{deg}$, presented in **Figure 5.2**. Hence, the specific parameters will be handled as separate variables, following the formulation justified below.

For the simple case of harmonic loading, the sliding block mechanism results in displacement accumulation, which is proportional to equation (5.1):

$$\frac{v^2_{max}}{a_{max}} N = a_{max} T^2 N \qquad (5.1)$$

where:

v_{max} is the maximum velocity of the applied excitation

a_{max} the maximum acceleration magnitude of the applied excitation

T the period of the applied excitation

N the number of cycles

It can be further shown from equation (5.2) that:

$$a_{max} T^2 N = \pi^2 \int_{t=0}^{t=N\cdot T} |v(t)|\, dt \qquad (5.2)$$

where v(t) is the applied velocity time history.

The main advantage stemming from the use of such an expresion is that an analytical relation for ρ_{dyn}, initially developed for harmonic motions can be subsequently extended to any type of input motion.

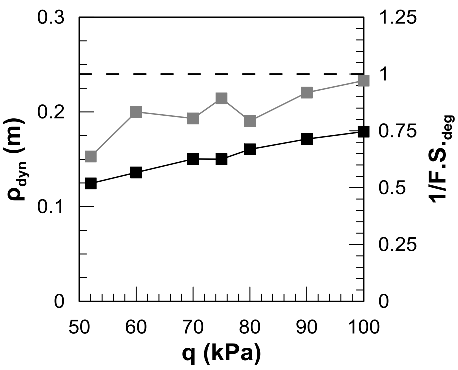

Figure 5.1: Effect of contact pressure q, in ρ_{dyn} and $1/F.S._{deg}$

Σχήμα 5.1: Επίδραση της πίεσης επαφής q, στο ρ_{dyn} και στο $1/F.S._{deg}$

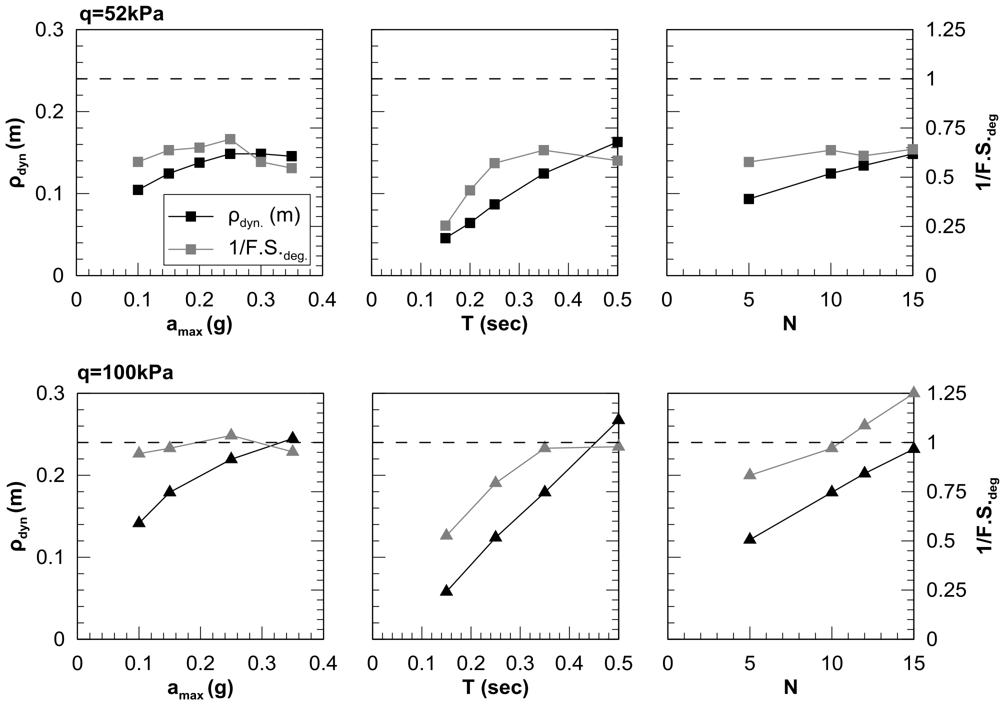

Figure 5.2: Effect of excitation parameters in ρ_{dyn} and $1/F.S._{deg}$ for two loading levels (52 and 100kPa)

Σχήμα 5.2: Επίδραση των παραμέτρων της δόνησης στο ρ_{dyn} και στο $1/F.S._{deg}$ για δύο στάθμες φόρτισης (52 και 100kPa)

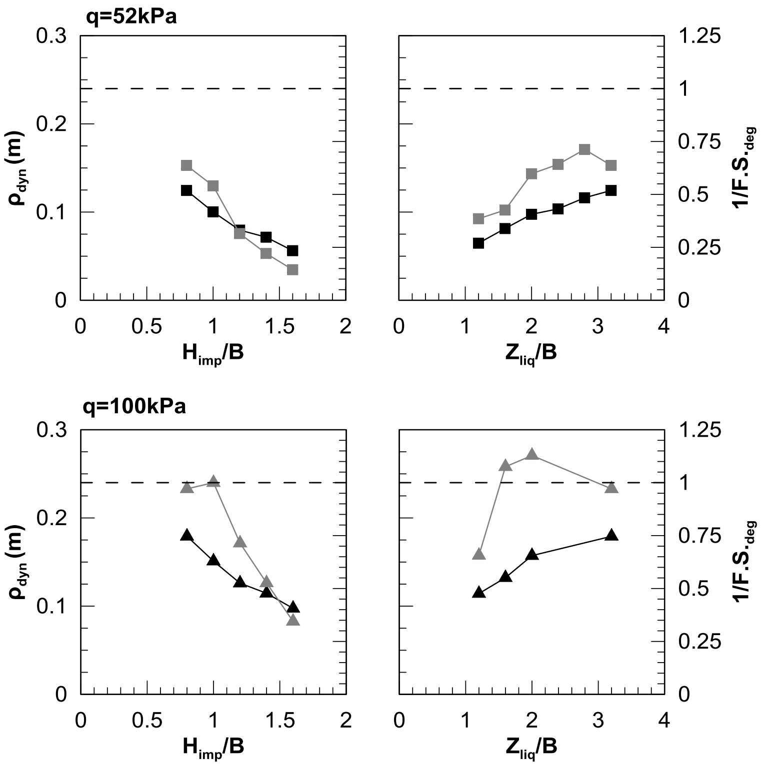

Figure 5.3: Effect of geometry parameters in ρ_{dyn} and $1/F.S._{deg}$ for two loading levels

Σχήμα 5.3: Επίδραση των γεωμετρικών παραμέτρων στο ρ_{dyn} και στο $1/F.S._{deg}$ για δύο στάθμες φόρτισης

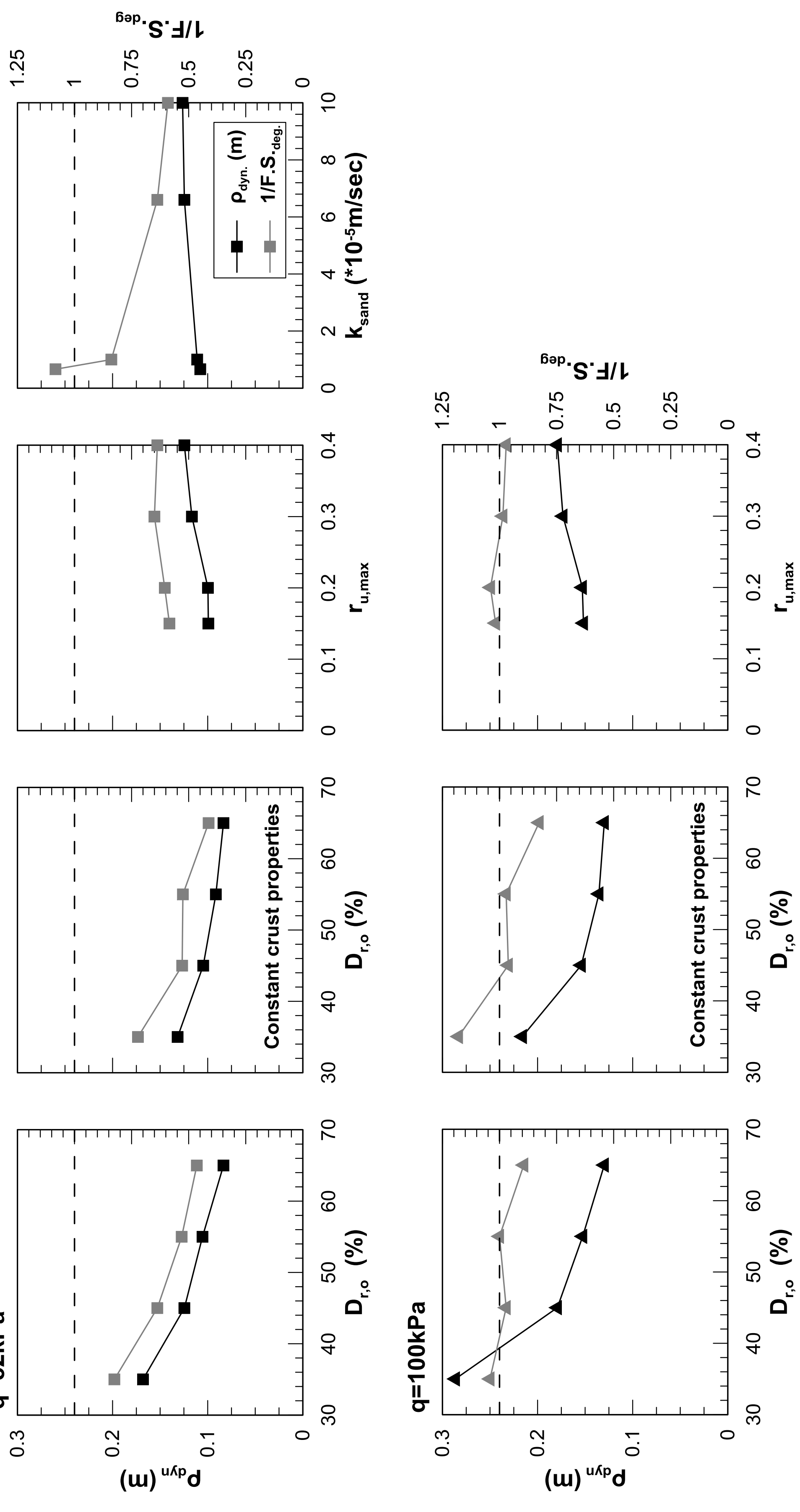

Figure 5.4: Effect of soil parameters in ρ_{dyn} and $1/F.S._{deg}$ for two loading levels (52 and 100kPa)
Σχήμα 5.4: Επίδραση των εδαφικών παραμέτρων στο ρ_{dyn} και στο $1/F.S._{deg}$ για δύο στάθμες φόρτισης (52 και 100kPa)

Integration of the applied velocity time-history in the performed numerical analyses was found equal to $\alpha_{max}T^2(N_o+2)$, where N_o is the number of significant cycles of the motion. The total number of loading cycles is increased by two, to account for the additional cycles of varying amplitude, added at the beginning and at the end of the applied excitation.

In extend of the above, the numerically predicted ρ_{dyn} values were normalized against $\alpha_{max}T^2(N_o+2)$ and correlated to the inverse of the degraded factor of safety. This correlation is illustrated in **Figure 5.5**. Observe that there is a consistent trend of the data points, expressed analytically as:

$$\frac{\rho_{dyn}}{a_{max}T_{exc}{}^2(N_o+2)} = 0.06 \cdot \left(\frac{1}{FS_{deg}}\right)^{0.45} \cdot \left[1 + 0.3 \cdot \left(\frac{1}{FS_{deg}}\right)^5\right] \qquad (5.3)$$

but the associated scatter is considerable and may limit the use of equation (5.3) in practical applications. This is mainly attributed to the fact that soil amplification effects, during propagation of the seismic motion from the base to the ground surface, where the settlements accumulate, are overlooked. Namely, while the seismic motion parameters (v_{max}, α_{max}, T) should refer to the base of the "sliding block", in the present application they refer to seismic excitation at the base of the soil column. To account for this mandatory drawback a number of theory-inspired modifications were applied as described below.

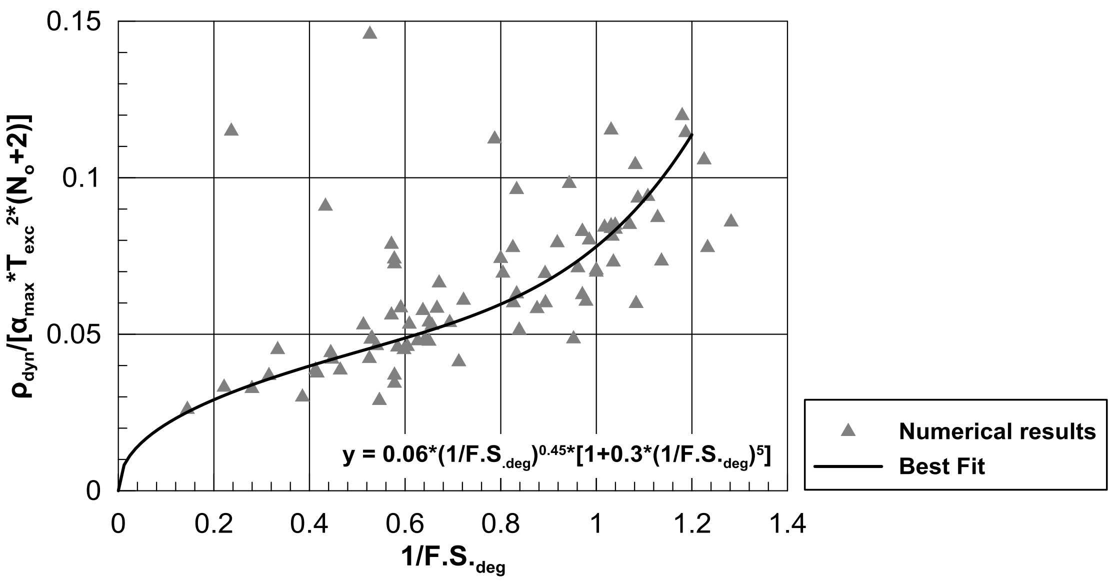

Figure 5.5: Correlation of normalized settlements ρ_{dyn} against $1/FS_{deg.}$ considering the Newmark approach

Σχήμα 5.5: Συσχέτιση των ανηγμένων καθιζήσεων ρ_{dyn} με το $1/FS_{deg}$, κατά Newmark

Incorporation of the fundamental soil period T_{soil}.- To reduce the scatter in **Figure 5.5**, the excitation period was averaged with the elastic soil period T_{soil}, the latter being expressed as:

$$T_{soil} = \frac{4H_{crust}}{V_{S,crust}} + \frac{4H_{sand}}{V_{S,sand}} \tag{5.4}$$

where $V_s = \sqrt{G_{max}/\rho}$ denotes the shear wave velocity and the maximum shear modulus G_{max} is approximately computed according to the following equation (Hardin 1978):

$$G_{max} = 600 \frac{p_{atm}}{0.3+0.7 \cdot e^2} \sqrt{\frac{p}{p_{atm}}} \tag{5.5}$$

in terms of the void ratio of the sand (e), the atmospheric pressure (p_{atm} = 100kPa) and the mean effective pressure (p in kPa) at the mid-depth of each encountered layer (i.e. improved crust and natural sand layer) (kPa).

In more detail, equation (5.3) was rewritten in a more general form with T_{exc} replaced by (T_{exc} + a×T_{soil}):

$$\rho_{dyn} = c_1 \cdot \alpha_{max} \left(T_{exc} + a \cdot T_{soil}\right)^2 \left(N_o + 2\right) \left(\frac{1}{FS_{deg}}\right)^{c_2} \left[1 + c_3 \left(\frac{1}{FS_{deg}}\right)^{c_4}\right] \tag{5.6}$$

In the sequel, a non-linear regression analysis was performed leading to the following values of the coefficients in equation (5.6): **c_1=0.019**, **c_2=0.45**, **c_3=0.25 c_4=4.5** and **a=0.633**. The correlation of the normalized seismic settlements with the inverse degraded factor of safety is shown in **Figure 5.6**.

The scatter of the data points is now significantly reduced, verifying the beneficial effect of introducing the fundamental soil period. Based on the one-to-one comparison of **Figure 5.7**, between numerical and analytical predictions of ρ_{dyn} it is further observed that about *83.3%* of the predictions with equation (5.6) lay within a range of ±25% of the numerical results. The relative error, expressed as the ratio of (Predicted – Observed)/Observed values, is presented in **Figure 5.8** with regard to the observed values of dynamic settlements, ρ_{dyn}^{num}. The uniform scatter around zero is indicative of the good and unbiased predictive accuracy of the proposed equation (5.6), which is further verified by the Standard deviation of relative error calculated equal to about 21%.

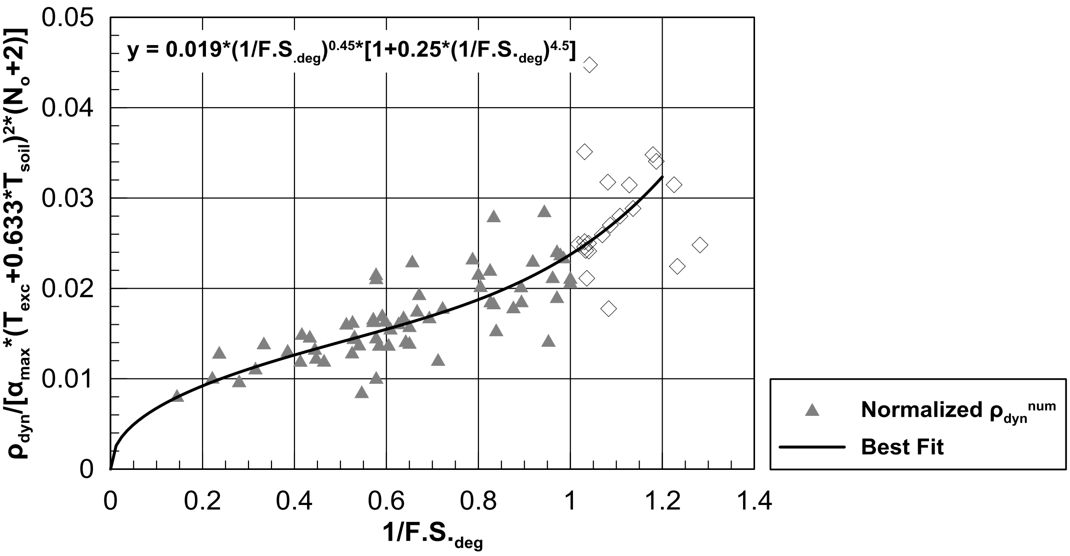

Figure 5.6: Correlation of normalized settlements ρ_{dyn} against $1/F.S._{deg.}$ considering the Newmark approach, incorporating the period of the soil column T_{soil}

Σχήμα 5.6: Συσχέτιση των ανοιγμένων καθιζήσεων ρ_{dyn} με το $1/F.S._{deg}$, κατά Newmark, ενσωματώνοντας την ιδιοπερίοδο της εδαφικής στήλης T_{soil}

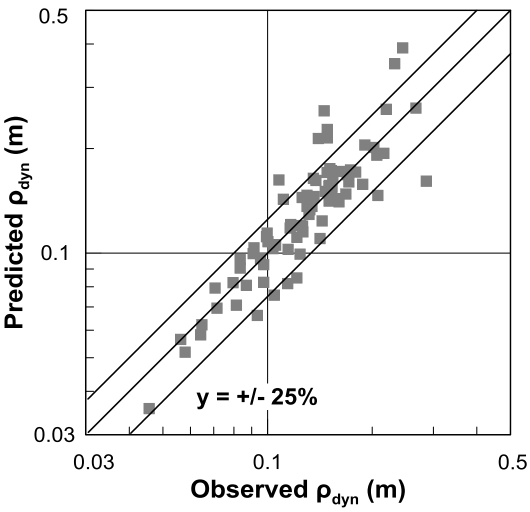

Figure 5.7: Numerical versus predicted values

Σχήμα 5.7: Σύγκριση αριθμητικών και εκτιμώμενων τιμών

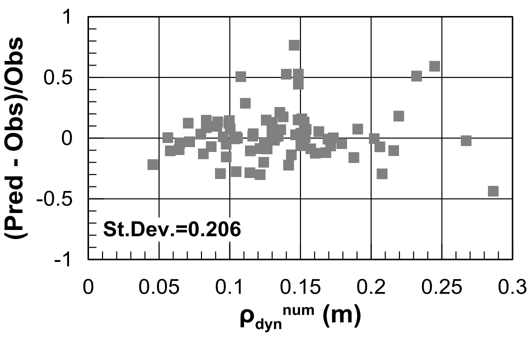

Figure 5.8: Relative error versus the numerically derived values of settlement ρ_{dyn}^{num}

Σχήμα 5.8: Σχετικό σφάλμα συναρτήσει των αριθμητικά εκτιμώμενων καθιζήσεων ρ_{dyn}^{num}

5.2.2 Unit-dependent analytical expression

The purpose of the following investigation is to explore whether there is hidden bias in the analytical predictions obtained from the use of equation (5.6), and appropriately modify it, in order to improved its accuracy. To achieve this goal, the ratio of the Observed (numerical) over the Predicted (analytical) values of ρ_{dyn} is plotted against each one of the four basic variables appearing in equation (5.6), and presented in **Figure 5.9**.

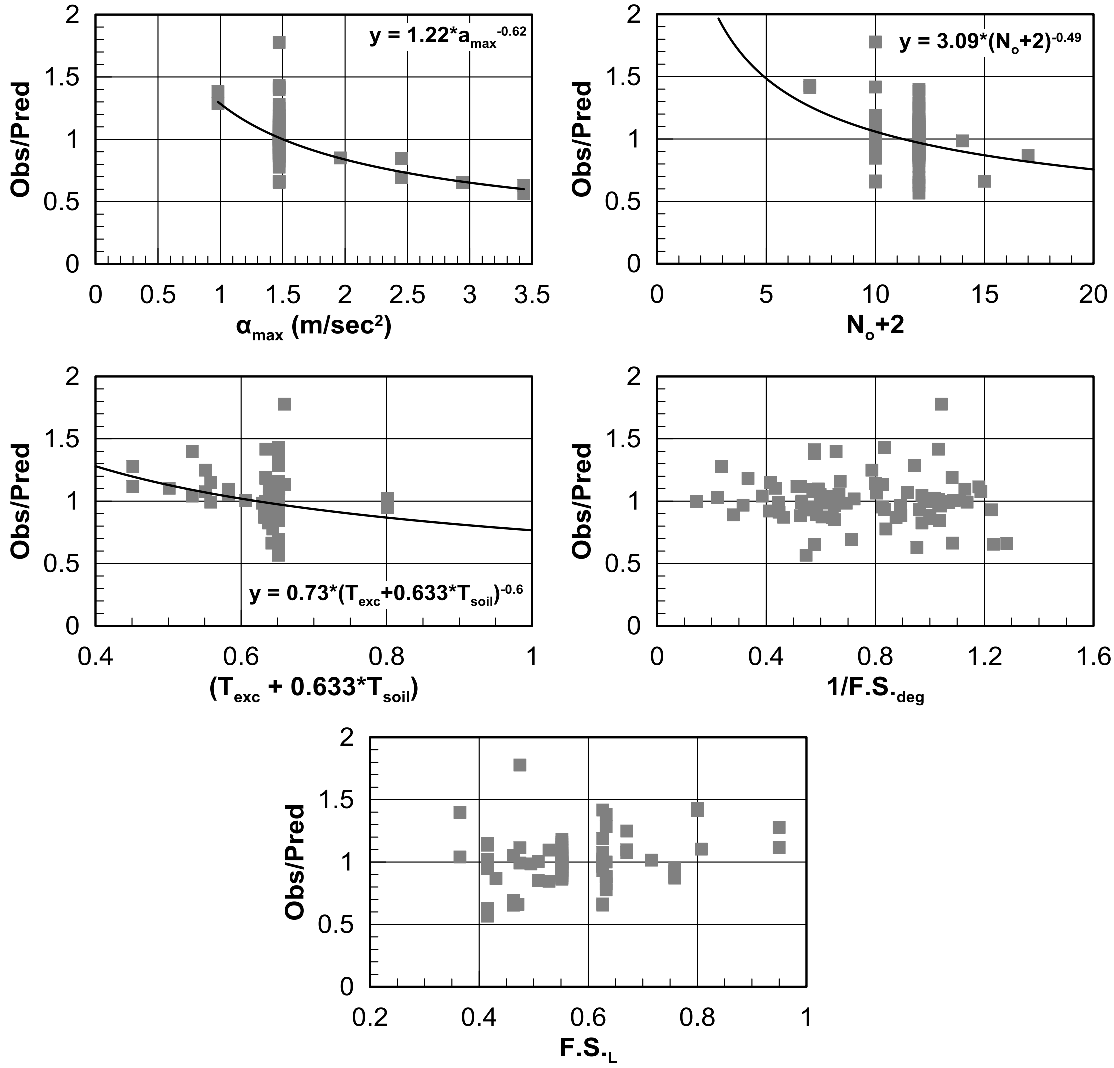

Figure 5.9: Introduced bias for the involved variables and the $F.S._L$

Σχήμα 5.9: Συσχέτιση σφάλματος με τις εξεταζόμενες μεταβλητές και το $F.S._L$

The last chart summarizes the ratio of Obs./Pred. values plotted against the factor of safety against liquefaction $F.S._L$. This particular figure is generated because the correlation of seismic-induced settlements to the total number of loading cycles implies that the onset of liquefaction coincides with the onset of seismic shaking, which is not entirely true. Also, the introduction of the inverse of the degraded factor of safety ($1/F.S._{deg.}$) into the analytical expression for the dynamic settlements is not conclusive whether it appropriately captures any possible effect of the "delayed" liquefaction. Hence, to explore this skepticism, the ratio of observed over predicted values of ρ_{dyn} is plotted against the factor of safety against liquefaction $F.S._L$, computed based on equation (5.7) below (Bouckovalas 2013; personal communication):

$$F.S._L = \frac{N^{0.35}+3.3}{N^{0.35}+3.3(N/N_L)} \tag{5.7}$$

where N is the total number of cycles and N_L is the number of cycles required to initiate liquefaction, at the mid-depth of the soil configuration, obtained from free-field numerical analyses (for r_u>0.90).

Based on **Figure 5.9**, it is found that the analytical predictions are indeed biased with regard to all three seismic excitation parameters, as opposed to the inverse relation with the degraded factor of safety, as well as the factor of safety against liquefaction $F.S._L$, where the predictions are evenly scattered around the observed values. This observation does not necessarily revoke the validity of the assumed sliding block mechanism, but essentially reveals that merely introducing the elastic soil period was not adequate in order to account for soil effects on seismic excitation characteristics. Hence, the power functions describing the bias of each variable in **Figure 5.9,** are introduced in equation (5.6), and a new non-linear regression analysis was performed to define coefficients c_1 - c_4. Thus, the empirical relation for the computation of seismic settlements now becomes:

$$\rho_{dyn} = 0.06\alpha_{max}^{0.40}\left(T_{exc} + 0.633T_{soil}\right)^{1.40}\left(N_o+2\right)^{0.50}\left(\frac{1}{FS_{deg}}\right)^{0.45}\left[1+0.4\left(\frac{1}{FS_{deg}}\right)^2\right] \tag{5.8}$$

The correlation of the normalized seismic settlements with the inverse degraded factor of safety is illustrated in **Figure 5.10**. The scatter of the data points is further reduced, verifying the beneficial effect of introducing the correction factors mentioned above.

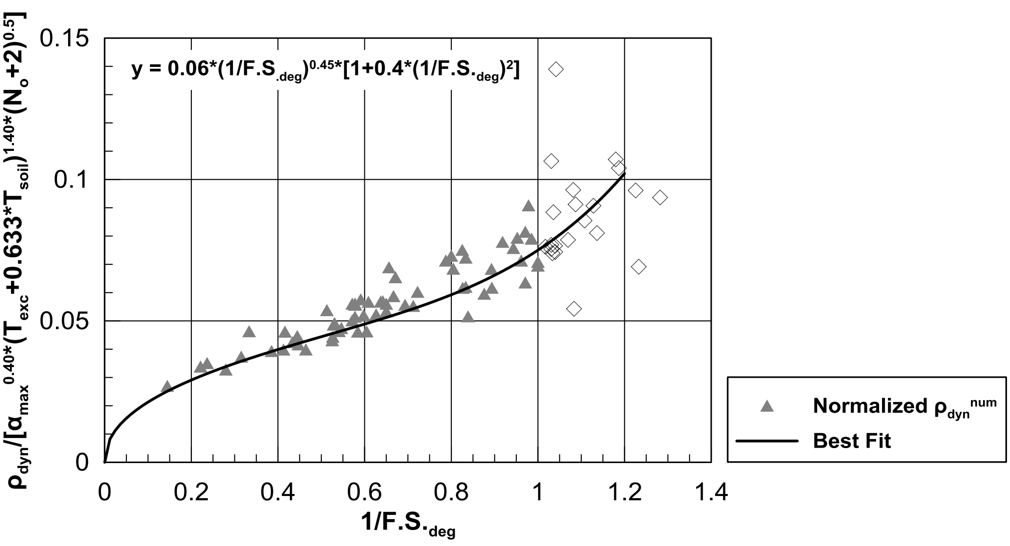

Figure 5.10: Correlation of normalized settlements ρ_{dyn} against $1/F.S._{deg}$ after bias corrections
Σχήμα 5.10: Συσχέτιση των ανοιγμένων καθιζήσεων ρ_{dyn} με το $/F.S._{deg}$ μετά τις διορθώσεις

The updated one-to-one comparison between numerical and analytical predictions is shown in **Figure 5.11**. Observe that the scatter of the data points has been considerably reduced, with *95%* of the predictions laying within a ±25% range from the numerical results and 91.6% of the predictions within a ±20% range, as shown in the corresponding figure. The relative error is evaluated in **Figure 5.12** with regard to the observed values of dynamic settlements, ρ_{dyn}^{num}. The even more uniform scatter around zero is indicative of the good and unbiased predictive accuracy of equation (5.8), which is further verified by the reduced Standard deviation of relative error calculated equal to 14%.

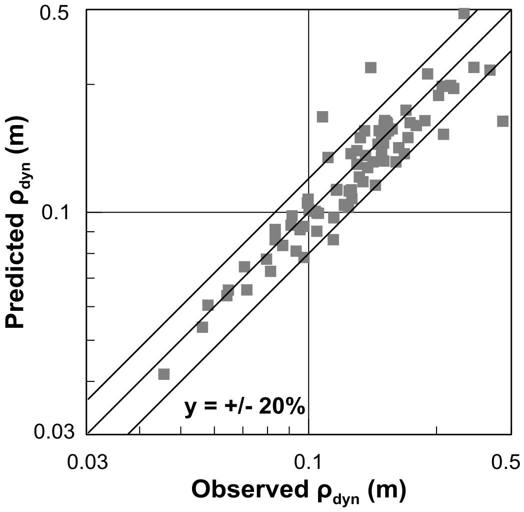

Figure 5.11: Observed versus analytically predicted values after the bias correction
Σχήμα 5.11: Σύγκριση πραγματικών τιμών με τις αναλυτικές προβλέψεις μετά τη διόρθωση

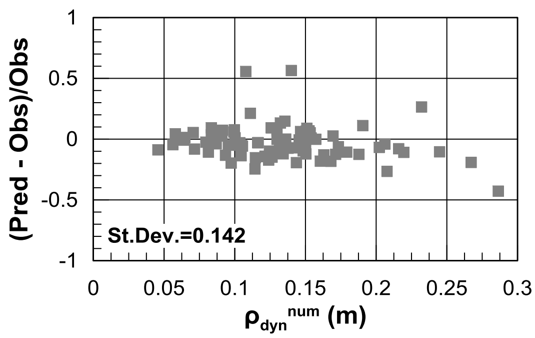

Figure 5.12: Relative error versus the numerically derived values of settlement ρ_{dyn}^{num}
Σχήμα 5.12: Σχετικό σφάλμα συναρτήσει των αριθμητικά εκτιμώμενων καθιζήσεων ρ_{dyn}^{num}

5.3 Post-shaking degraded Bearing Capacity

5.3.1 Theoretical Background and Modifications

The second part of the proposed analytical methodology focuses on the post-shaking bearing capacity of the surface foundation, which has substantially degraded compared to the initial value under static conditions, due to liquefaction of the unimproved natural soil. For that purpose, an analytical relationship for the evaluation of the degraded bearing capacity $q_{ult.}^{deg}$ (kPa) is formulated, based on theory as well as on the results of the numerical analyses.

The proposed analytical methodology is based on a modified version of the Meyerhof & Hanna (1978) analytical solution for the bearing capacity of shallow foundations on two-layered cohesionless soil profiles. According to this methodology, the bearing capacity of shallow foundations located on top of a two-layered sand formation (without embedment) is evaluated as:

$$q_{ult,deg} = \min\left\{\begin{matrix} \frac{1}{2}\gamma_1' B N\gamma_1 \\ \gamma_1' H_1^2 K_s \frac{\tan\varphi_1}{B} - \gamma_1' H_1 + \frac{1}{2}\gamma_1' B N_{\gamma 2} + \gamma_1' H_1 N_{q2} \end{matrix}\right\} \tag{5.9}$$

where

$$N_q = \tan^2(45+\varphi/2e)^{\pi\tan\varphi} \tag{5.10}$$

$$N_\gamma = 2(N_q+1)\tan\varphi \tag{5.11}$$

The coefficient K_s in equation (5.9) is evaluated based on the chart of **Figure 5.13**, as a function of the q_2/q_1 ratio, and the friction angle of the upper layer φ_1. Bearing capacities q_1 and q_2 refer to the top and the underlying layers respectively, and they are computed based on the first line of Equation (5.10). Assuming the same unit weight for both layers, the q_2/q_1 ratio is reduced to $N\gamma_2/N\gamma_1$.

In the problem at hand, it has been noticed that at the end of shaking a transition zone of non-liquefied natural ground (with $0 < r_u < 1.0$) is formed between the improved crust and the liquefied sand, as a result of the fast dissipation of the seismic induced excess pore pressures towards the much more permeable improved crust (see also **Figure 5.14**). This transitional zone acts as a secondary crust and essentially causes the Prandtl-type failure surface to develop underneath it. If the thickness of the aforementioned layer is expressed as a portion α of the thickness of the improved soil crust, and the unit soil weight is considered uniform ($\gamma_1=\gamma_2=\gamma$), the Meyerhof & Hanna (1978) analytical expression is modified as follows:

$$q_{ult,deg} = \min\left\{\begin{matrix} \frac{1}{2}\gamma' B N\gamma_1 \\ \gamma' H_1^2 K_s \frac{\tan\varphi_1}{B} + \gamma'\cdot\left[(1+\alpha)^2 - 1\right]\cdot H_1^2 K_s \frac{\tan\varphi_2}{B} - \gamma'(1+\alpha)H_1 + \\ + \frac{1}{2}\gamma' B N_{\gamma 2} + \gamma'(1+\alpha)H_1 N_{q2} \end{matrix}\right\} \tag{5.12}$$

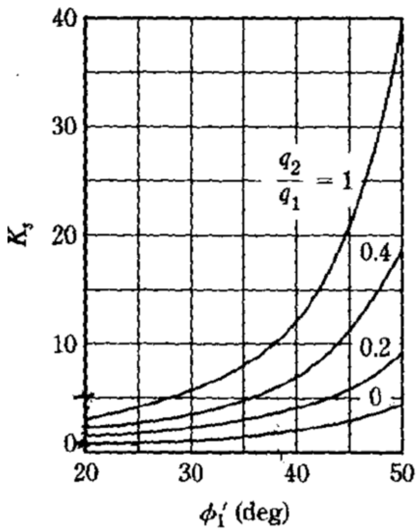

Figure 5.13: Chart for estimating the K_s coefficient in the Meyerhof & Hanna (1978) analytical methodology

Σχήμα 5.13: Διάγραμμα εκτίμησης του συντελεστή K_s στην αναλυτική μεθοδολογία των Meyerhof & Hanna (1978)

Note that the friction angles appearing in equation (5.12) above should be appropriately reduced in order to account for the excess pore pressure build up that is anticipated at the end of seismic shaking. To this extent, it will be approximately assumed that:

$$\varphi_i = \tan^{-1}\left[\left(1-U_i\right)\tan\varphi_{i,ini}\right] \qquad (5.13)$$

where the subscript "ini" denotes the friction angle of the ground at the beginning of shaking, while i= 1 for the improved crust, 2 for the transition zone and 3 for the liquefied sand.

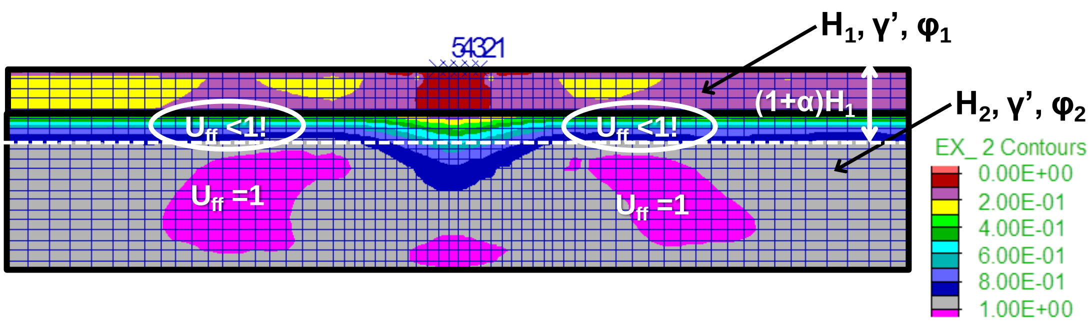

Figure 5.14: Excess pore pressure ratio contours at the end of shaking, indicating the formation of the non-liquefied layer of natural ground

Σχήμα 5.14: Ισοκαμπύλες του δείκτη υπερπιέσεων πόρων στο τέλος της δόνησης, που δείχνουν το σχηματισμό της μη-ρευστοποιημένης κρούστας στο φυσικό έδαφος

5.3.2 Calibration of necessary parameters

Coefficient *a*._ The thickness of the transition crust ($a \cdot H$) has been defined as the thickness of the natural ground over which the free field at the end of shaking is lower than 0.90. The variation of coefficient ***a*** against each one of the examined problem parameters is provided in **Figure 5.15**. Based on that, it is concluded that ***a*** mainly depends on the properties of the improved layer ($H_{imp.}$, $k_{eq.}$) and the features of the applied excitation (T, N). Furthermore, **Figure 5.16** shows that a more or less unique trend is formed when "***a***" is related to the combined parameter $k_{eq} \cdot T \cdot N/H_{imp}$. Namely, "***a***" may be written as:

$$\alpha = C_\alpha \left[\frac{k_{eq} T N}{H_{imp}} \right]^{0.256} \tag{5.14}$$

The coefficient C_α receives an average value equal to 3.76 with a Standard Deviation equal to St.Dev.=±0.50. The minimum and maximum values are equal to $C_{\alpha,min}$=3 and $C_{\alpha,max}$=4.5 respectively.

Note that the permeability of the natural soil, k_{sand}, was not included in equation (5.14) for two reasons: the particular effect is indirectly included in the equivalent coefficient of permeability (k_{eq}), while the associated correlation shown in **Figure 5.15** is rather weak.

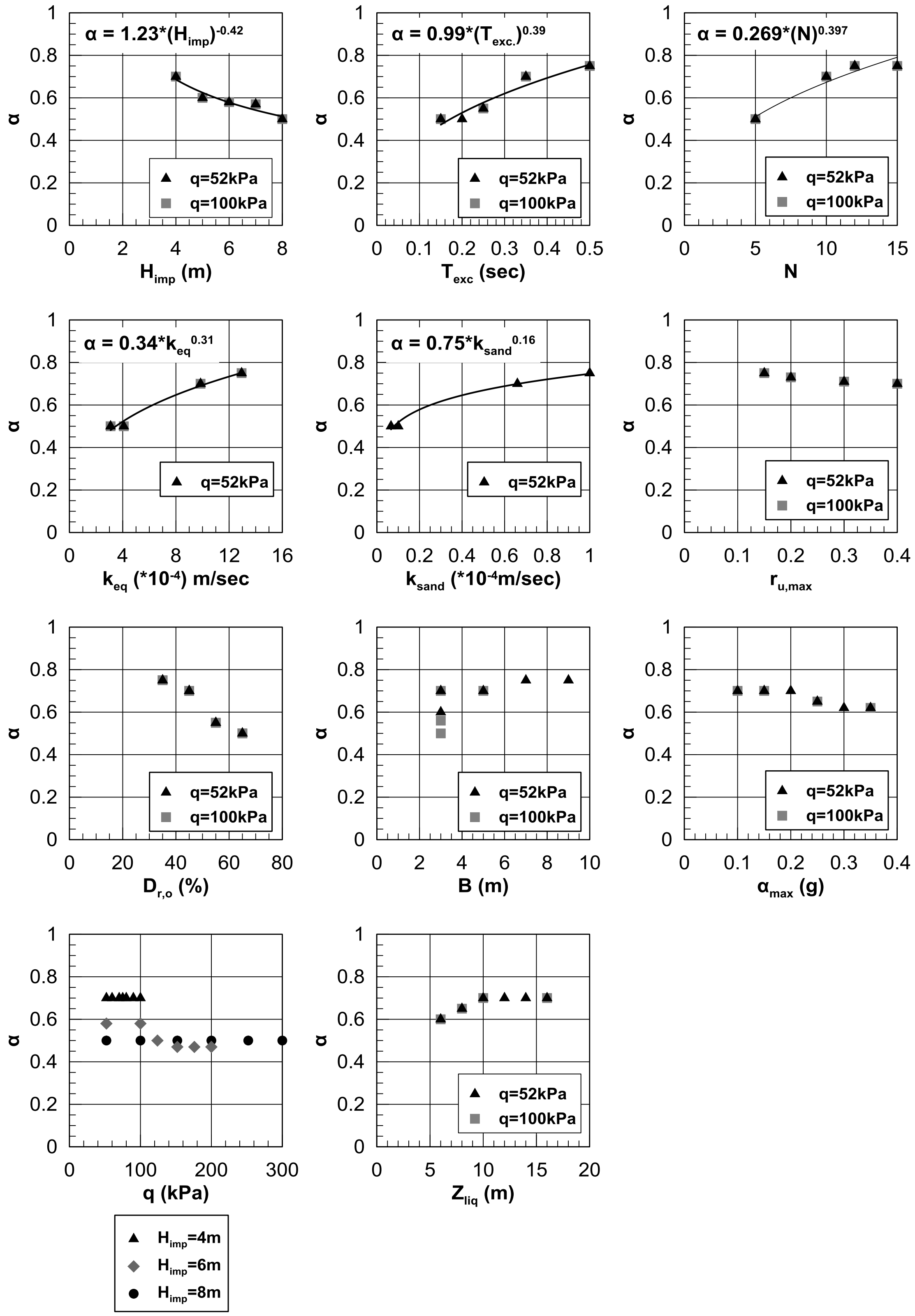

Figure 5.15: Variation of parameter α against each problem parameter

Σχήμα 5.15: Μεταβολή της παραμέτρου α συναρτήσει των εξεταζόμενων παραμέτρων

The accuracy of equation (5.14), for the average value of C_α=3.76, is evaluated in **Figure 5.17a** & **b**. In **Figure 5.17a** the numerically derived values of ***a*** are one-to-one compared to the analytical predictions, while the relative prediction error is plotted against the numerical observations in **Figure 5.17b**. It is observed that the scatter of the data points is narrow whereas the relative error is less than ±20% for the majority of the observed values. Additionally, the proposed analytical expression is checked for potential bias with regard to each separate problem parameter in **Figure 5.18.** It is thus observed that in all cases, the observed (numerical) over predicted (analytical) ***a*** ratio receives values close to unity, without exhibiting any significant and consistent trend.

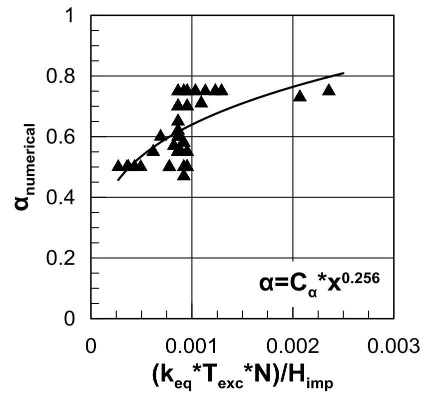

Figure 5.16: Numerical values of coefficient α against the term $(k_{eq}.TN)/H_{imp}$.
Σχήμα 5.16: Αριθμητικές τιμές του συντελεστή α συναρτήσει του όρου $(k_{eq}.TN)/H_{imp}$.

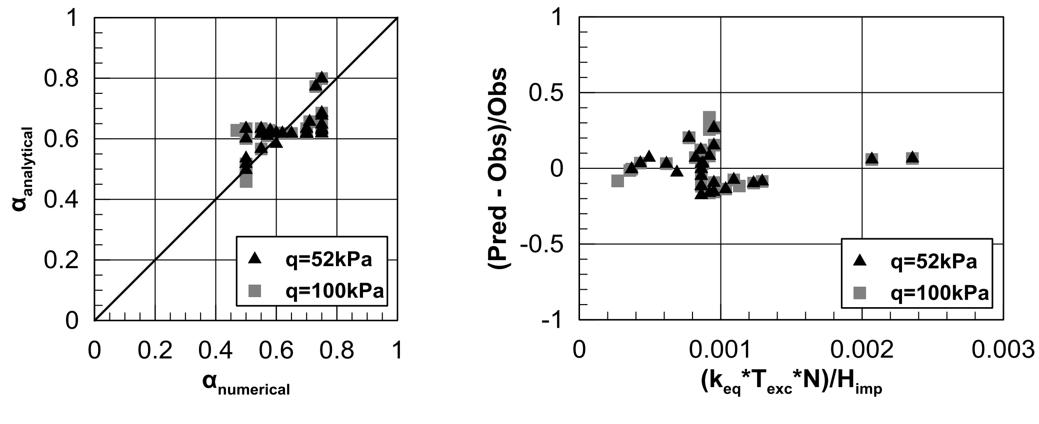

Figure 5.17: (a) One-to-one comparison of analytically computed against numerically derived *a* values (b) Relative error of predicted values
Σχήμα 5.17: (a) Ένα-προς-ένα σύγκριση αναλυτικών και αριθμητικά εκτιμώμενων τιμών του *a* (b) Σχετικό σφάλμα των εκτιμώμενων τιμών

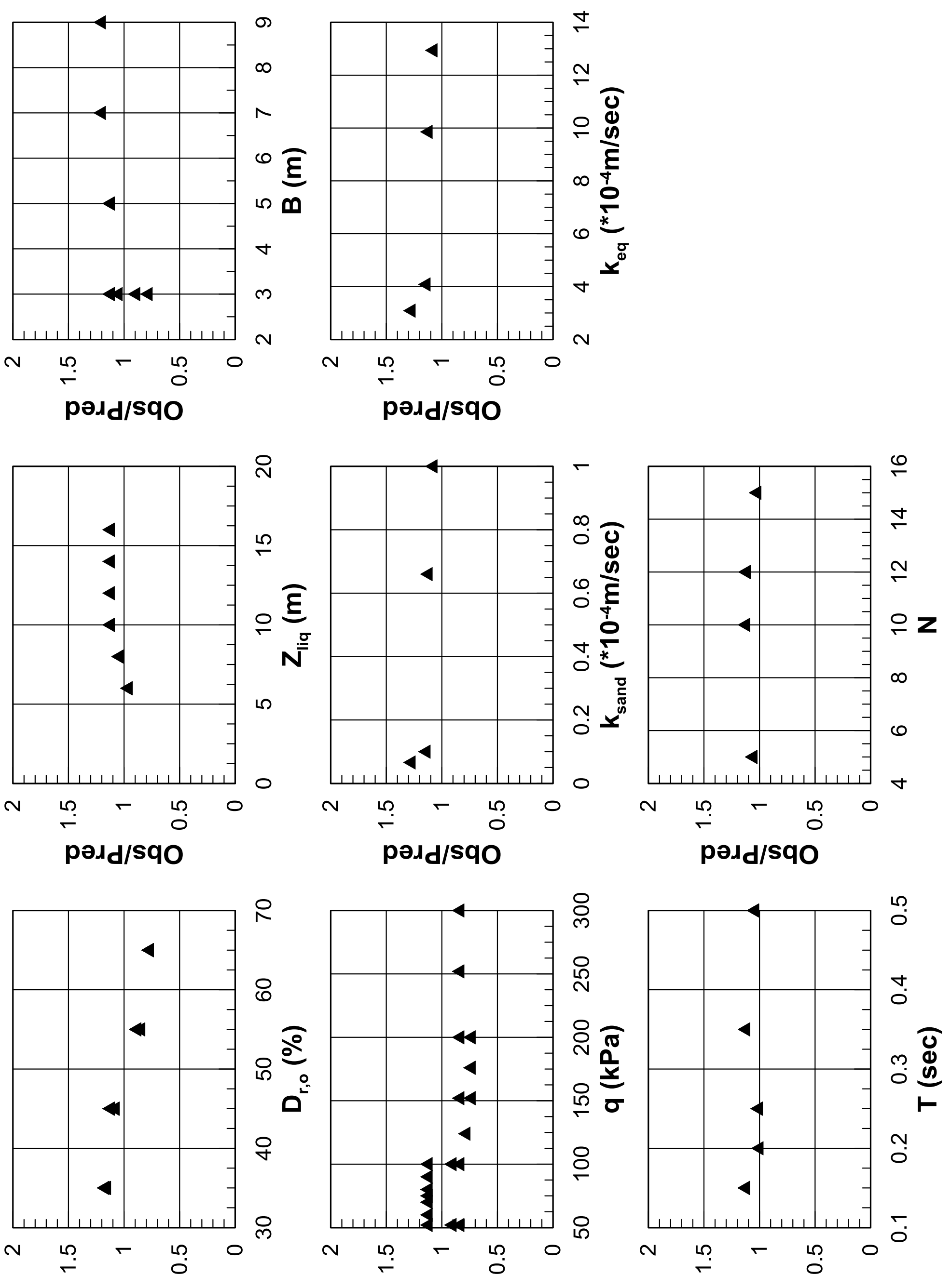

Figure 5.18: Sensitivity analysis for the mathematical expression for α coefficient
Σχήμα 5.18: Ανάλυση ευαισθησίας για την μαθηματική έκφραση του συντελεστή α

Excess pore pressure ratio U_1 in the improved crust.- The average excess pore pressure ratio U_1 refers to free field conditions and at the end of shaking. To facilitate the performed comparisons, U_1 will be expressed hereafter as a portion of the design excess pore pressure ratio, U_{design}, determined from the relevant charts formulated and presented in Chapter 4. The variation of ratio $\beta = U_1/U_{design}$ against the various problem parameters is summarized in **Figure 5.19**.

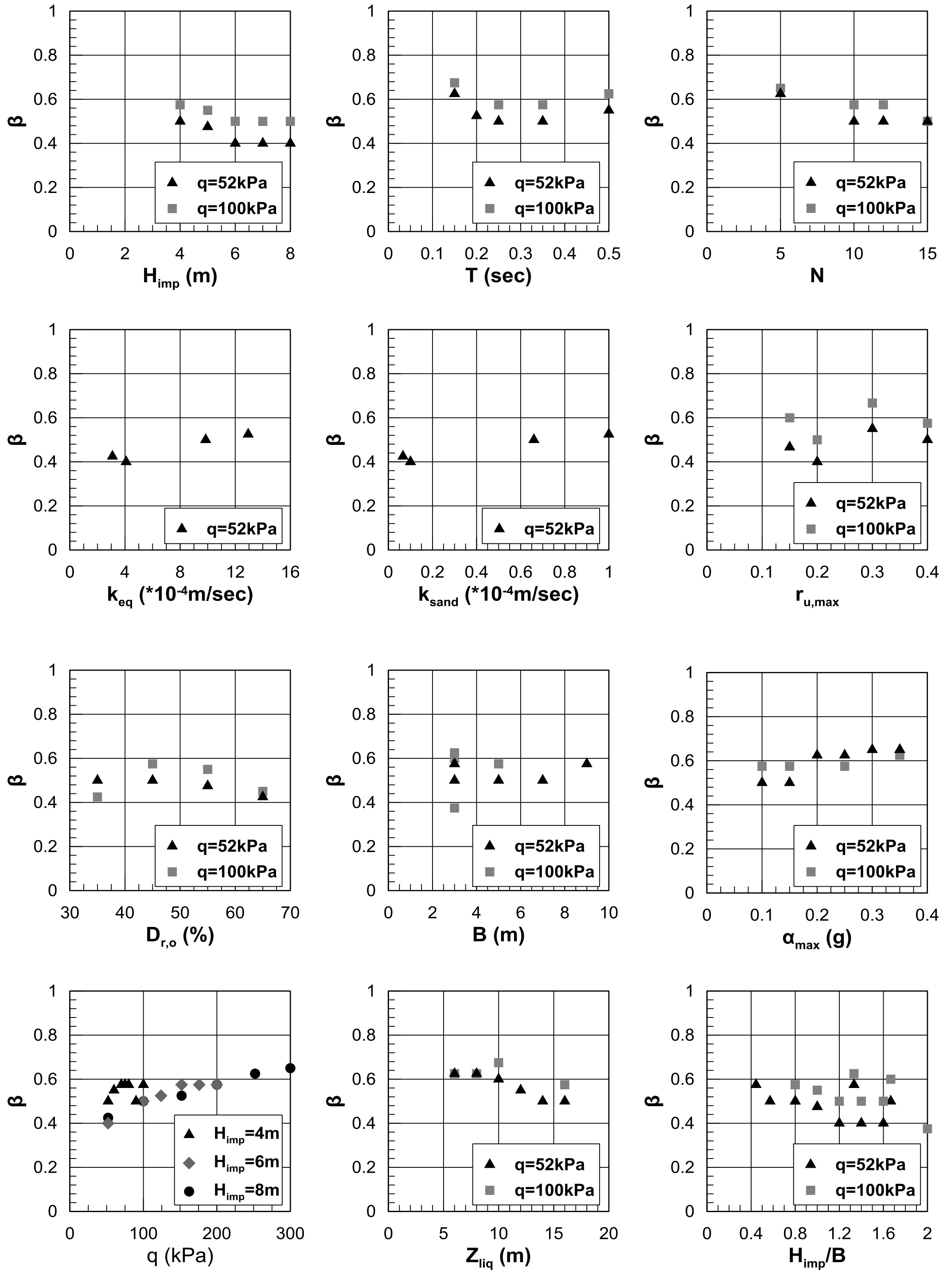

Figure 5.19: Variation of parameter β against each problem parameter

Σχήμα 5.19: Μεταβολή της παραμέτρου β συναρτήσει των εξεταζόμενων παραμέτρων

It is thus concluded that the examined problem parameters have relatively little effect on the obtained β values. Hence, β is not expressed through another analytical expression, but instead the average value from all numerical analyses will be considered. To gain more insight regarding the range of variation of the specific parameter, **Figure 5.20** summarizes all the numerically obtained β values plotted against the ultimate degraded bearing capacity q_{ult}^{num}. Based on that, β is set equal to:

$$\beta = 0.54 \pm 0.08 \tag{5.15}$$

The minimum and maximum values are equal to β_{min}=0.375 and β_{max}=0.675 respectively.

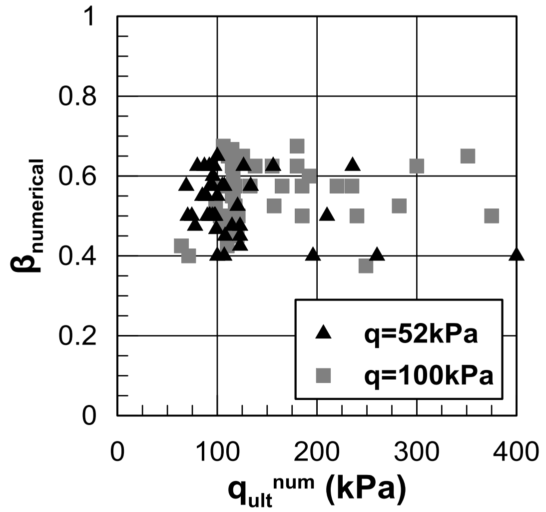

Figure 5.20: Range of variation of parameter β against the numerically derived values of degraded bearing capacity $q_{ul.t}^{num}$

Σχήμα 5.20: Έκταση της μεταβολής της παραμέτρου β συναρτήσει των αριθμητικά εκτιμώμενων τιμών της απομειωμένης φέρουσας ικανότητας $q_{ul.t}^{num}$

Excess pore pressure ratio in the transition zone U_2.- Parameter U_2, corresponds to the average excess pore pressure ratio in the transitional non-liquefied zone of the natural ground and is estimated as the average between U_1 and the excess pore pressure ratio in the liquefied soil, which equals unity. Thus, U_2 is equal to:

$$U_2 = \frac{(1+U_1)}{2} = \frac{(1+\beta \cdot U_{design})}{2} \tag{5.16}$$

Initial Friction angle for each layer $\varphi_{i,ini}$.- Since the seismic response of the soil profile is described with the use of the NTUA-SAND constitutive model, the initial friction angle values assigned to each layer are chosen based on the model's predictions. Since loading and drainage conditions are not uniform across the activated failure surface, initial friction angle values for both layers are estimated, based on equation (5.17), considering the average among TX Compression, TX Extension and Direct Simple Shear loading under undrained and drained conditions.

$$\varphi_{i,ini} = \frac{\varphi_{i,TX-C} + \varphi_{i,TX-E} + \varphi_{i,DSS}}{3} \tag{5.17}$$

Coefficient K_s.- This parameter reflects the shear strength mobilized across the partially liquefied improved and transitional soil zones, below the edges of the footing. The developing mechanism is schematically demonstrated in **Figure 5.21.**

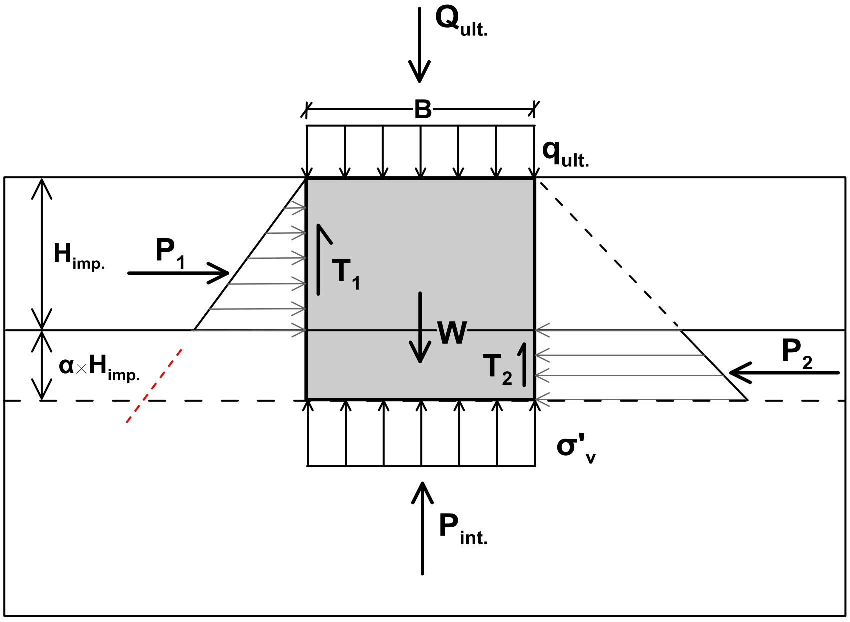

Figure 5.21: Punch through mechanism and developing forces for the determination of coefficient K_s

Σχήμα 5.21: Μηχανισμός διάτρησης και αναπτυσσόμενες δυνάμεις για την καθορισμό του συντελεστή K_s

The forces appearing in the figure are explained below:

- $Q_{ult.}$ is the ultimate load to cause post-shaking failure of the shallow foundation and is computed based on Equation (5.18) :

$$Q_{ult.} = q_{ult}^{num} \cdot B \qquad (5.18)$$

where q_{ult}^{num} is the numerically derived ultimate bearing capacity of the foundation and B the width of the footing

- Weight (W) of the soil is estimated as follows:

$$W = \gamma' \cdot (1+\alpha) H_{imp} \cdot B \qquad (5.19)$$

where $\gamma'$is the effective unit weight of the soil, H_{imp} the thickness of the improved layer and a the portion by which the thickness of the improved layer is increased in order to account for the development of the transition zone.

- $P_{int.}$ is the force developing at the interface between the transition zone and the totally liquefied soil underneath the footing. It is computed using equation (5.20):

$$P_{int} = \sigma'_v \cdot B \qquad (5.20)$$

where σ'_v is the numerical effective vertical stresses measured at the specific depth

- Shear force T is composed of two components (T_1 and T_2) corresponding to the shear strength developing across the sides of the improved layer and the transition zone respectively. It can be readily shown that the particular forces are computed based on the following equations (5.21) and (5.22) respectively:

$$T_1 = K_s \cdot P_1 = \frac{1}{2}\gamma' \cdot H_{imp}^2 \cdot K_s \cdot \tan\varphi_{1,deg} \quad (5.21)$$

$$T_2 = K_s \cdot P_2 = \frac{1}{2}\gamma' \cdot H_{imp}^2 \cdot K_s \left[(1+\alpha)^2 - 1\right]\tan\varphi_{2,deg} \quad (5.22)$$

Applying force equilibrium in the vertical direction, it comes out that:

$$P_{int.} + 2 \cdot T = W + Q_{ult.} \quad (5.23)$$

yielding the following analytical expression for K_s:

$$K_s = \frac{W + Q_{ult.} - P_{int.}}{\gamma' H_{imp}^2 \left\{\tan\varphi_{1,deg} + \left[(1+\alpha)^2 - 1\right]\tan\varphi_{2,deg}\right\}} \quad (5.24)$$

To gain insight regarding the magnitude of K_s, and derive a suitable analytical expression, K_s was estimated according to equation (5.24) for 27 cases, which are summarized in **Table 5.1**. The degraded values of the required friction angles, $\varphi_{deg,i}$ which depend on the excess pore pressure ratios U_1 and U_2, defined earlier, as well as coefficient a were considered equal to the numerically derived values for each numerical analysis. It was thus found that K_s depends mainly on the normalized thickness of the improved zone $H_{imp.}/B$, as well as on the bearing pressure q. These effects are graphically shown in **Figure 5.22a** and **Figure 5.22b**, which also explain the following analytical expression for the computation of K_s:

$$K_s = C_{K_s}\left(\frac{q}{p_\alpha}\right)^{-0.30}\left(\frac{H_{imp}}{B}\right)^{-0.50} \quad (5.25)$$

where p_a is the atmospheric pressure (p_α = 98.1kPa).

Coefficient C_{Ks} takes an average value equal to 1.00 with a Standard Deviation equal to St.Dev.=±0.15. The minimum and maximum values were estimated equal to **$C_{Ks,min}$=0.75** and **$C_{Ks,max}$=1.30** respectively.

The accuracy of equation (5.25), for the average value of C_{Ks} = 1.00, is evaluated in **Figure 5.23a** & **b**. The numerically derived values of K_s are plotted on a one-to-one basis against the analytically predicted ones in **Figure 5.23a,** while the relative error is plotted against the analytical predictions in **Figure 5.23b**. It can be observed that the scatter of the data points is rather narrow (±30% of the numerical predictions), with only a few cases overestimating K_s. This particular observation was taken into account when proposing minimum and maximum C_{Ks} values.

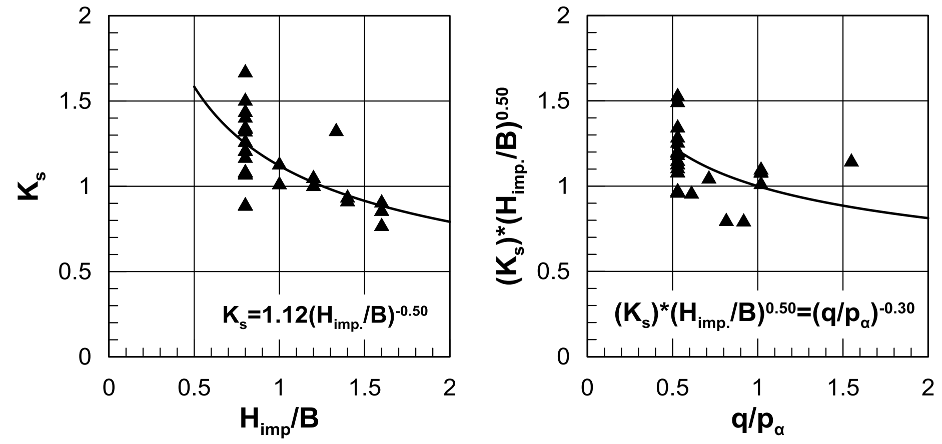

(a) **(b)**

Figure 5.22: Variation of (a) K_s coefficient against H_{imp}/B ratio and (b) $K_s/(H_{imp}/B)^{0.50}$ against contact pressure q normalized against the atmospheric pressure

Σχήμα 5.22: Μεταβολή του (a) συντελεστή K_s με τον λόγο H_{imp}/B και (b) $K_s/(H_{imp}/B)^{0.50}$ με την τάση επαφής q ανοιγμένη προς την ατμοσφαιρική πίεση

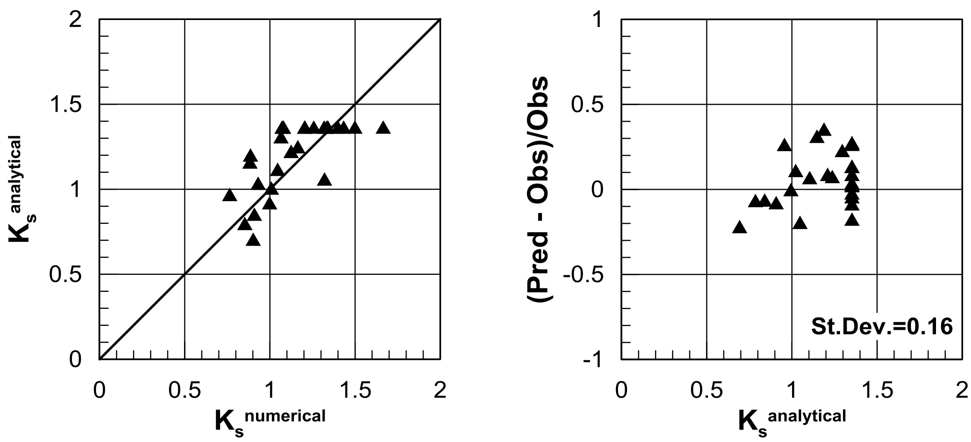

(a) **(b)**

Figure 5.23: (a) One-to-one comparison of predicted K_s against numerically computed values (b) Relative error of predicted values and standard deviation

Σχήμα 5.23: (a) Ένα-προς-ένα σύγκριση αναλυτικών και αριθμητικά εκτιμώμενων τιμών του K_s (b) Σχετικό σφάλμα και τυπική απόκλιση των εκτιμώμενων τιμών

Table 5.1: Analyses considered for the evaluation of the K_s coefficient
Πίνακας 5.1: Σύνοψη αναλύσεων που χρησιμοποιήθηκαν στην εκτίμηση του συντελεστή K_s

	H_{imp}	B (m)	q (kPa)	q_{ult} (kPa)	$F.S._{deg}$	$D_{r,o}$ (%)	Z_{liq} (m)	T (sec)	α_{max} (g)	N	K_s
1	4	5	52	82	1.57	45	16	0.35	0.15	10	1.08
2	**5**	5	52	96	1.85	45	16	0.35	0.15	10	1.12
3	**6**	5	52	165	3.17	45	16	0.35	0.15	10	1.05
4	**7**	5	52	235	4.52	45	16	0.35	0.15	10	0.93
5	**8**	5	52	360	6.92	45	16	0.35	0.15	10	0.76
6	4	**3**	52	116	2.24	45	16	0.35	0.15	10	1.32
7	4	5	**60**	72	1.20	45	16	0.35	0.15	10	1.07
8	4	5	**70**	87	1.24	45	16	0.35	0.15	10	1.16
9	4	5	**80**	100	1.25	45	16	0.35	0.15	10	0.89
10	4	5	**90**	98	1.09	45	16	0.35	0.15	10	0.88
11	**6**	5	**100**	150	1.50	45	16	0.35	0.15	10	1.00
12	**8**	5	**100**	300	3.00	45	16	0.35	0.15	10	0.85
13	**8**	5	**152**	174	1.14	45	16	0.35	0.15	10	0.90
14	**5**	5	**100**	100	1.00	45	16	0.35	0.15	10	1.01
15	**7**	5	**100**	195	1.95	45	16	0.35	0.15	10	0.91
16	4	5	52	98	1.88	**55**	16	0.35	0.15	10	1.07
17	4	5	52	112	2.15	**65**	16	0.35	0.15	10	1.20
18	4	5	52	75	1.44	45	**14**	0.35	0.15	10	1.34
19	4	5	52	83	1.60	45	**12**	0.35	0.15	10	1.43
20	4	5	52	87	1.67	45	**10**	0.35	0.15	10	1.67
21	4	5	52	125	2.40	45	**8**	0.35	0.15	10	1.50
22	4	5	52	135	2.60	45	**6**	0.35	0.15	10	1.40
23	4	5	52	91	1.75	45	16	**0.25**	0.15	10	1.08
24	4	5	52	90	1.73	45	16	**0.5**	0.15	10	1.21
25	4	5	52	73	1.40	45	16	0.35	**0.25**	10	1.33
26	4	5	52	95	1.83	45	16	0.35	**0.35**	10	1.26
27	4	5	52	85	1.64	45	16	0.35	0.15	**12**	1.32

Excess pore pressure ratio in the liquefied ground *U_3*.- The excess pore pressure ratio ***U_3*** refers to the liquefied ground, over a representative area underneath the footing and below the improved crust. To gain insight regarding the variation of U_3, its value has been back-calculated considering the numerically derived values for ***a***, ***U_1***, (and hence ***U_2***) and q_{ult} and the initial values for the friction angles ***$\varphi_{ini1,2}$*** described earlier.

Following a sensitivity analysis on the ***U_3*** dependence on the various problem parameters, it was concluded that the various effects could be collectively represented through a composite problem variable, namely the degraded ultimate bearing capacity $q_{ult.}$ at the end of shaking. This is shown in **Figure 5.24**, where the back-calculated values of ***U_3*** are related to the ultimate bearing capacity ratio q_{ult}/p_a. Observe that all data points form a narrow band fitted by the following average analytical relation:

$$U_3 = C_{U_3}\left(\frac{q_{ult}}{p_\alpha}\right)^{-0.18} \leq 1.00 \qquad (5.26)$$

The average C_{U3} coefficient is equal to 0.86 with a Standard Deviation equal to ±0.03, while the minimum and maximum values are $\mathbf{C_{U3,min}=0.81}$ and $\mathbf{C_{U3,max}=0.95}$.

The accuracy of equation (5.26) is evaluated in **Figure 5.25a** & **b**. Namely, the back-calculated values of U_3 are plotted in **Figure 5.25a** against the analytical predictions, in a one-to one comparison, while the relative prediction error is plotted against the numerically derived ultimate bearing capacity ratio $q_{ult.}^{num}/p_{\alpha}$ in **Figure 5.25b.** It is observed that the scatter of the data points is relatively narrow, and the relative error is less than ±10% (St.Dev. = 4%).

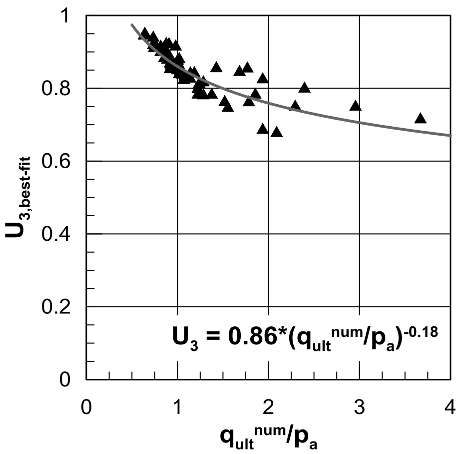

Figure 5.24: Back-calculated values of U_3 plotted against the numerically obtained values of degraded bearing capacity $q_{ult.}^{num}$ normalized against the atmospheric pressure

Σχήμα 5.24: Συσχέτιση των τιμών του U_3 από αντίστροφες αναλύσεις με τις αριθμητικά εκτιμώμενες τιμές της απομειωμένης φέρουσας ικανότητας $q_{ult.}^{num}$ ανοιγμένης προς την ατμοσφαιρική πίεση

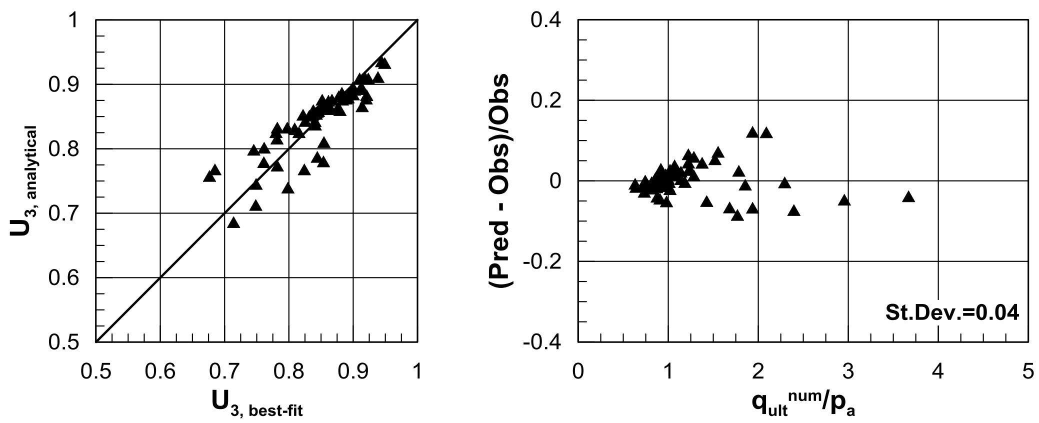

(a) **(b)**

Figure 5.25: (a) One-to-one comparison of analytically predicted versus back-calculated U_3 values (b) Relative error of predicted values against $q_{ult.}^{num}/p_{\alpha}$

Σχήμα 5.25: (a) Σύγκριση αναλυτικών και εκτιμώμενων με αντίστροφες αναλύσεις τιμών του U_3 (b) Σχετικό σφάλμα των εκτιμώμενων τιμών συναρτήσει του $q_{ult.}^{num}/p_{\alpha}$

5.3.3 Analytical computation of q_{ult}^{deg}

Following the analytical definition of the parameters required for the computation of the degraded bearing capacity, the associated relationships will be applied for all parametric numerical analyses in order to evaluate the overall accuracy of the proposed methodology. It is noted in advance that, due to the dependence of $\boldsymbol{U_3}$ on q_{ult} the relevant equations (equations (5.12) and (5.26)*)* are solved concurrently. Two different iterative procedures are used for this purpose, as explained below.

Simplified iterative solution.- The associated analytical expressions are programmed in an Excel spreadsheet and, based on the available input data, all necessary parameters are evaluated. In the sequel, the proposed methodology is solved iteratively, following the Steps outlined below:

Step 1: An initial value for $\boldsymbol{U_{3,i}}$ is assumed and the ultimate bearing capacity $q_{ult.}^{analyt}$ is computed from equation (5.12).

Step 2: The above value of $q_{ult.}^{analyt}$ is introduced to equation (5.26) and a new excess pore pressure ratio $\boldsymbol{U_{3,i+1}}$ is calculated

Step 3: The relative error between the values of $\boldsymbol{U_3}$ obtained in Steps 1 & 2 is calculated as follows:

$$U_{3,rel.err.} = \frac{\left|U_{3,i+1} - U_{3,i}\right|}{U_{3,i}} \tag{5.27}$$

Step 4: If the resulting relative error is greater than 0.001, the average of the computed values of $\boldsymbol{U_3}$ (i.e. $U_{3,i}$ and $U_{3,i+1}$) is derived and Steps 1 to 3 are repeated. The constraint of $U_{3i+2} \leq 1.0$ also applies in the current calculation step.

The iterative procedure is repeated, separately for each parametric numerical analysis, until the relative error becomes less than 0.001.

Automated iterative solution.- To facilitate and speed up the calculation process, the iterative solution may also be performed using the Solver Add-In, which is a built-in tool for Excel spreadsheet computations. The particular application is based on the optimization method of Lagrange multipliers, *"which is a strategy for finding the local maxima or minima of a function subject to equality constraints"*. In its generalized form, the particular optimization method requires two different functions, namely f(x,y) and g(x,y), which are somehow interrelated. For example, the minimization of function f(x,y) may be requested, while function g(x,y) is subject to a specific condition i.e. g(x,y)=c. To satisfy the requested condition, the method is based on deriving the gradients of the two functions, therefore for the application of the specific method the functions f(x,y) and g(x,y) need to have continuous first partial derivatives. In the optimization process a new extra variable (λ), called Lagrange multiplier, is introduced and defined as:

$$\Lambda(x,y,\lambda) = f(x,y) + \lambda\left[g(x,y) - c\right] \tag{5.28}$$

The auxiliary function presented above is solved by adding or subtracting the Lagrange multiplier λ to satisfy the following condition:

$$\nabla_{x,y,\lambda}\Lambda(x,y,\lambda)=0 \tag{5.29}$$

In our case, the solution process follows the steps outlined below:

Step 1: A starting value for U_3 is assumed and the ultimate bearing capacity $q_{ult.}^{U3}$ computed from equation (5.12).

Step 2: Considering the same starting value for U_3 the ultimate bearing capacity $q_{ult.}^{analyt}$ is computed from equation (5.26).

Step 3: The relative error between the two obtained values of $q_{ult.}$ is calculated based on equation (5.30):

$$q_{ult.rel.err.}=\frac{\left|q_{ult.}^{analyt.}-q_{ult.}^{U3}\right|}{q_{ult.}^{analyt.}} \tag{5.30}$$

Step 4: In the sequel, U3 is automatically altered until satisfaction of the requested convergence condition. The convergence criterion is specified by the user and in the particular case is set to $q_{ult.rel.err.}$ = 0.001

Additionally, throughout the iterative procedure U_3 is constrained to be less than or equal to unity, i.e. $U_3 \leq 1.0$.

Evaluation of analytical predictions.- Considering the average values of the C_i coefficients in equations (5.14), (5.15), (5.25), and (5.26) both convergence approaches, described above, were applied for the assessment of excess pore pressure ratio U_3 and the associated post-shaking ultimate bearing capacity $q_{ult}^{analytical}$. Obtained $\mathbf{U_3}$ values with the two approaches turned out to be identical for the majority of the numerical analyses outlined in the Chapter 4. In some cases though, Solver Add-In did not converge to a feasible solution which satisfied the convergence condition dictated in equation (5.30). This occurred for large values of $\mathbf{U_3}$, close to unity, where equation (5.26) does not have a continuous first partial derivative, as required by the Lagrange multiplier method. To deal with this particular inconsistency, it was decided to preserve the Solver Add-In result for relative error values less than 5% and adopt the result from the simplified method in the remaining cases (namely set $\mathbf{U_3}$ equal to unity and obtain a conservative prediction for the ultimate degraded bearing capacity $q_{ult}^{analytical}$).

The resulting analytical predictions for the ultimate degraded bearing capacity, the degraded Factor of Safety, and its inverse value are evaluated in **Figure 5.26.** Additionally, $1/F.S._{deg}^{analytical}$ is plugged into equation (5.6) for the computation and the subsequent evaluation of seismic settlement ratio $\rho_{dyn}^{analytical}/B$. The grey data points in all graphs, correspond to the non-converging cases according to the conditions discussed previously. The left column of figures summarizes the comparison between the analytical predictions against the numerically observed values, while the right column plots summarize the relative error in the prediction of the above quantities in relation to the analytically derived values.

Observe that, despite the caution exercised in calibrating the analytical methodology for the computation of $q_{ult.}$, it becomes strikingly over-conservative for low values of $q_{ult.}$ (< 150 kPa), whereas it is consistently under-conservative for larger $q_{ult.}$values. The above observation has an immediate effect on the derived $F.S._{deg}$, as well as on seismic settlements computation $\rho_{dyn.}$

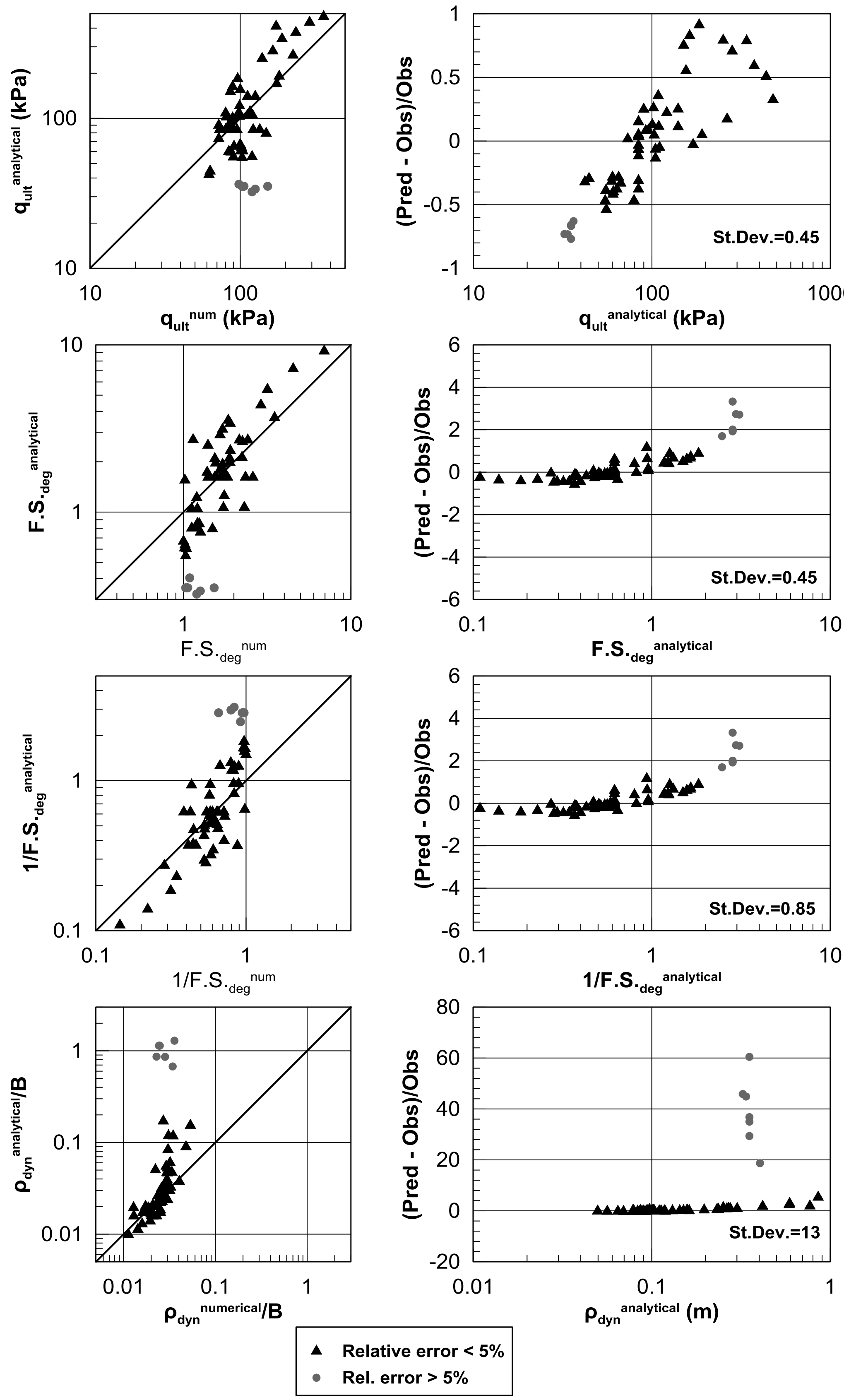

Figure 5.26: Overall evaluation of analytical predictions in terms of q_{ult}, $F.S._{deg}$, $1/F.S._{deg}$ and ρ_{dyn}/B

Σχήμα 5.26: Συνολική αξιολόγηση των αναλυτικών προβλέψεων σε όρους q_{ult}, $F.S._{deg}$, $1/F.S._{deg}$ και ρ_{dyn}/B

5.3.4 Correction of the degraded Factor of Safety

To improve the accuracy of the proposed methodology, the analytically obtained value of $F.S._{deg}$ is corrected, in view of the relative error in predicted q_{ult}, shown in **Figure 5.27**. Namely, the degraded factor of safety obtained analytically, based on the Meyerhof & Hanna failure mechanism is considered as a "bearing capacity index" and is hereafter referred to as $F.S._{deg}^{*}$. In the sequel, the "actual" value of the degraded Factor of Safety $F.S._{deg}$ is re-evaluated by applying the depicted mathematical expressions, each one corresponding to a different level of conservatism. Namely, the equation plotted with the black line corresponds to a best-fit approach, and when solving for the Observed value, the following equation (5.31) results:

$$FS_{deg} = \frac{FS^{*}_{deg}}{0.05 + 0.60\left(FS^{*}_{deg}\right)^{0.85}} > 0.60 \cdot FS^{*}_{deg} \qquad (5.31)$$

The above correction is applied to all analytical predictions and the final outcome is summarized and evaluated in **Figure 5.28**, preserving the layout described in **Figure 5.26**. Evidently, the corrected analytical predictions for the degraded bearing capacity $q_{ult.}$ have been improved, presenting a significantly narrower scatter around the diagonal. Note that the corrected analytical predictions appear to slightly overestimate $q_{ult.}$, nevertheless the obtained relative error has been considerably reduced as proven by the Standard Deviation, which is estimated equal to St.Dev.=0.22. Additionally, the predictions for the degraded Factor of Safety, $F.S._{deg.}$, are in very good agreement with the numerical observations. Indeed, the specific parameter no longer receives values less than unity, indicating post-shaking failure of the foundation, which did not occur in any of the performed numerical analyses. Moreover, the obtained relative error is decreased compared to the initial prediction, ranging roughly between ±40% with a reduced Standard Deviation equal to St.Dev.=0.22.

The previous satisfactory agreement is preserved with respect to the inverse $F.S._{deg.}$, and the predicted dynamic settlements. Indeed, the $\rho_{dyn}^{analyt.}/B$ ratio compares consistently well with the associated numerical predictions. Namely, the data points appear evenly distributed around the diagonal, with a minor tendency to underestimate dynamic settlements in the higher range of ρ_{dyn}/B. Moreover, as a result of the appropriate estimation of $1/F.S._{deg.}$, dynamic settlements are satisfactorily predicted by ±22%, as dictated by the standard deviation in the relative error.

Conservative (Upper bound) predictions.- The previous approach, provided the best-fit evaluation of the degraded factor of safety $F.S._{deg.}^{analytical}$ and the associated seismic settlements ρ_{dyn}. Taking into account the complexity of the problem analyzed herein, and the associated uncertainties in the proposed soil-foundation model, equation (5.32), also plotted in **Figure 5.27** with the grey line, provides a reasonable upper bound (conservative) prediction for the degraded factor of safety:

$$FS_{deg} = \frac{FS^{*}_{deg}}{0.20 + 0.60\left(FS^{*}_{deg}\right)^{0.85}} > 0.55 \cdot FS^{*}_{deg} \tag{5.32}$$

The conservative analytical predictions according to equation (5.32) are presented in **Figure 5.29**, following the same layout as in **Figure 5.26** and **Figure 5.28**. It is now observed that the analytical methodology overall underestimates the degraded bearing capacity $q_{ult.}$(kPa) throughout the examined range of $q_{ult.}$, with only few exceptions. The calculated relative error is reduced and appears to be restrained between -50% and +20%, with a Standard Deviation equal to St. Dev. = 0.19. Additionally, the degraded Factor of Safety $F.S._{deg}$ also appears to be underestimated in most cases, as opposed to the best-fit solution, whereas the obtained relative error is also reduced with a Standard Deviation equal to St. Dev. = 0.19.

The above observation is not verified in the case of the inverse of $F.S._{deg.}$, which appears slightly overestimated, with the associated relative error ranging between -20% and +50% with a higher Standard Deviation equal to St. Dev. = 0.29, compared to the best-fit solution. This has an immediate impact on the obtained dynamic settlements, ρ_{dyn}, which present a clear tendency for overprediction in the majority of cases. This is also evident in the obtained relative error. Indeed, standard deviation of relative error has increased from St. Dev.=0.22 to St. Dev.=0.54.

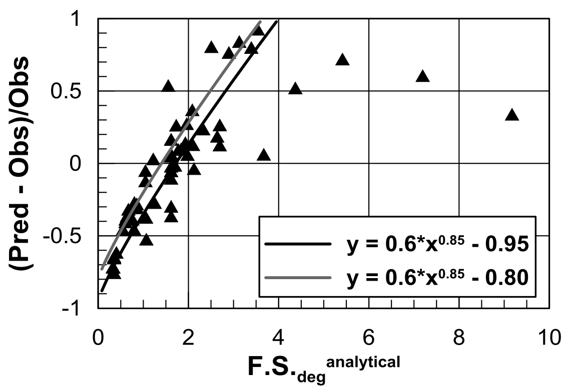

Figure 5.27: Correction factors applied upon the analytically computed degraded factor of safety $F.S._{deg}$

Σχήμα 5.27: Διορθωτικοί συντελεστές που χρησιμοποιήθηκαν στις αναλυτικά εκτιμώμενες τιμές του απομειωμένου συντελεστή ασφαλείας $F.S._{deg}$

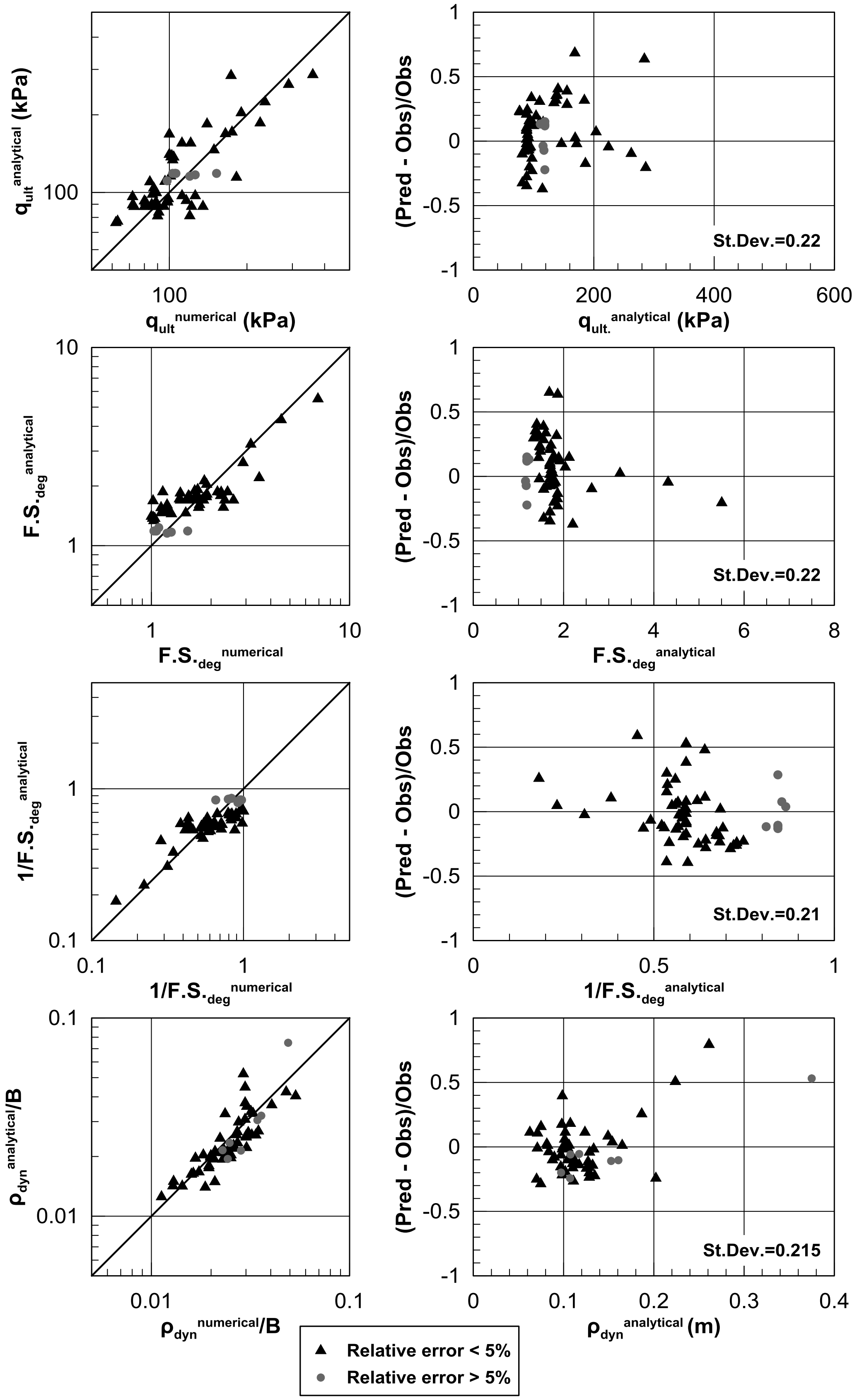

Figure 5.28: Overall evaluation of analytical predictions after the F.S.$_{deg}$ correction in terms of q_{ult}, F.S.$_{deg}$, 1/F.S.$_{deg}$ and ρ_{dyn}/B

Σχήμα 5.28: Συνολική αξιολόγηση των αναλυτικών προβλέψεων, μετά τη διόρθωση του F.S.$_{deg}$, σε όρους q_{ult}, F.S.$_{deg}$, 1/F.S.$_{deg}$ και ρ_{dyn}/B

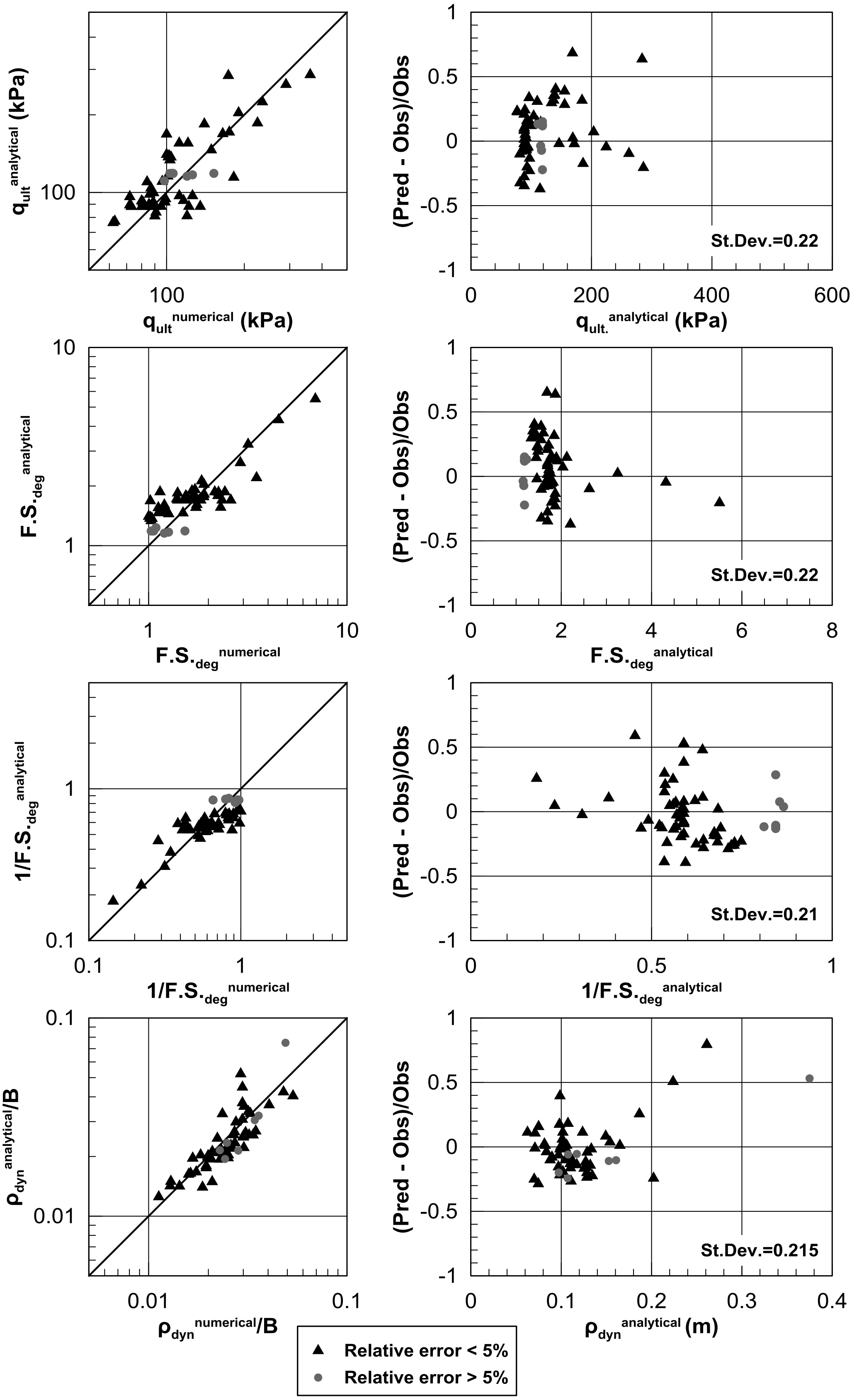

Figure 5.29: Overall evaluation of analytical predictions after the upper bound $F.S._{deg}$ correction in terms of q_{ult}, $F.S._{deg}$, $1/F.S._{deg}$ and ρ_{dyn}/B

Σχήμα 5.29: Συνολική αξιολόγηση των αναλυτικών προβλέψεων, μετά τη διόρθωση του άνω ορίου του $F.S._{deg}$, σε όρους q_{ult}, $F.S._{deg}$, $1/F.S._{deg}$ και ρ_{dyn}/B

6

Effect of Ground Improvement Dimensions

6.1 Introduction

The analytical methodology developed in the previous chapter is applicable to "infinitely" extending two-layered soil profiles, hence it does not incorporate the influence of the lateral extend of the performed improvement (L_{imp}). The specific parameter is necessary in the design of the required improvement scheme, and is generally determined in accordance to the ground improvement method.

In the following, the available guidelines are summarized for determining the soil improvement area when using the ground compaction method. Note that, in all guidelines, the depth of improvement extends down "*to the deepest part of the liquefiable soil layer*", following standard practice procedures. Furthermore they do not provide quantitative means for evaluating the foundation performance in the case of a smaller or a larger area is improved.

Japanese Fire Defense Agency (1978).- The JFDA (1974) guidelines for oil tanks recommend that the soil improvement area, in excess to the footing width, also denoted as SL, equals two thirds of the improvement depth and must be within 5m < SL < 10m, as illustrated in **Figure 6.1**.

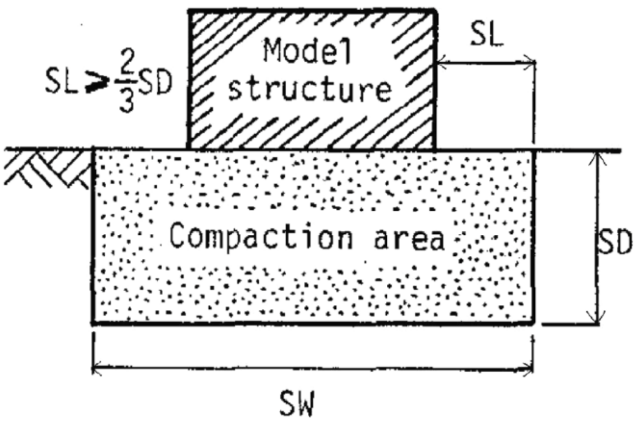

Figure 6.1: Design of soil improvement area of tank foundation (JFDA, 1978)
Σχήμα 6.1: Εύρος βελτίωσης εδάφους γύρω από τη θεμελίωση (JFDA, 1978)

Tsuchida et al. (1976).- recommends that the improvement width around a slightly embedded structure is correlated to the friction angle (φ) of the soil as presented in **Figure 6.2**. Specifically, α_1 is the passive failure angle and α_2 the active failure angle, also defined in the figure. SD is the depth of improvement, which, as stated earlier, equals the total thickness of the liquefiable layer.

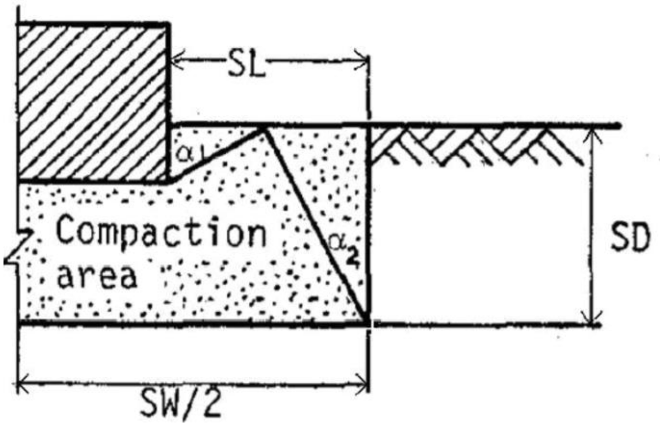

α_1: Passive failure angle
$= 45^o + \varphi/2$
α_2: Active failure angle
$= 45^o - \varphi/2$

Figure 6.2: Specification of lateral extent of improvement based on the friction angle of the soil (Tsuchida et al., 1976)

Σχήμα 6.2: Μέθοδος προσδιορισμού εύρους βελτίωσης με βάση τη γωνία τριβής του εδάφους (Tsuchida et al., 1976)

PHRI (1997).- The Port and Harbour Research Institute (1997) widely refers to the work performed by Iai (1991) covering the required improvement extend for various types of structures. In the specific study, the excess pore pressure ratio r_u appears to be the controlling design parameter. Namely, based on undrained cyclic loading laboratory test results, excess pore pressure ratio values r_u below 0.5 induced practically negligible loss of strength in the sand specimen. On the contrary, for r_u values above 0.5, the cyclic shearing led to significant shear strength loss in the soil and should be accounted for in the design.

According to Iai (1991), the shear strength of the liquefied un-improved soil should be considered totally lost, especially for loose to medium sands. Moreover, they indicated that the area in which r_u exceeds 0.5 is adequately described by the area ACD in **Figure 6.3**. Therefore, the particular area does not contribute to the bearing capacity of the soil, which depends only on the shear resistance mobilized along the surface EFG. Hence, given the depth of improvement, the extent of the improvement area is associated to the above surface, which provides the necessary shear resistance to ensure the stability of the foundation. Moreover, pressures from the liquefied sand may also be included in the stability analysis of the structure. The specific static pressure corresponds to an earth pressure coefficient K_o=1 after subtracting the dynamic earth pressures. The particular pressures are applied upon the GG′ surface.

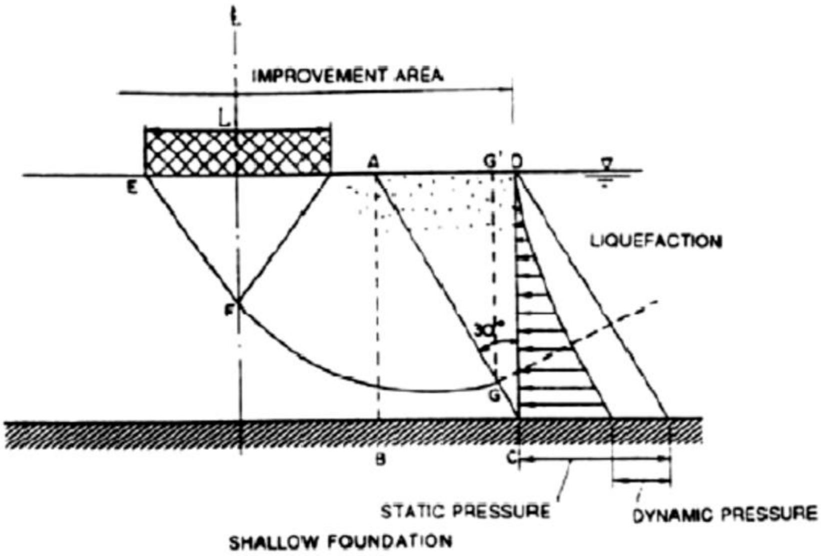

Figure 6.3: Schematic figure to determine improvement area against liquefaction for a shallow foundation (Iai 1991)

Σχήμα 6.3: Σχηματικό διάγραμμα για τον προσδιορισμό του εύρους βελτίωσης επιφανειακής θεμελίωσης έναντι ρευστοποίησης (Iai 1991)

Based on the above, it appears that there are relatively few experimental studies that examine the effect of the improvement width on the seismic response of shallow foundations, so that the limits, given by regulations, define a simple extend for common applications. Moreover, all guidelines assume the treatment of the entire thickness of the liquefiable soil, which may potentially lead to over-conservative and costly improvement solutions.

In the above context, the influence of the lateral extend of the applied improvement is numerically investigated through a separate set of analyses, which are presented in section 6.2 below. Namely, the effect of the improvement width (L_{imp}) on the dynamic settlements (ρ_{dyn}) and the degraded Factor of Safety ($F.S._{deg}$) is quantified with reference to the results for "infinite" ground improvement (i.e. $L_{imp} \rightarrow \infty$), discussed extensively in the previous chapter. Particular modifications are further compared to the existing guidelines mentioned earlier and an updated set of design charts is developed for application.

6.2 Description of Numerical Analyses

The plan of parametric analyses is summarized in **Table 6.1** and consists of 12 different sets, which exhibit different soil, excitation and geometric characteristics. Each set examines the effect of an individual parameter, the value of which appears in the second column of the table. The remaining problem parameters are given the values of the reference analysis, namely: q = 52kPa, $D_{r,o}$ = 45%, Z_{liq} = 16m, H_{imp} = 4, B = 5m, a_{max} = 0.15g, N = 5, and T = 0.35s. Moreover, in each set, the infinitely extending improved layer is considered the reference analysis, and subsequently, the width of the improved layer (L_{imp}) is progressively reduced down to nearly the width B of the footing itself. The different values of L_{imp} normalized against the footing width B, are listed in the last column of the table. **Figure 6.4** presents the basic symbol definitions associated with the geometry of the examined problem.

The assumptions of the numerical methodology, as well as the three distinct phases of the loading sequence, have been thoroughly explained in Chapter 3, and are maintained in the present numerical investigation. It is observed that the L_{imp}/B ratio systematically receives values greater than unity. The particular observation is attributed to numerical reasons and particularly to the simulation approach of the shallow footing. As it is mentioned in Chapter 3, the numerical simulation of the bearing pressure q of the shallow footing is performed through applying vertical velocity at specific grid points. This velocity varies linearly from the value at the last grid point upon which it is applied, to zero at the adjacent grid point. Hence, half the width of the adjacent zones should be added to the actual footing width. On the other hand, soil properties are assigned to zones, implying that the width of the improved zone is always going to be at least equal to the number of zones upon which the bearing stresses are applied, further increased by two, one at each side of the footing.

Table 6.1: Overview of numerical analyses
Πίνακας 6.1: Σύνοψη αριθμητικών αναλύσεων

Case No.	Examined Parameter	L_{imp}/B
1	q= 52Kpa	1.2, 2, 5.4, 7.8, 10.2, 12, 13.2, 14.8, 17.2, 19.6, 21
2	B=3m	1.3, 4, 7.3, 12.33, 17,21
3	D_{ro}= 55%	1.2, 2, 5.4, 7.8, 10.2, 12, 13.2, 14.8, 17.2, 19.6, 21
4	Z_{liq} = 8m	1.2, 2, 5.4, 10.2, 13.2, 14.8, 17.2, 19.6
5	Z_{liq} = 12m	1.2, 2, 5.4, 10.2, 13.2, 14.8, 17.2, 19.6, 21
6	a_{max}= 0.30g	1.2, 2, 5.4, 7.8, 10.2, 12, 13.2, 14.8, 17.2, 19.6, 21
7	N= 5	1.2, 2, 5.4, 10.2, 13.2, 14.8, 17.2, 19.6, 21
8	T= 0.50sec	1.2, 2, 5.4, 7.8, 10.2, 12, 13.2, 14.8, 17.2, 19.6, 21
9	H_{imp}=6m	1.2, 2, 5.4, 10.2, 13.2, 14.8, 21
10	H_{imp}= 8m	1.2,2, 5, 5.4, 9.8, 13.4, 15.2, 20, 24.8
11	H_{imp}=6m (a_{max}=0.30g)	1.2, 2, 5.4, 10.2, 13.2, 14.8, 21
12	H_{imp}= 8m (a_{max}=0.30g)	1.2, 2, 5, 5.4, 9.8, 13.4, 15.2, 20, 24.8

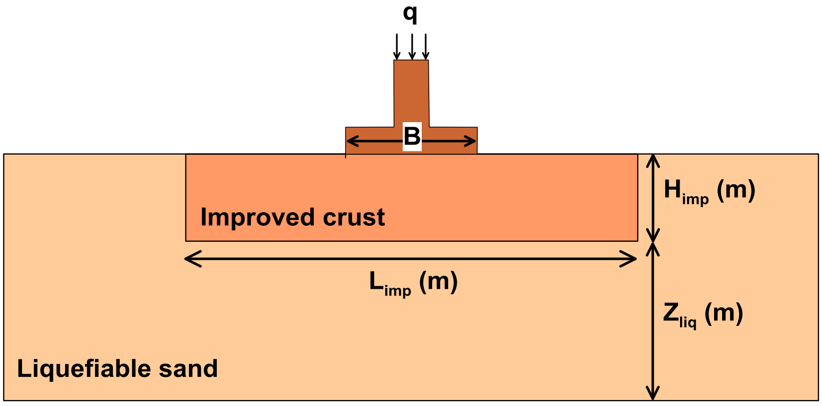

Figure 6.4: Definition of basic symbols
Σχήμα 6.4: Ορισμός βασικών παραμέτρων

6.3 Effect of L_{imp} on earthquake-induced foundation settlements ρ_{dyn}

To visualize the effect of the lateral extent of the improved zone (L_{imp}) on the accumulation of dynamic settlements (ρ_{dyn}), **Figure 6.5** summarizes the obtained dynamic settlements (ρ_{dyn}) from the entire group of analyses, plotted against L_{imp}/B ratio. In each set of analyses the obtained dynamic settlements appear normalized against the corresponding value for conditions of "infinite" improvement (ρ_{dyn}^{inf}). The black color corresponds to the baseline analysis (case No. 1 in **Table 6.1**), while the data sets examining the effect of the different problem parameters are plotted with different tints of grey.

Based on **Figure 6.5**, it is concluded that, among the examined parameters, only the thickness of the improved zone (H_{imp}) is significantly influencing the accumulation of dynamic settlements for different L_{imp} configurations. All other parameters have a relatively minor effect, which may be initially neglected in the formulation of the corresponding analytical expression for ρ_{dyn}. Hence, the effects of the width (L_{imp}) and depth (H_{imp}) of the improved zone are independently examined for the formulation of a suitable analytical expression as described in the following sections. To produce a dimensionless expression, both parameters (L_{imp} and H_{imp}) are normalized hereafter against the footing width B.

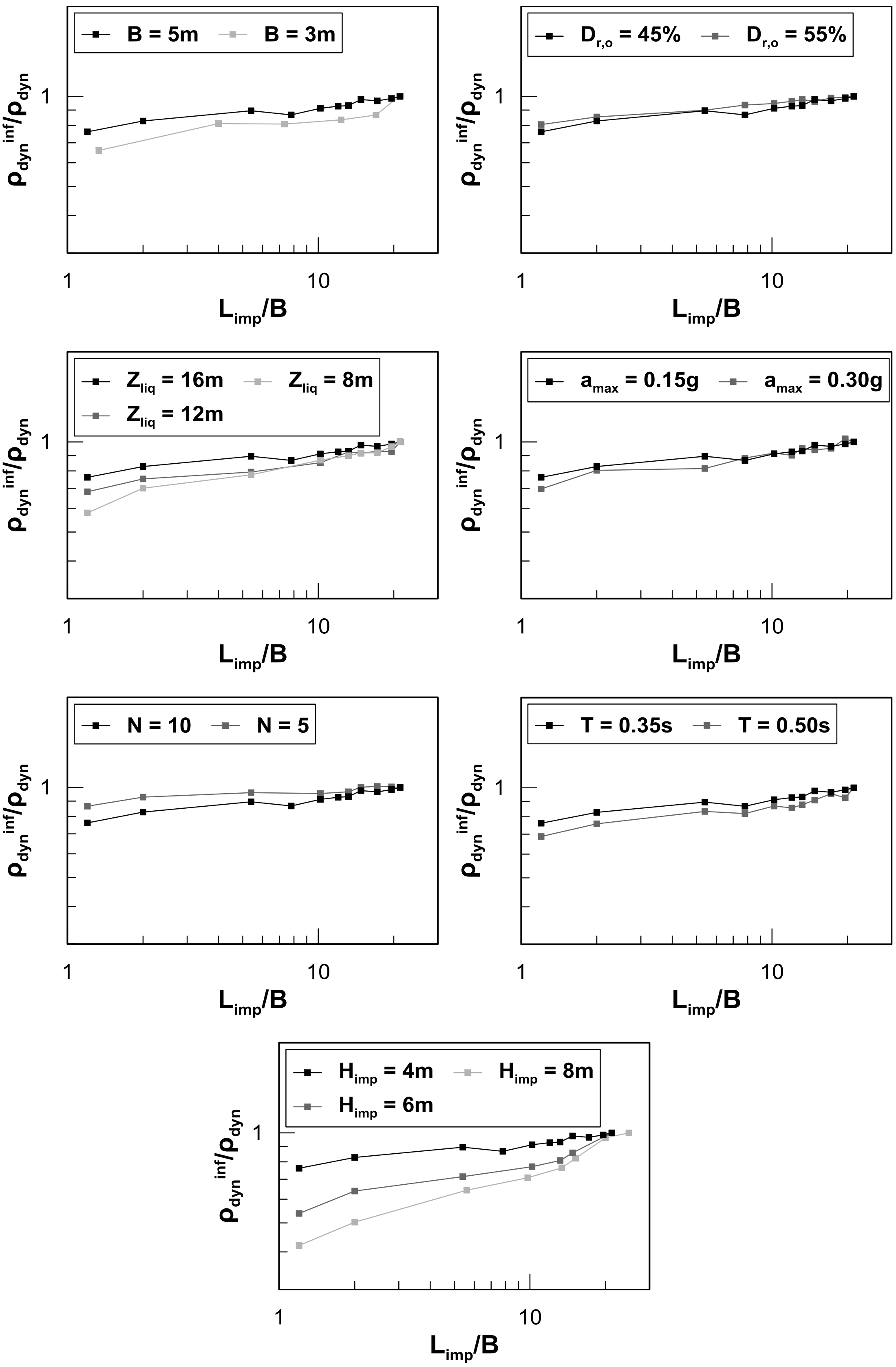

Figure 6.5: Effect of different problem parameters on dynamic settlements ρ_{dyn} normalized against the "infinite" value ($\rho_{dyn,inf}$) versus L_{imp}/B

Σχήμα 6.5: Επίδραση των διάφορων παραμέτρων στις δυναμικές καθιζήσεις ρ_{dyn} ανοιγμένες ως προς τις καθιζήσεις για "άπειρη βελτίωση" ($\rho_{dyn,inf}$) σε σχέση με το L_{imp}/B

Effect of L_{imp}/B.- Based on **Figure 6.5**, the trend of the inverse of the normalized dynamic settlement ($\rho_{dyn}^{inf}/\rho_{dyn}$) ranges between zero and unity as the ratio of L_{imp}/B ranges between zero to "infinite" improvement. The particular trend is mathematically expressed below:

$$\frac{\rho_{dyn}^{inf}}{\rho_{dyn}} = 1 - \exp\left[-C_1\left(\frac{L_{imp}}{B}\right)^{C_2}\right] \tag{6.1}$$

To visualize the effect of L_{imp}/B on the ratio of dynamic settlements $\rho_{dyn}^{inf}/\rho_{dyn}$, Equation (6.1) is re-arranged, as described in equation (6.2), and plotted in a logarithmic axis-system as illustrated in **Figure 6.6**.

$$-\ln\left(1 - \frac{\rho_{dyn}^{inf}}{\rho_{dyn}}\right) = C_1\left(\frac{L_{imp}}{B}\right)^{C_2} \tag{6.2}$$

The solid lines correspond to sets of analyses with different H_{imp}/B values with all other parameters preserved constant, namely Cases 1, 2, 3, 9 and 10 of **Table 6.1**. It is observed that each data set is satisfactorily described through a power function, also plotted with the thicker lines. This essentially verifies the validity of the selected formulation. With regard to coefficient C_1, it equals $-\ln(1-\rho_{dyn,inf}/\rho_{dyn})$ when the width of improvement equals the footing width (L_{imp}/B = 1), exhibiting a wide range of variation depending on the ever-current H_{imp}/B ratio. Coefficient C_2, corresponds to the inclination of the thick lines in **Figure 6.6**, displaying a narrower range of variation for different H_{imp}/B values. Based on the particular observation C_2 is taken as the average of the eight different values obtained from the fitting curves and it is set equal to C_2 = 0.30.

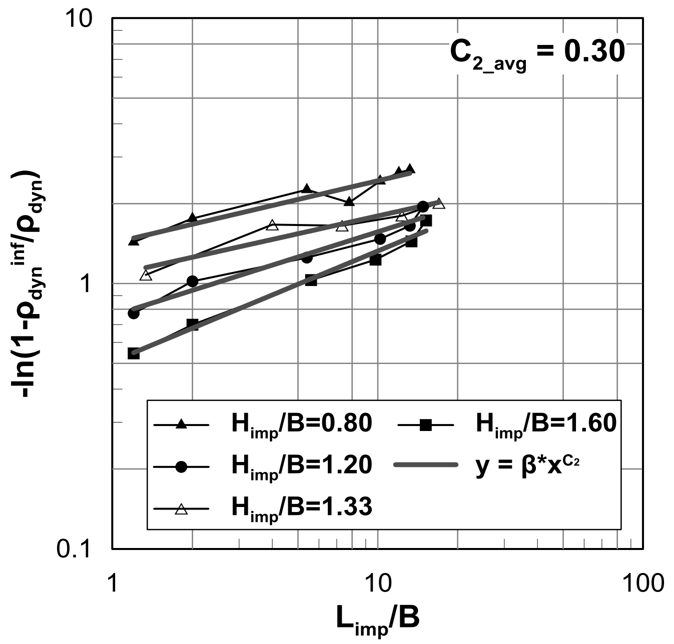

Figure 6.6: Effect of L_{imp}/B on the normalized dynamic settlements $\rho_{dyn,inf}/\rho_{dyn}$ for five different H_{imp}/B values – evaluation of coefficient C_2

Σχήμα 6.6: Επίδραση του L_{imp}/B στις ανοιγμένες δυναμικές καθιζήσεις $\rho_{dyn,inf}/\rho_{dyn}$ για πέντε διαφορετικές τιμές του λόγου H_{imp}/B – αξιολόγηση του συντελεστή C_2

Effect of H_{imp}/B.- To further investigate the observation that coefficient C_1 depends on the ever-current H_{imp}/B ratio, the effect of the thickness of the improved crust, H_{imp}, on the ratio of $\rho_{dyn}^{inf}/\rho_{dyn}$ is appraised in **Figure 6.7** for different L_{imp}/B values. Indeed, the increase of the earthquake-induced settlements ρ_{dyn}, becomes more prominent and the corresponding ratio of $\rho_{dyn}^{inf}/\rho_{dyn}$ decreases significantly with increasing thickness of the improved zone H_{imp}. Nevertheless, the particular observation does not imply that more settlements will accumulate, for thicker improved zones and decreasing L_{imp}/B values. As thoroughly exhibited in Chapter 5, under "infinite" improvement conditions the selection of a thicker improved zone results in drastically reduced settlements, ρ_{dyn}^{inf}. Therefore, the ratio of $\rho_{dyn}^{inf}/\rho_{dyn}$ may be lower for increasing H_{imp}/B values but it is still possible to obtain the same or even a lower amount of settlement, for greater H_{imp} values, depending on the selected L_{imp}/B value.

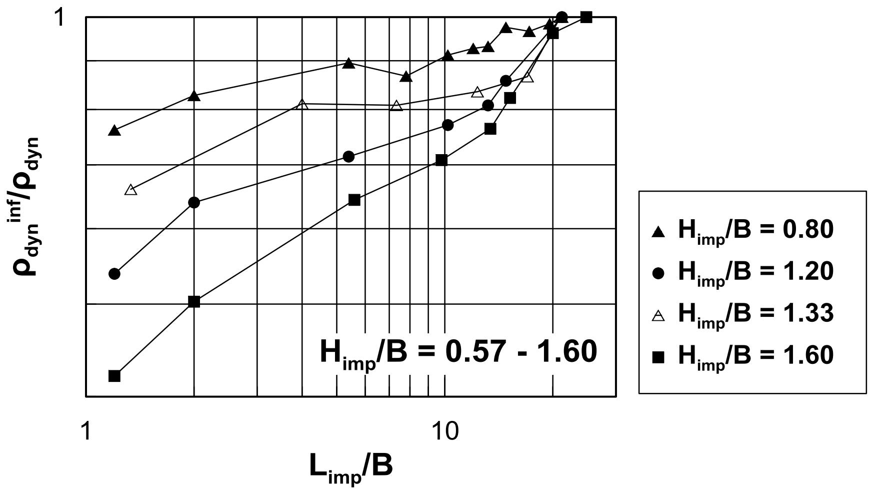

Figure 6.7: Effect of H_{imp}/B on the normalized dynamic settlements $\rho_{dyn,inf}/\rho_{dyn}$ for different L_{imp}/B values

Σχήμα 6.7: Επίδραση του H_{imp}/B στις ανοιγμένες δυναμικές καθιζήσεις $\rho_{dyn,inf}/\rho_{dyn}$ για διαφορετικές τιμές του λόγου L_{imp}/B

Based on the above, the effect of the crust thickness ratio H_{imp}/B, is going to be incorporated in the final analytical expression and specifically in the formulation of coefficient C_1. To achieve this, equation (6.2) is solved for coefficient C_1, after setting coefficient C_2 equal to 0.30:

$$C_1 = \frac{\ln\left[1-\left(\rho_{dyn}^{inf}/\rho_{dyn}\right)\right]}{\left(L_{imp}/B\right)^{0.30}} \qquad (6.3)$$

The different C_1 values obtained from equation (6.3) for each L_{imp}/B value are plotted with regard to the specific H_{imp}/B case in **Figure 6.8** with the black symbols. The grey rhombuses correspond to the average C_1 values obtained from the different data sets. The power function drawn among the above symbols renders the following adopted analytical expression:

$$C_1 = 0.944\left(\frac{H_{imp}}{B}\right)^{-1} \tag{6.4}$$

Hence, the final analytical expression for the conservative lower-bound estimation of the dynamic settlements for different widths of improvement is provided through equation (6.5) as follows:

$$\frac{\rho_{dyn}^{inf}}{\rho_{dyn}} = 1-\exp\left[-0.944\left(\frac{H_{imp}}{B}\right)^{-1}\left(\frac{L_{imp}}{B}\right)^{0.30}\right] \tag{6.5}$$

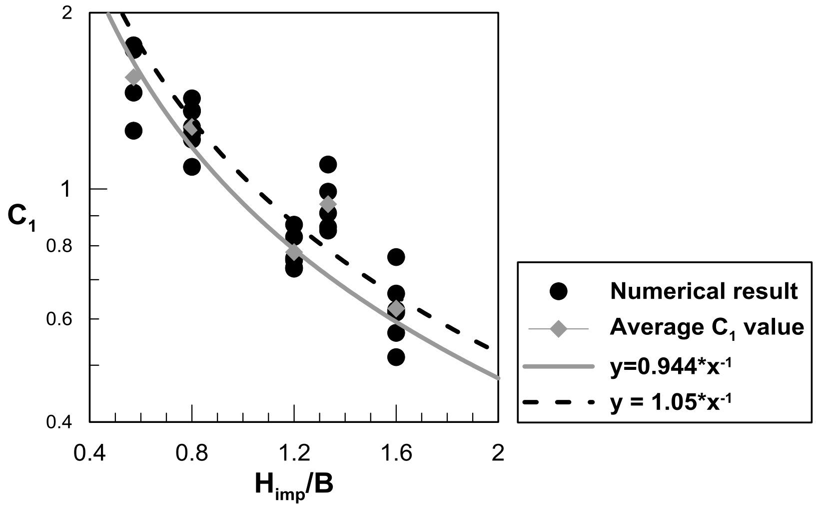

Figure 6.8: Effect of H_{imp}/B on coefficient C_1
Σχήμα 6.8: Επίδραση του H_{imp}/B στο συντελεστή C_1

Effect of other problem parameters.- So far, the proposed analytical expression incorporates only the effect of the geometry of the improved area, namely the thickness H_{imp} and lateral width of the improved zone L_{imp}. The effect of the excluded parameters may be accounted for by appropriately modifying the constant factor 0.944. Namely, equation (6.5) is re-arranged as presented below:

$$Y = \frac{-\ln\left(1-\frac{\rho_{dyn}^{inf}}{\rho_{dyn}}\right)}{\left(\frac{H_{imp}}{B}\right)^{-1}\left(\frac{L_{imp}}{B}\right)^{0.30}} \tag{6.6}$$

and subsequently, Y is estimated for all the numerical analyses having L_{imp}/B ratio less than or equal to $L_{imp}/B \leq 15$. Typical results from the analyses so far excluded from the statistical processing 0are summarized in **Figure 6.9.** The fitting curve in each figure corresponds to the average Y values obtained for each set of analyses. Based on **Figure 6.8**, the average value of Y, turned out equal to Y=1.05 and the final analytical expression is modified accordingly:

$$\frac{\rho_{dyn}^{inf}}{\rho_{dyn}} = 1-\exp\left[-1.05\left(\frac{H_{imp}}{B}\right)^{-1}\left(\frac{L_{imp}}{B}\right)^{0.30}\right] \tag{6.7}$$

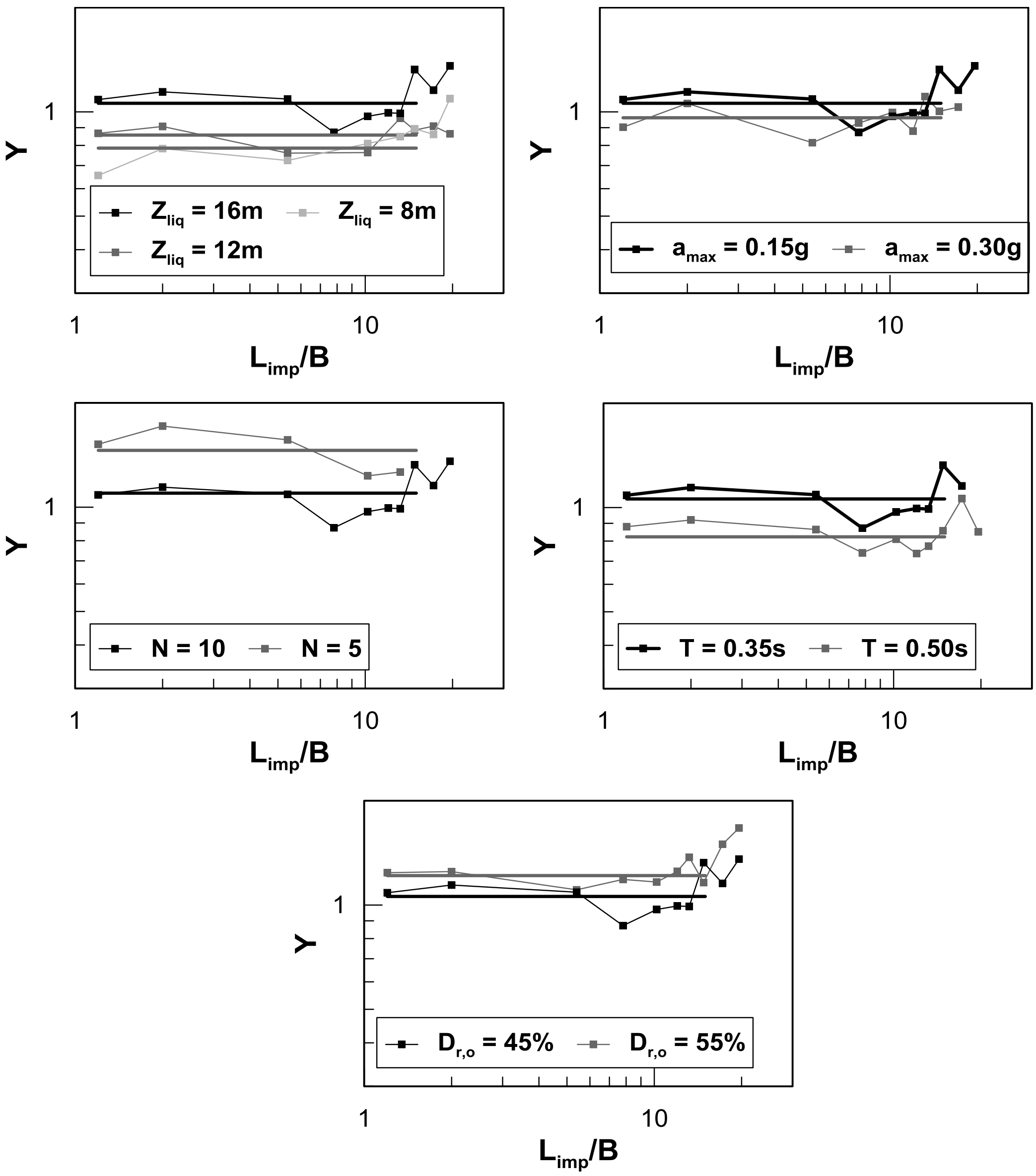

Figure 6.9: Effect of Z_{liq}(m), α_{max}(g), T(sec), N, $D_{r,o}$(%) on the ratio of $-\ln(\rho_{dyn,inf}/\rho_{dyn})$ normalized against $(H_{imp}/B)^{-1}(L_{imp}/B)^{-0.30}$, versus different widths of improvement (L_{imp}) normalized against the footing width B

Σχήμα 6.9: Επίδραση των Z_{liq}(m), α_{max}(g), T(sec), N, $D_{r,o}$(%) στο λόγο $-\ln(\rho_{dyn,inf}/\rho_{dyn})$ ανοιγμένο προς το $(H_{imp}/B)^{-1}(L_{imp}/B)^{-0.30}$, για διαφορετικά πλάτη βελτίωσης (L_{imp}) ανοιγμένα προς το πλάτος θεμελίου B

Evaluation of analytical expression.- The analytical predictions obtained from equation (6.7) are compared against the numerical results in terms of the inverse of the normalized settlement, i.e. $(\rho_{dyn}^{inf}/\rho_{dyn})$ in **Figure 6.10a**. The relative error between numerical and analytically obtained values of the above ratio is also plotted with regard to the numerical results in **Figure 6.10b**. The black symbols correspond to the numerical results used in the formulation of the proposed analytical relation (i.e $L_{imp}/B \leq 15$), whereas, the white symbols represent the excluded numerical analyses with L_{imp}/B ratio greater than $L_{imp}/B > 15$. It is observed that the proposed analytical expression predicts with relatively good accuracy the inverse of the seismically induced settlement for "limited" improvement widths, normalized against the corresponding value for "infinite" improvement conditions. The specific satisfactory behavior is observed even for the excluded cases, which do not deviate significantly from the main group of datapoints. Particularly, the proposed analytical expression under-predicts the specific $\rho_{dyn}^{inf}/\rho_{dyn}$ values by approximately 20%, which essentially corresponds to the maximum obtained relative error. The latter ranges between ±20% with a standard deviation equal to St. Dev.=0.10.

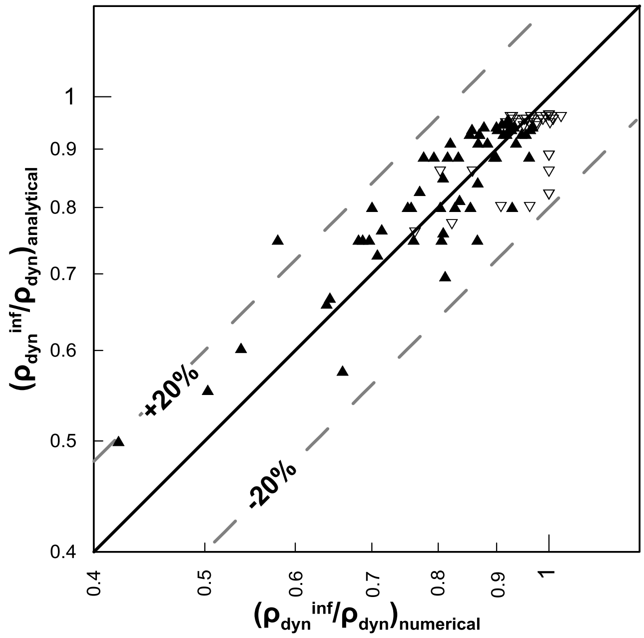

(a)

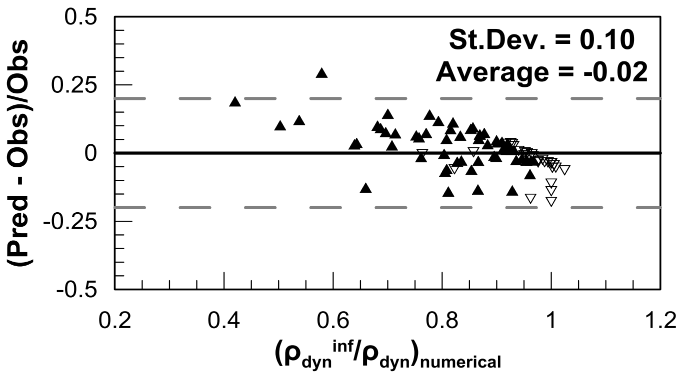

(b)

Figure 6.10: (a) Evaluation of the proposed analytical relation with regard to the ratio of $\rho_{dyn}^{inf}/\rho_{dyn}$ for limited lateral improvement, on a one-to-one basis, (b) Obtained relative error plotted against the numerically derived ratio of $\rho_{dyn}^{inf}/\rho_{dyn}$

Σχήμα 6.10: (a) Αξιολόγηση της προτεινόμενης αναλυτικής εξίσωσης σε όρους $\rho_{dyn}^{inf}/\rho_{dyn}$ για περιορισμένο πλάτος βελτίωσης – σύγκριση ένα-προς-ένα, (b) Σχετικό σφάλμα συναρτήσει της αριθμητικά εκτιμώμενης τιμής του $\rho_{dyn}^{inf}/\rho_{dyn}$

The accuracy of the proposed analytical relation is further verified from **Figure 6.11a & b**, in terms of the obtained settlements for given extent of improvement L_{imp}, preserving the same format considering the color of the used symbols. The specific values of ρ_{dyn}, as well as the associated relative error, are calculated based on the numerical values of $\rho_{dyn,}^{inf}$ and equation (6.7). Hence, **Figure 6.8a** allows the evaluation of the proposed relation, independently of the introduced error stemming from the analytical expression used in the evaluation of ρ_{dyn}^{inf}, presented in Chapter 5. Also, based on **Figure 6.8b**, the particular relative error ranges between ±20% and exhibits a standard deviation equal to St. Dev.=0.7.

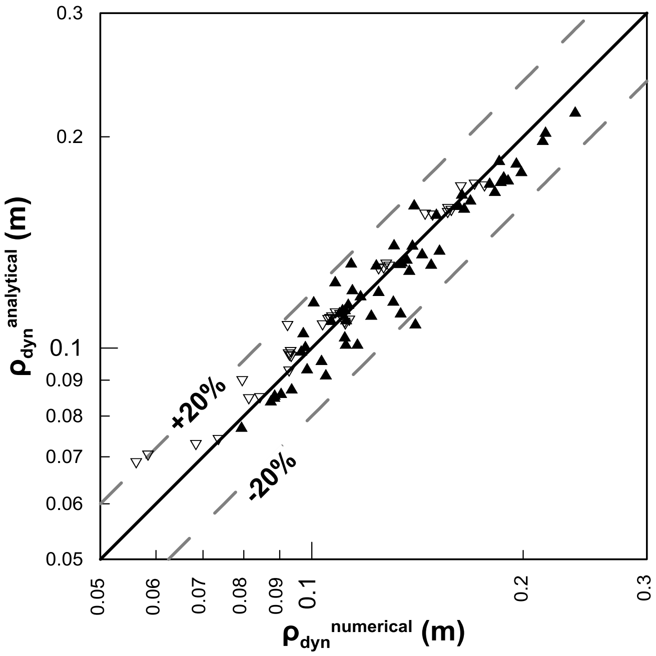

(a)

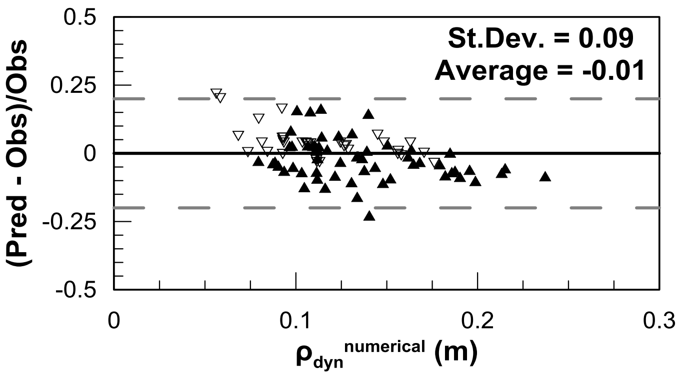

(b)

Figure 6.11: (a) Evaluation of the proposed analytical relation with regard to the obtained value of dynamic settlement ρ_{dyn}, on a one-to-one basis (b) Obtained relative error plotted against the numerically derived value of ρ_{dyn}

Σχήμα 6.11: (a) Αξιολόγηση της προτεινόμενης αναλυτικής εξίσωσης σε όρους ρ_{dyn} για περιορισμένο πλάτος βελτίωσης – σύγκριση ένα-προς-ένα, (b) Σχετικό σφάλμα συναρτήσει της αριθμητικά εκτιμώμενης τιμής του ρ_{dyn}

In the sequel, equation (6.7) is applied for different improvement geometries in order to produce a practical design chart. The outcome is presented in **Figure 6.12** in which both dimensions, i.e. lateral extent (L_{imp}) and thickness (H_{imp}) of the improved zone are expressed as a portion of the footing width (B). Namely, the thickness of the improved crust (H_{imp}) ranges from 0.5B to 2.00B, whereas the lateral extent (L_{imp}) starts from 30B and narrows down to 1B.

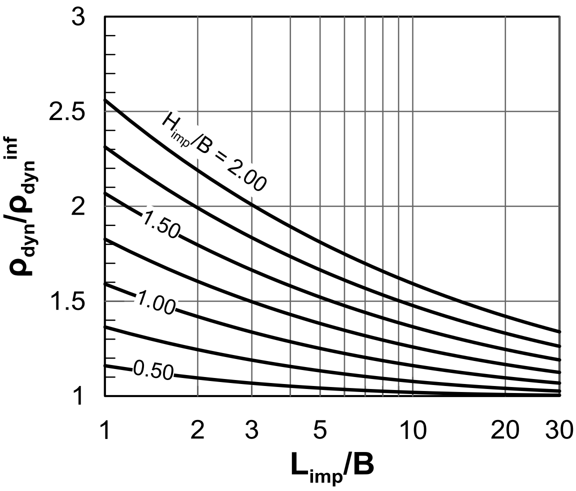

Figure 6.12: Design chart for the evaluation of the amount of dynamic settlement ρ_{dyn}, given the geometry of the improvement scheme, described through the width (L_{imp}) and thickness (H_{imp}) of the crust, normalized against the footing width (B)

Σχήμα 6.12: Διάγραμμα σχεδιασμού για την εκτίμηση της δυναμικής καθίζησης ρ_{dyn} για δεδομένο εύρος βελτίωσης, πλάτους L_{imp} και πάχους H_{imp}, κανονικοποιημένα προς το πλάτος θεμελίου (B)

There are two worthy observations in the particular figure. The first is that dynamic settlements decrease steadily with increasing width of the improved zone. In other words, there is not a certain width in terms of L_{imp}/B ratio, beyond which dynamic settlements stabilize to their minimum value. The second observation is that a fairly extensive improvement may be required in order to get the total benefit of ground improvement. For instance, in the common case of H_{imp}/B = 1.00 – 1.50, a L_{imp}/B ratio equal to L_{imp}/B = 20 – 40 is required to reduce settlement values that are only 10% higher, compared to the theoretical low for infinite improvement.

6.4 Effect of L_{imp} on the post-shaking degraded Factor of Safety $F.S._{deg}$.

The effect of the improvement width ratio L_{imp}/B, on the post-shaking degraded factor of safety, $F.S._{deg}$, is depicted in **Figure 6.13**, for all the examined cases. It is observed that, opposite to the uniformity of the data regarding the dynamic settlements, the scatter in the obtained values of $FS._{deg}$ is considerably larger.

Regarding the numerical aspect of the problem, it is mentioned that the last stage of the loading sequence, i.e. the evaluation of the degraded bearing capacity $q_{ult.}$(kPa), is performed based on an analysis under static conditions. Also, according to Itasca (2005), in FLAC, a static solution is reached by artificially damping the relevant equations of motion, when the rate of change in kinetic energy in a model approaches a negligible value,. Hence, even though the magnitude of the applied velocity upon the corresponding grid-points of the footing is very small, numerical instabilities are still likely to occur, even in areas of the grid far away from the footing. Different approaches to locate and resolve the particular issue were investigated, with minor effects on the obtained results. Moreover, the consideration of applying an even smaller magnitude of vertical velocity was abandoned, given the required excessive computational time, which would prohibit the execution of a broad parametric investigation. It is indicatively mentioned that the post-shaking static analysis required on average 4 days for the "infinite" improvement scheme and 2 days for different L_{imp}/B values (with FLAC v5.0).

Due to the considerable scatter of numerical predictions, the development of a suitable analytical expression for evaluating $F.S._{deg}$ followed a different approach compared to the procedure for the dynamic settlements. More specifically, settlements in equation (6.7) were expressed in terms of the degraded factor of safety, for infinite and for limited ground improvement, using the general equation (5.6) derived in Chapter 5. In the sequel, the resulting relationship was solved for the $F.S._{deg}/F.S._{deg}^{inf}$ ratio and used to express the desired effects of ground improvement dimensions. Note that, for this approach to be valid, it is essential that the ρ_{dyn} – $F.S._{deg}$ relationship of Chapter 5 is unique, i.e. it applies regardless of ground improvement dimensions. Hence, this issue was given priority to the following investigation. The data sets exhibiting a widespread scatter, i.e. Cases 6, 10, 11 & 12, as well individual data points with $F.S._{deg}$ less than $F.S._{deg} < 1.15$ were considered unstable analyses and hence were excluded from the statistical evaluation. The particular cases are marked with white symbols in **Figure 6.13.** Overall, out of the 96 performed numerical analyses only 48 were used for the statistical processing presented in the subsequent paragraphs.

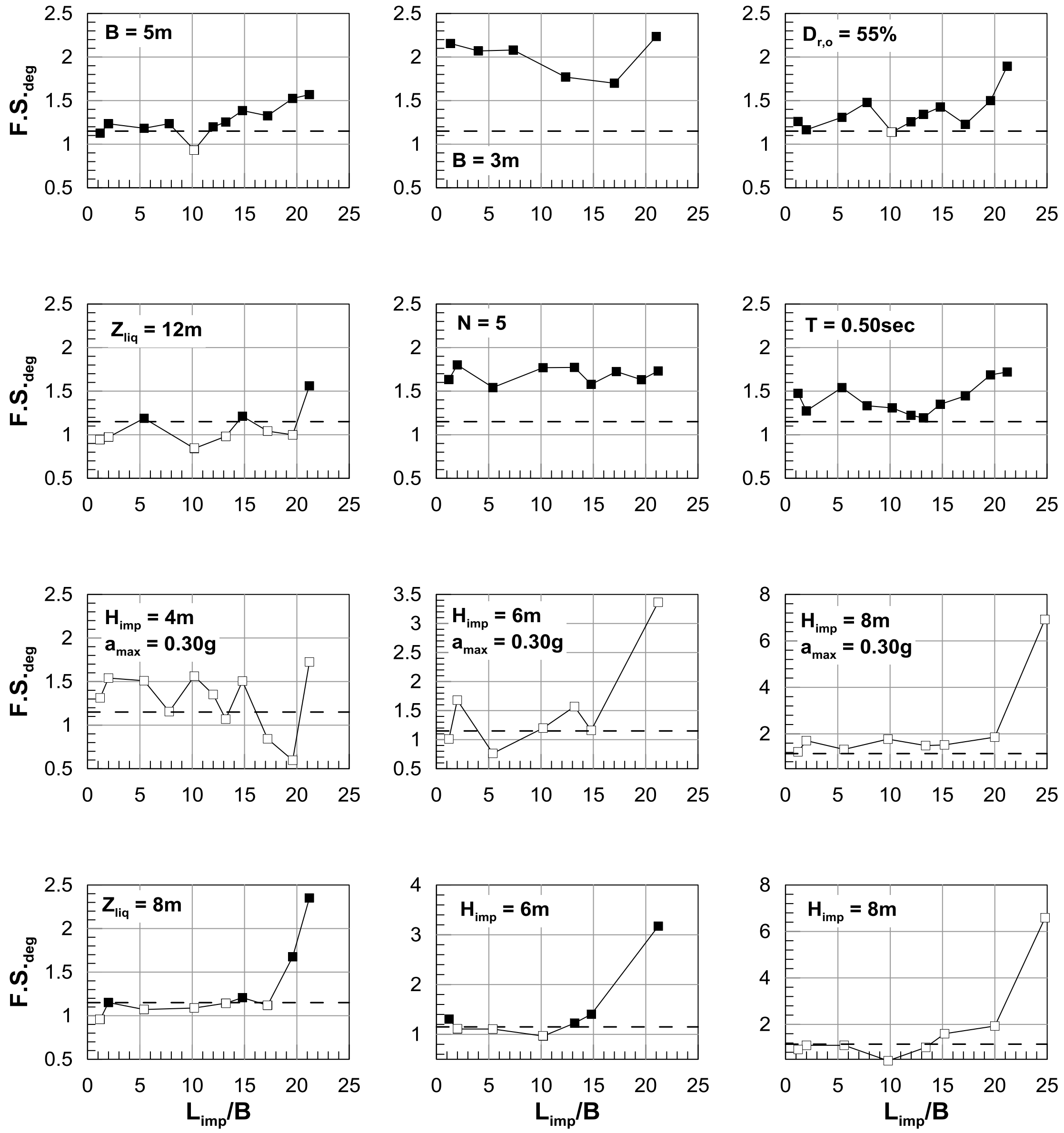

Figure 6.13: Summary of numerical results of degraded Factor of Safety and excluded "toxic" cases (white symbols)

Σχήμα 6.13: Σύνοψη αριθμητικών αποτελεσμάτων του απομειωμένου συντελεστή ασφαλείας και απορριπτόμενες "τοξικές" περιπτώσεις (λευκά σύμβολα)

The ρ_{dyn} - $F.S._{deg}$ relation.- In Chapter 5, dynamic settlements are expressed as a function of the degraded Factor of Safety $F.S._{deg}$. In the current paragraph it is examined whether the above relation can be extended to describe the dynamic settlement accumulation in the case of "limited" improvement width. Hence, equation (5.6) is applied for stable numerical analyses with $F.S._{deg}^{num} > 1.15$, considering the associated numerically derived degraded factor of Safety $F.S._{deg}$. The dynamic settlements obtained in this way are summarized in **Figure 6.14**. The numerical results and analytical predictions are plotted in the gray and black symbols respectively. Based on the above figure it is concluded that the two data sets are in fairly good agreement.

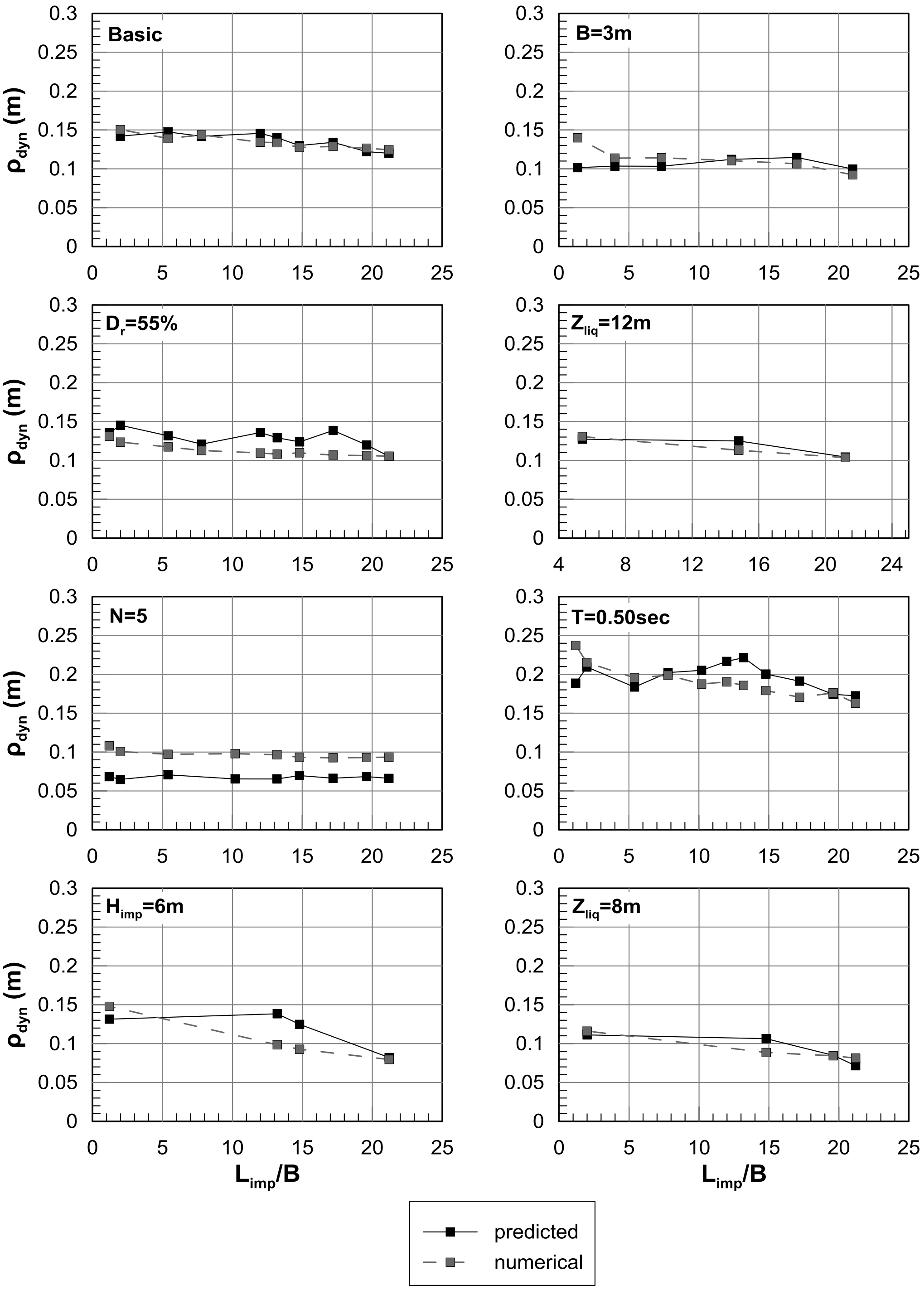

Figure 6.14: Comparison between numerically derived dynamic settlements (grey symbols) and analytical predictions based on the analytical expression for conditions of "infinite" improvement (black symbols)

Σχήμα 6.14: Σύγκριση αριθμητικά εκτιμώμενων δυναμικών καθιζήσεων (γκρι) και αναλυτικών προβλέψεων με βάση την αναλυτική σχέση για συνθήκες "άπειρης" βελτίωσης (μαύρο)

The above satisfactory agreement is better appraised in **Figure 6.15a**, presenting the analytically predicted dynamic settlements against the numerical results on a one-to-one basis. **Figure 6.15b** provides the relative error plotted against the analytically computed dynamic settlements from which it is concluded that the relative error of the analytical predictions ranges between ±25% and the standard deviation of relative error is equal to St. Dev. = 0.19.

Based on the above, it is concluded that the proposed correlation between dynamic settlements and degraded factor of safety for "infinite" ground improvement apples to cases of finite improvement dimensions as well.

Analytical expression for the degraded factor of safety.- Given the applicability of equation (5.6) for cases of "limited" improvement, it is used in the formulation of an analytical expression for the computation of the associated degraded factor of safety. Particularly, equation (5.6) is applied once for conditions of "infinite" improvement and secondly for "limited" improvement width. In the sequel, the resulting equations are divided against each other, leading to the following analytical expression for the dynamic settlement ratio:

$$\frac{\rho_{dyn}^{inf}}{\rho_{dyn}}=\left(\frac{FS_{deg}}{FS_{dyn}^{inf}}\right)^{-0.45}\frac{\left(FS_{deg}^{inf}\right)^{4.5}+0.25\left(\frac{FS_{deg}}{FS_{deg}^{inf}}\right)^{4.5}}{\left(FS_{deg}^{inf}\right)^{4.5}+0.25} \qquad (6.8)$$

In the sequel, the combination of equations (6.7) and (6.8), and the rearrangement of the expression with regard to the ratio of $F.S._{deg}/F.S._{deg}^{inf}$, results to the following non-linear equation for its computation:

$$\left(\frac{FS_{deg}}{FS_{deg}^{inf}}\right)^{-0.45}=\left\{1-\exp\left[-1.05\left(\frac{H_{imp}}{B}\right)^{-1}\left(\frac{L_{imp}}{B}\right)^{0.30}\right]\right\}\frac{\left(FS_{deg}^{inf}\right)^{4.5}+0.25\left(\frac{FS_{deg}}{FS_{deg}^{inf}}\right)^{4.5}}{\left(FS_{deg}^{inf}\right)^{4.5}+0.25} \qquad (6.9)$$

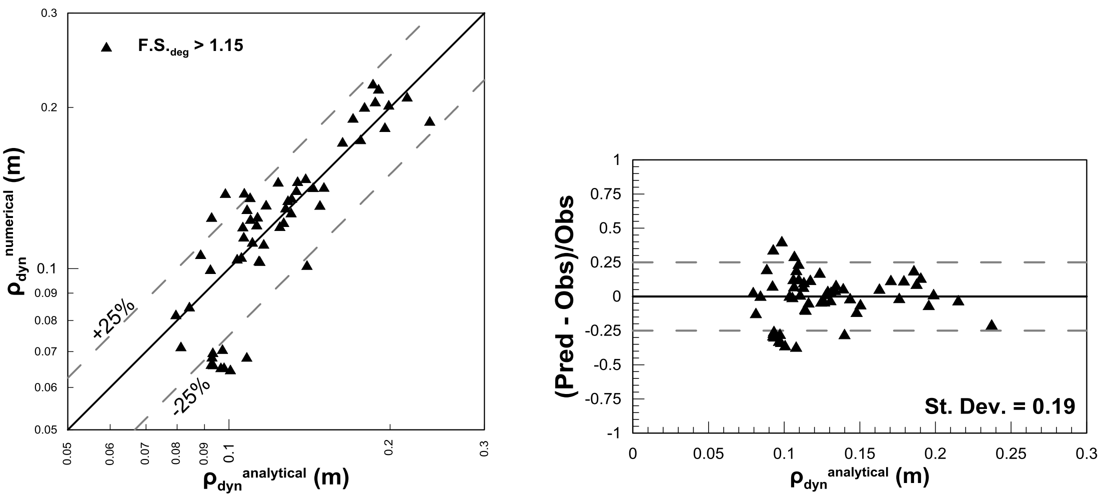

(a) **(b)**

Figure 6.15: Evaluation of the analytical relation for conditions of «infinite» improvement: (a) one-to-one basis (b) Relative error

Σχήμα 6.15: Αξιολόγηση της αναλυτικής λύσης για «άπειρη» βελτίωση: (α) ένα-προς-ένα σύγκριση (β) Σχετικό σφάλμα

The above analytical expression correlates the geometric features of the improved area, (thickness H_{imp} and width L_{imp}) to the degraded factor of safety for "infinite" improvement conditions $F.S._{deg}^{inf}$, as well as to the ratio of the degraded factor of safety for "limited" over that for "infinite" improvement conditions, i.e. $F.S._{deg}/F.S._{deg}^{inf}$. Note that the $F.S._{deg}/F.S._{deg}^{inf}$ ratio appears in both sides of equation (6.9), meaning that an iterative solution is required.

The accuracy of equation (6.9) is appraised in **Figure 6.16a & b**, in terms of the ratio of the degraded factor of safety for "limited" over the corresponding value for "infinite" improvement. In **Figure 6.16a** the comparison is performed against the numerical predictions on a one-to-one basis, and refers to the numerically stable analyses. Note that the numerically derived value of $F.S._{deg}^{inf}$ is plugged into the ratio of the analytical predictions, so that the efficiency of the current analytical expression is evaluated independently of the generated error due to the analytical expression proposed for the computation of $F.S._{deg}^{inf}$ presented in Chapter 5. The relative error is plotted against the analytical predictions in **Figure 6.16b**. Based on the above figures it is observed that, with minor exceptions, equation (6.9) predicts with substantial accuracy the degraded factor of safety $F.S._{deg}$, with a deviation ranging between ±25%. Relative error of the predictions ranges between ±25% with a standard deviation equal to St. Dev. = 0.25.

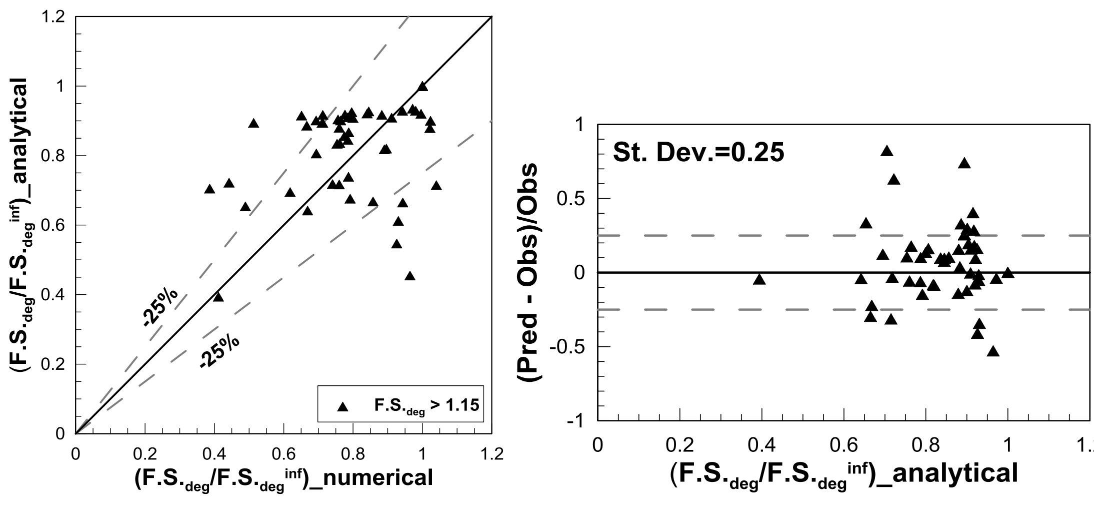

(a) **(b)**

Figure 6.16: (a) Evaluation of the analytically obtained ratio of $F.S._{deg}/F.S._{deg}^{inf}$ with regard to the numerically derived ratio, on a one-to-one basis (b) Obtained relative error plotted against the numerically derived ratio of $F.S._{deg}/F,.S._{deg}^{inf}$

Σχήμα 6.16: (a) Σύγκριση της αναλυτικής πρόβλεψης του λόγου $F.S._{deg}/F.S._{deg}^{inf}$ με τις αριθμητικές εκτιμήσεις (b) Σχετικό σφάλμα συναρτήσει του αριθμητικά εκτιμώμενου λόγου $F.S._{deg}/F.S._{deg}^{inf}$

To facilitate the use of the complex analytical expression presented above, equation (6.9) is solved for four different values of H_{imp}/B (= 0.5, 1.0, 1.5, 2.0) and three different values of the degraded factor of safety for "infinite" improvement conditions, namely $F.S._{deg}^{inf}$ = 1.0, 2.0 & 3.0. The outcome is presented in the form of design charts in **Figure 6.17**. It is interesting to note that for increasing values of crust thickness, the influence of the degraded factor of safety for "infinite" improvement conditions, $F.S._{deg}^{inf}$, becomes more pronounced, disclosing the sensitivity of the results at thicker improvement schemes. Moreover it turns out that the effect of $F.S._{deg}^{inf}$ is not excessive, even for the cases of very thick crust, i.e. $H_{imp}/B = 2.0$. Hence, in view of the overall uncertainties in determining $F.S._{deg}$, discussed in previous sections, it is permissible to overlook the effect of $F.S._{deg}^{inf}$ in equation (6.9), assuming an average value of $F.S._{deg}^{inf} = 2.0$. The resulting simplifications are discussed next.

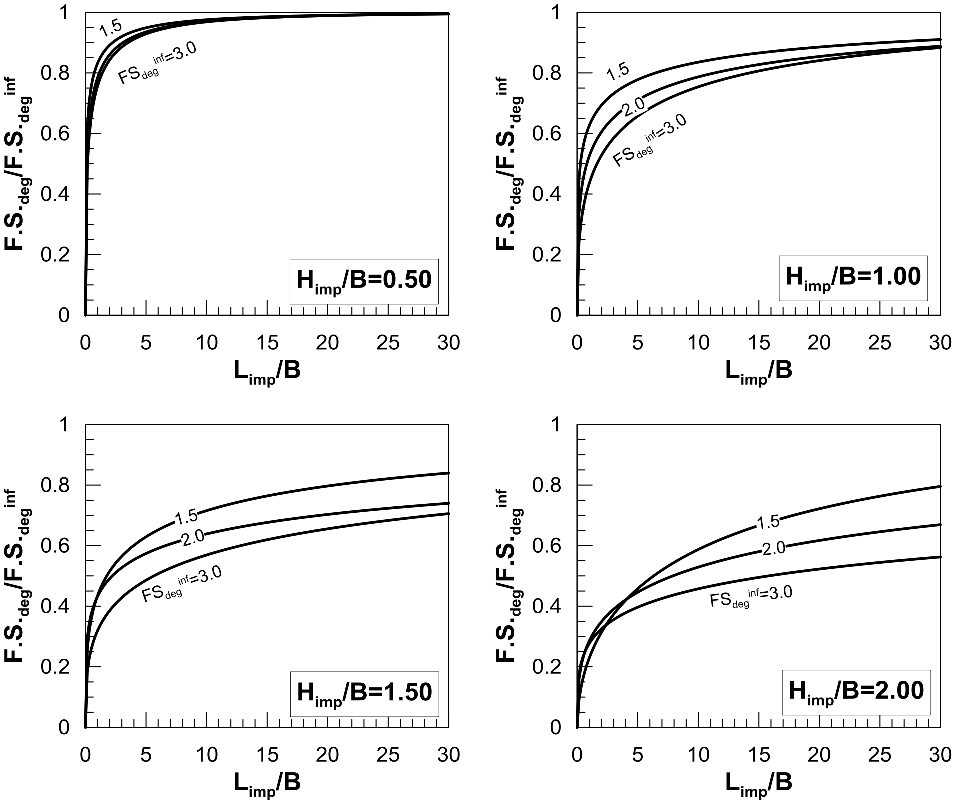

Figure 6.17: Design charts relating the $F.S._{deg}/F.S._{deg}^{inf}$ ratio to the normalized - against the footing width B - lateral width of improvement (L_{imp}/B) for four distinct H_{imp}/B values

Σχήμα 6.17: Διαγράμματα σχεδιασμού του λόγου $F.S._{deg}/F.S._{deg}^{inf}$ συναρτήσει του ανοιγμένου πλάτους βελτίωσης (L_{imp}/B) για τέσσερις διακριτές τιμές του H_{imp}/B

Simplified analytical expression.- Given the drawbacks in the use of equation (6.9), in the present paragraph a simplified analytical expression is formulated, which enables the direct evaluation of the degraded factor of safety $F.S._{deg}$ for "limited" improvement conditions. In its generalized form, this simplified relation is described in the form of equation (6.10):

$$\frac{FS_{deg}}{FS_{deg}^{inf}} = 1 - \exp\left[-C_3\left(\frac{L_{imp}}{B}\right)^{C_4}\right] \tag{6.10}$$

where coefficients C_3 and C_4 will have to be appropriately specified.

To facilitate the evaluation of coefficients C_3 and C_4 the above expression is transformed into equation (6.11):

$$-\ln\left(1-\frac{FS_{deg}}{FS_{deg}^{inf}}\right)=C_3\left(\frac{L_{imp}}{B}\right)^{C_4} \tag{6.11}$$

The cases included in the statistical processing, exhibit a degraded factor of safety under conditions of "infinite" improvement, on average, equal to two. Hence, coefficients C_3 and C_4 are calculated based on equation (6.11), setting $F.S._{deg}^{inf}$ equal to two and different H_{imp}/B ratios, i.e. H_{imp}/B = 0.5, 1.0, 1.5, 2.0. The resulting curves are summarized in **Figure 6.18** plotted against the lateral width of improvement, L_{imp}, normalized against the footing width B, in a double logarithmic axis system.

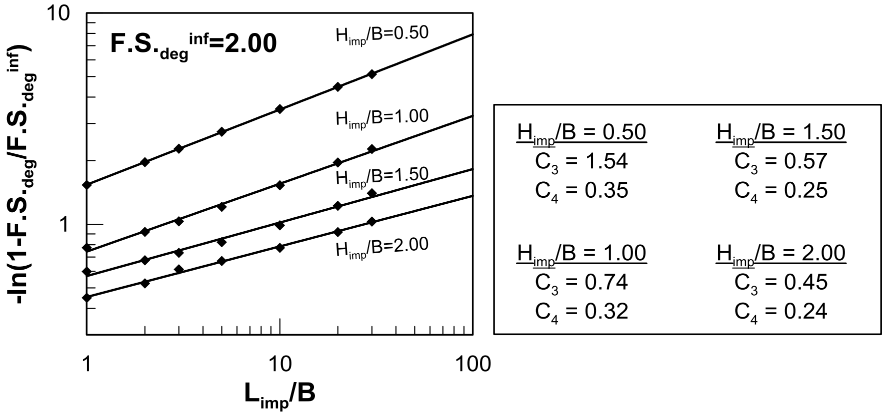

Figure 6.18: Evaluation of coefficients C_3 and C_4 for four distinct values of H_{imp}/B
Σχήμα 6.18: Αξιολόγηση των συντελεστών C_3 και C_4 για τέσσερις διακριτές τιμές του H_{imp}/B

Coefficient C_4.- Given the form of the resulting curves, coefficient C_4 corresponds to the inclination of each one of them, which is independent of the L_{imp}/B ratio and may be considered constant and, at an average, equal to **C_4 = 0.29**.

Coefficient C_3.- It corresponds to the value of $-\ln(F.S._{deg}/F.S._{deg}^{inf})$ for L_{imp}/B equal to unity and it turns out that it depends on the thickness of the improved zone, H_{imp}, normalized against the footing width B. Substituting C_4 with the previously specified value and rearranging equation (6.11), C_3 can be evaluated as follows:

$$C_3=\frac{-\ln\left(1-\frac{FS_{deg}}{FS_{deg}^{inf}}\right)}{\left(\frac{L_{imp}}{B}\right)^{0.29}} \tag{6.12}$$

The application of equation (6.12) for different values of L_{imp}/B (= 1, 2, 3, 5, 10, 20, 30) and the four different H_{imp}/B ratios mentioned earlier, leads to the different values of C_3 plotted in **Figure 6.19** with regard to H_{imp}/B. The power function drawn amongst the presented data points is described by equation (6.13) and is hereafter going to be used for the evaluation of C_3:

$$C_3 = 0.82\left(\frac{H_{imp}}{B}\right)^{-1.03} \tag{6.13}$$

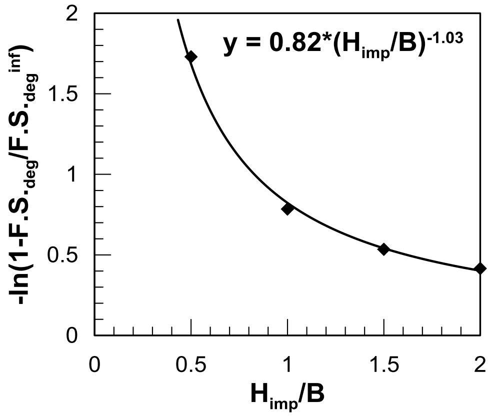

Figure 6.19: Dependence of coefficient C_3 on the considered H_{imp}/B range
Σχήμα 6.19: Συσχέτιση του συντελεστή C_3 με το εύρος τιμών του H_{imp}/B

In the above context, the simplified expression for evaluating $F.S._{deg}$ for "limited" improvement width is transformed as follows:

$$\frac{FS_{deg}}{FS_{deg}^{inf}} = 1 - \exp\left[-0.82\left(\frac{H_{imp}}{B}\right)^{-1.03}\left(\frac{L_{imp}}{B}\right)^{0.29}\right] \tag{6.14}$$

Note that equation (6.14) is formulated considering a degraded factor of safety for "infinite" improvement width equal to $F.S._{deg}^{inf}$ = 2.0 and applies over a specific range of H_{imp}/B values, namely H_{imp}/B = 0.5 – 2.0. **Figure 6.20a** presents the comparison between the obtained analytical predictions and the numerical results, exhibiting $F.S._{deg}^{inf}$ values within a slightly wider range, i.e. $F.S._{deg}^{inf}$ = 1.5 – 2.5. It is thus concluded that, equation (6.14) can be applied with substantial accuracy for a slightly wider range of $F.S._{deg}^{inf}$. The obtained relative error, plotted against the analytical predictions, is presented in **Figure 6.20b**, from which it is concluded that it ranges between ±25% with a standard deviation equal to St. Dev. = 0.23.

Given the predictive efficiency of the equation (6.14), the particular process is repeated for $F.S._{deg}^{inf}$ = 3.0 & 4.0. The resulting analytical expressions are provided below in the form of equations (6.15) and (6.16) respectively:

$$\frac{FS_{deg}}{FS_{deg}^{inf}} = 1 - \exp\left[-0.64\left(\frac{H_{imp}}{B}\right)^{-1.30}\left(\frac{L_{imp}}{B}\right)^{0.34}\right] \tag{6.15}$$

$$\frac{FS_{deg}}{FS_{deg}^{inf}} = 1 - \exp\left[-0.56\left(\frac{H_{imp}}{B}\right)^{-1.30}\left(\frac{L_{imp}}{B}\right)^{0.38}\right] \tag{6.16}$$

To facilitate the use of the simplified relations provided earlier, equations (6.14), (6.15) and (6.16) are solved for seven (7) different values of H_{imp}/B, i.e. 0.5, 0.75, 1.00, 1.25, 1.50, 1.75, 2.00 and a lateral width of improvement ranging from 30B down to

1B. The outcome of the above process is a set of suitable and handy design charts presented in **Figure 6.21**.

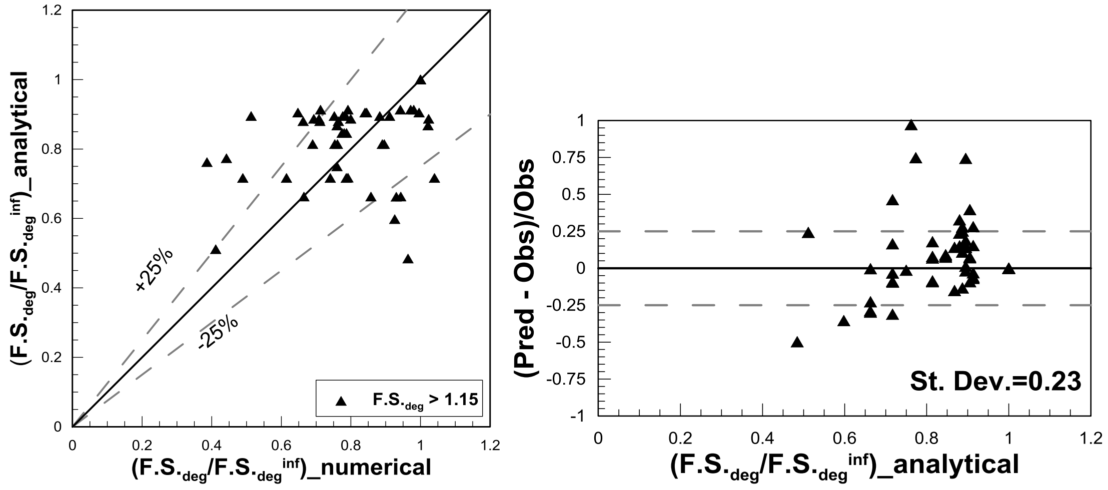

(a) **(b)**

Figure 6.20: Evaluation of the analytical methodology for $F.S._{deg}/F,.S._{deg}^{inf}$: (a) one-to-one comparison (b) Relative error

Σχήμα 6.20: Αξιολόγηση αναλυτικής μεθοδολογίας του λόγου $F.S._{deg}/F.S._{deg}^{inf}$: (α) Ένα-προς-ένα σύγκριση (β) Σχετικό σφάλμα.

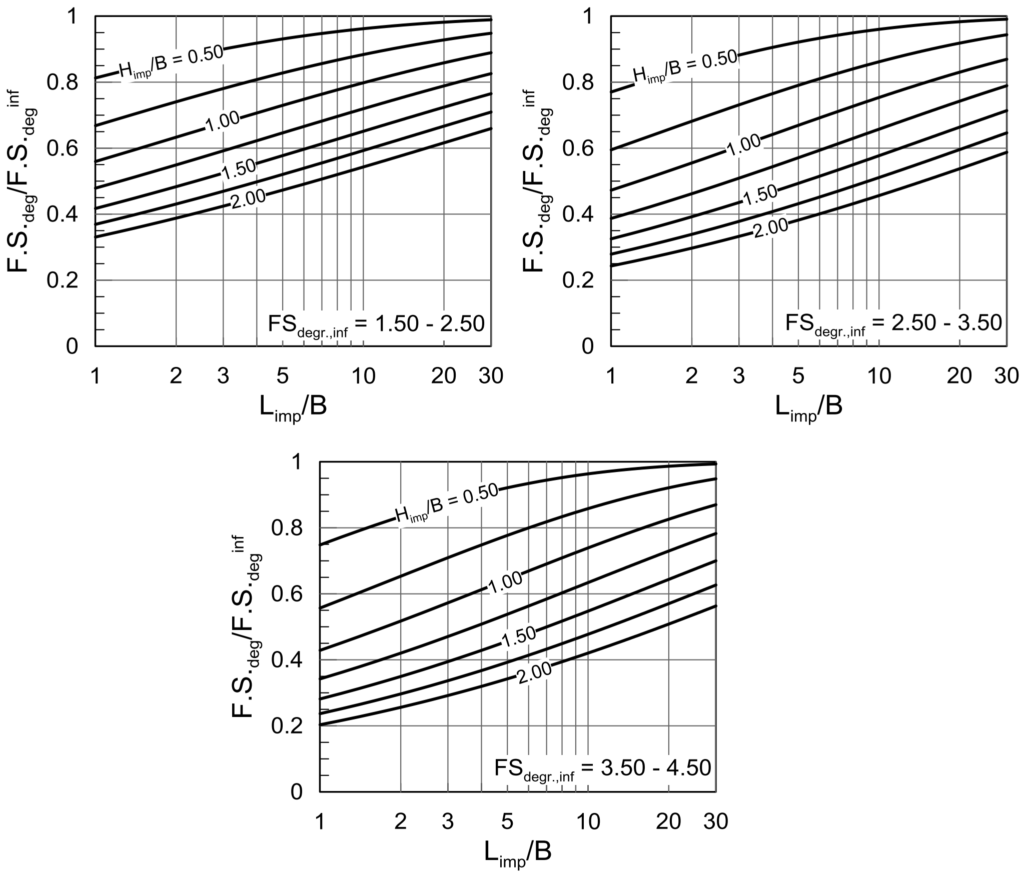

Figure 6.21: Design charts relating the $F.S._{deg}/F.S._{deg}^{inf}$ ratio to the L_{imp}/B value

Σχήμα 6.21: Διαγράμματα σχεδιασμού του λόγου $F.S._{deg}/F.S._{deg}^{inf}$ συναρτήσει του L_{imp}/B.

6.5 Overview of Analytical Methodology and Design Charts

Evaluation of degraded Factor of Safety $F.S._{deg}$- The first step of the proposed analytical methodology, includes the evaluation of the degraded factor of safety of the shallow foundation, immediately after the end of shaking and while the underlying soil is still under a liquefied state. This is accomplished through equation (6.9), allowing the evaluation of $F.S._{deg}$ for any improved zone geometry (depth H_{imp} and width L_{imp}). The specific analytical expression is provided in a non-linear formulation, requiring an iterative solution. Moreover, it requires the prior knowledge of the degraded factor of safety for "infinite" improvement conditions, which is obtained through the application of equation (5.12).

To reduce the computational effort required for the evaluation of $F.S._{deg}$, equation (6.9) is solved for different $F.S._{deg}^{inf}$ and H_{imp}/B values and the outcome is presented in **Figure 6.21**. The particular design charts summarize the effect of the lateral width of improvement normalized against the footing width B (L_{imp}/B) on the degraded factor of safety, normalized against the corresponding values for conditions of "infinite" improvement.

Moreover, the formulation of a set of simplified equations [(6.14), (6.15) & (6.16)] allows the direct evaluation of the degraded factor of safety for "limited" lateral width of improvement. The particular set of simplified equations is subsequently plotted in an additional set of design charts, presented in **Figure 6.22**, for three different values of $F.S._{deg}^{inf}$.

Evaluation of dynamic settlements ρ_{dyn}.- Similarly to the analytical expressions proposed for the degraded factor of safety, the evaluation of the seismic-induced settlements ρ_{dyn} requires the prior assessment of ρ_{dyn}^{inf}. The specific parameter is evaluated using equation (5.6), given the necessary input data, namely the characteristics of the seismic excitation and the degraded factor of safety for conditions of "infinite" width of improvement, $F.S._{deg}^{inf}$, as specified above. In the sequel, the ratio of $\rho_{dyn}/\rho_{dyn}^{inf}$ is computed as a function of the width and depth of improvement, normalized against the footing width B - L_{imp}/B, H_{imp}/B respectively, as illustrated in **Figure 6.12**.

Design Charts for L_{imp}/H_{imp}.- To gain additional insight regarding the practical application of the previously generated design charts, the corresponding analytical expressions are appropriately modified to incorporate the ratio of the width over the depth of the improved zone, L_{imp}/H_{imp}. Hence, equation (6.7) is transformed into equation (6.17) *:*

$$\frac{\rho_{dyn}^{inf}}{\rho_{dyn}} = 1 - \exp\left[-1.05\left(\frac{H_{imp}}{B}\right)^{-0.7}\left(\frac{L_{imp}}{H_{imp}}\right)^{0.30}\right] \qquad (6.17)$$

Accordingly, the simplified analytical expressions for $F.S._{deg}$ are transformed into equations (6.18), (6.19) and (6.20) respectively:

$$\frac{FS_{deg}}{FS_{deg}^{inf}} = 1 - \exp\left[-0.82\left(\frac{H_{imp}}{B}\right)^{-0.74}\left(\frac{L_{imp}}{H_{imp}}\right)^{0.29}\right] \quad (F.S._{deg}{}^{inf} = 2.00) \tag{6.18}$$

$$\frac{FS_{deg}}{FS_{deg}^{inf}} = 1 - \exp\left[-0.64\left(\frac{H_{imp}}{B}\right)^{-0.86}\left(\frac{L_{imp}}{H_{imp}}\right)^{0.34}\right] \quad (F.S._{deg}{}^{inf} = 3.00) \tag{6.19}$$

$$\frac{FS_{deg}}{FS_{deg}^{inf}} = 1 - \exp\left[-0.56\left(\frac{H_{imp}}{B}\right)^{-0.92}\left(\frac{L_{imp}}{H_{imp}}\right)^{0.38}\right] \quad (F.S._{deg}{}^{inf} = 4.00) \tag{6.20}$$

The above equations are solved for seven (7) distinct H_{imp}/B ratios (= 0.50, 0.75, 1.00, 1.25, 1.50, 1.75, 2.00) and the outcome is summarized in an updated set of design charts, as exhibited in **Figure 6.22** and **Figure 6.23**. The thicker grey lines correspond to the points on the different curves beyond which increasing the ratio of L_{imp}/H_{imp} renders a rate of variation less than 5%, i.e. the cost-effect ratio is high.

Design Charts for V_{imp}/B^2.- The correlation between the selected dimensions of an improved zone around the shallow foundation to the generated cost becomes a lot more straightforward when incorporating the resulting volume of improvement V_{imp}, which is a more direct cost indicator. For the plane strain conditions considered in the problem, the volume of the improved area is defined as the product of the depth (H_{imp}) times the width (L_{imp}) of the improved zone. To preserve the dimensionless form of the initially proposed equations, volume is divided by B^2 and the outcome of the modification is exhibited in equations (6.21), (6.22), (6.23) and (6.24).

$$\frac{\rho_{dyn}^{inf}}{\rho_{dyn}} = 1 - \exp\left[-1.05\left(\frac{H_{imp}}{B}\right)^{-1.30}\left(\frac{V_{imp}}{B^2}\right)^{0.30}\right] \tag{6.21}$$

$$\frac{FS_{deg}}{FS_{deg}^{inf}} = 1 - \exp\left[-0.82\left(\frac{H_{imp}}{B}\right)^{-1.32}\left(\frac{V_{imp}}{B^2}\right)^{0.29}\right] \tag{6.22}$$

$$\frac{FS_{deg}}{FS_{deg}^{inf}} = 1 - \exp\left[-0.64\left(\frac{H_{imp}}{B}\right)^{-1.54}\left(\frac{V_{imp}}{B^2}\right)^{0.34}\right] \tag{6.23}$$

$$\frac{FS_{deg}}{FS_{deg}^{inf}} = 1 - \exp\left[-0.56\left(\frac{H_{imp}}{B}\right)^{-1.68}\left(\frac{V_{imp}}{B^2}\right)^{0.38}\right] \tag{6.24}$$

The normalized dynamic settlements and the degraded factor of safety are plotted against V_{imp}/B^2 in **Figure 6.24** and **Figure 6.25** respectively. Note that the grey line connects the points on the different curves beyond which increasing the volume of the performed improvement renders a rate of variation less than 5%. The orange and blue lines correspond to the empirical methodologies proposed by JDFA (1974) and Tsuchida et al. (1976) respectively. The above guidelines have been presented in the introduction of the current chapter and provide an estimate of the width of the compacted zone around shallow or slightly embedded structures. Note however, that both empirical methodologies refer to compaction as the main improvement technology and hence do not incorporate the drainage effects offered by the presence of gravel drains. Additionally, in the specific studies, it is recommended that the entire thickness of the liquefiable sand layer is mitigated. Hence, in the relevant Figures, both recommendations are applied for relatively thin liquefiable layers, ranging from 0.5 – 2 times the width of the footing. The consideration of a 20m thick liquefiable layer (as it is assumed in the numerical investigation) is going to shift the resulting curves to the right, hence severely increasing the volume of the mitigated soil and increasing the associated cost.

Based on the above sets of design charts it is concluded that the rate of variation in the ratio of dynamic settlements becomes significant, i.e. exceeds 5%, for L_{imp}/H_{imp} values greater than about 5, in the case of the maximum improvement thickness examined herein. For low values of H_{imp}/B dynamic settlements experience only a minor increase, especially for narrow widths of improvement.

Regarding the degraded factor of safety, there is a rather abrupt change in the values of the normalized ratio even for large L_{imp}/H_{imp} values, which was obvious already from the execution of the parametric investigation. Namely, even a minor reduction in the improvement width was leading to a major decline in the obtained degraded factor of safety $F.S._{deg}$. This was even more evident for greater values of improvement depth, H_{imp}.

Conditions of "infinite" width of improvement render a very un-conservative estimate both in terms of dynamic settlements and degraded factor of safety. The specific conditions are attained for at least 20 times the footing width. Such a design width is practically prohibited and can lead to excessive construction costs. Hence, the examined method of ground improvement becomes technically and financially efficient for improvement widths within 2 – 5 times the depth of the improvement, namely L_{imp} = (2 – 5) H_{imp}.

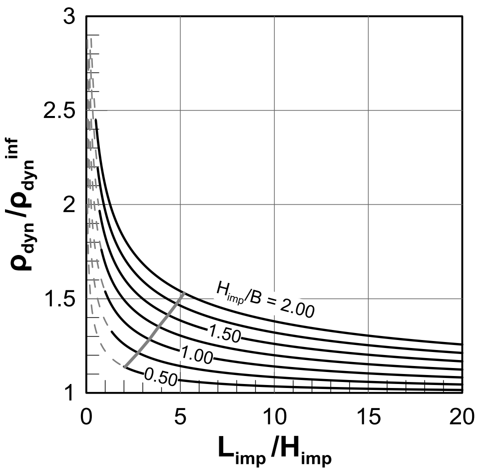

Figure 6.22: Normalized dynamic settlements plotted with respect to L_{imp}/H_{imp} for different H_{imp}/B values

Σχήμα 6.22: Ανοιγμένες δυναμικές καθιζήσεις συναρτήσει του λόγου L_{imp}/H_{imp} για διάφορες τιμές του H_{imp}/B

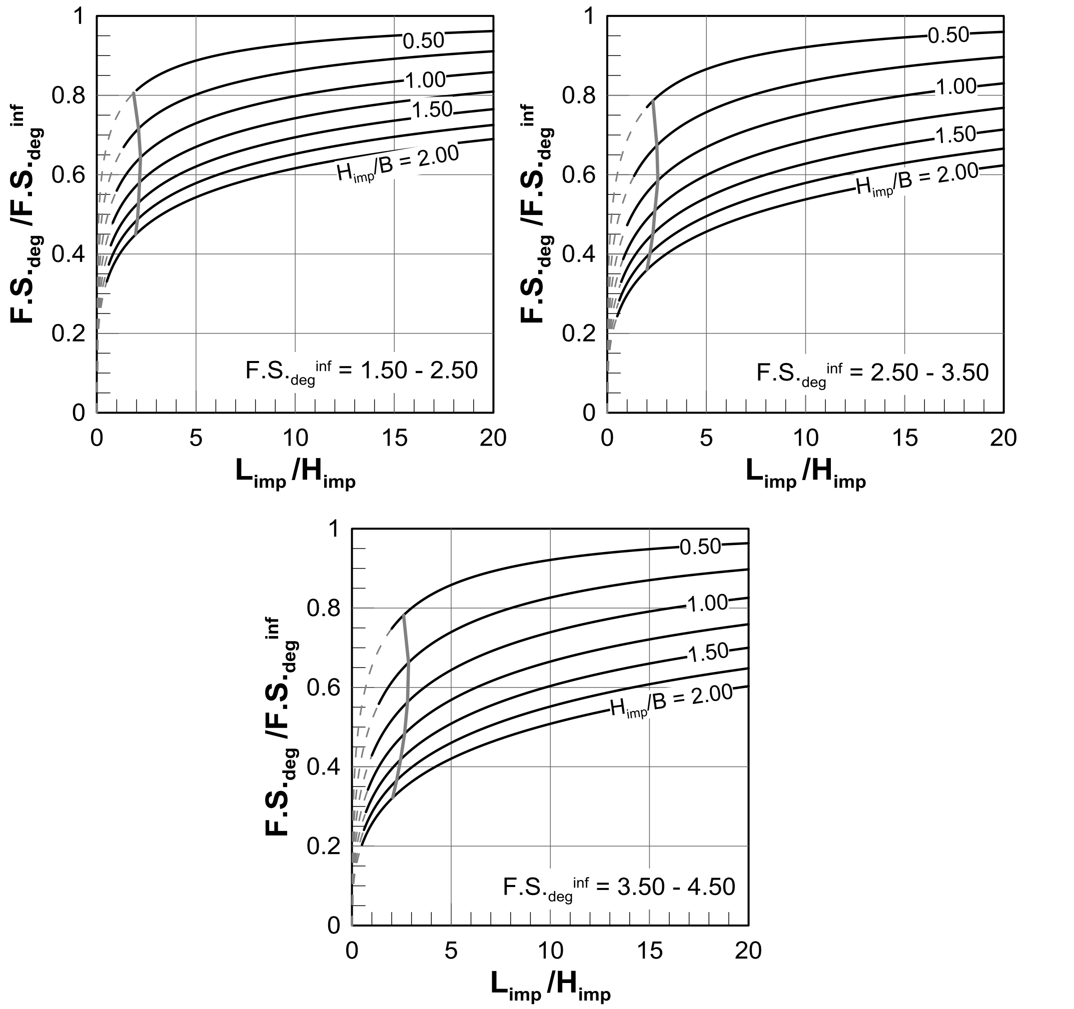

Figure 6.23: Normalized degraded factor of safety plotted with respect to L_{imp}/H_{imp} for different H_{imp}/B values and three values of $F.S._{deg}^{inf}$

Σχήμα 6.23: Ανοιγμένες τιμές του απομειωμένου συντελεστή ασφάλειας συναρτήσει του λόγου L_{imp}/H_{imp} για διάφορες τιμές του H_{imp}/B και τρεις τιμές του $F.S._{deg}^{inf}$

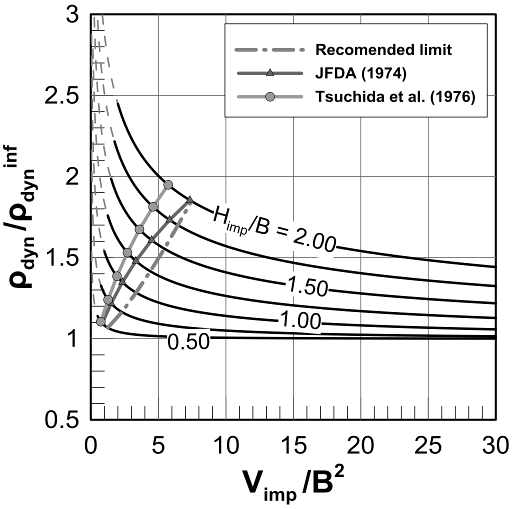

Figure 6.24: Normalized dynamic settlements versus V_{imp}/B^2 for different H_{imp}/B values

Σχήμα 6.24: Ανοιγμένες δυναμικές καθιζήσεις συναρτήσει του V_{imp}/B^2 για διάφορα H_{imp}/B

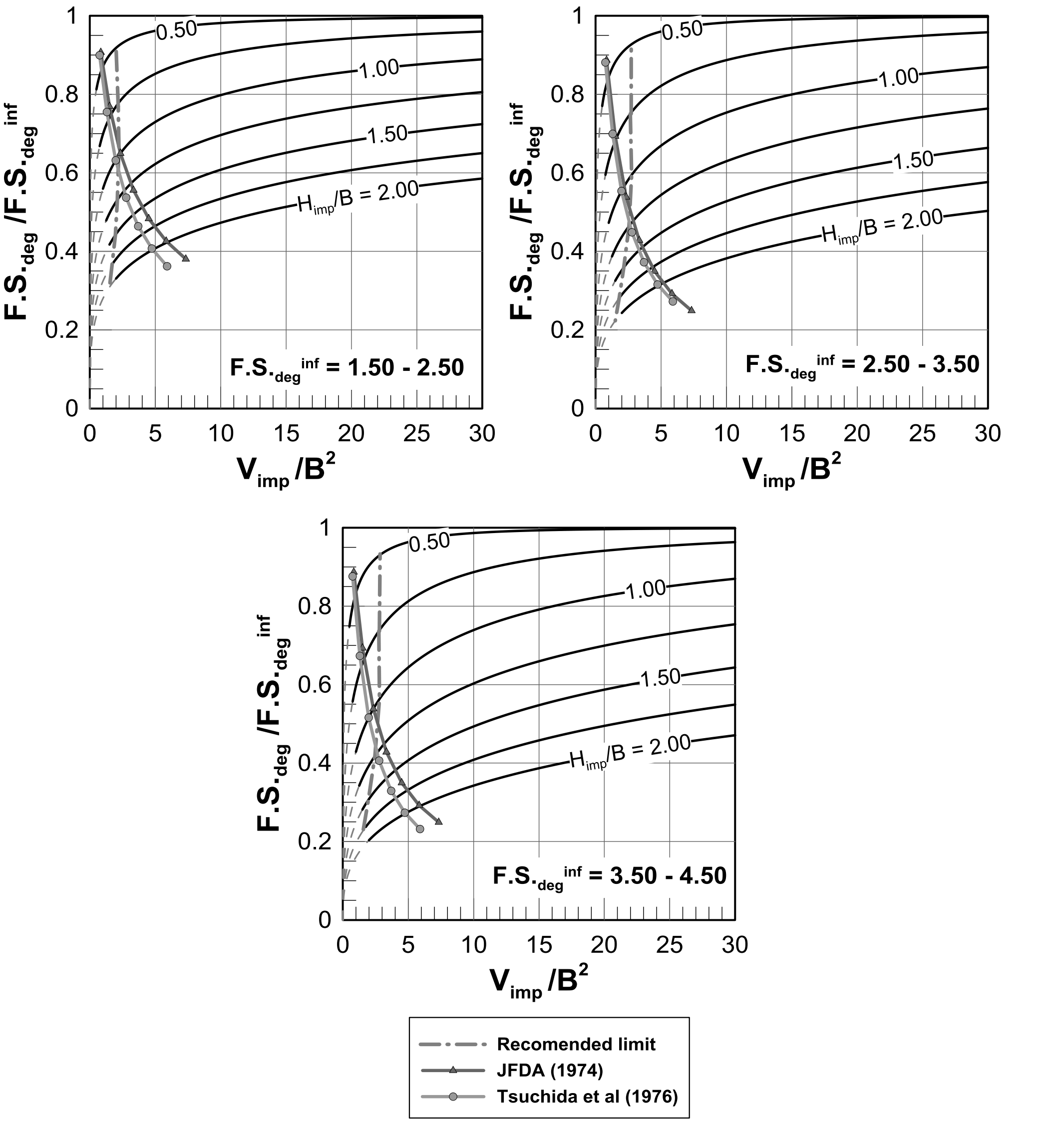

Figure 6.25: Normalized degraded factor of safety plotted with respect to V_{imp}/B^2 for different H_{imp}/B values and three values of $F.S._{deg}^{inf}$

Σχήμα 6.25: Ανοιγμένες τιμές του απομειωμένου συντελεστή ασφάλειας συναρτήσει του λόγου V_{imp}/B^2 για διάφορες τιμές του H_{imp}/B και τρεις τιμές του $F.S._{deg}^{inf}$

7

Performance-Based-Design of shallow foundations on liquefiable ground

7.1 General

Design of a structure by employing a performance-based approach requires evaluation of the response in terms of all possible deformation modes. For the case of bridges, considered herein, possible deformation patterns are schematically presented in **Figure 7.1** and include the following (Barker et al. 1991):

- **Uniform settlement (ρ)** is described as the rather theoretical situation in which each of the bridge foundations settles by the same amount (**Figure 7.1a**). Even though no distortion of the superstructure occurs, excessive uniform settlement can lead to issues such as insufficient clearance at underpasses, as well as discontinuities at the juncture between approach slabs and the bridge deck, [also referred to as "the bump at the end of the bridge" (Wahls 1990) and inadequate drainage at the end of the bridge.
- **Uniform tilt (ω) or rotation (θ) along the bridge axis**, which relates to settlements that vary linearly along the length of the bridge (**Figure 7.1b**). This type of deformation is most likely to occur in very stiff superstructures and single-span bridges. Usually, no distortion occurs in the superstructure, except in the case of non-monolithic connection between bridge components. In terms of traffic disturbance the same problems (bumps, drainage and clearance height) as mentioned above may occur.
- **Non-uniform settlements** lead to deformation when the superstructure is continuous over three or more foundations, which causes distortion in the superstructure especially in continuous span bridges. It may be either regular or irregular as noted in **Figures 7.1c & d**. A regular pattern in deformation is characterized by a symmetrical distribution of settlement, from both ends of the bridge towards the center. In the irregular pattern, deformation is randomly distributed along the length of the bridge. Operational problems caused by non-uniform settlements include bumps at junctures with approach slabs, or between subsequent spans, inadequate drainage and insufficient clearance height at underpasses.

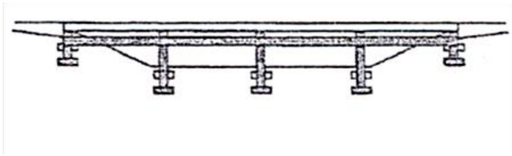

a. Uniform Settlement

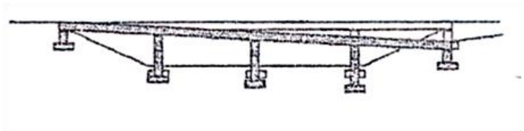

b. Uniform tilt (ω) or rotation (θ)

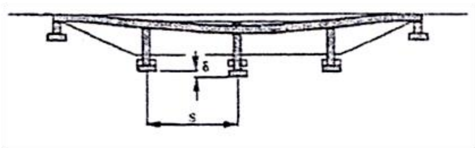

c. Non uniform settlement
(Regular pattern of settlement)

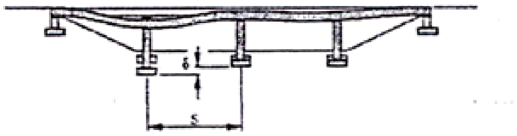

d. Non-uniform settlement
(Irregular pattern of settlement)

Figure 7.1: Components of settlement and angular distortion in bridges (Barker et al., 1991).
Σχήμα 7.1: Μορφές καθίζησης και στροφικής καταπόνησης γεφυρών (Barker et al., 1991).

In view of the above, performance based design of footings supporting bridge piers under seismic loading and soil liquefaction, should account for the following deformation patterns:

- Seismic settlements ρ_{dyn}
- Differential settlements δ_{dyn} or angular distortion $\beta_{dyn}=\delta_{dyn}/S$
- Tilting θ_{dyn} (relative to the vertical axis)

In the following, each one of these components is analyzed separately. For the case of seismic settlements, the major outcomes of the research described in the previous chapters are summarized, while evaluation of differential settlements and tilt is based on existing recommendations.

7.2 Seismic settlements ρ_{dyn}

The mechanisms of seismic settlement accumulation have been extensively analyzed in the previous chapters. The present section outlines the basic steps for their evaluation, for the case where the liquefiable layer is overlaid by of an impermeable clay crust, as well as, for the case of an artificial, permeable crust of improved sand.

7.2.1 Foundations on clay crust

The **degraded bearing capacity, $q_{ult,deg}$,** can be estimated based on the composite failure mechanism of Meyerhof and Hanna (1978):

$$q_{ult,deg} = \min\left\{\begin{matrix}(\pi+2)c_u F_{cs} \\ q_{ult,deg}^{c-s}\end{matrix}\right\} \quad (7.1)$$

$$q_{ult,deg}^{c-s} = 2c_u \frac{H}{B} s - \gamma' H + \frac{1}{2}\gamma' B N_\gamma F_{\gamma s} + \gamma' H N_q F_{qs} \quad (7.2)$$

where B is the width of the foundation, H is the thickness of the clay crust, c_u is the crust's undrained shear strength and γ′ is the buoyant weight, which is considered to be the same for both the sand and the clay layers. The bearing capacity factors are computed according to Vesic (1973):

$$N_q = \tan^2\left(45 + \frac{\phi}{2}\right) e^{\pi \tan \phi_{deg}}$$

$$N_\gamma = 2\left(N_q + 1\right) \tan \phi_{deg}$$

The shape factors are computed according to De Beer (1970):

$$F_{cs} = 1 + \frac{1}{\pi + 2} \frac{B}{L}$$

$$F_{\gamma s} = 1 - 0.4 \frac{B}{L}$$

$$F_{qs} = 1 + \frac{B}{L} \tan \phi$$

and the factor s in Equation (2.20) is computed according to Meyerhof & Hanna (1978):

$$s = 1 + \frac{B}{L}$$

In the above equations, the effect of liquefaction is taken into account as a degradation of the sand's friction angle:

$$\phi_{deg} = a\tan\left[\left(1 - U\right) \tan \phi_o\right] \tag{7.3}$$

where:

ϕ_o the initial friction angle of the non-liquefied sand

U the excess pore pressure ratio developing in the sand layer

The uniform excess pore pressure ratio U is computed as:

$$U = \frac{U_{foot} + \left(1 + B/L\right) \cdot U_{ff}}{2 + B/L} \tag{7.4}$$

where:

$U_{ff} \approx 1.0$: Excess pore pressure ratios at the free field

U_{foot}: Excess pore pressure ratios underneath the footing

The excess pore pressure ratio underneath the footing can be estimated as follows:

$$U_{foot} = \frac{1 - 6.0 \, \rho_{dyn}/B}{1 + \Delta\sigma_{v,c}/\sigma'_{vo,c}} \tag{7.5}$$

where:

ρ_{dyn}: Dynamic settlements

$\Delta\sigma_{v,c}$: Additional vertical stress imposed by the foundation load at the characteristic depth z_c

$\sigma'_{vo,c}$: Initial (pre-shaking) vertical effective stress applied at the characteristic depth z_c

Finally, the characteristic depth z_c is estimated as:

$$z_c = H + \left[1.0 - 0.5\left(\frac{B}{L}\right)^3\right]B \tag{7.6}$$

Dynamic settlements, ρ_{dyn}, can be evaluated from the following expression:

$$\rho_{dyn} = c \cdot a_{max} T^2 N \left(\frac{Z_{liq}}{B}\right)^{1.5} \left(\frac{1}{FS_{deg}}\right)^3 \tag{7.7}$$

where:

a_{max}: Peak input acceleration

T: Excitation period

N: Number of cycles

Z_{liq}: Thickness of the liquefiable sand layer

B: Footing width

FS_{deg}: Post-liquefaction degraded factor of safety

Coefficient c in Eq. (2.25) is equal to 0.008 and 0.035 for square and strip foundations, while for intermediate aspect ratios L/B, it may be approximately computed as:

$$c = c'\left(1 + 1.65\frac{L}{B}\right) \leq 11.65c' \tag{7.8}$$

where c′=0.003

Finally, for the case of non-sinusoidal input motions equation (2.25) is applied by substituting the term $a_{max}T^2N$ with $\pi^2 \cdot \int |v(t)| dt$ where v(t) is the applied velocity time-history.

The equations presented in the previous paragraphs were consequently used to derive practice-oriented **design charts**. More specifically, seismic settlements ρ_{dyn} of both strip footings and square foundations, normalized against the footing's width B, can be computed in terms of the following non-dimensional problem parameters:

- the average bearing pressure $q/\gamma' B$,
- the thickness of the clay crust H/B,
- the undrained shear strength of the clay crust $c_u/\gamma' H$, and

- the intensity of seismic motion and the extent of liquefaction expressed as ρ_o/B, according to Equation (2.27):

$$\frac{\rho_o}{B} = \left(\frac{a_{max} T^2 N}{B}\right)\left(\frac{Z_{liq}}{B}\right)^{1.5} \tag{7.9}$$

The corresponding design charts for strip and square foundations are shown in **Figure 7.2** and **Figure 7.3** respectively for ρ_o/B=1.0, 2.0 and 5.0.

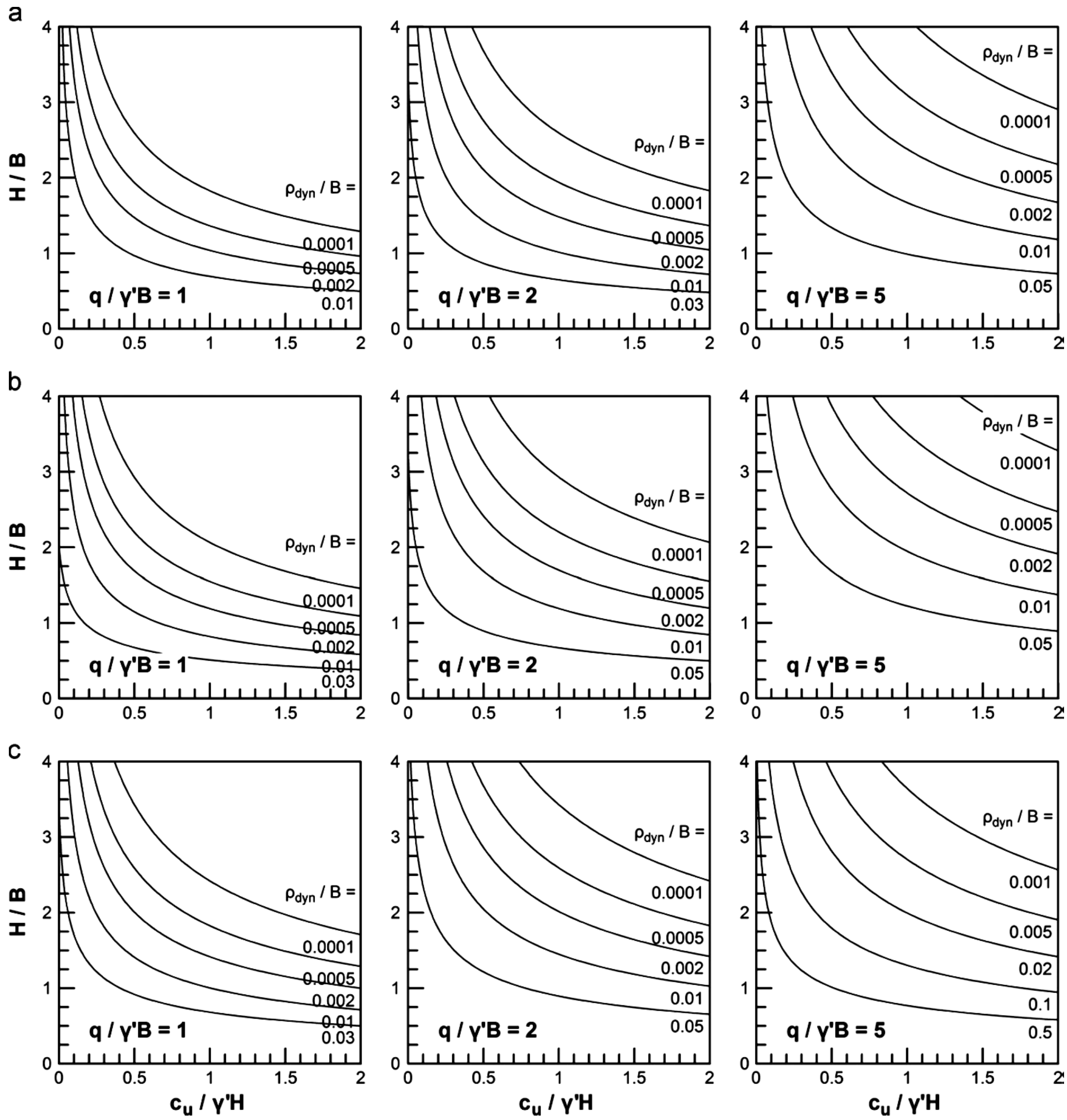

Figure 7.2: Design charts for the estimation of ρ_{dyn} for (a) ρ_o/B = 1.0, (b) ρ_o/B = 2.0 and (c) ρ_o/B = 5.0 – Strip footings

Σχήμα 7.2: Διαγράμματα σχεδιασμού για τον υπολογισμό των δυναμικών καθιζήσεων ρ_{dyn} για (a) ρ_o/B = 1.0, (b) ρ_o/B = 2.0 and (c) ρ_o/B = 5.0 – Λωριδωτά θεμέλια

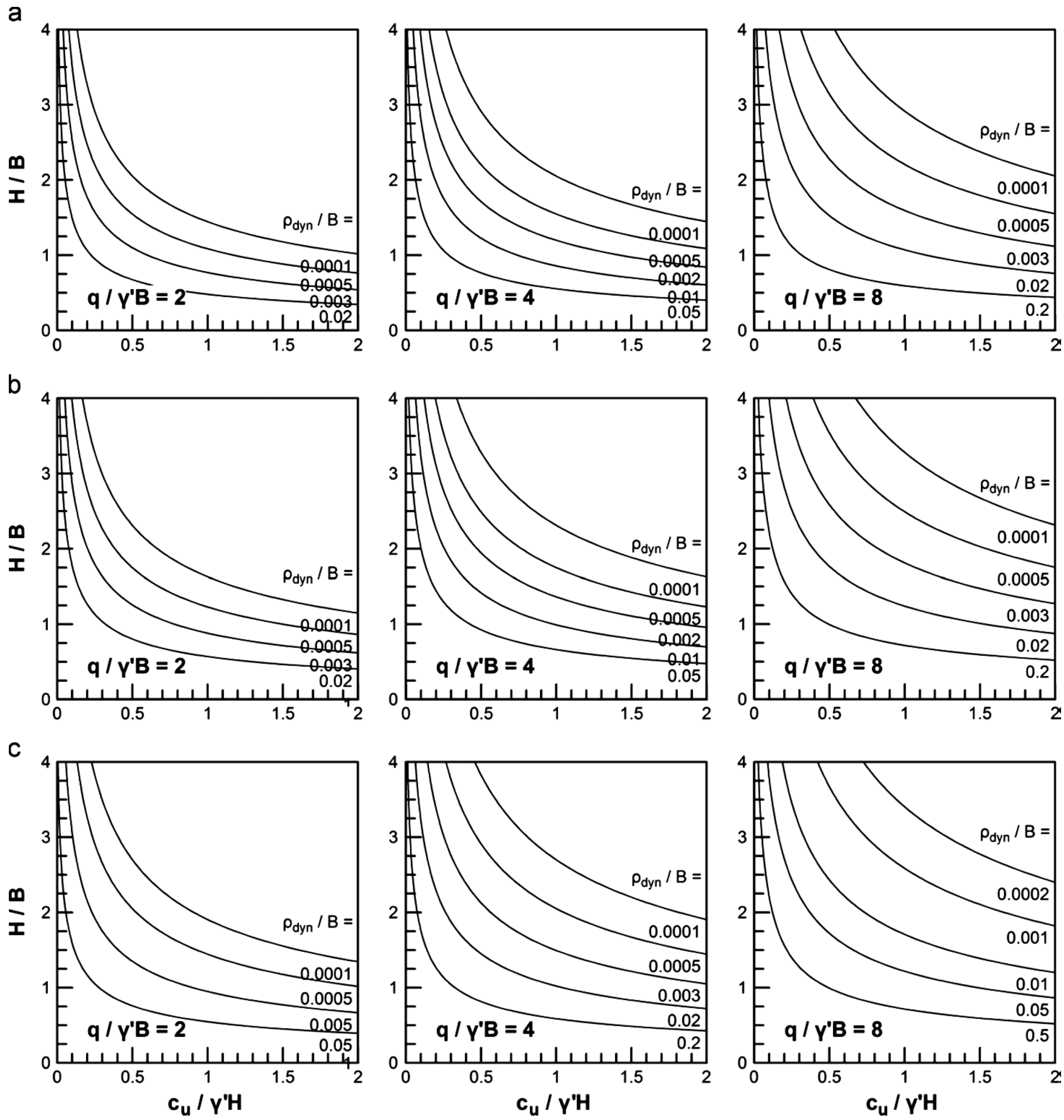

Figure 7.3: Design charts for the estimation of $ρ_{dyn}$ for (a) $ρ_o/B$ = 1.0, (b) $ρ_o/B$ = 2.0 and (c) $ρ_o/B$ = 5.0 – Square footings

Σχήμα 7.3: Διαγράμματα σχεδιασμού για τον υπολογισμό των δυναμικών καθιζήσεων $ρ_{dyn}$ για (a) $ρ_o/B$ = 1.0, (b) $ρ_o/B$ = 2.0 and (c) $ρ_o/B$ = 5.0 – Τετραγωνικά θεμέλια

7.2.2 Foundation on improved ground

The methodology for the case of the footing resting upon improved ground is summarized in the following steps:

<u>Step 1</u>: Determination of the replacement ratio $α_s$.- The replacement ratio a_s is estimated through **Figure 4.9** considering the following input parameters:

- Initial relative density of the treated soil, **$D_{r,o}$ (%)**,
- Thickness of the performed improvement **H_{imp}(m)** as well as
- Maximum excess pore pressure ratio **$r_{u,max}$** allowed to develop within the improved zone, which according to current practice, is equal to $r_{u,max}$= 0.30 - 0.50.

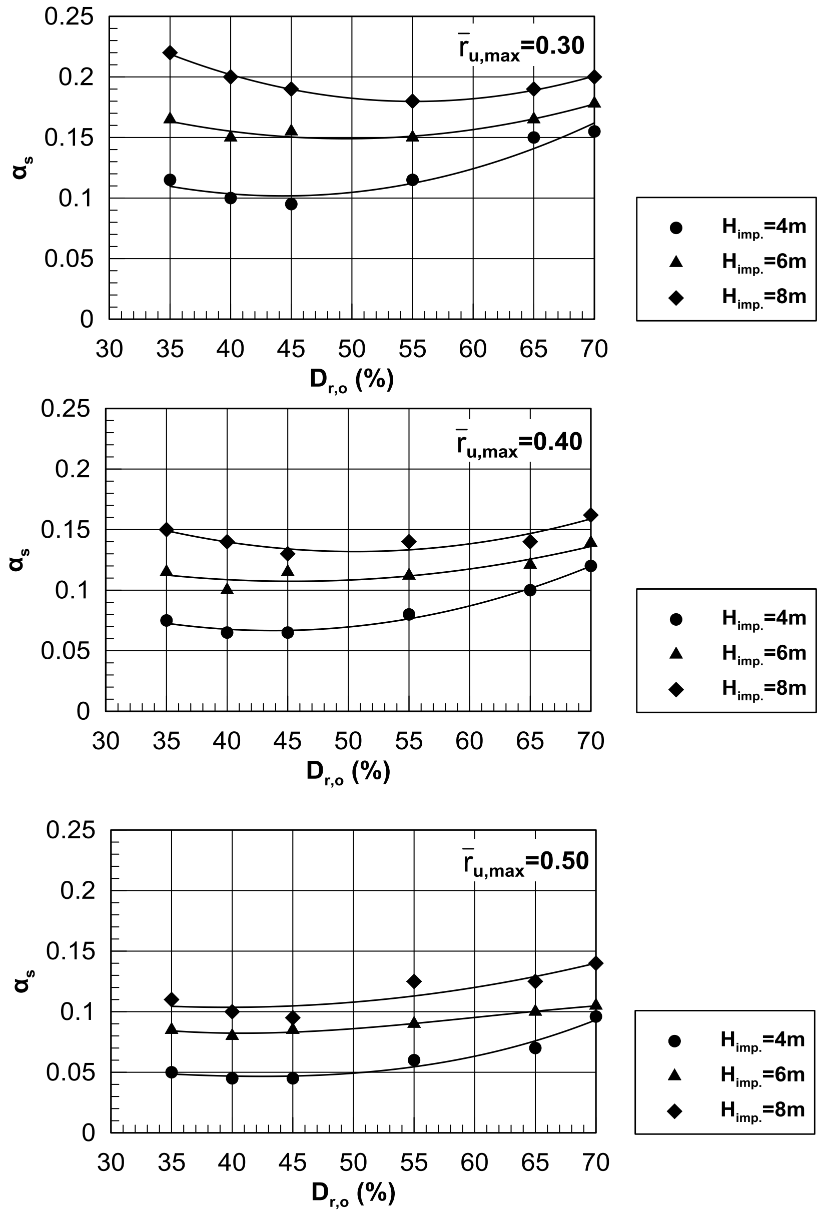

Figure 7.4: Required replacement ratio α_s with regard to initial relative density $Dr_{,o}$(%) and three allowable levels of $r_{u,max}$.

Σχήμα 7.4: Απαιτούμενος λόγος αντικατάστασης α_s συναρτήσει της αρχικής σχετικής πυκνότητας $Dr_{,o}$(%) και τρία επιτρεπόμενα επίπεδα λόγου $r_{u,max}$.

<u>**Step 2**</u>**: Determination of the equivalent properties of the improved zone.-** The permeability, k_{eq}, and the relative density, $D_{r,imp}$, of the improved zone are evaluated through **Figure 7.5** as a function of the replacement ratio α_s and the initial relative density of the liquefiable sand $D_{r,o}$ (%).

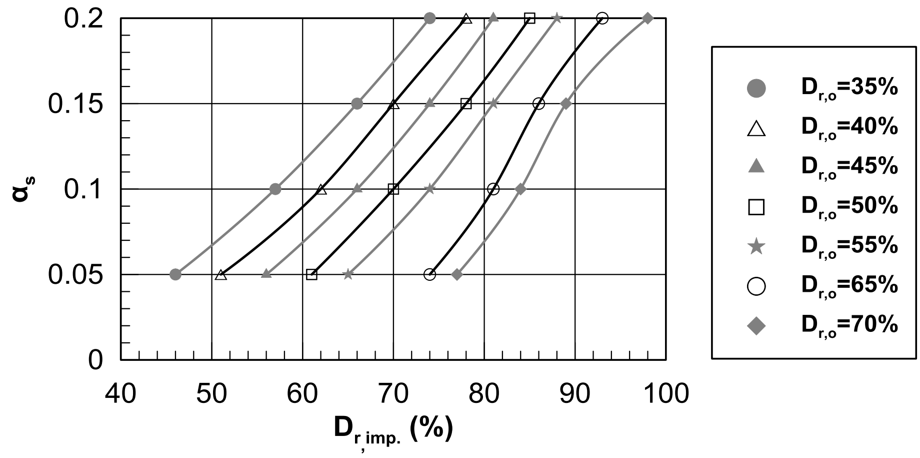

(a)

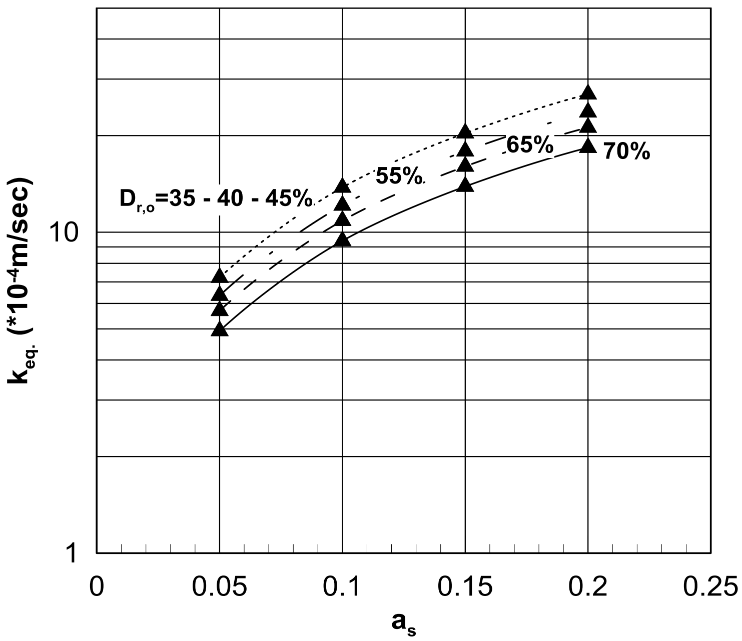

(b)

Figure 7.5: Assessment of the improved properties (a) relative density $D_{r,imp}$(%) and (b) permeability $k_{eq.}$(m/sec), as a function of replacement ratio α_s.

Σχήμα 7.5: Εκτίμηση ιδιοτήτων βελτιωμένου εδάφους (α) σχετική πυκνότητα $D_{r,imp}$(%) και (β) διαπερατότητα $k_{eq.}$(m/sec), συναρτήσει του λόγου αντικατάστασης α_s.

<u>Step 3</u>: Evaluation of seismic performance of the shallow foundation under conditions of "Infinite" Improvement.

<u>Dynamic settlements ρ_{dyn}^{inf}</u>

Seismically-induced settlements are evaluated based on the following Newmark-based relation:

$$\rho_{dyn}^{inf} = 0.019 \cdot a_{max} \left(T_{exc} + 0.633 \cdot T_{soil}\right)^2 \cdot (N_o + 2) \cdot \left(\frac{1}{FS_{deg}^{inf}}\right)^{0.45} \cdot \left[1 + 0.25 \cdot \left(\frac{1}{FS_{deg}^{inf}}\right)^{4.5}\right] \quad (7.10)$$

where:

a_{max}: Peak bedrock acceleration

T_{exc}: Predominant excitation period

T_{soil}: Elastic fundamental period of the soil column

N_o: Number of significant loading cycles

FS_{deg}^{inf}: Degraded factor of safety

Degraded bearing capacity $q_{ult,deg}^{inf}$ and associated FS_{deg}^{inf}

Degraded bearing capacity $q_{ult,deg}^{inf}$ is calculated based on the modified analytical relation initially proposed by Meyerhof & Hanna (1978) as follows:

$$q_{ult,deg}^{inf} = \min \left\{ \begin{matrix} \frac{1}{2}\gamma' \cdot B \cdot N_{\gamma 1} \\ \gamma' H_1^2 K_s \frac{\tan\varphi_{1,deg}}{B} + \gamma'[(1+\alpha)^2 - 1] H_1^2 K_s \cdot \frac{\tan\varphi_{2,deg}}{B} - \gamma'(1+\alpha)H_1 + \\ + \frac{1}{2}\gamma' B N_{\gamma 2} + \gamma'(1+\alpha)H_1 N_{q2} \end{matrix} \right\} \quad (7.11)$$

where B is the footing width, H_1 the thickness of the improved crust and γ' the effective unit weight of the soil. Coefficients N_q and N_γ are calculated according to Vesic (1973):

$$\begin{aligned} N_q &= \tan^2(45+\varphi_{deg}/2)e^{\pi\tan\varphi_{deg}} \\ N_\gamma &= 2(N_q+1)\tan\varphi_{deg} \end{aligned} \quad (7.12)$$

Between the improved crust and the liquefied sand a transition zone of non-liquefied natural ground (with $0 < r_u < 1.0$) is formed, as a result of the fast dissipation of the seismic induced excess pore pressures towards the much more permeable improved crust. Coefficients α and K_s are associated to the thickness and shear strength mobilized along this transition zone:

$$\alpha = 3.76 \cdot \left[\frac{k_{eq} \cdot T \cdot N}{H_{imp}}\right]^{0.256} \quad (7.13)$$

$$K_s = 1.0 \cdot \left(\frac{q}{p_\alpha}\right)^{-0.30} \left(\frac{H_{imp}}{B}\right)^{-0.50} \quad (7.14)$$

The effects of liquefaction and excess pore pressure build-up are considered by appropriately reducing the friction angle of the soil:

$$\varphi_{i,deg} = \tan^{-1}[(1-U_i)\tan\varphi_{i,ini}] \quad (7.15)$$

where the subscript "ini" denotes the friction angle of the ground at the beginning of shaking, while i=1 for the improved crust, 2 for the transition zone and 3 for the liquefied sand. The associated excess pore pressure ratios U_i are separately evaluated below.

- **Excess pore pressure ratio U_1 in the improved crust.-** The average epp ratio U_1 refers to free field conditions and at the end of shaking and is expressed as a portion of the allowable excess pore pressure ratio, U_{design}, set equal to:

$$U_1 = 0.54U_{design} \tag{7.16}$$

- **Excess pore pressure ratio in the transition zone U_2.-** Parameter U_2, corresponds to the average excess pore pressure ratio in the transitional non-liquefied zone of the natural ground and is estimated as the average between U_1 and the excess pore pressure ratio in the liquefied soil, which equals unity. Thus, U_2 is equal to:

$$U_2 = \frac{(1+U_1)}{2} = \frac{(1+0.54U_{design})}{2} \tag{7.17}$$

- **Excess pore pressure ratio in the liquefied ground U_3.-** The excess pore pressure ratio U_3 refers to the liquefied ground, over a representative area underneath the footing and below the improved crust:

$$U_3 = 086 \cdot \left(\frac{q_{ult,deg}^{inf}}{p_a}\right)^{-0.18} \le 1.00 \tag{7.18}$$

Due to the dependence of U_3 on $q_{ult,deg}$, Equations (7.11) and (7.18) are solved concurrently until convergence and in the sequel, the degraded factor of safety $F.S._{deg}^{inf*}$ is derived. To further improve the accuracy of the proposed methodology, a correction factor is applied on the initially obtained value as shown below:

$$FS_{deg}^{inf} = \frac{FS_{deg}^{inf*}}{0.05 + 0.60\left(FS_{deg}^{inf*}\right)^{0.85}} > 0.60FS_{deg}^{inf*} \tag{7.19}$$

Step 4: Evaluation of seismic performance of the shallow foundation under conditions of "Finite" Improvement.- In real applications, soil improvement is applied over a designated area of limited dimensions. The determination of the particular area should grant the optimum solution between the required performance criteria specified for the shallow foundation and the associated construction costs. Hence, the current step summarizes the proposed analytical expressions to evaluate the appropriate improvement area dimensions. Note that both aspects of the seismic performance of the foundation (i.e ρ_{dyn} & $F.S._{deg}$) appear with reference to the results for "infinite" ground improvement, implying their prior assessment.

Dynamic settlements ρ_{dyn}

The ratio of $\rho_{dyn}^{inf}/\rho_{dyn}$ is analytically evaluated as follows:

$$\frac{\rho_{dyn}^{inf}}{\rho_{dyn}} = 1 - \exp\left[-1.05\left(\frac{H_{imp}}{B}\right)^{-1}\left(\frac{L_{imp}}{B}\right)^{0.30}\right] \tag{7.20}$$

where H_{imp} and L_{imp} the width and the length of the improvement zone respectively.

Degraded bearing capacity q_{ult}^{deg} and Factor of Safety F.S.$_{deg}$

The ratio of $F.S._{deg}/F.S._{deg}^{inf}$ is computed through the following non-linear equation:

$$\left(\frac{FS_{deg}}{FS_{deg}^{inf}}\right)^{-0.45} = \left\{1 - \exp\left[-1.05\left(\frac{H_{imp}}{B}\right)^{-1}\left(\frac{L_{imp}}{B}\right)^{0.30}\right]\right\}\frac{\left(FS_{deg}^{inf}\right)^{4.5} + 0.25\left(\frac{FS_{deg}}{FS_{deg}^{inf}}\right)^{4.5}}{\left(FS_{deg}^{inf}\right)^{4.5} + 0.25} \tag{7.21}$$

Given the complexity in the use of (7.21), a set of simplified analytical expressions is formulated, which enable the direct evaluation of the degraded factor of safety $F.S._{deg}$ for "limited" improvement conditions. The following set of equations are expressed with regard to the required L_{imp}/H_{imp} ratio and each one of them is applicable for a different range of FS_{deg}^{inf}.

$$FS_{deg}^{inf} = 1.50 - 2.50: \ \frac{F.S._{deg}}{F.S._{deg}^{inf}} = 1 - \exp\left[-0.82\left(\frac{H_{imp}}{B}\right)^{-1.03}\left(\frac{L_{imp}}{B}\right)^{0.29}\right] \tag{7.22}$$

$$FS_{deg}^{inf} = 2.50 - 3.50: \ \frac{F.S._{deg}}{F.S._{deg}^{inf}} = 1 - \exp\left[-0.64\left(\frac{H_{imp}}{B}\right)^{-1.30}\left(\frac{L_{imp}}{B}\right)^{0.34}\right] \tag{7.23}$$

$$FS_{deg}^{inf} = 3.50 - 4.50: \ \frac{F.S._{deg}}{F.S._{deg}^{inf}} = 1 - \exp\left[-0.56\left(\frac{H_{imp}}{B}\right)^{-1.30}\left(\frac{L_{imp}}{B}\right)^{0.38}\right] \tag{7.24}$$

Step 5: Selection of ground improvement dimensions.- Figure 7.6 through **Figure 7.8** allow the assessment of the **ratio of dynamic settlements $\rho_{dyn}/\rho_{dyn}^{inf}$** as a function of three different variables, namely L_{imp}/B, L_{imp}/H_{imp} and V_{imp}/B^2. The ratio of dynamic settlements is plotted for seven (7) distinct H_{imp}/B values (= 0.50, 0.75, 1.00, 1.25, 1.50, 1.75, 2.00).

The thicker dotted grey lines in **Figure 7.7** and **Figure 7.8** correspond to the points on the different curves beyond which, increasing the dimensions of ground improvement renders a rate of settlement decrease less than 5%, i.e. the cost-benefit ratio is high.

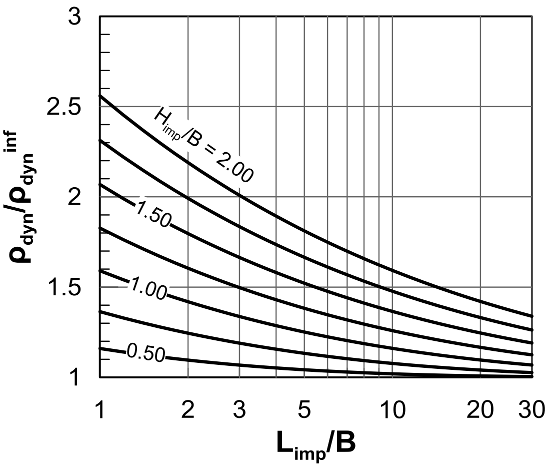

Figure 7.6: Design chart for the evaluation of the ratio of dynamic settlements $\rho_{dyn}/\rho_{dyn}^{inf}$, with regard to L_{imp}/B ratio for different H_{imp}/B values.

Σχήμα 7.6: Διάγραμμα εκτίμησης των δυναμικών καθιζήσεων $\rho_{dyn}/\rho_{dyn}^{inf}$, συναρτήσει του λόγου L_{imp}/B για διάφορες τιμές του H_{imp}/B.

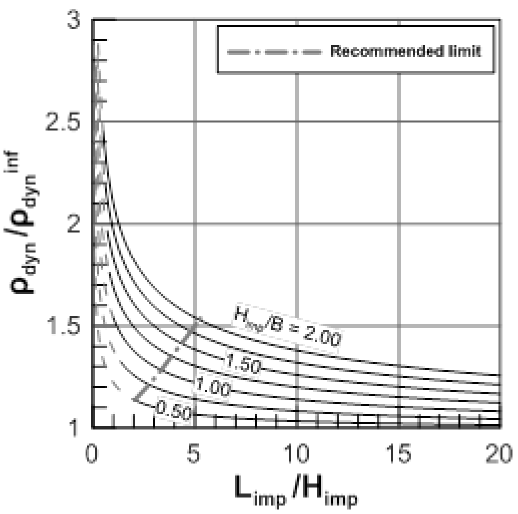

Figure 7.7: Normalized dynamic settlements plotted with respect to L_{imp}/H_{imp} for different H_{imp}/B values.

Σχήμα 7.7: Αδιαστατοποιημένες δυναμικές καθιζήσεις συναρτήσει του λόγου L_{imp}/H_{imp} για διάφορες τιμές του αδιαστατοποιημένου πάχους βελτίωσης H_{imp}/B.

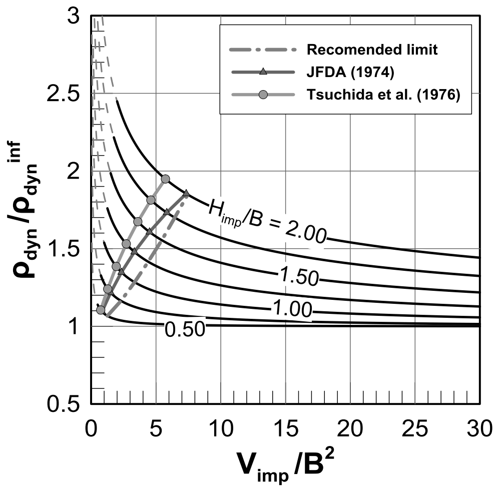

Figure 7.8: Normalized dynamic settlements versus V_{imp}/B^2 for different H_{imp}/B values.
Σχήμα 7.8: Αδιαστατοποιημένες δυναμικές καθιζήσεις συναρτήσει του λόγου V_{imp}/B^2 για διάφορες τιμές του αδιαστατοποιημένου πάχους βελτίωσης H_{imp}/B.

The corresponding design charts for **the degraded factor of safety**, $F.S._{deg}/F.S._{deg}^{inf}$ are summarized in **Figure 7.9** to **Figure 7.11**. The specific charts present the $F.S._{deg}/F.S._{deg}^{inf}$ ratio also with regard to L_{imp}/B, L_{imp}/H_{imp} and V_{imp}/B^2. In these figures also, the thicker dotted grey lines correspond to the points on the different curves beyond which, increasing the dimensions of ground improvement renders a rate of settlement decrease less than 5%, i.e. the cost-benefit ratio is high.

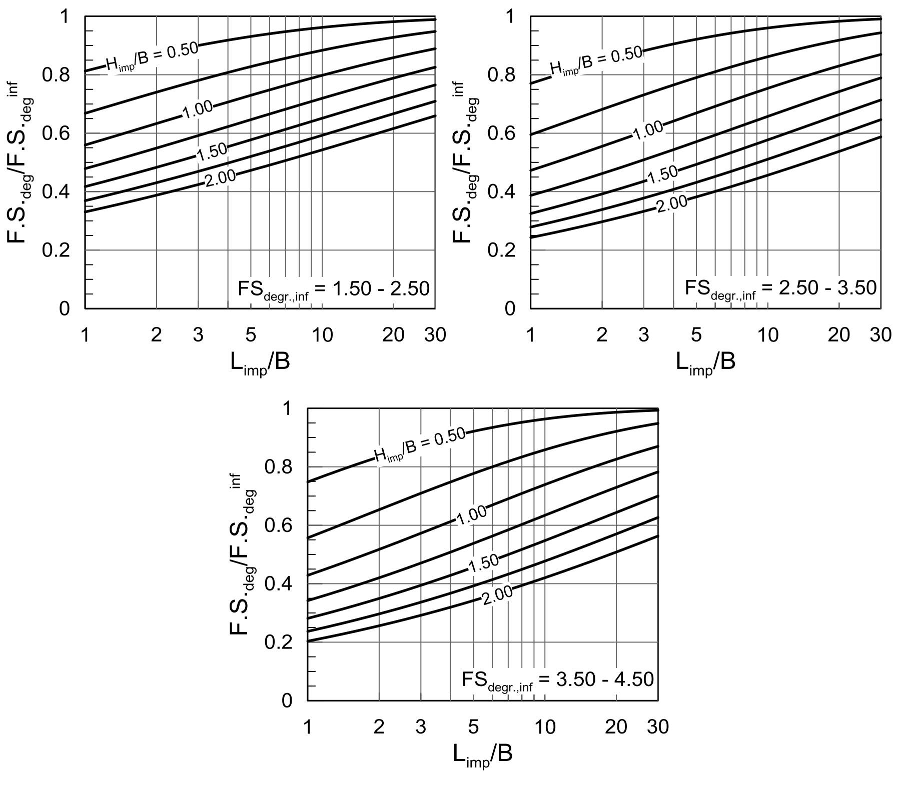

Figure 7.9: Design charts for FS_{deg}/FS_{deg}^{inf} relevant to L_{imp}/B for three initial FS_{deg}^{inf} values.
Σχήμα 7.9: Διαγράμματα σχεδιασμού του λόγου FS_{deg}/FS_{deg}^{inf} συναρτήσει του λόγου L_{imp}/B για τρεις τιμές του αρχικού FS_{deg}^{inf}.

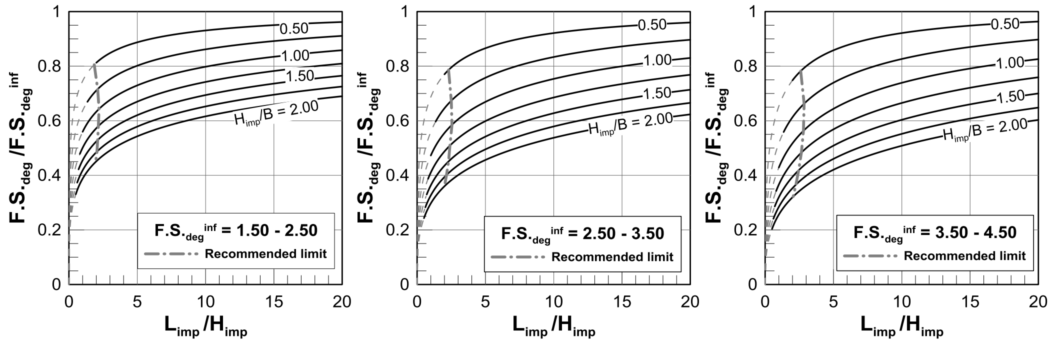

Figure 7.10: Normalized degraded factor of safety plotted with respect to L_{imp}/H_{imp} for different H_{imp}/B values and three values of FS_{deg}^{inf}.

Σχήμα 7.10: Αδιαστατοποιημένος απομειωμένος συντελεστής ασφαλείας συναρτήσει του λόγου L_{imp}/H_{imp} για διάφορες τιμές του αδιαστατοποιημένου πάχους H_{imp}/B και τρεις τιμές του FS_{deg}^{inf}.

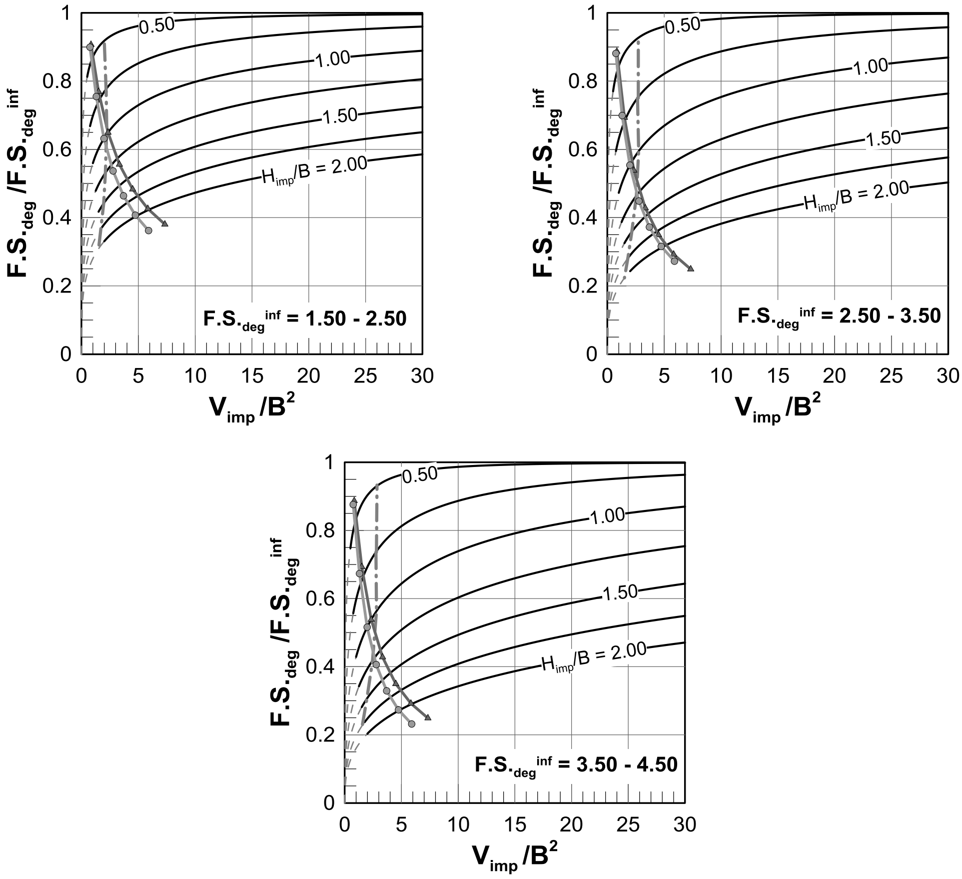

Figure 7.11: Normalized degraded factor of safety plotted with respect to V_{imp}/B^2 for different H_{imp}/B values and three values of FS_{deg}^{inf}.

Σχήμα 7.11: Αδιαστατοποιημένος απομειωμένος συντελεστής ασφαλείας συναρτήσει του λόγου V_{imp}/B^2 για διάφορες τιμές του αδιαστατοποιημένου πάχους H_{imp}/B και τρεις τιμές του FS_{deg}^{inf}.

7.3 Differential settlements *δ* & angular distortion *β=δ/S*

Differential settlements between two footings usually appear along with the occurrence of total settlements in the case where *(i)* the foundation soil is not absolutely uniform along the foundation area, *(ii)* the dead-to-live load ratio is different between the two footings or *(iii)* there are discrepancies in the built dimensions of the footings (e.g. a slight not intended eccentricity). Among the above cases, only case (ii) is computationally predictable, while cases (i) and (iii) are accidental and cannot be predicted directly. Hence, due to the complexity and uncertainty involved in their estimation many researchers have correlated differential settlements to maximum absolute settlements.

The correlation between total and differential settlement greatly depends on the type of foundation. In general, stiffer foundations, such as raft (mat) foundations (operating more like a single reinforced-concrete slab), are expected to experience lower differential settlements, compared to isolated foundations (e.g. spread footings which essentially support one single column). The magnitude of differential settlements is also greatly affected by the subsurface soil conditions. Sandy soil profiles present a greater degree of heterogeneity, even within the limits of the same structure; therefore significant differential settlements are more likely to occur. On the contrary, clay deposits are generally more uniform and lower differential settlements are expected compared to sandy soils for a known total settlement.

At this point, it is critical to point out that little investigation has been dedicated so far to the development of differential settlements and rotation due to earthquake-induced deformations. Hence, application of a performance-based design methodology can currently be based on correlations developed for static loading conditions, such as the ones outlined in the following. Still, further research is definitely required in order to establish a robust methodology based on performance criteria.

Skempton & MacDonald (1956).- The proposed correlations by Skempton and MacDonald (1956) between total settlement ρ and angular distortion β, as a function of soil and foundation type are summarized in **Table 7.1**. Note however, that the above correlation has received an extensive criticism from Terzaghi (1956), in the case of thick clay layers, where long-term consolidation settlements dominate. Anyhow, this criticism is not relevant to the present study.

Table 7.1: Ratio of maximum total settlement to maximum angular distortion ρ/β (Skempton and MacDonald, 1956).
Πίνακας 7.1: Λόγος μέγιστης συνολικής καθίζησης προς μέγιστη γωνιακή παραμόρφωση ρ/β (Skempton and MacDonald, 1956).

Soil Type	Isolated Foundations	Mat Foundations
Sand/sandy fill	$15L_R^*$	$20L_R^*$
Clay	$25L_R^*$	$30L_R^*$

L_R = the reference length = 1m = 40in

Sowers (1962).- The following relationships are proposed for the case of small buildings:

$$\delta = 0.75 \cdot \rho \text{ (for sands)} \tag{7.25}$$

$$\delta = 0.50 \cdot \rho \text{ (for clays)} \tag{7.26}$$

Bjerrum (1963).- Bjerrum (1963) studied the development of differential settlements and angular distortion for the case of spread footings. Note that the majority of his data were obtained from buildings in Scandinavia, where the soft soil conditions induce large settlements. Independent correlations of differential settlements δ and angular distortions β to total settlements ρ are shown in **Figure 7.12a** and **b** for sandy soils, and in **Figure 7.13a** and **b** for clayey soils. Note that, in the figures below, angular distortion is calculated considering adjacent columns, while differential settlement considering the two columns that yield the maximum value, hence not necessarily adjacent. It can be observed that the average estimate is in remarkable agreement with equation (7.25) proposed by Sowers (1962).

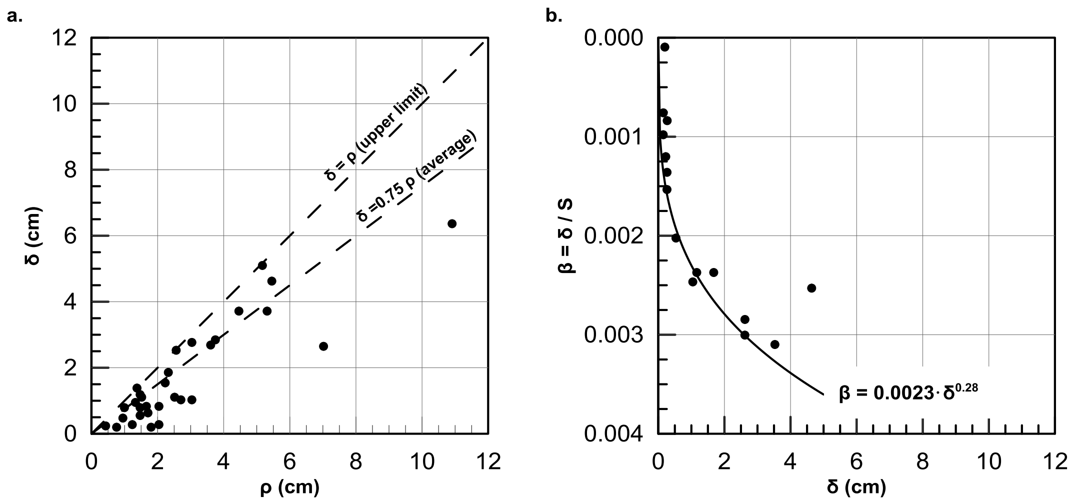

Figure 7.12: Correlation of maximum absolute settlement to (a) maximum differential settlement and (b) angular distortion for buildings on sandy foundation soils (Bjerrum, 1963).

Σχήμα 7.12: Συσχέτιση μέγιστης απόλυτης καθίζησης (α) μέγιστης διαφορικής καθίζησης και (β) γωνιακής παραμόρφωσης για κτίρια επί μη συνεκτικών εδαφών (Bjerrum, 1963).

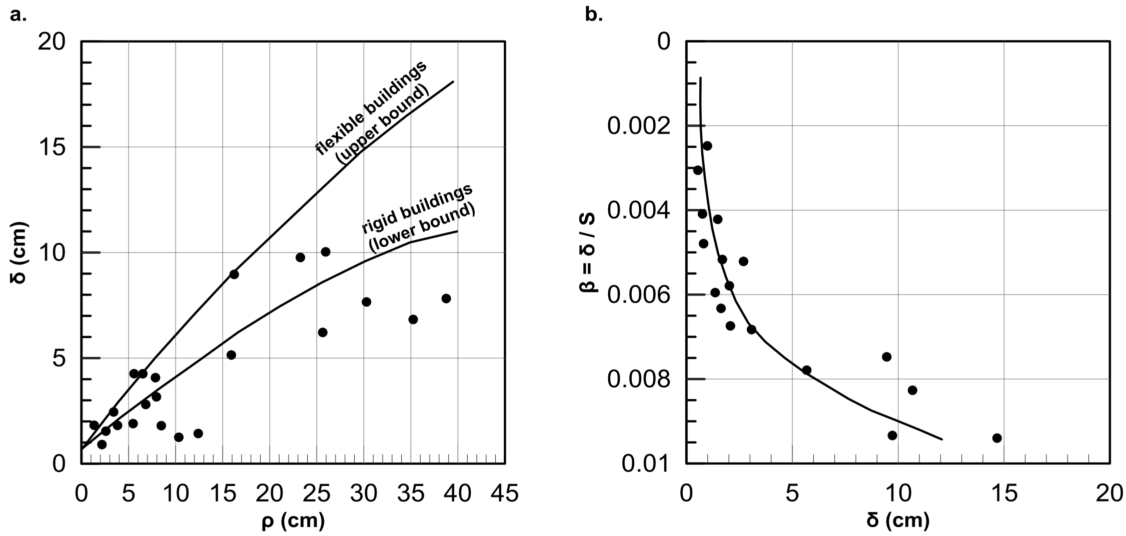

Figure 7.13: Correlation of maximum absolute settlement to (a) maximum differential settlement and (b) angular distortion for buildings on clayey soils (Bjerrum, 1963).

Σχήμα 7.13: Συσχέτιση μέγιστης απόλυτης καθίζησης (α) μέγιστης διαφορικής καθίζησης και (β) γωνιακής παραμόρφωσης για κτίρια επί συνεκτικών εδαφών (Bjerrum, 1963).

Burland et al. (1977).- Based on the data by Skempton & MacDonald (1956) and others, Burland et al. correlated the degree of damage observed in buildings to the maximum settlement *ρ* and the maximum differential settlement *δ*. These correlations refer to uniform clay layers and they are summarized in **Figure 7.14**, separately for framed buildings on isolated foundations (**Figure 7.14a**) and for buildings on raft foundations (**Figure 7.14b**).

In the case of bridges, the first of the above correlations may be used to estimate differential settlements *δ* between neighboring piers, while the second figure may be approximately used to obtain the angle of tilting *θ* relative to the vertical, assuming a reasonable value for the width of the raft foundation [e.g. $\theta = \tan^{-1}(\delta/B)$, with B=10÷20m].

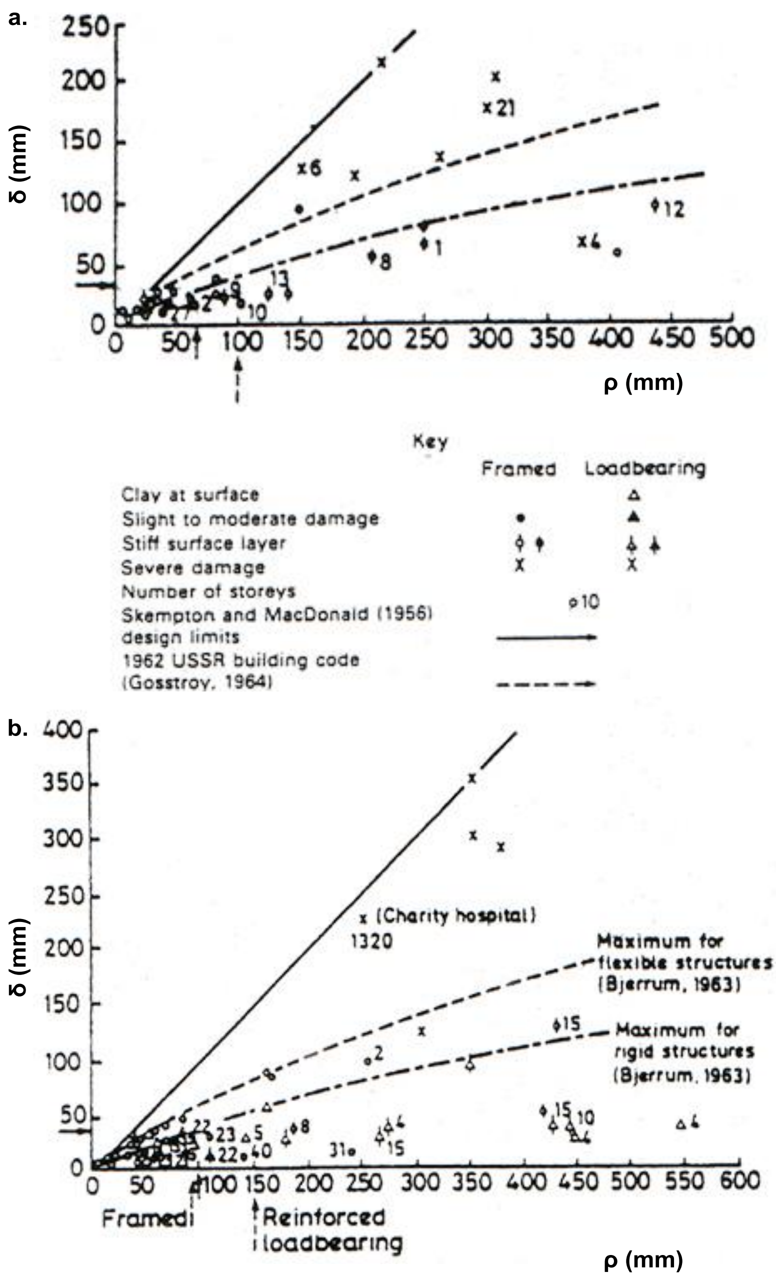

Figure 7.14: Observed maximum and differential settlements in buildings on (a) isolated and (b) raft foundations on uniform clay layers (Burland et al., 1977).

Σχήμα 7.14: Μέγιστες και διαφορικές καθιζήσεις σε κτίρια με (α) μεμονωμένα πέδιλα και (β) κοιτόστρωση επί αργιλικών στρώσεων (Burland et al., 1977).

Justo (1987).- More recently, similar correlations were proposed by Justo (1987), based on observations from different researchers. Namely, in **Figure 7.15a**, the maximum angular distortion β is correlated to the maximum settlement ρ for *isolated* foundations, located either on clays or sands. The trends shown in the figures can be approximated with the following expressions (Grant et al. 1974):

$$\beta = 0.000667 \cdot \rho(\text{cm}) \text{ (for sands)} \tag{7.27}$$

$$\beta = 0.000333 \cdot \rho(\text{cm}) \text{ (for clays)} \tag{7.28}$$

Similarly, **Figure 7.15b**, correlates the maximum angular distortion β with maximum differential settlements δ based on the data for sands and clays.

$$\beta = 0.0011 \cdot \delta(\text{cm}) \text{ (for sands)} \tag{7.29}$$

$$\beta = 0.000606 \cdot \delta(\text{cm}) \text{ (for clays)} \tag{7.30}$$

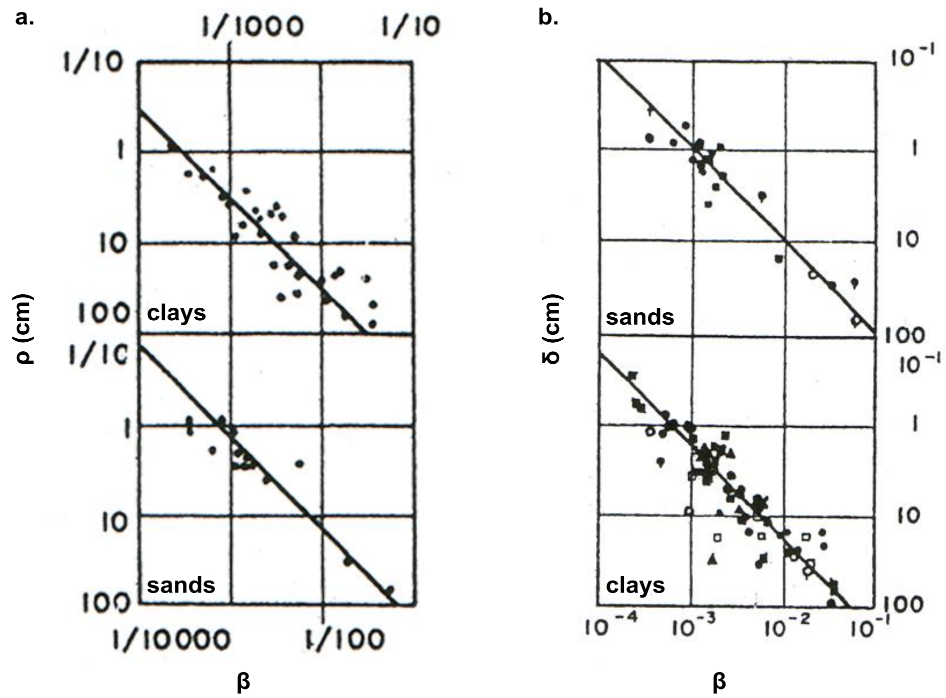

Figure 7.15: (a) Correlation between maximum angular distortion β_{max} and maximum settlement s_{max}, for isolated foundations on clays and sands- fills. (b) Correlation between maximum angular distortion β_{max} and maximum settlement s_{max}, for buildings on clays and sands-fills (Justo, 1987).

Σχήμα 7.15: (α) Συσχέτιση μέγιστης στροφικής παραμόρφωσης, β_{max}, – μέγιστης καθίζησης, s_{max}, μεμονωμένης θεμελίωσης σε αργίλους και άμμους. (β) Συσχέτιση μέγιστης στροφικής παραμόρφωσης, β_{max}, – μέγιστης καθίζησης, s_{max}, κτιρίων σε αργίλους και άμμους (Justo, 1987).

The above recommendations are comparatively evaluated, for the case of sandy soils, in **Figure 7.16** and **Figure 7.17**, in terms of differential settlement and angular distortion respectively. In **Figure 7.16** the Skempton and MacDonald methodology, which concerns angular distortion, has been applied for a footing-to-footing distance S=10m. Similarly, in **Figure 7.17**, Sowers' and Bjerrum's equations are shown for S=10m. It can be observed that the various recommendations form a relatively narrow band both for the case of differential settlement as well as for angular distortion.

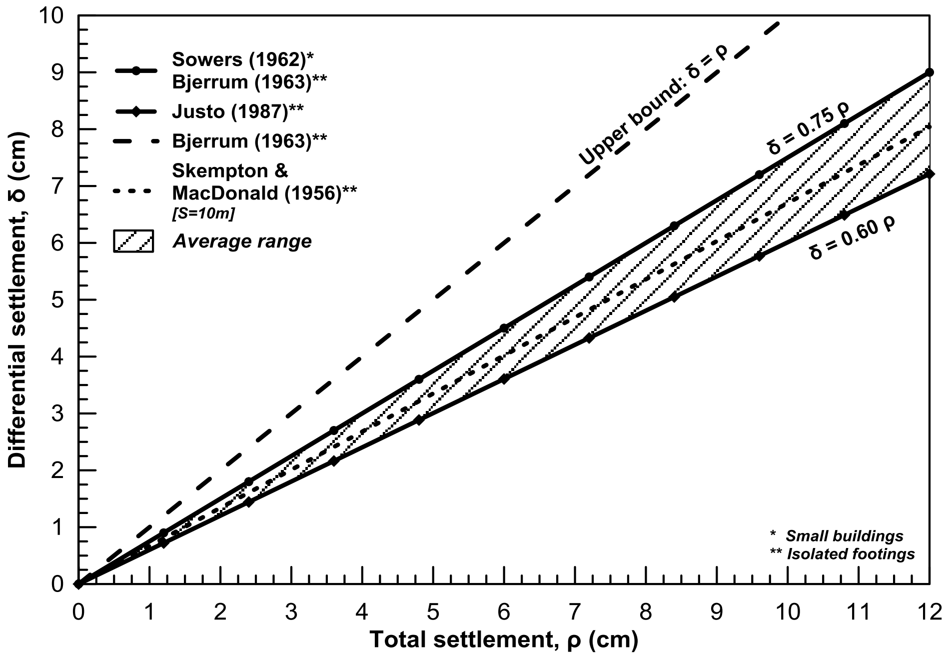

Figure 7.16: Evaluation of differential settlements in cohesionless soils.
Σχήμα 7.16: Εκτίμηση διαφορικών καθιζήσεων σε μη-συνεκτικά υλικά.

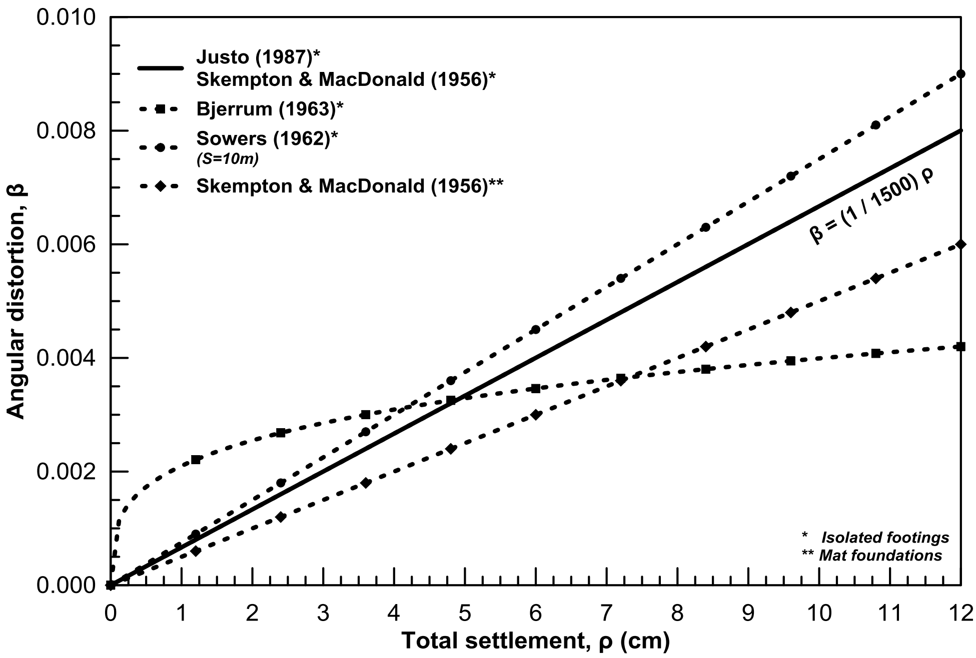

Figure 7.17: Angular distortion in cohesionless soils based on various recommendations.
Σχήμα 7.17: Γωνιακή παραμόρφωση σε μη-συνεκτικά υλικά.

7.4 Tilting θ (relative to the vertical axis)

The only studies found in the literature which refers specifically to the tilting of buildings on shallow foundations, due to earthquake - induced liquefaction, are those of Yasuda et al. (2001) and Yasuda (2014) who collected data from the Kocaeli (1999), the Niigata (1964) and the Luzon (1990) earthquakes and correlated the angle of tilting θ (deg) to the seismic-induced settlement ρ_{dyn} (**Figure 7.18**):

$$\theta(\text{deg}) = 0.05\rho_{dyn}(\text{cm}) \tag{7.31}$$

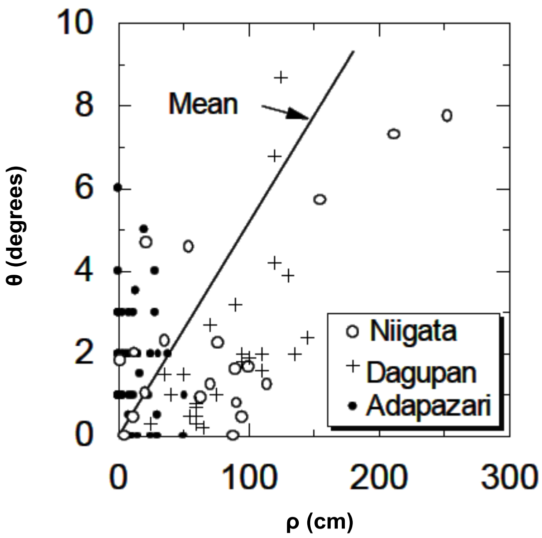

Figure 7.18: Relationship between total settlement and angle of inclination (Yasuda et al., 2014).
Σχήμα 7.18: Συσχέτιση συνολικής καθίζησης – στροφής (Yasuda et al., 2014).

Figure 7.19 compares Yasuda's recommendations (applicable for dynamic loading) to the methodologies described previously for differential settlements and angular distortion (applicable for static loading). The "static" methodologies are applied assuming that the angular distortion is equal to the tilt (β=θ). For the case of raft foundations (Skempton and MacDonald) this is a rational estimate, while for the case of spread footings it serves only as a rough approximation. In any case, the comparison shown in the figure reveals that in order to account for dynamic loading, the "static" methodologies should be multiplied by a factor of 1.35.

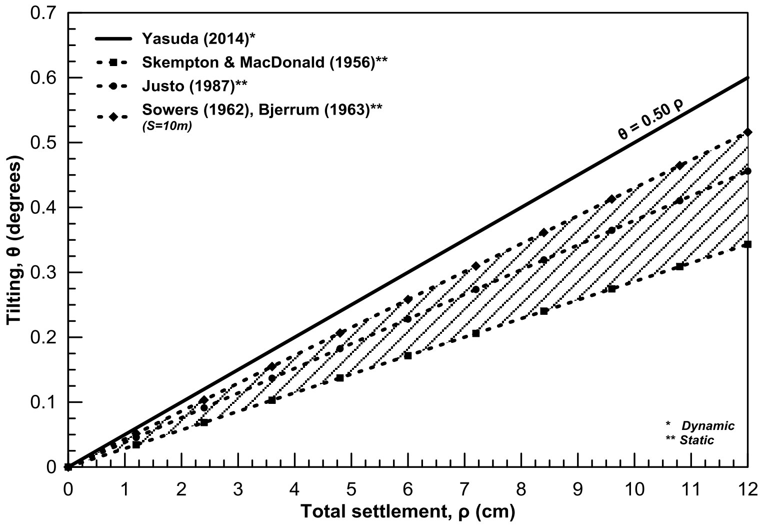

Figure 7.19: Tilting in cohesionless soils for static and dynamic loading conditions.
Σχήμα 7.19: Εκτίμηση στροφής σε μη-συνεκτικά υλικά για στατική και δυναμική φόρτιση.

References

Acacio, A., Kobayashi, Y., Towhata, I., Bautista, R., and Ishihara, K. (2001). "Subsidence of building foundation resting upon liquefied subsoil case studies and assessment." *Soils and Foundations*, 41(6), 111–128.

Adalier, K., Elgamal, A., Meneses, J., and Baez, J. . (2003). "Stone columns as liquefaction countermeasure in non-plastic silty soils." *Soil Dynamics and Earthquake Engineering*, 23(7), 571–584.

Andrianopoulos, K. I., Papadimitriou, A. G., and Bouckovalas, G. D. (2010). "Bounding surface plasticity model for the seismic liquefaction analysis of geostructures." *Soil Dynamics and Earthquake Engineering*, 30(10), 895–911.

Arulmoli, K., Muraleetharan, K. K., Hossain, M. M., and Fruth, L. S. (1992). "VELACS: verification of liquefaction analyses by centrifuge studies; Laboratory Testing Program – Soil Data Report." *Research Report, The Earth. Technology Corporation*.

Barker, R. M., Duncan, J. M., Rojiani, K. B., Ooi, P. S. K., Tan, C. K., and Kim, S. G. (1991). "Manuals for the design of bridge foundations." *National Cooperative Highway Research Program (NCHRP) Report 343, TRB, National Research Council*, Washington, D.C.

Been, K., and Jefferies, M. G. (1985). "A state parameter for sands." *Géotechnique*, 35(2), 99–112.

De Beer, E. E. (1970). "Experimental Determination of the Shape Factors and the Bearing Capacity Factors of Sand." *Geotechnique*, 20(4), 387–411.

Bouckovalas, G., Allen Marr, W., and Christian, J. (1986). "Analyzing Permanent Drift Due to Cyclic Loads." *Journal of Geotechnical Engineering*, American Society of Civil Engineers, 112(6), 579–593.

Bouckovalas, G. D., Karamitros, D. K., Papadimitriou, A. G., Loukidis, D., and Vavourakis, V. (2012). *THALIS-NTUA: Innovative Design of Bridge Piers on Liquefiable Soils with the Use of Natural Seismic Isolation – Work Package 2: Software development for the numerical analysis of the coupled liquefiable soil-foundation-bridge pier response*.

Bouckovalas, G. D., Valsamis, A. I., and Andrianopoulos, K. I. (2005). "Pseudo static vs. performance based seismic bearing capacity of footings on liquefiable soil." *Procedings of the Geotechnical Earthquake Engineering Satellite Conference of the TC4 Committee, ISSMGE, on Performance Based Design in Earthquake Geotechnical Engineering: Concepts and Research*, Osaka, Japan.

Bouckovalas, G., Whitman, R., and Marr, W. (1984). "Permanent Displacement of Sand With Cyclic Loading." *Journal of Geotechnical Engineering*, American Society of Civil Engineers, 110(11), 1606–1623.

Burland, J. B., Broms, B. B., and DeMello, V. F. (1977). "Behavior of Foundations and Structures." " *State of the art report, 9th International Conference on Soil Mechanics and Foundation Engineering*, Tokyo, 495–546.

Byrne, P. M. (1991). "A model for predicting liquefaction induced displacement." *Procedings of the 2nd International Conference on Recent Advances in Geotechnical Earthquake Engineering and Soil Dynamics*.

Byrne, P. M., and Beaty, M. (1998). "An effective stress model for predicting liquefaction." *Geotechnical Special Publication*.

Cascone, E., and Bouckovalas, G. D. (1998). "Seismic bearing capacity of footings on saturated sand with a clay cap." *Procedings of the 11th European Conference on Earthquake Engineering*.

Chaloulos, Y. K., Bouckovalas, G. D., and Karamitros, D. K. (2013). "Pile response in submerged lateral spreads: Common pitfalls of numerical and physical modeling techniques." *Soil Dynamics and Earthquake Engineering*, 55, 275–287.

Chaloulos, Y. K., Bouckovalas, G. D., and Karamitros, D. K. (2014). "Analysis of Liquefaction Effects on Ultimate Pile Reaction to Lateral Spreading." *Journal of Geotechnical and Geoenvironmental Engineering*, (http://dx.doi.org/10.1061/(ASCE)GT.1943-5606.0001047).

Coelho, P. A. L. F., Haigh, S. K., and Madabhushi, S. P. G. (2004). "Centrifuge modelling of the effects of earthquake-induced liquefaction on bridge foundations." *Proc. 11th International Conferene on Soil Dynamics and Earthquake Engineering*, Berkeley, California.

Dashti, S., Bray, J. D., Pestana, J. M., Riemer, M., and Wilson, D. (2010). "Mechanisms of Seismically Induced Settlement of Buildings with Shallow Foundations on Liquefiable Soil." *Journal of Geotechnical and Geoenvironmental Engineering*, American Society of Civil Engineers, 136(1), 151–164.

Elgamal, A., Lu, J., and Yang, Z. (2005). "Liquefaction-induced settlement of shallow foundations and remediation: 3D numerical simulation." *Journal of Earthquake Engineering*, Department of Structural Engineering, University of California, San Diego, San Diego, CA 92093, United States, 9(SPEC. ISS.), pp. 17–45.

Ghosh, B., and Madabhushi, S. P. G. (2003). "A numerical investigation into effects of single and multiple frequency earthquake motions." *Soil Dynamics and Earthquake*

Engineering, Geotechnical Research Group, Department of Engineering, University of Cambridge, Cambridge, United Kingdom, 23(8), pp. 691–704.

Grant, R., Christian, J. T., and Vanmarcke, E. H. (1974). "Differential Settlement of Buildings." *Journal of the Geotechnical Engineering Division*, ASCE, 100(9), 973–991.

Hardin, B. O. (1978). *NATURE OF STRESS-STRAIN BEHAVIOR FOR SOILS.* ASCE, 3–90.

Iai, S. (1991). "A strain space multiple mechanism model for cyclic behavior of sand and its application." *Earthquake Engineering Research Note No. 43*, Port and Harbor Researh Institute, Ministry of Transport, Japan.

Ishihara, K. (1985). "Stability of Natural Deposits during Earthquakes." *Procedings of the 11th International Conference on Soil Mechanics and Foundation Engineering*.

Ishihara, K. (1995). "Effects of at-depth liquefaction on embeded foundations." *Procedings of the 11th Asian RegionalConference on Soil Mechanics and Foundation Engineering*.

Ishihara, K., and Yoshimine, M. (1992). "Evaluation of settlements in sand deposits following liquefaction during earthquakes." *Soils and Foundations*, 32(1), 173–188.

Iwasaki, T., Arawaka, T., and Tokida, K. (1982). "Simplified procedures for assessing soil liquefaction during earthquakes." *Procedings of the conference on Soil Dynamics and Earthquake Engineering*, Southampton, UK.

Iwasaki, T., Tatsuoka, F., Tokida, K., and Yasuda, S. (1978). "A practical method for assessing soil liquefaction potential based on case studies at various sites in Japan." *Procedings of the 2nd International Conference on Microzonation*, San Francisco, California, USA.

JFDA. (1974). "Notification specifying detailed provisions of technical criteria for regulating dangerous articles." *Fire Defence Agency*, (in Japanese).

JGS. (1998). *Remedial measures against soil liquefaction: from investigation and design to implementation.* Japanese Geotechnical Society, Rotterdam; Brookfield, Vt.: A.A. Balkema, 443.

Juang, C., Jiang, T., and Andrus, R. (2002). "Assessing Probability-based Methods for Liquefaction Potential Evaluation." *Journal of Geotechnical and Geoenvironmental Engineering*, American Society of Civil Engineers, 128(7), 580–589.

Juang, C., Yuan, H., Li, D. K., Yang, S. H., and Christopher, R. A. (2005). "Estimating severity of liquefaction-induced damage near foundation." *Soil Dynamics and Earthquake Engineering*, 25(5), 403–411.

Justo, J. L. (1987). "Some applications of the finite element method to soil-structure interaction problems." *Actes Coll. Int. Interactions Sols-Structures*, Presses de l'ENPC Paris, 41.

Karamitros, D., Bouckovalas, G., and Chaloulos, Y. (2012). "Insight into the Seismic Liquefaction Performance of Shallow Foundations." *Journal of Geotechnical and Geoenvironmental Engineering*, American Society of Civil Engineers, 139(4), 599–607.

Karamitros, D. K. (2010). "Development of a Numerical Algorithm for The Dynamic Elastoplastic Analysis of Geotechnical Structures in Two and Three Dimensions." PhD Thesis, Dept of Civil Engineering, NTUA, Athens.

Karamitros, D. K., Bouckovalas, G. D., and Chaloulos, Y. K. (2013). "Seismic settlements of shallow foundations on liquefiable soil with a clay crust." *Soil Dynamics and Earthquake Engineering*, 46(0), 64–76.

Karamitros, D. K., Bouckovalas, G. D., Chaloulos, Y. K., and Andrianopoulos, K. I. (2013). "Numerical analysis of liquefaction-induced bearing capacity degradation of shallow foundations on a two-layered soil profile." *Soil Dynamics and Earthquake Engineering*, 44(0), 90–101.

Kawasaki, K., Sakai, T., Yasuda, S., and Satoh, M. (1998). "Earthquake-induced settlement of an isolated footing for power transmission power." *Centrifuge 98*, 271–276.

Liu, L., and Dobry, R. (1997). "Seismic response of shallow foundation on liquefiable sand." *Journal of Geotechnical and Geoenvironmental Engineering*, ASCE, 123(6), pp. 557–566.

Manzari, M. T., and Dafalias, Y. F. (1997). "A critical state two-surface plasticity model for sands." *Geotechnique*, 47(2), 255–272.

Meek, J. W., and Wolf, J. . (1993). "Why cone models can represent the elastic half-space." *Earthquake Engineering and Structural Dynamics*, 22(9), 759–771.

Men, F.-L., and Cui, J. (1997). "Influence of building existence on seismic liquefaction of subsoils." *Earthquake Engineering and Structural Dynamics*, 26(7), 691–699.

Meyerhof, G. G., and Hanna, A. M. (1978). "Ultimate bearing capacity of foundations on layered soils under inclined loads." *Canadian Geotechnical Journal*, 15(4), 565–572.

Naesgaard, E., Byrne, P. M., and Ven Huizen, G. (1998). "Behaviour of light structures founded on soil 'crust' over liquefied ground." *Geotechnical Special Publication*, 75, 422–433.

Papadimitriou, A. G., and Bouckovalas, G. D. (2002). "Plasticity model for sand under small and large cyclic strains: A multiaxial formulation." *Soil Dynamics and Earthquake Engineering*, Department of Geotechnical Engineering, Faculty of Civil Engineering, National Technical University of Athens, 42 Patission Street, 10682 Athens, Greece, 22(3), pp. 191–204.

Papadimitriou, A. G., Bouckovalas, G. D., and Dafalias, Y. F. (2001). "Plasticity model for sand under small and large cyclic strains." *Journal of Geotechnical and Geoenvironmental Engineering*, ASCE, 127(11), pp. 973–983.

Popescu, R., Prevost, J. H., Deodatis, G., and Chakrabortty, P. (2006). “Dynamics of nonlinear porous media with applications to soil liquefaction.” *Soil Dynamics and Earthquake Engineering*, Faculty of Engineering and Applied Science, Memorial University, St. John’s, Nfld. A1B 3X5, Canada, 26(6-7), pp. 648–665.

Port and Harbour Research Institute, Japan. (1997). *Handbook on liquefaction remediation of reclaimed land*. *Handbook on liquefaction remediation of reclaimed land*, A.A. Balkema.

Richards, R., and Elms, D. G. (1979). “Seismic behavior of gravity retaining walls.” *Journal of geotechnical engineering*, 105, 449–464.

Richards, R., Elms, D. G., and Budhu, M. (1993). “Seismic Bearing Capacity and Settlements of Foundations.” *Journal of Geotechnical Engineering*, American Society of Civil Engineers, 119(4), 662–674.

Seed, H. B., and Idriss, M. I. (1971). “Simplified Procedure for Evaluating Soil Liquefaction Potential.” *Journal of the Soil Mechanics and Foundations Division*, 97(9), 1249–1273.

Skempton, A. W., and MacDonald, D. H. (1956). “THE ALLOWABLE SETTLEMENTS OF BUILDINGS.” *ICE Proceedings: Engineering Divisions*, Thomas Telford, 5(6), 727–768.

Sowers, G. F. (1962). “Shallow Foundations.” *Foundation Engineering*, McGraw-Hill, New York, NY.

Terzaghi, K. (1956). “Discussion on: A. W. Skempton and D. H. MacDonald, Allowable settlements of buildings.” *Institution of Civil Engineers. Proceedings*, 5(3), 775–777.

Tokimatsu, K., and Seed, H. B. (1987). “Evaluation of Settlement in Sands due to Earthquake Shaking.” *Journal of geotechnical engineering*, Tokyo Inst of Technology, Tokyo, Jpn, Tokyo Inst of Technology, Tokyo, Jpn, 113(8), pp. 861–878.

Towhata, I., Orense, R., and Toyota, H. (1999). “Mathematical principles in prediction of lateral ground displacement.” *Soils and Foundations*, 39*(2), 1–19.

Tsuchida, H., Iai, S., and Kurata, E. (1976). “On zone of soil property improvement of soils.” *14th Meeting of Earthquake Engineering*, 9–12 (in Japanese).

Valsamis, A. I., Bouckovalas, G. D., and Papadimitriou, A. G. (2010). “Parametric investigation of lateral spreading of gently sloping liquefied ground.” *Soil Dynamics and Earthquake Engineering*, Geotechnical Department, School of Civil Engineering, National Technical University of Athens, 9 Iroon Polytechniou Street, 15780 Zographou, Greece, 30(6), pp. 490–508.

Vesic, A. S. (1973). “Analysis of ultimate loads of shallow foundations.” *Journal of the Soil Mechanics and Foundations Division*, 99, 45–73.

Wahls, H. E. (1990). *Design and construction of bridge approaches.* Transportation Research Board, National Research Council, TG425 .W34 1990, Washington, D.C., 45.

Yasuda, S. (2014). "Allowable Settlement and Inclination of Houses Defined After the 2011 Tohoku: Pacific Ocean Earthquake in Japan." *Earthquake Geotechnical Engineering Design SE - 5*, M. Maugeri and C. Soccodato, eds., Springer International Publishing, 141–157.

Yasuda, S., Abo, H., Yoshida, N., Kiku, H., and Uda, M. (2001). "Analyses of liquefaction-induced deformation of grounds and structures by a simple method." *Procedings of the 4th International Conference on Recent Advances in Geotechnical Engineering and Soil Dynamics and Symposium in Honor of Professor W.D. Liam Finn*, San Diego, California.

Yasuda, S., Irisawa, T., and Kazami, K. (2001). "Liquefaction-induced settlements of buildings and damages in coastal areas during Kocaeli and other earthquakes." *Proceedings of Fifteenth International Conference on Soil Mechanics and Geotechnical Engineering Satellite Conference*, 33–42.

Yasuda, S., Terauchi, T., Morimoto, H., Erken, A., and Yoshida, N. (1998). "Post liquefaction behavior of several sands." *Procedings of the 11th European Conference on Earthquake Engineering*, Paris, France.

Yasuda, S., Yoshida, N., Adachi, K., Kiku, H., and Gose, S. (1999). "A simplified analysis of liquefaction-induced residual deformation." *Procedings of the 2nd International Conference on Earthquake Geotechnical Engineering (SICEGE)*, Lisbon, Portugal.

Yasuda, S., Yoshida, N., Kiku, H., and Uda, M. (2000). "Estimation of liquefaction-induced deformation of river levees by a simple method." *Procedings of GeoEng 2000: An International Conference on Geotechnical and Geological Engineering*, Melbourne, Australia.

Yoshimi, Y., and Tokimatsu, K. (1977). "Settlement of Buildings on Saturated Sand During Earthquakes." *Soils and Foundations1*, 17(1), 23–38.

Youd, T., Idriss, I., Andrus, R., Arango, I., Castro, G., Christian, J., Dobry, R., Finn, W., Harder, L., Hynes, M., Ishihara, K., Koester, J., Liao, S., Marcuson, W., Martin, G., Mitchell, J., Moriwaki, Y., Power, M., Robertson, P., Seed, R., and Stokoe, K. (2001). "Liquefaction Resistance of Soils: Summary Report from the 1996 NCEER and 1998 NCEER/NSF Workshops on Evaluation of Liquefaction Resistance of Soils." *Journal of Geotechnical and Geoenvironmental Engineering*, American Society of Civil Engineers, 127(10), 817–833.